AGH

AGH University of Science and Technology

FIELD OF SCIENCE: NATURAL SCIENCES

SCIENTIFIC DISCIPLINE: PHYSICAL SCIENCES

DOCTORAL THESIS

Measurement of photon-induced processes in heavy-ion collisions with the ATLAS detector

Author: Agnieszka Ogrodnik

Supervisor: prof. dr hab. inż. Iwona Grabowska-Bołd

Completed in: AGH University of Science and Technology,
Faculty of Physics and Applied Computer Science,
Department of Particle Interactions and Detection Techniques

Kraków, 2022

Declaration of the author of this dissertation:
Aware of legal responsibility for making untrue statements I hereby declare that I have written this dissertation myself and all the contents of the dissertation have been obtained by legal means.

date, author's signature

Declaration of the thesis Supervisor:
This dissertation is ready to be reviewed.

date, supervisor's signature

Acknowledgements

I would like to express my gratitude to my supervisor, Prof. Iwona Grabowska-Bołd, who introduced me to the field of particle physics, shared with me her knowledge and guided me through subsequent steps of the physics analysis. Her patience, understanding and support are invaluable.

Many thanks to all those who contributed to the analyses discussed in this thesis, I really enjoyed working with you all. In particular, I would like to thank Jakub Kremer and Mateusz Dyndał for useful discussions and advice. Thanks to all the people from AGH UST and from ATLAS experiment that I had the pleasure to cooperate with in the last several years.

I would like to also thank my family, especially my husband, Wojtek, and my parents, who supported me through all the years of my studies and were there for me for better and for worse.

This work was partly supported by the National Science Centre of Poland under grants number UMO-2020/37/B/ST2/01043 and UMO-2020/36/T/ST2/00086, and by PL-GRID infrastructure. This research project was also partly supported by the program „Excellence initiative – research university" for the AGH University of Science and Technology.

Contents

Streszczenie

Zderzenia ultrarelatywistycznych ciężkich jonów stanowią podstawę do szerokiej gamy badań oddziaływań silnych, słabych i elektromagnetycznych. Pomiary opisane w tej rozprawie obejmują procesy wywołane przez fotony w ultraperyferycznych zderzeniach ciężkich jonów. Analizowane są dane ze zderzeń jąder ołowiu przy energii 5.02 TeV na parę nukleonów zebrane przez detektor ATLAS na akceleratorze LHC w laboratorium CERN. Poruszającym się z relatywistyczną prędkością jonom towarzyszy pole elektromagnetyczne, które można również interpretować jako strumień fotonów. Dzięki temu, poza oddziaływaniem nukleon-nukleon obserwuje się także oddziaływania foton-nukleon oraz foton-foton. Te ostatnie stają się dominujące w zderzeniach ultraperyferycznych, kiedy odległość między oddziałującymi jądrami jest większa niż suma promieni tych jąder. Interakcje foton-foton zachodzą również w zderzeniach proton-proton, między polami elektromagnetycznymi ultrarelatywistycznych protonów. Jednak strumienie fotonów rosną w kwadracie wraz z liczbą atomową jonu, Z, co w przypadku oddziaływań foton-foton przekłada się na wzrost przekrojów czynnych na dany proces proporcjonalnie do Z^4. W związku z tym, ultraperyferyczne zderzenia ciężkich jonów umożliwiają pomiary rzadkich procesów, a także poszukiwanie nowych zjawisk i cząstek będących sygnałami tzw. Nowej Fizyki.

Ta rozprawa podsumowuje badania dotyczące ultraperyferycznych zderzeń ołów-ołów, w które znaczący wkład wniosła autorka tej pracy w trakcie studiów dotoranckich. W centrum zainteresowania rozprawy doktorskiej są dwa procesy: rozpraszanie foton-foton, $\gamma\gamma \to \gamma\gamma$, oraz główne źródło tła dla tego procesu, czyli ekskluzywna produkcja par elektron-pozyton, $\gamma\gamma \to e^+e^-$. W Modelu Standardowym reakcja $\gamma\gamma \to \gamma\gamma$ jest dozwolona poprzez pętle z wirtualnymi naładowanymi fermionami lub bozonami $W^\pm$. Proces ten może również stanowić tło dla Nowej Fizyki, którego przykładem są rozpady cząstek typu aksjonów. Jego precyzyjne pomiary umożliwią zatem wyznaczenie nowych ograniczeń dla kilku procesów spoza Modelu Standardowego. Natomiast ekskluzywna produkcja par elektron-pozyton, będąca jednym z podstawowych procesów elektrodynamiki kwantowej, jest istotna jako pomiar referencyjny do wielu analiz wykorzystujących dane ze zderzeń ultraperyferycznych. Precyzyjne pomiary tego procesu pozwolą również na udoskonalenie symulacji Monte Carlo dla interakcji foton-foton, w szczególności modelowania strumieni fotonów towarzyszących naładowanym wiązkom jądrowym. Obserwacja par lepton-antylepton pochodzących z interakcji fotonów jest również możliwa w przypadkach z równoczesnym oddziaływaniem hadronowym. Pomiary procesów wywołanych przez fotony w takich przypadkach może stanowić nowe źródło badań nad plazmą kwarkowo-gluonową (ang. Quark-Gluon Plasma, QGP).

Przekroje czynne na procesy wywołane przez fotony w zderzeniach ultraperyferycznych maleją wraz ze wzrostem energii w centrum masy układu foton-foton. Energia poprzeczna fotonów/elektronów w stanie końcowym sięga kilkunastu/kilkudziesięciu GeV, przy czym spektrum jest zdominowane przez kontrybucję od cząstek o energiach kilku GeV. Stanowi to wyzwanie pomiarowe dla detektora ATLAS, który był projektowany i optymalizowany pod detekcję wysokoenergetycznych cząstek o pędzie poprzecznym powyżej 20 GeV. Cechą charakterystyczną rozpatrywanych procesów jest również mała akoplanarność układu fotonów/elektronów w stanie końcowym, co oznacza, że poruszają się one w przeciwnych kierunkach w kącie azymutalnym.

Istotnym elementem, niezbędnym do późniejszego przeprowadzenia badań było przygotowanie przez autorkę rozprawy wydajnego trygera, czyli algorytmu umożliwiającego wstępną selekcję przypadków w czasie rzeczywistym w trakcie zbierania danych przez eksperyment ATLAS. Ten etap wymagał przygotowania dedykowanej strategii, implementacji selekcji i jej optymalizacji zarówno na pierwszym, hardware'wym, poziomie, jak i na drugim, software'owym. Selekcja trygera jest ściśle dopasowana do poszukiwanych procesów: zapisywano przypadki

o niskiej aktywności w centralnej części detektora, niewielkiej aktywności detektora śladów oraz bardzo niskiej aktywności w obszarze „do przodu". Wielkie wyzwanie stanowiła niska energia cząstek w poszukiwanych procesach, będąca na granicy poziomu szumu elektroniki detektora. Dzięki optymalizacji selekcji, znacząco poprawiono wydajność trygera używanego w czasie zbierania danych ze zderzeń ołów-ołów w 2018 r. względem tego używanego w 2015 r.

W rozprawie przedstawione są wyniki pomiarów całkowitych oraz różniczkowych przekrojów czynnych na rozpraszanie foton-foton oraz ekskluzywną produkcję par elektron-pozyton. Przekroje czynne zbadane zostały w kilku zmiennych kinematycznych. Zaprezentowane wyniki porównane są z kilkoma przewidywaniami teoretycznymi dla badanych procesów.

Abstract

Collisions of ultrarelativistic heavy ions provide a mean to study a variety of strong, weak and electromagnetic interactions. Measurements described in this thesis include photon-induced processes in ultraperipheral collisions of heavy ions. The analysed data from collisions of lead nuclei at the energy of 5.02 TeV per nucleon pair were recorded by the ATLAS detector at the LHC in CERN. The ions travelling at relativistic velocities are accompanied by the electromagnetic field, which can also be interpreted as a flux of photons. Due to this fact, apart from nucleon-nucleon interactions, one can also observe photon-nucleon and photon-photon interactions. The latter become dominant in ultraperipheral collisions, when the distance between interacting nuclei is greater than the sum of their radii. Photon-photon interactions occur also in proton-proton collisions, between electromagnetic fields of ultrarelativistic protons. However, each photon flux scales quadratically with the ion atomic number, Z, what in case of photon-photon beams leads to a Z^4 enhancement of the cross-sections for the given process. Therefore, ultraperipheral heavy-ion collisions enable measurements of rare processes, and also searches for new phenomena and new particles, being signals of so-called New Physics.

This thesis discusses measurements of ultraperipheral lead-lead collisions, with a significant contribution of the author of this thesis, during her doctoral studies. The thesis is focused on two processes: photon-photon scattering or light-by-light scattering, $\gamma\gamma \to \gamma\gamma$, and the main background for this process, exclusive production of electron-positron pairs, $\gamma\gamma \to e^+e^-$. In the Standard Model, the $\gamma\gamma \to \gamma\gamma$ reaction is allowed through loops involving virtual charged fermions or $W^\pm$ bosons. This process can also be considered as background for the New Physics, for example for decays of axion-like particles. Precision measurements of the process would enable setting the new limits for several processes beyond the Standard Model.

The exclusive production of electron-positron pairs, which is one of the fundamental processes of quantum electrodynamics, is a benchmark process for other analyses of ultraperipheral collision data. Precision measurements of this process would help improve the Monte Carlo simulations for photon-photon interactions, in particular modelling of the photon fluxes, associated to charged nuclear beams. Production of lepton-antilepton pairs originating from photon-photon interactions is also possible in events with simultaneous hadronic interactions. Measurement of photon-induced processes in such events provides a new probe of Quark-Gluon Plasma.

The cross-sections for photon-induced processes in ultraperipheral collisions are decreasing with the centre-of-mass energy of the photon-photon system. The transverse energy of photons/electrons in the final state reaches out to tens of GeV, but the spectrum is dominated by particles with the energy of a few GeV. Its efficient detection poses a challenge for the ATLAS detector, which was designed and optimised for high-energy particles, with transverse momenta above 20 GeV. A characteristic feature of the considered processes is also low acoplanarity of the photon-photon or electron-positron final states Acoplanarity quantifies a difference in the azimuthal angles between final-state particles. Its value close to zero means that they have opposite directions in the azimuthal angle.

The important aspect of successful measurements with low transverse momentum photons and electrons was preparation of the efficient trigger, i.e. a set of algorithms that enables the online selection during the data taking in the ATLAS experiment, done by the author of this thesis. This step required development of the dedicated strategy, implementing online selection and its optimisation both at the first, hardware level, and at the second, software level. Trigger selection is tightly related to the studied processes: events with low activity in the central detector, minor activity in the tracking system and very low activity in the forward direction were recorded. A great challenge was the low energy of the final state particles in the studied processes, which was close to the noise threshold of the detector electronics. Thanks to the selection optimisation, the trigger efficiency was significantly improved in the 2018 Pb+Pb

data taking with respect to the trigger used in the 2015 Pb+Pb run.

In this thesis, the results of the integrated and differential fiducial cross-sections are presented for light-by-light scattering and exclusive production of electron-positron pairs. The second process is measured with high precision. In particular the statistical uncertainty on the integrated fiducial cross-section is at the level of 0.6%, while the systematic uncertainty is dominated by the electron reconstruction and identification component and it amounts to 10%. The differential cross-sections are measured in several kinematic variables or both processes. The presented results are compared with theoretical predictions from STARLIGHT and SUPERCHIC for the measured processes. The measurements become important input to further improvement of the modelling of photon-induced processes in ultraperipheral collisions of relativistic nucleus-nucleus beams.

Chapter 1

Introduction

The collisions of ultrarelativistic heavy ions were first proposed as a mean to study hot and dense state of matter called a quark-gluon plasma (QGP). The QGP is considered to be a form of matter that existed $10^{-10} - 10^{-6}$ s after the Universe was born and consists of deconfined quarks and gluons. The heavy-ion collisions enable studies of the strong, weak and electromagnetic (EM) interactions that can occur simultaneously due to multiple nucleon-nucleon interactions. However, the EM interactions, being in the centre of interest of this dissertation, become dominant when two interacting nuclei pass each other at the distance larger than twice the ion radius. Such a class of collisions is called the ultraperipheral collisions (UPC). The large EM fields associated to ultrarelativistic ions can be considered as coherently produced fluxes of photons.

This dissertation focuses on measurements of two processes that might occur in the UPC: the exclusive production of electron-positron pairs, $\gamma\gamma \to e^+e^-$, and the light-by-light scattering, $\gamma\gamma \to \gamma\gamma$. Both were measured, with a leading contribution of the author of this dissertation, using lead-lead collision data recorded in 2015 and 2018 with the ATLAS detector at the LHC. To be able to measure these two processes, first the data needed to be collected. The collision rate at the LHC reaches up to 40 MHz during the proton-proton data taking, which makes it impossible to record all the events. For this purpose in modern particle detectors, a trigger system is used, which selects the interesting events for further study. The author of the thesis was responsible for developing a strategy, implementation and optimisation of the trigger strategy for the 2018 data taking and later for the measurement of the trigger efficiency for $\gamma\gamma$ and e^+e^- event candidates. Apart from the electron reconstruction/identification studies and the forward activity analysis, the measurement of the cross-section for the exclusive production of the electron pairs was done by the author of this thesis.

The first part of this dissertation provides a theoretical introduction to the physics of photon-photon interactions, which is followed by the description of the ATLAS detector in Chapter 3. Later, in Chapter 4 the discussion of the trigger developments pursued to efficiently collect the data in 2018 is given. In Chapters 5 and 6, the results of the cross-section measurements for the two considered processes are presented. The dissertation is finalised by the conclusions and outlook in Chapter 7.

The work done by the author was published in the following scientific articles authored by the ATLAS Collaboration:

- ATLAS Collaboration, "Observation of light-by-light scattering in ultraperipheral Pb+Pb collisions with the ATLAS detector", Phys. Rev. Lett. 123 (2019) 052001
- ATLAS Collaboration, „Measurement of light-by-light scattering and search for axion-like particles with 2.2 nb^{-1} of Pb+Pb data with the ATLAS detector” JHEP03 (2021) 243, 1-49

- ATLAS Collaboration, "Exclusive dielectron production in ultraperipheral Pb+Pb collisions at $\sqrt{s_{\mathrm{NN}}}$ =5.02 TeV with ATLAS", conference note ATLAS-CONF-2022-025
- ATLAS Collaboration, "Exclusive dielectron production in ultraperipheral Pb+Pb collisions at $\sqrt{s_{\mathrm{NN}}}$ =5.02 TeV with ATLAS", submitted to Journal of High Energy Physics, arXiv:2207.12781

and in the following conference proceedings:

- Agnieszka Ogrodnik, "Triggering on light-by-light scattering in the ATLAS experiment" PoS LHCP2018 (2018) 030
- Agnieszka Ogrodnik, „Light-by-light scattering in lead-lead collisions in the ATLAS experiment" Acta Physica Polonica, B 50 (2019) 1159
- Agnieszka Ogrodnik, „Exclusive dilepton production in ultraperipheral lead-lead collisions in the ATLAS experiment", Acta Physica Polonica, B 52 (2021) 1039
- Agnieszka Ogrodnik, "Exclusive dilepton production in ultraperipheral Pb+Pb collisions in ATLAS", LHCP2022 proceedings in preparation

Author presented results of this work on behalf of the ATLAS Collaboration at the following international conferences:

- Sixth Annual Large Hadron Collider Physics LHCP 2018, Bologna, VI 2018, poster: „Triggering on light-by-light scattering in the ATLAS experiment"
- XXV Cracow Epiphany Conference on Advances in Heavy Ion Physics, Kraków, 9 I 2019, talk: „Light-by-light scattering in lead-lead collisions in the ATLAS experiment"
- ATLAS Week, Geneva, 11 II 2019, poster: „Triggering on light-by-light scattering in 2018 Pb+Pb collisions"
- XIV Polish Workshop on Relativistic Heavy-Ion Collisions, Kraków, 6 IV 2019, talk: „Light-by-light scattering in lead-lead collisions in the ATLAS experiment - from evidence to observation"
- Interpreting the LHC Run 2 Data and Beyond, Triest, 29 V 2019, talk: „Observation of light-by-light scattering in lead-lead collisions in the ATLAS experiment"
- XXVII Cracow Epiphany Conference on Future of Particle Physics, 10 I 2021, talk: „Exclusive dilepton production in ultraperipheral lead-lead collisions in the ATLAS experiment"
- VI-th International Conference on the Initial Stages of High-Energy Nuclear Collisions, 12 I 2021, poster: „Light-by-light scattering in ultra-peripheral Pb+Pb collisions with ATLAS"
- XXIXth International Conference on Ultra-relativistic Nucleus-Nucleus Collisions (Quark Matter 2022), Kraków, 6 IV 2022, talk: "Beyond Standard Model searches in ultraperipheral heavy-ion collisions with ATLAS"
- The Tenth Annual Large Hadron Collider Physics (LHCP2022), online, 17 V 2022, poster: "Exclusive dilepton production in ultraperipheral Pb+Pb collisions in ATLAS"
- 51st International Symposium on Multiparticle Dynamics (ISMD2022), Pitlochry, 1 VIII 2022, talk: "Photon-photon fusion and tau $g-2$ measurement in ATLAS"

Chapter 2

Theoretical introduction

2.1 Standard Model

The theory that best describes our current understanding of the particle physics is the Standard Model (SM). It includes three out of four fundamental forces: strong, weak and electromagnetic.

The foundations of the SM were laid in 1954 by Yang and Mills [1] who constructed a gauge theory that was meant to describe strong interactions. Several years after, based on his gauge theory approach, Glashow [2] proposed the unified description for the weak and electromagnetic interactions. This unification was independently described also by Salam and Ward [3] and Weinberg [4], along with the mechanism of spontaneously broken symmetry in publications of Weinberg [4] and Salam [5]. The inclusion of this mechanism completed the theory of the electroweak interactions. The mechanism of the spontaneously broken symmetry itself explained the origin of particles' mass and was developed by Higgs [6], Brout and Englert [7], and also by Guralnik, Hagen and Kibble [8]. The modern theory of strong interactions have its origin in mid-1960s, when the idea of quarks was introduced by Gell-Mann [9] and Zweig [10], and extended by Greenberg [11] to include the colour charge. Finally, the concept of asymptotic freedom of strongly interacting particles was introduced to the theory by Gross and Wilczek [12], and Politzer [13].

Mathematically, the SM is described by the group theory notation as: $SU(3) \times SU(2) \times U(1)$, with $SU(3)$ being the gauge symmetry group of the strong interaction, and $SU(2) \times U(1)$ refers to the symmetry group of the unified electroweak interaction.

The SM describes the world as matter built from fermions, and interactions, mediated by bosons. The fermions can be divided into leptons and quarks. Each group consist of six particles and their six antiparticle counterparts. Leptons do not undergo strong interactions. Both leptons and quarks are ordered by their mass in three generations. Only the lightest elementary particles, an electron and up and down quarks form matter which surrounds us.

The quarks cannot be observed as free particles, but always stay in bound forms as mesons (quark-antiquark pairs) or baryons (built from three quarks). Only the heaviest top quark does not form composite particles, as it decays almost immediately after it is created. The gauge bosons of the SM: massless photons, massive $W^{\pm}$ and Z bosons and massless gluons mediate electromagnetic, weak and strong interactions, respectively. The last elementary particle is the Higgs boson, which existence explains the origin of mass of $W^{\pm}$ and Z bosons.

The great success of the SM was its ability to predict the existence and properties of the electroweak bosons, gluons, charm and top quarks, and the Higgs boson. The precision tests of the SM are performed in a wide variety of measurements. Figure 2.1 summarises some of the cross-section measurements of the SM processes performed by the ATLAS Collaboration along with the comparison to theory predictions. In general, the results agree very well with

the SM expectations. However, phenomena exist which are not explained by the SM, e.g. the asymmetry in the observed amount of matter and antimatter, the neutrino oscillations, the nature of dark matter or dark energy. Therefore, apart from precision tests of the SM, also searches for the Beyond Standard Model (BSM) phenomena are performed, based on theories extending the SM description of the particle physics.

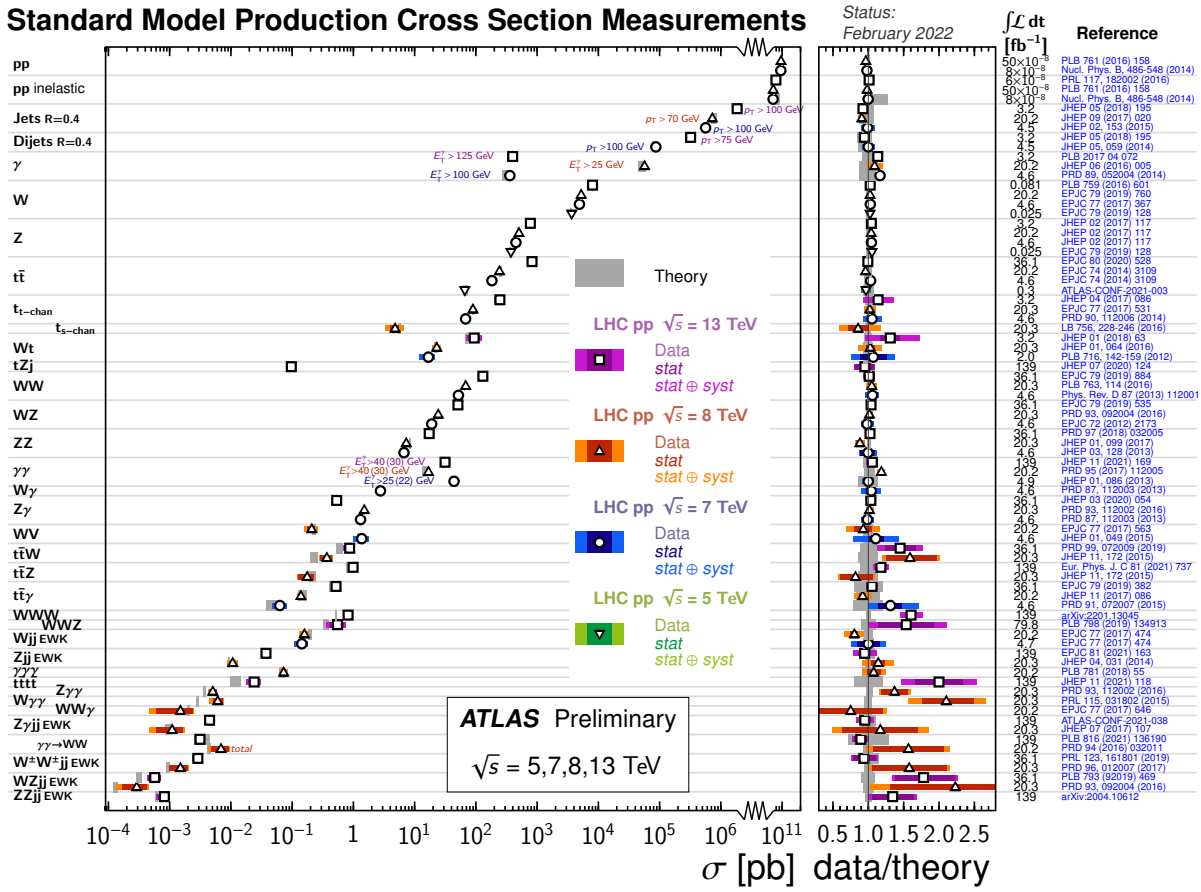

Figure 2.1: Summary of a variety of SM total and fiducial production cross-section measurements from the ATLAS experiment at the LHC, corrected for branching fractions, compared to the corresponding theoretical expectations. The right panel shows ratios of the data over theory. In some cases, the fiducial selection is different between measurements in the same final state for different centre-of-mass energies $\sqrt{s}$, resulting in lower cross-section values at higher $\sqrt{s}$ [14].

2.2 Heavy-ion collisions

The collisions of relativistic heavy ions are considered a mean to study matter under extreme conditions of temperature and particle density, similar to the ones that existed between 10^{-10} – 10^{-6} s after the Big Bang. In this state of matter, also called a quark-gluon plasma, the quarks and gluons are not confined in hadrons. This lack of strong bounds is also called asymptotic freedom.

A schematic view of the heavy-ion (HI) collision is depicted in Fig. 2.2. The relativistic ions get thinner due to Lorentz contraction. The nucleons taking part in the collision are called participants, while remaining nucleons are named spectators. The distance between the ion barycentres in the plane perpendicular to the ion velocity is called the impact parameter, b.

The values of b close to 0 are characteristic for central, "head-on", collisions, while b close to $2R_A$, where R_A is the ion radius, occur for so-called peripheral collisions. When $b > 2R_A$, the ultraperipheral collisions (UPC) are considered. The value of b is not accessible experimentally, but many observables in the HI physics depend on the size of the overlap region between two nuclei. Therefore, a collision centrality has been defined, to quantitatively describe how peripheral the collision is. The 10% of most central events belong to the $0 - 10\%$ centrality class, while the $80 - 100\%$ class consists of 20% of the least central events.

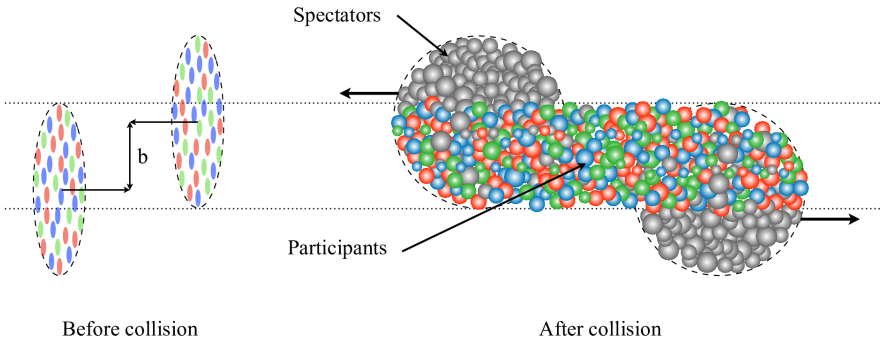

Figure 2.2: The schematic view of the HI collision. The participants and spectators are shown along with the impact parameter, b [15].

Based on the fact that a characteristic feature of the central collisions is a high number of produced particles, one of the experimental measures of the centrality is the level of detector activity in the forward region. In the ATLAS experiment, the event centrality is determined by transverse energy deposited in the Forward Calorimeters (FCal). As shown in Fig. 2.3, the 10% of most central events have the highest energy deposits in FCal, what corresponds to the centrality of 0–10%. The most peripheral events have a very low sum of transverse energy in FCal. In fact for the UPC events, it is consistent with the noise level in the FCal. The transverse energy deposit in FCal is well correlated with the total number of charged particles in the event, as shown in Fig. 2.4. Therefore, since UPC events have a very low FCal energy deposit, they are also characterised by the low activity in the whole detector. The physics processes characteristic for events in this class of HI collisions are discussed in the following sections.

2.3 Physics of two-photon interactions in ultraperipheral collisions

Heavy ions are a source of EM fields, which for ions at relativistic velocities are transverse to the direction of their propagation. At impact parameters larger than twice the nuclear radius there is no overlap of the interacting nuclei. Instead, EM fields may interact. Already in 1924 Enrico Fermi proposed that the EM fields can be treated as fluxes of virtual photons [18]. This idea was extended to calculate the virtual photon fluxes from the relativistic ions by Weizsäcker and Williams [19]. The theory they developed is referred to as the equivalent photon approximation (EPA) or the Weizsäcker-Williams method. For photons emitted coherently from the ions (i.e. photon wavelength must be greater than R_A) one can estimate a maximum transverse momentum scale from the uncertainty principle, and it is at the level of $O(\hbar c/R_A) \approx$

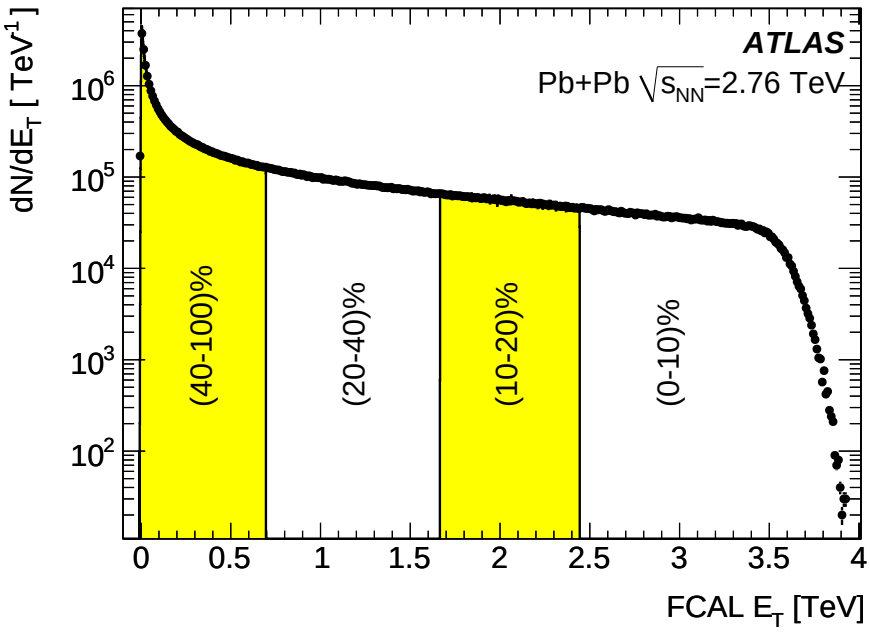

Figure 2.3: Distribution of uncorrected sum of transverse energy, ΣE_T for minimum-bias lead-lead collisions in the Forward Calorimeter (FCal). Bins in event activity or "centrality" are indicated by the alternating bands and labelled according to an increasing fraction of total lead-lead cross-section starting from the largest measured ΣE_T [16].

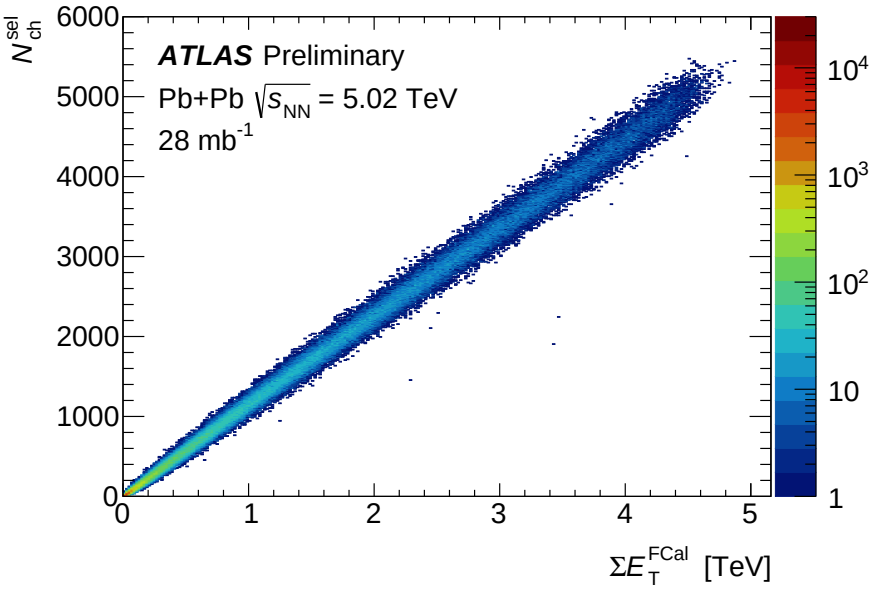

Figure 2.4: Number of reconstructed charged particles $N_{\mathrm{ch}}^{\mathrm{sel}}$, versus total transverse energy ΣE_T in the FCal. Events were selected online based on the presence of neutrons emitted at small angles with respect to the beam and have a reconstructed primary vertex. Tracks are selected from a pseudorapidity range $|\eta| = |-\ln\tan\frac{\theta}{2}| < 2.5$ with transverse momentum $p_{\mathrm{T}} > 0.3\,\mathrm{GeV}$. [17].

30 MeV. It translates to the photon virtuality of $Q < 10^{-3}\,\mathrm{GeV}^2$. The longitudinal momentum of photons is multiplied by the Lorentz factor, γ_L, which for the case of the lead-lead (Pb+Pb) collisions at $\sqrt{s_{\mathrm{NN}}} = 5.02$ TeV at the LHC is $\gamma_L \approx 2900$. Thus, photon longitudinal momentum reaches up to about 90 GeV. This implies that the $\gamma\gamma$ collision energy, calculated as $W = \sqrt{4k_1k_2}$, where $k_{1,2}$ are energies of the two photons, does not exceed 200 GeV.

In the EPA approach, the total cross-section for the production of the final state X in the $\gamma\gamma$ interaction in ion-ion, A_1A_2 UPC can be defined as follows:

$$\sigma^{EPA,\gamma\gamma}_{A_1A_2\to A_1A_2X} = \int dk_1 \int dk_2 \frac{n_1(k_1)}{k_1}\frac{n_2(k_2)}{k_2}\sigma_{\gamma\gamma\to X}, \tag{2.1}$$

where $n_{1,2}(k_{1,2})$ is the yield of equivalent photons originating from $A_{1,2}$ ions as a function of photon energy $k_{1,2}$, and $\sigma_{\gamma\gamma\to X}$ is the elementary cross-section to produce the X state.

The photon flux can be determined from the photon number density, which is the photon flux per unit area as:

$$n(k) = \int N(k,b)d^2b \tag{2.2}$$

The photon number density is defined as follows:

$$N(k,b) = \frac{Z^2\alpha_{\mathrm{EM}}}{\pi^2kb^2}x^2\left[K_1^2(x) + \frac{1}{\gamma_L^2}K_0^2(x)\right] \tag{2.3}$$

where Z is the atomic number of the ion, $x = kb/\gamma_L\hbar c$, α_{EM} is the EM fine structure constant, K_0 and K_1 are modified Bessel functions. The first term of Eq.2.3 is dominant at relativistic velocities. Typically, the coherent emission of the photon leaves the emitting source (proton/ion) intact. However, the exchange of multiple photons can result in the excitation of the outgoing ion. It is usually followed by the nucleus dissociation and neutron emission along the direction of the ion beam.

The coherent photons give rise to a variety of final states, in both $\gamma\gamma$ and γA interactions. The overview of these processes can be found in Refs. [20–23]. The cross-sections for the photon-induced processes strongly depend on the collision system, what is related with the Z^2 scaling of the photon flux, see Eq. 2.3. It is therefore translated to the Z^2 enhancement of the cross-sections in the proton-ion (pA) system or Z^4 increase in the AA system with respect to the pp collisions. The ratio of the cross-sections for the $\gamma\gamma$ production in pA and AA over the cross-section in the pp system is shown in Fig. 2.5. The total cross-sections calculated using the EPA formalism, should in principle be corrected for the presence of additional soft activity in the event, that would spoil the exclusivity of the final state (survival effects).

2.4 Modelling of photon-photon interactions in UPC

There are two Monte Carlo (MC) generators commonly used to simulate photon-initiated processes: STARLIGHT [25] and SUPERCHIC [24, 26]. They both implement the total cross-section calculation based on the convolution of the EPA-based calculation of the initial photon flux with the elementary reaction cross-section at the leading-order level. The differences in the implementation of the former between the two generators are discussed in the following sections.

2.4.1 STARLIGHT MC generator

The STARLIGHT MC generator [25, 27] is a program allowing calculation of the cross-section for multiple processes originating from photon-photon or photon-nucleon interactions. Apart from

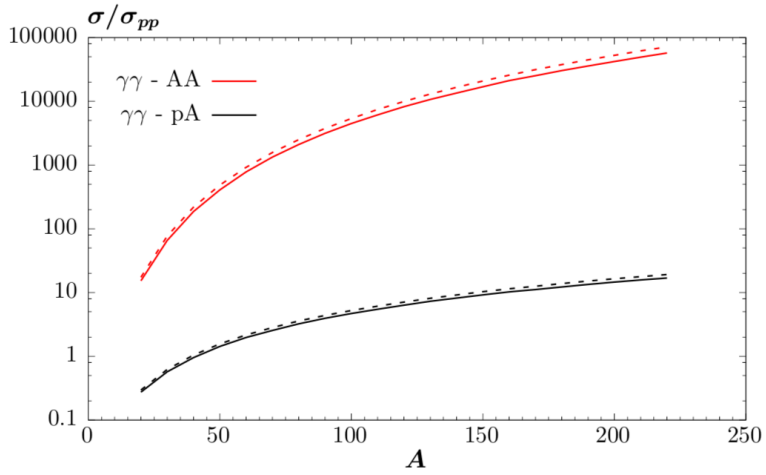

Figure 2.5: Ratio of cross-sections for light-by-light scattering at $\sqrt{s_{\rm NN}}$ =5.02 TeV in pA and AA) collisions to the pp result. Results with (without) survival effects are shown by the solid (dashed) lines [24].

providing the cross-section calculation as a function of the invariant mass of the initial system, W, and the system rapidity, it is capable of generation of individual events, which might be used in the simulation of the detector response.

In the STARLIGHT formalism the photon number density is dependent on the photon energy and the impact parameter. The photon density implemented in STARLIGHT is as follows:

$$N(k,b) = \frac{Z^2\alpha_{\rm EM}}{\pi^2 k b^2} x^2 K_1^2(x), \tag{2.4}$$

which is an expression from Eq. 2.3 simplified to the case when $\gamma_L \gg 1$. As a result, the two-photon flux is calculated as follows:

$$\frac{d^2N}{dk_1 dk_2} = \int_{b_1>R_A} d^2b_1 \int_{b_2>R_A} d^2b_2 N_1(k_1,b_1) N_2(k_2,b_2)(1 - P_{\rm had}(|\vec{b_1} - \vec{b_2}|)) P_{\rm fwd}(b), \tag{2.5}$$

where $\vec{b}_{1,2}$ are the vectors pointing from the barycentres of individual ions to the place where the interaction occurs, such that the impact parameter $b = |\vec{b}| = |\vec{b_1} - \vec{b_2}|$. $1 - P_{\rm had}(|\vec{b_1} - \vec{b_2}|)$ is the probability of no hadronic interaction, and $P_{\rm fwd}(b)$ is the probability of a forward neutron emission. Neutrons are emitted in the forward direction due to the Coulomb excitation of the ion. STARLIGHT is capable of simulating a few cases of the forward neutron production: either it simulates no neutrons (0n), or one neutron (1n) or any non-zero number of neutrons (Xn) emerging from an individual nucleus. The probability of Coulomb breakup for the specific nucleus can be determined following Refs. [27, 28] as:

$$P_{X\rm n}(b) = \int_{E_{\rm min}}^{E_{\rm max}} dk N(k,b) \sigma_{\gamma_L A \to A^*}(k), \tag{2.6}$$

where $E_{\rm min}$ is the minimal photon energy needed for neutron emission, $E_{\rm max} = \gamma_L \hbar c/b$ is the maximum photon energy with the significant flux, N is taken from Eq. 2.4 and $\sigma_{\gamma A \to A^*}(k)$ is the excitation cross-section, determined using data collected at the wide range of energies [29]. More precisely, $P^1_{X\rm n}(b)$ is the mean number of excitations, as at small impact parameters it exceeds one, and so cannot be interpreted as a probability. The unitarization procedure is done to determine the excitation probability. It is assumed that the probability of having a given

number of excitations follows the Poisson distribution with a mean defined in Eq. 2.6. Thus, probability of at least one neutron excitation is calculated as:

$$P_{Xn}(b) = 1 - \exp\left(-P_{Xn}(b)\right). \tag{2.7}$$

The probability of a given configuration of neutron emission in Pb+Pb collisions simulated by STARLIGHT as a function of impact parameter is shown in Fig. 2.6. Three forward activity topologies are considered: 0n0n, with no neutron emission from any nucleus, Xn0n, with neutrons emitted from only one of nuclei, and XnXn, with neutrons emitted from both nuclei. At impact parameters below 15 fm the dominating topology is XnXn, for b close to 20 fm the Xn0n topology has the largest probability. Choosing the 0n0n topology, mainly $b > 40$ fm range can be probed.

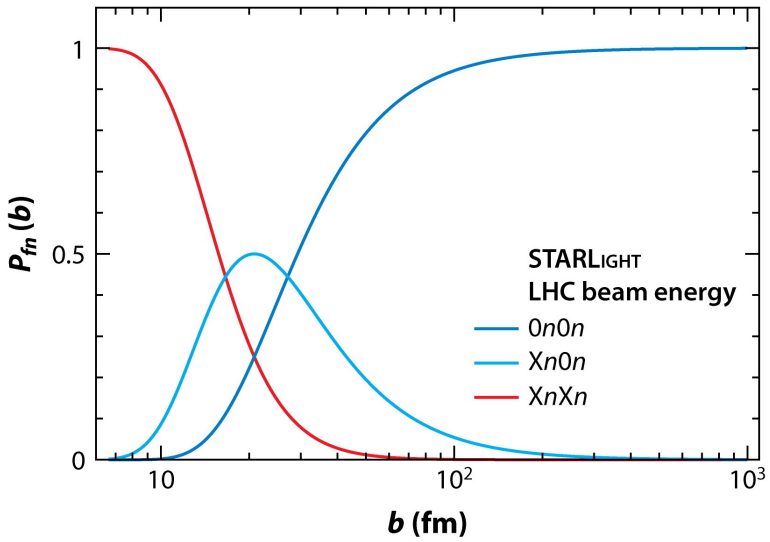

Figure 2.6: Impact parameter dependence of the probabilities of three forward neutron topologies simulated by STARLIGHT: 0n0n, Xn0n, XnXn. Each topology probes different b ranges [23].

The probability of the hadronic interaction, P_{had} is calculated using the Glauber model [30]. In this model, the nuclear distributions for heavy nuclei follow the Woods-Saxon distribution with parameters obtained from e^+e^- scattering data [31].

As STARLIGHT provides the cross-section calculation as a function of invariant mass of the initial two-photon system, W, and the system rapidity, Y, these quantities are determined from the energies of the initial photons by relations:

$$W = \sqrt{4k_1k_2} \tag{2.8}$$

and

$$Y = \frac{1}{2}\ln\frac{k_1}{k_2}. \tag{2.9}$$

The limitation of the STARLIGHT formalism is the sharp cutoff on the nuclear distributions (integrals calculated in $b_1 > R_A, b_2 > R_A$ ranges). These requirements ensure that the final state is produced outside of the nuclei. Otherwise, the final state particles could interact with the nucleus and lead to nuclear breakup.

2.4.2 SUPERCHIC MC generator

The SUPERCHIC MC generator [24, 26] enables simulation of central exclusive production in pp, proton-ion and ion-ion systems, both for photon-induced and QCD-induced processes.

The simulation for the ion beams was introduced starting from version v3.0. The SuperChic calculations for photon-induced processes follow in principle the EPA method to calculate the total cross-section as a convolution of the photon fluxes and elementary cross-section. The photon flux is however defined as follows:

$$N(x_i) = \frac{\alpha}{\pi^2 x_i} \int \frac{d^2 q_{i_\perp}}{q_{i_\perp}^2 + x_i^2 m_{N_i}^2} \left(\frac{q_{i_\perp}^2}{q_{i_\perp}^2 + x_i^2 m_{N_i}^2} (1 - x_i) F_E(Q_i^2) + \frac{x_i^2}{2} F_M(Q_i^2) \right), \tag{2.10}$$

where $q_{i_\perp}$ and x_i are transverse and longitudinal momentum fractions of the i-th parent nucleus. The electric and magnetic form factors, $F_E(Q_i^2)$ and $F_M(Q_i^2)$ depend on the modulus of the photon virtuality, Q_i^2. For nucleus-nucleus collisions, the magnetic form factor is dropped, as it scales with Z, in contrary to the electric form factor that scales with Z^2. The nucleus form factor is the Fourier transform of the nucleus charge density which is assumed to follow the Woods-Saxon distribution.

The SuperChic implements also a so-called soft survival factor, which represents the probability of no additional activity in the event, that could affect the exclusivity of the final state. It is defined as a function of $\vec{b}_1$ and $\vec{b}_2$ and calculated at the amplitude level. The survival factor can be expressed as:

$$\langle S_{\rm surv}^2 \rangle = \frac{\int \mathrm{d}^2 b_{1\perp} \mathrm{d}^2 b_{2\perp} |\tilde{T}(s, b_{1\perp}, b_{2\perp})|^2 \exp\left(-\Omega_{A_1 A_2}(s, b_\perp)\right)}{\mathrm{d}^2 b_{1\perp} \mathrm{d}^2 b_{2\perp} |\tilde{T}(s, b_{1\perp}, b_{2\perp})|^2}, \tag{2.11}$$

where $\tilde{T}(s, b_{1\perp}, b_{2\perp})$ is the process amplitude in impact parameter space, $\Omega_{A_1 A_2}(s, b_\perp))$ is the ion-ion opacity, while $\exp\left(-\Omega_{A_1 A_2}(s, b_\perp)\right)$ represents the probability that no inelastic scattering occurs at impact parameter $b_\perp$. The survival factor is also implemented for pp collisions. In this case the ion-ion opacity is replaced by proton-proton opacity, $\Omega(s, b_\perp))$. Qualitatively, at large impact parameters there is less additional particle production and the survival factor gets closer to unity. In general, the soft survival factor is larger in photon-induced processes, than in QCD-induced processes, because the former are favoured at large b. The dependence of the soft survival factor on the invariant mass of the system is shown in Fig. 2.7 for the production of $\mu^+\mu^-$ pair in pp collisions at $\sqrt{s} = 14\,\mathrm{TeV}$. The decreasing trend can be explained by the fact, that the photon momentum fraction is proportional to the invariant mass of the system, $x_\gamma \propto M_X$, what means that high invariant masses occur more likely at smaller impact parameters. For those, more additional soft interactions are expected. In photon-photon interactions in ion-ion collisions, the soft survival effects modify the final cross-sections by about 10-20%. Additionally, the polarisation effects are included in the SuperChic generator, as cross-sections for $\gamma\gamma \to X$ processes are summed up at the amplitude level over the incoming photon transverse polarisations. However, a limitation of SuperChic is the lack of the simulation of the forward neutron emission.

2.5 Exclusive dilepton production

The exclusive dielectron production, $\gamma\gamma \to e^+e^-$, sometimes referred to as a Breit-Wheeler process [33], is one of the most fundamental processes occurring in the photon-photon interactions. It is a non-resonant two-photon scattering to opposite-sign electron pairs (hereafter electrons and positrons are collectively called electrons). In the left panel of Fig. 2.8, the Feynman diagram for this process is presented at the lowest order. The characteristic feature of this process, is the clean detector signature consisting only of an e^+e^- pair in the back-to-back topology in the central detector. The outgoing ions stay intact. The event when an electron radiates a

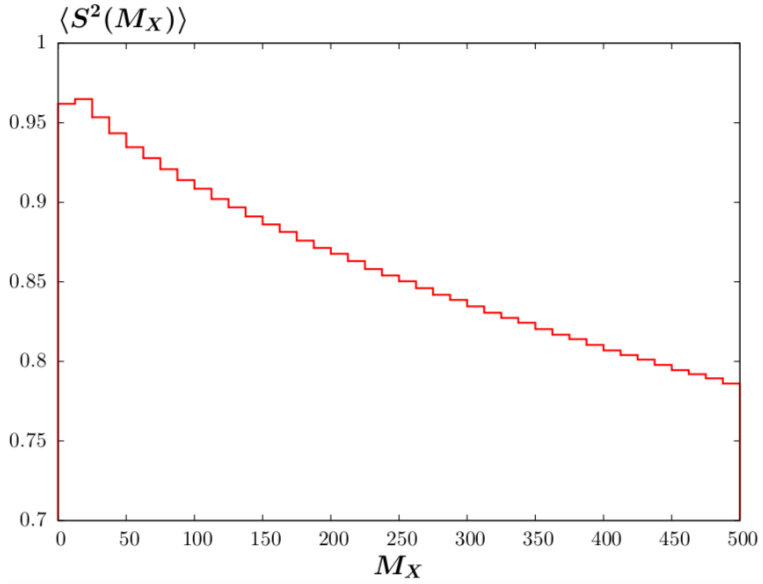

Figure 2.7: The average soft survival factor as a function of the invariant mass of the $\mu^+\mu^-$ pair, M_X, produced in pp collisions at $\sqrt{s} = 14\,\text{TeV}$. The selected muons have transverse momenta above 2.5 GeV and pseudorapidity in the range of $|\eta| < 2.5$ [32]

.

photon in the final state (FSR, final-state radiation) is also considered a signal process. In principle higher order diagrams also contribute to the total cross-section for the exclusive dielectron production.

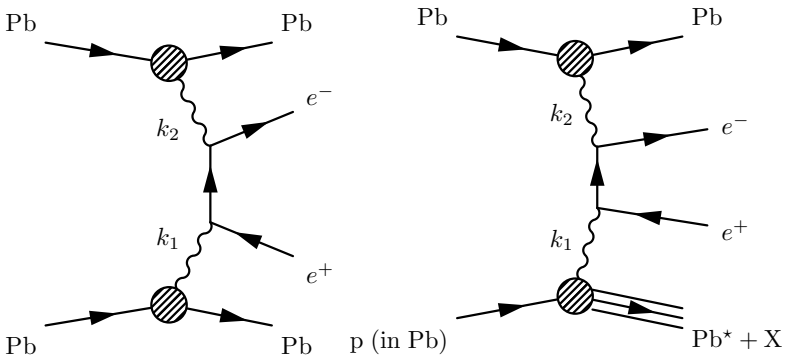

Figure 2.8: Feynman diagrams of the exclusive dielectron production (left) and the dissociative electron pair production (right) in UPC Pb+Pb collisions. The star symbol denotes excitation of the outgoing lead ion.

The same production mechanism is also valid for other lepton pairs. The elementary cross-section for the exclusive dilepton production may be determined based on the lepton mass, m, and invariant mass of the pair, W as:

$$\sigma_{\gamma\gamma\to l^+l^-} = \frac{4\pi\alpha_{\text{EM}}^2}{W^2}\left[(2+\frac{8m^2}{W^2}-\frac{16m^4}{W^4})\ln\left(\frac{W+\sqrt{W^2-4m^2}}{2m}\right)-\sqrt{1-\frac{4m^2}{W^2}}\left(1+\frac{4m^2}{W^2}\right)\right]. \tag{2.12}$$

The dissociative dielectron production, which is schematically shown in the right panel of Fig. 2.8, is the main background in the photon-induced exclusive dielectron production. In the case of single(double) dissociation one(both) photon(s) is(are) emitted from the nucleon

substructure leading to nucleus breakup. It appears that dielectrons originating from the dissociative events are less back-to-back than the ones from the signal process. This behaviour appears to be a feature of both pp and Pb+Pb systems. That topology reflects the transverse momentum of the $\gamma\gamma$ system, which is driven by the transverse momenta of the initial photons. For photons emitted coherently from the nucleus, the transverse momentum is of the order of $O(\hbar c/R_A) \approx 30\,\text{MeV}$, while the typical p_T scale for dissociative events in the Pb+Pb system is of the order of $O(\text{GeV})$. In case of dilepton production in pp collisions, the typical initial p_T scale is about 200 MeV. Convolution of photon fluxes originating from either proton or ion with photons emitted from the nucleon substructure is always dominated by the harder spectrum of the latter. This aspect is important, as at the time of writing this thesis, there is no simulation of the dissociative production of lepton pairs available in nucleus-nucleus collisions, but the recent release of the SuperChic MC generator in version 4.0 provided the simulation of this process in the pp system. The characteristic transverse momentum scales for coherent and incoherent photons can be identified in Fig. 2.9, presenting the p_T spectrum of the J/Ψ candidates decaying to a pair of muons. Exclusive muon pairs, being the continuum contribution, have the peak below 50 MeV, incoherent J/Ψ is peaked around 300 MeV, while dissociative production has a much wider p_T distribution with maximum above 600 MeV.

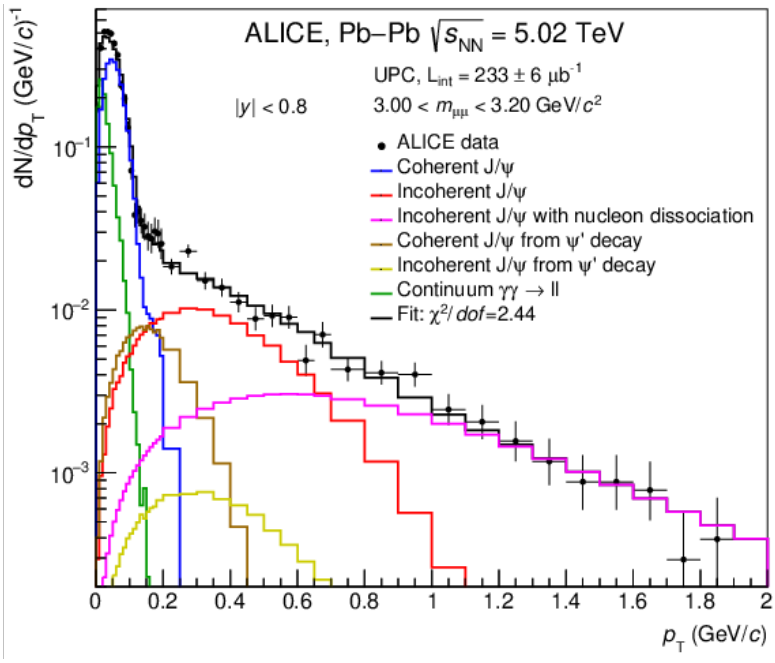

Figure 2.9: Spectrum of p_T for J/Ψ candidates decaying to a pair of opposite-charge muons measured by ALICE [34]. Data points are shown as markers, while histograms present contributions to the p_T spectrum modelled with the MC simulation. Blue and red histograms present the coherent and incoherent J/Ψ production, respectively, while brown and yellow histograms present the J/Ψ from decays of coherent and incoherent Ψ', respectively. The incoherent J/Ψ with nucleon dissociation is presented with pink histogram, while continuum $\gamma\gamma \to \mu^+\mu^-$ as green histogram. The black histogram shows the fit to the data, obtained by leaving the normalisation free for coherent J/Ψ, incoherent J/Ψ and dissociative J/Ψ production.

Studying the exclusive dielectron production is a powerful tool to validate the modelling of photon fluxes in nucleus-nucleus collisions as well as elementary cross-sections. Knowing that the additional Coulomb excitation of the nucleus followed by the neutron emission is possible, the exclusive dielectron pairs provide a way to study the probabilities and effects of the nuclear breakup. The analysis of the forward neutron production is also related with the studies of

the dissociative processes. Such measurements of neutrons emitted at very small angles with respect to the beam are possible with Zero-Degree Calorimeters, which are in operation by the ALICE, ATLAS and CMS experiments at the LHC.

The exclusive dielectron production provides a benchmark for other photon-induced processes. It has been proposed to be utilised as reference in measurements of the τ-lepton anomalous magnetic moment quantified by the $g-2$ factor. Such measurement is possible using the $\gamma\gamma \to \tau^+\tau^-$ events, in order to reduce the impact of the correlated systematic uncertainties [35, 36]. The exclusive dimuon events were already used for this purpose in the recent ATLAS measurement of the τ-lepton $g-2$ [37]. The dilepton pairs contribute to backgrounds for other processes, e.g. quarkonia production. In particular, the electron pairs were studied as background for the light-by-light scattering measurements by ATLAS [38–40] and CMS [41]. Due to the relatively high cross-sections, characteristic back-to-back topology and event exclusivity, dilepton pairs can also be used for lepton performance studies in UPC events.

The exclusive dilepton final states have been previously measured in many different collision systems and energies. Muon pairs were observed in ep collisions at HERA [42]. In $p\overline{p}$ collisions at the Tevatron, dilepton pairs were studied [43–45]. Exclusive $\mu^+\mu^-$ and e^+e^- pairs were also measured in pp collisions at the LHC at $\sqrt{s} = 7\,\text{TeV}$ by ATLAS [46] and CMS [47, 48] and at $\sqrt{s} = 13\,\text{TeV}$ by both these collaborations [49–51]. The dilepton production was studied in heavy-ion collisions at RHIC [52–55]. The recent STAR measurement [55] included the studies of angular correlations between pair momentum and single-electron momenta, that reflect the linear polarisation of the initial photons. At the LHC, electron pair production was measured in Pb+Pb collisions at $\sqrt{s_{\text{NN}}} = 2.76\,\text{TeV}$ by the ALICE Collaboration [56] in the kinematic range limited to absolute rapidity below 0.9. At higher energy, $\sqrt{s_{\text{NN}}} = 5.02\,\text{TeV}$, the exclusive dimuon production was studied in Pb+Pb collisions for muons with transverse momentum above 4 GeV and absolute pseudorapidity below 2.4, and dimuon invariant mass above 10 GeV by ATLAS [57]. The CMS Collaboration observed the broadening of the angular distributions in exclusive dimuon events as a function of the forward topology. Finally, dilepton pairs originating from photon-photon interactions were studied by ATLAS [58] and STAR [53] in events where the nuclei overlap and interact hadronically. A significant broadening of angular distributions was observed in these events, suggesting that the processes of interest may provide a new probe of the QGP medium.

2.6 Light-by-light scattering

Light-by-light (LbyL) scattering is a process allowed by the quantum electrodynamics (QED) at the lowest order via loop diagrams involving charged fermions or $W^\pm$ bosons, as shown in the left panel of Fig. 2.10. Due to four vertices, the cross-section for this process is of the order of $O(\alpha_{\text{EM}}^4) \approx 2.8 \times 10^{-9}$, making it extremely rare. The theoretical description of LbyL scattering was developed already in 1930s [59, 60], however the direct experimental evidence was not possible for decades. The proposition to measure this process at the LHC was made by Refs. [61] and [62]. As discussed in Sec.2.3, the total cross-section in the HI UPC is a convolution of the elementary cross-section with the incoming photon fluxes. Thus, experimentally it is possible to observe the LbyL process in the Pb+Pb collisions as the cross-section is enhanced by the Z^4 factor with respect to the pp collisions. A signature of LbyL scattering in the detector is simple: it consists of two photons without any additional detector activity, in particular no charged-particle tracks originating from the Pb+Pb interaction point are allowed. The outgoing nuclei generally stay intact, however the nucleus excitation followed by the neutron emission is also possible.

One of the most important sources of background for LbyL scattering is central exclusive

production (CEP) via three-gluon exchange, which Feynman diagram is shown in the middle panel of Fig. 2.10. In this process, a pair of photons is produced via the strong interaction through a quark loop in the exchange of two gluons in a colour-singlet state. Due to incomplete knowledge of gluon densities [63] and the lack of measurements, the CEP has large theoretical uncertainty.

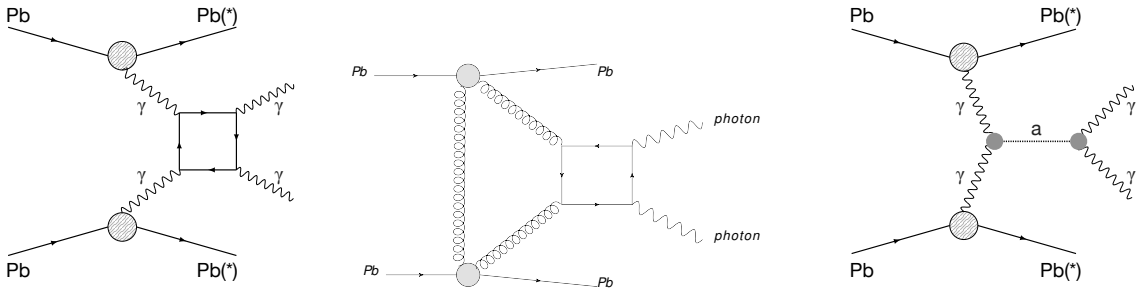

Figure 2.10: The Feynman diagram of LbyL scattering (left), CEP (middle) and the axion-like particle production (right) in UPC Pb+Pb collisions. The star symbol denotes possible excitation of the Pb ion.

The LbyL scattering is considered to be sensitive to multiple BSM effects. The modifications in the measured cross-section may be related to the existance of extra spatial dimensions [64] or new exotic particles [65]. The LbyL is also sensitive to various extensions of the Standard Model: the presence of space-time non-commutativity in QED [66], Lorentz-violating operators in electrodynamics [67] or Born-Infeld extensions of the QED [68]. Also the diphoton mass spectrum measured in the LbyL process offers an opportunity to search for hypothetical new neutral axion-like particles (ALP) (see the right panel of Fig. 2.10), which may contribute to the distribution as a narrow diphoton resonance [69].

The two photon final states were previously measured in the Delbrück scattering process, when photon scatters of a Coulomb field of the nucleus [70–73] and in the photon splitting measurement [74]. The LbyL itself was indirectly tested in the measurements of the anomalous magnetic moment of the electron and muon [75, 76]. The first direct evidence for LbyL was provided by the ATLAS [38] and CMS [41] experiments, using Pb+Pb collision data collected at $\sqrt{s_{\mathrm{NN}}} = 5.02\,\mathrm{TeV}$ in 2015. These measurements were followed by the observation of the LbyL scattering process with significance of 8.2σ by ATLAS [39], using the larger 2018 Pb+Pb dataset.

Chapter 3

The ATLAS experiment at the LHC

3.1 The Large Hadron Collider

The Large Hadron Collider (LHC) [77] at CERN is a circular particle accelerator with a circumference of 27 km, what makes it the world's largest machine of this type. It is located between 45 and 170 m beneath the ground level at the French-Swiss border near Geneva. The LHC operates in connection with the CERN accelerator complex, which is schematically shown in Fig. 3.1. The LHC is accommodated to accelerate and collide bunches of protons or heavy ions. Two linear accelerators (LINAC 4 and 3) provide protons and ions, later injected to the system of circular accelerators. The protons are subsequently injected to PS, Booster, SPS and finally LHC. The ions travel through LEIR, PS and SPS, before they reach the LHC. In each successive accelerator, hadrons are subsequently gaining energy up to 6.8 TeV for protons and 2.76 TeV per nucleon for lead ions. The two counter rotating beams are collided with an unprecedented centre-of-mass energy in four points at the LHC ring where the major detectors: ALICE, ATLAS, CMS, and LHCb, are installed. The ATLAS and CMS detectors are general purpose multi-layer detectors primarily oriented for precision measurements of Higgs boson properties and searches of rare processes at high collision rates. The main interest of the ALICE experiment are collisions of heavy ions, with precision measurements down to very low energy. The LHCb experiment focuses on studies of b-quark decays that potentially violate the Charge-Parity symmetry. The LHC accommodates also several smaller experiments: LHCf (measurements to verify astroparticle hadron models), MOEDAL (magnetic monopole searches) and TOTEM (measurement of total elastic scattering and diffractive cross-section). Starting from Run 3, the new experiment, FASER, designed to search for light and extremely weakly interacting particles, is going to be operational. Additionally, a variety of other experiments is located at pre-accelarators and make use of lower-energy hadrons.

Inside the LHC ring separate pipelines are installed for two counter-rotating beams. Ultra-high vacuum is maintained in the beam pipes as the interaction with the gas would disturb the beam trajectory. The beam pipes are encapsulated in one tube, where the superconducting dipole and quadrupole electromagnets are placed subsequently along the ring to bend and focus the beams. The magnets are cooled down using liquid helium to the temperature of 1.9 K to keep them in the superconducting state. In between the magnet sections, the radio-frequency cavities are installed to accelerate the particles. The latter are injected to the accelerator complex in packages called bunches, each containing 1.15×10^{11} protons. Bunches are organised in so-called trains with a defined scheme of filled and empty bunch slots. The train structure determines the collision scheme in each of the LHC experiments. Bunches circulate in the LHC ring separated in time by at least 25 ns, what results in maximum 40 MHz collision rate.

From the experimental point of view, there are two most important parameters of the

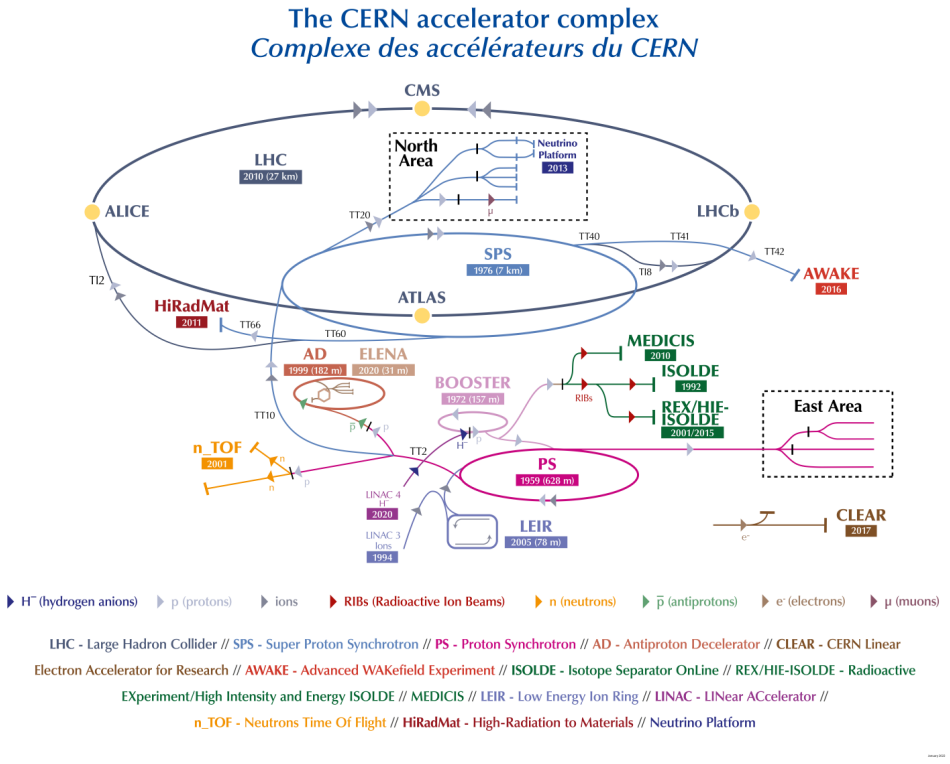

Figure 3.1: Schematic view of the CERN accelerator complex [78].

particle collider: the centre-of-mass energy and the luminosity provided by the machine. The collision energy available at the LHC reaches 13.6 TeV for proton-proton (pp) collisions and 5.52 TeV per nucleon pair in lead-lead (Pb+Pb) collisions. The luminosity $\mathcal{L}$ is defined as:

$$\mathcal{L} = \frac{1}{\sigma}\frac{\mathrm{d}N}{\mathrm{d}t}, \tag{3.1}$$

where σ is the production cross-section for a given process, and $\frac{\mathrm{d}N}{\mathrm{d}t}$ is the number of events of the process of interest per second. At the LHC, the luminosity reached $2.1 \cdot 10^{34}$ cm^{-2}s^{-1} for the pp system, and $6.2 \cdot 10^{27}$ cm^{-2}s^{-1} for the Pb+Pb system. The luminosity can also be expressed in variables characterizing properties of beams, assuming they are the same for both beams:

$$\mathcal{L} = \frac{N_b^2 n_b f_{\mathrm{rev}} \gamma_L}{4\pi\epsilon_n \beta^*} F, \tag{3.2}$$

where N_b is the number of protons in the bunch, n_b is the number of bunches, f_{rev} is the revolution frequency, γ_L is the relativistic gamma factor, ϵ_n is the normalised transverse beam emittance, β^* is the beta function at the collision point and F is the geometric luminosity reduction factor, due to the crossing angle at the interaction point. The ϵ_n characterizes spatial and momentum distributions of protons in the bunch. In the beam with low emittance, particles are well collimated and have the same momentum. The beta-function describes how well the beam is focused towards the interaction point. It can be referred to as a distance at which the beam is spread twice of its size at the collision point.

Another useful variable is the integrated luminosity:

$$\mathcal{L}_{\mathrm{int}} = \int \mathcal{L}\, dt, \tag{3.3}$$

that is a characteristic feature of a collected dataset. It allows to estimate the expected number of events from a given process, after multiplying by the production cross-section.

The LHC is primarily the pp collider, however the heavy-ion collisions are usually provided for one month per year. The LHC operated and provided collisions since the end of 2010 to the beginning of 2013 (so-called Run 1), and from 2015 to 2018 (referred to as Run 2). The analyses presented in this thesis are based on Pb+Pb collision data collected in 2015 and 2018, as well as xenon-xenon (Xe+Xe) collision data collected in 2017. The periods 2013-2015 and 2018-2021 are called Long Shutdown 1 and 2, respectively. They were scheduled to perform required upgrades of the detectors at the LHC. In 2022, the next data taking period is starting, named Run 3.

3.2 ATLAS detector

The ATLAS (A Large Toroidal LHC ApparatuS) detector [79] at the LHC is a multi-layer cylindrical detector enabling precise measurements of particles' energies and momenta. ATLAS uses a right-handed coordinate system with its origin at the nominal interaction point (IP) in the centre of the detector and the z-axis along the beam pipe. The x-axis points from the IP to the centre of the LHC ring, and the y-axis points upward. The side-A of the detector is defined as that with positive z and side-C is that with negative z. Cylindrical coordinates (r, ϕ) are used in the transverse plane, ϕ being the azimuthal angle around the z-axis. The pseudorapidity is defined in terms of the polar angle θ as $\eta = -\ln\tan(\theta/2)$. Angular distance is measured in units of $\Delta R \equiv \sqrt{(\Delta\eta)^2 + (\Delta\phi)^2}$. The photon (electron) transverse energy is $E_{\mathrm{T}} = E/\cosh(\eta)$, where E is its energy.

ATLAS covers almost the full solid angle around the IP. It consists of an inner tracking detector surrounded by a thin superconducting solenoid, EM and hadronic calorimeters, and a muon spectrometer incorporating three large superconducting air-core toroidal magnets. In the barrel region sub-detectors are placed as consecutive concentric cylinders, while in the end-cap region they are arranged as disks perpendicular to the beam axis. The scheme of the ATLAS detector is shown in Fig. 3.2.

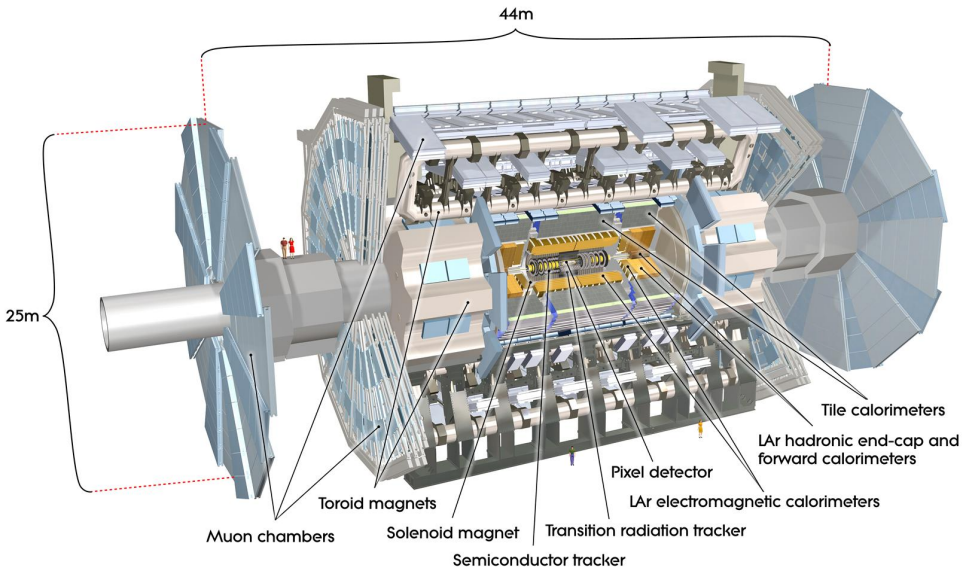

Figure 3.2: Schematic view of the ATLAS detector [80].

The Inner Detector (ID) is immersed in a 2 T axial magnetic field generated by the central solenoid what enables reconstruction of particles' trajectories (tracks) and measurement of charged particles' momenta. The measured tracks are used for reconstruction of the interaction vertex. There are 3 consecutive layers of the ID: the pixel detector, the silicon microstrip tracker (SCT) and transition radiation tracker (TRT). The innermost pixel detector consists of four layers, with the one closest to the beam pipe being the insertable B-layer (IBL) installed in Long Shutdown 2 in preparation to Run 2 [81, 82]. The ID is built out of silicon pixel sensors having a minimum size of $50\,\mu$m in $r-\phi$ plane and $400\,\mu$m in the z direction. It typically provides four measurements per track, the first hit normally being in the IBL. The SCT consists of four layers of stereo pairs of microstrip sensors. It provides the measurement of the traversing particle with the accuracy of $17\,\mu$m in the $r-\phi$ plane and $580\,\mu$m in the z direction . Typically four measurements per track are read out from the SCT. Both pixel and SCT detectors cover the $|\eta| < 2.5$ region. The TRT is constructed out of the 4 mm diameter straw tubes providing the additional tracking information in the $r-\phi$ plane with the accuracy of 130 μm per straw. In the barrel region the straws are placed parallel to the beam axis, while in end-caps they are arranged radially in wheels. Only the region with $|\eta| < 2.0$ is covered by the TRT. The particle track is typically read out by 36 straws. The TRT enables the electron identification based on detection of transition radiation X-ray photons. Since the emission of the transition radiation is much less likely for pions, than for electrons at the same momentum, the TRT enables electron-hadron discrimination by measuring the fraction of hits above the higher energy-deposit threshold.

The energy measurement in the central part of the detector is provided by the EM and hadronic calorimeter system with a coverage in $|\eta|$ up to 3.2. The precise measurement of EM showers is done using high-granularity lead/liquid argon (LAr) sampling calorimeters. In the range up to $|\eta| < 2.5$ it consists of three layers, while for larger $|\eta|$ (in the inner wheel of end-caps) a two-layer structure with coarser granularity is used. An additional thin LAr presampler covering $|\eta| < 1.8$ is placed to correct for energy loss in material upstream of the calorimeters. The region of $1.37 < |\eta| < 1.52$ is called the transition region (between barrel and end-cap parts) and is often excluded in the analyses involving electrons/photons, due to lower reconstruction efficiency. A typical energy resolution of the EM calorimeter is $\sigma_E/E = 10\% \times \sqrt{\text{GeV}}/\sqrt{E} \oplus 0.2\%$. The first term is stochastic, while the second reflects the local non-uniformities in the calorimeter response.

The hadron calorimetry is realised with a steel/scintillator-tile sampling calorimeter with coverage up to $|\eta| < 1.7$ in the barrel and with a copper/LAr sampling calorimeter covering $1.5 < |\eta| < 3.2$ in the end-caps. It is segmented radially into three layers in the barrel and into four layers in the end-caps. Additionally, forward calorimeters (FCal) with one layer of copper/LAr EM calorimeter and three layers of tungsten/LAr hadronic calorimeters are used. The FCal covers the range of $3.2 < |\eta| < 4.9$.

To be able to select minimum-bias events during data taking, Minimum Bias Trigger Scintillators (MBTS) are deployed. They consist of two sets of sixteen scintillator counters installed on the front face of the end-cap calorimeter. Each set of counters consist of inner and outer rings, covering a $2.07|\eta| < 3.86$ range. Each ring is segmented in eight units in ϕ.

To measure muons, which escape the calorimeters, the Muon Spectrometer (MS) is assembled as the outermost layer of the ATLAS detector. It is a system of muon chambers immersed in a magnetic field generated by the large superconducting air-core toroid magnets, that deflects the muon tracks. In the barrel region, tracks are measured in chambers arranged in three cylindrical layers around the beam axis; in the transition and end-cap regions, the chambers are installed in planes perpendicular to the beam, also in three layers. The muon tracking system covers the $|\eta| < 2.7$ range.

To provide the luminosity measurement for ATLAS, the LUCID (LUminosity Cherenkov

Integrating Detector) [83] detector is used. There are two detectors installed, one in each end-cap region of ATLAS, at a distance of approximately ±17 m from the IP. At each side, it consist of sixteen photomultipliers with 10 mm diameter arranged in four groups around the beampipe and with four bundles of quartz fibers read out by four additional photomultipliers situated about 1.5 m further away from the detector. The photomultipliers measure the Cherenkov radiation generated in thin quartz windows.

The Zero-Degree Calorimeters (ZDC) are additional forward detectors located at ±140 m from the IP, just beyond the point where the common straight-section vacuum-pipe divides back into two independent beam-pipes. Their position with respect to the central detector is schematically shown in Fig. 3.3. They consist of four longitudinal compartments on each side of the IP. The ZDC measure neutral particles at pseudorapidities $|\eta| \geq 8.3$. They are of particular importance in HI collisions, as they enable detection of non-interacting (spectator) neutrons originating from the incoming nuclei. In this thesis, the ZDC detectors are used to measure a contribution of background processes with nucleus dissociation. The ZDC modules consist of layers of alternating quartz rods as active material and tungsten plates as absorbers. The particles passing through the ZDC generate Cherenkov radiation, which is detected by the photomultipliers. The ZDC calibration is performed in each set of four modules using photonuclear processes that deposit one or more neutrons on one side, and a single neutron, carrying the full per-nucleon beam energy, on the other. Time-dependent weights are determined for each module in short time intervals to minimize the variance around the nominal per-nucleon beam energy. Energy resolutions achieved are typically around $\Delta E/E \approx 16\%$.

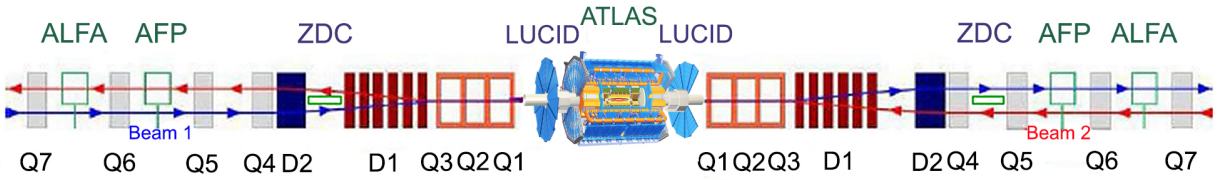

Figure 3.3: Schematic view of the ZDC subdetectors with respect to ATLAS detector [84].

3.2.1 Reconstruction and identification of electrons and photons

The ATLAS experiment uses an extensive software suite [85] in the reconstruction and analysis of real and simulated data, in detector operations, and in the trigger and data acquisition systems of the experiment. Based on the signals from multiple readout channels, the signatures of physics objects, like electrons or photons are reconstructed, along with their position, energy and momentum. The reconstruction of photons is based on the energy deposits in the EM calorimeters, while for electrons additionally signals from the ID are included. Schematic view of the path of the electron in the detector is presented in Fig. 3.4. The electron first traverses the subsequent subsystems of the ID: pixel, SCT and TRT detector, and then enters the EM calorimeter. The detailed discussion of the electron and photon performance in the Run 2 data sets can be found in Ref. [86]. The ATLAS software used a dynamic clustering algorithm, that enables reconstructing variable-size clusters. This technique allows to recover the energy from bremsstrahlung photons or from electrons from photon conversions. The procedure is multistep, and starts from preparing clusters and tracks for later processing. The clusters, built of topologically connected EM and hadronic calorimeter cells [87] are called topoclusters. These clusters need to be geometrically matched to the ID tracks, which are re-fitted to account for bremsstrahlung. The algorithm builds the conversion vertices and associates the selected topoclusters to them. Then, the initial position corrections and energy calibrations are applied.

This is followed by supercluster building algorithm, which matches conversion vertices with photon superclusters and the ID tracks with electron superclusters. Later, the built objects have their energy calibrated and are also provided with some additional discriminating variables, in order to distinguish electrons from photons.

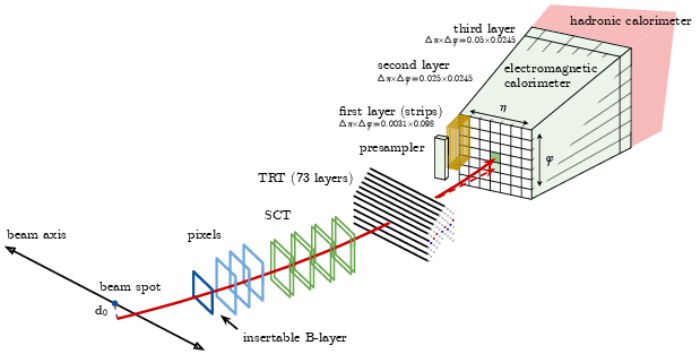

Figure 3.4: Schematic illustration of the electron path in the detector [88]. The red trajectory shows the hypothetical path of an electron, which first traverses the tracking system (pixel detectors, then SCT detectors and lastly the TRT) and then enters the EM calorimeter. The dashed red trajectory indicates the path of a photon produced by the interaction of the electron with the material in the tracking system.

The reconstructed objects are also labelled based on the "identification" selection criteria. Further, more restrictive requirements are put, to improve the purity of the sample. The particle identification (PID) for electrons relies on a likelihood discriminant constructed from quantities measured in the calorimeter, the ID and the combined ID and calorimeter. This discriminant is formed from likelihoods built for electrons to originate from the signal or the background. Additionally also, a cut-based method is used to provide PID. Several working points (WP) are defined for the identified electrons: Loose, Medium, or Tight [88] for the cut-based selection, and LHLoose, LHMedium, or LHTight [86] for the likelihood-based selection. They are optimised for pp collisions to have the average electron PID efficiency of 93%, 88% and 80% for (LH)Loose, (LH)Medium and (LH)Tight WP and gradually increase from low to high electron E_{T}. The lower efficiency for tighter criteria is the effect of better background rejection.

Usually, the ATLAS Egamma combined performance (CP) group provides efficiency measurements for electron/photon reconstruction and PID. They are determined in both data and the MC simulation. As some differences between data and MC simulation usually occur, also so-called scale factors are defined as a ratio of efficiencies in the data to the one in the MC simulation. They are used to reweigh the simulated events, so that the simulation describes the data even better.

The electron reconstruction efficiency as a function of E_{T} measured using pp collision data is presented in the left panel of Fig. 3.5. The efficiency is measured for electron E_{T} above 15 GeV, and in this range exceeds 98%. The right panel of Fig. 3.5 shows the electron PID efficiencies measured in pp collision data as a function of electron E_{T} for three likelihood-based WP. They are presented for electron E_{T} above 5 GeV. The tighter PID criteria result in better background rejection, but also have lower efficiency. In general efficiencies rise with increasing E_{T}. Since the optimisation of the likelihood discriminant requirements was performed using simulated event, the mismodelling of the variables used in the likelihood discriminant at low E_{T} leads to a higher PID efficiency in data in this region. Additionally, the scale factors deviate from

unity especially in the low-E_{T} region, which is studied in analysis presented in this thesis. That suggest that the dedicated measurement of scale factors might be required.

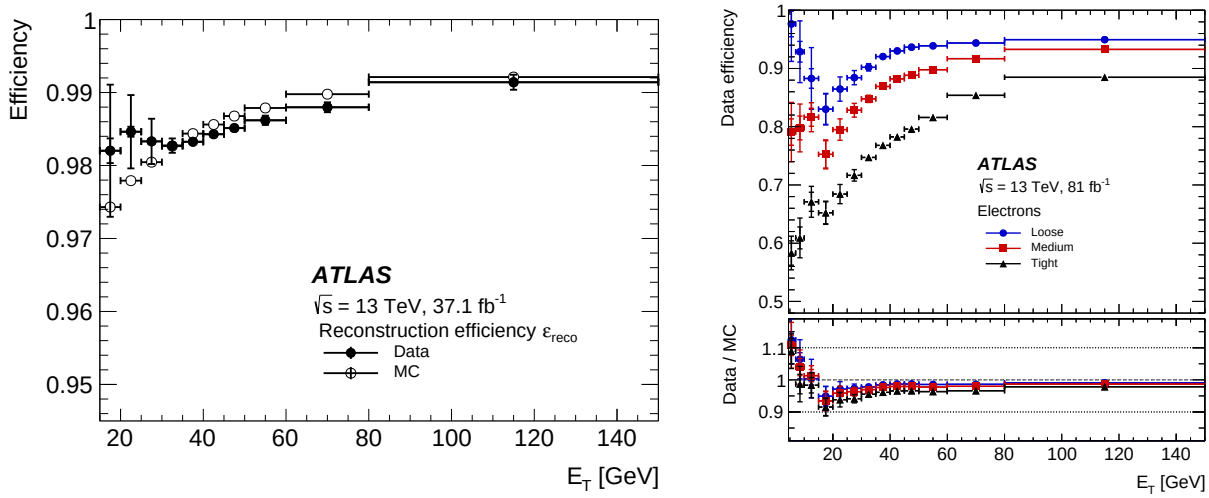

Figure 3.5: (Left) Electron reconstruction efficiency relative to reconstructed clusters, ϵ_{reco}, as a function of electron transverse energy E_{T} for $Z \to e^+e^-$ events in pp data (closed circles) and simulation (open circles). The inner uncertainties are statistical while the total uncertainties include both the statistical and systematic components [88]. (Right) Electron identification efficiency in $Z \to e^+e^-$ events in data as a function of E_{T} (left) for the likelihood-based Loose, Medium and Tight WP. The efficiencies are obtained by applying data-to-simulation efficiency ratios measured in $J/Psi \to e^+e^-$ and $Z \to e^+e^-$ events to $Z \to e^+e^-$ simulation. The inner uncertainties are statistical and the total uncertainties are the statistical and systematic uncertainties in the data-to-simulation efficiency ratio added in quadrature. The bottom panel shows the data-to-simulation ratios [86].

In ATLAS, photons are identified with a cut-based selection, using the shower shape variables [86]. The requirements are designed to efficiently select photons and reject backgrounds from hadronic jets. The identification criteria are optimised separately for converted and unconverted photons depending on photon E_{T}. Photon PID efficiency measured in pp collisions with three methods is shown in Fig. 3.6, for unconverted photons with $|\eta| < 0.6$. The first measurement method uses an inclusive-photon production data selection (matrix method), the second uses photons radiated from leptons in $Z \to \ell\ell\gamma$ decays (radiative Z), and the third uses electrons from $Z \to e^+e^-$ decays, with a method that transforms the electron shower shapes to resemble the photon shower shapes (electron extrapolation). The ratios of the efficiencies in data over MC simulation are measured for three methods and are combined for final efficiency scale factor measurement in ATLAS, as shown in the bottom panel of Fig. 3.6.

The electron/photon reconstruction and PID efficiencies provided by the ATLAS Egamma CP group are optimised and are available for particles with E_{T} larger than 10-15 GeV.

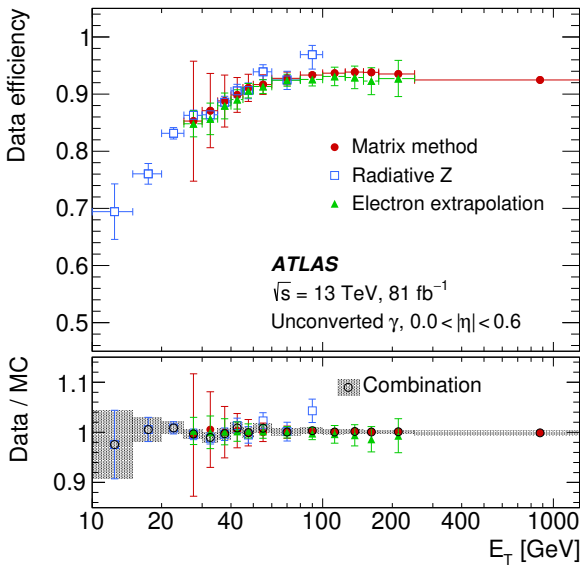

Figure 3.6: The photon identification efficiency, and the ratio of data to MC efficiencies, for unconverted photons, as a function of E_{T} for unconverted photons with $|\eta| < 0.6$. The combined scale factor, obtained using a weighted average of scale factors from the individual measurements, is also presented; the band represents the total uncertainty [86].

Chapter 4

Trigger

4.1 ATLAS trigger system

The ATLAS trigger system [89] is responsible for real-time processing of the collision data and selection of events to be recorded in the permanent storage. It consists of hardware-based Level-1 trigger (L1) and software-based High Level Trigger (HLT). The nominal collision rate of 40 MHz in the *pp* system exceeds the data recording capabilities in ATLAS and only a fraction of data can be stored. The efficient and reliable selection system is therefore essential for any physics analysis.

The schematic overview of the ATLAS trigger and data acquisition systems used during Run 2 is presented in Fig. 4.1. The L1 consists of several components and relies on the fast programmable logic, allowing the L1 decision within 2.5 μs. Signals from the EM and hadronic calorimeters are processed in reduced granularity by the L1Calo in order to find patterns characteristic for electrons/photons, τ-leptons, jets or high total transverse energy/ missing transverse energy. In parallel, the L1Muon trigger processes signals from the muon system. The outputs from L1Calo and L1Muon are combined in the L1Topo sub-system which enables topological selections on the calorimeter and muon trigger objects. These selections could include for example requirements on angular separation, invariant mass or summed transverse energy of trigger objects. The information from L1Calo, L1Muon and L1Topo (and also from a few additional sub-detectors, for example the ZDC) is later transferred to the Central Trigger Processor (CTP) which decides whether to accept or reject an event. The CTP then distributes the decision to the detector readout system and the HLT. It also defines Regions Of Interest (ROIs) using η and ϕ coordinates where the L1 trigger has identified interesting features and includes information on the type of this feature and the criteria passed (for example a E_{T} threshold). The RoIs are further processed at the HLT. The maximum output rate from the L1 is at the level of 100 kHz.

The HLT farm, consisting of about 40k processing units, receives the signals from all sub-detectors in full granularity. It runs offline-like reconstruction and selection algorithms either in the ROIs or in the full event. Typically, the event processing time is about 200 ms. If an event is accepted by the HLT, it is sent to the data storage for further offline processing. The output rate from the HLT typically ranges between 1 and 2 kHz.

The logical combination of requirements at L1 (L1 items) is referred to as a L1 seed and together with the set of selections in the HLT algorithms defines a so-called trigger chain. These are usually designed specifically for physics signatures and can be either chains to collect signal events for a given process (primary chains) or to collect representative samples for background or performance studies (supporting chains). The event is accepted if it passes the requirements of at least one of the trigger chains. The supporting chains can be prescaled during data taking,

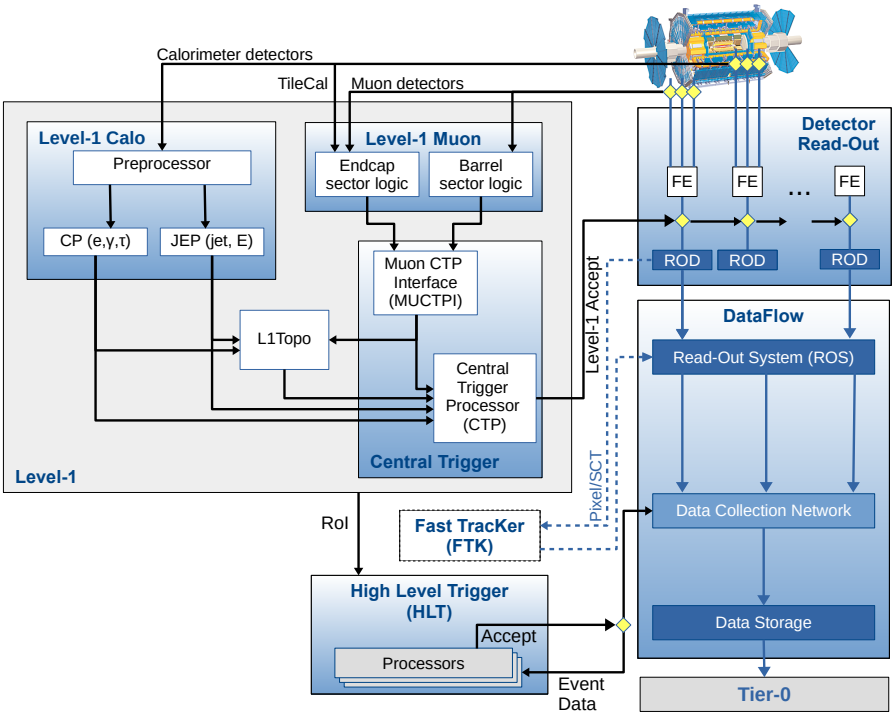

Figure 4.1: The ATLAS trigger and data acquisition system deployed for Run 2 [89].

what means that only a fraction of events accepted by those chains is recorded. The primary chains may also be prescaled very rarely, for example when a process of interest has a very high cross-section.

4.2 Trigger optimisation for dielectron/diphoton events

In this section work done by the author of this thesis in preparation to the 2018 Pb+Pb data taking is described. The standard electron/photon triggers, utilised in pp collisions, do not provide an adequate kinematic coverage to select event candidates from $\gamma\gamma \to e^+e^-$ and $\gamma\gamma \to \gamma\gamma$ processes. Therefore, a dedicated trigger strategy had to be developed, implemented and optimised. As a result, a set of efficient primary and supporting triggers was provided.

Despite the simplicity of the final state, triggering on UPC dielectron/diphoton events is challenging due to the very low electron/photon E_{T} requirement, starting from a few GeV. In this kinematic region, apart from a high rate of inelastic interactions, also electronic noise may contribute to the total rate at the level of kHz.

The trigger for diphoton events used in the 2015 Pb+Pb data taking was a starting point for optimisation of the trigger strategy for the 2018 run. It required total transverse energy $\sum E_{\mathrm{T}}^{\mathrm{L1}}$, between 5 and 200 GeV at the L1 and no more than one hit in the inner ring of MBTS and maximum of 10 hits reconstructed in the pixel detector at the HLT. This set of trigger requirements enabled the measurement of LbyL scattering for final-state photons with $E_{\mathrm{T}} > 3$ GeV [38]. As LbyL scattering cross-section decreases with photon E_{T}, before the 2018 data taking the improvement of the trigger strategy was implemented to be able to lower the minimum photon E_{T} requirement from 3 to 2.5 GeV.

To improve detector sensitivity to low-E_{T} particles, the L1 calorimeter noise settings have been optimised. The impact of these improved settings on the L1 trigger performance is pre-

sented in the following subsections along with the optimisation of $\sum E_{\mathrm{T}}^{\mathrm{L1}}$ requirements. The modifications introduced at the HLT are also described.

4.2.1 Event selection for early L1 trigger studies

At the L1 trigger, which does not include tracking information, dieletron and diphoton events have similar detector signatures. The common features of the final states of these two processes include low E_{T} EM particles, good correlation in E_{T} between them, and minor detector activity. Additionally, both photon and electron pairs have a back-to-back topology, what is expressed in low value of acoplanarity defined as $\alpha = 1 - |\Delta\phi|/\pi$, where $\Delta\phi$ stands for a difference in the azimuthal angles for outgoing particles. Because of that, performance studies of low-E_{T} diphoton triggers can be conducted using exclusive pairs of electrons. Due to much higher production cross-section, $\gamma\gamma \to e^+e^-$ events provide enough statistics for an efficiency measurement.

The optimised calorimeter trigger settings at L1 were first deployed for heavy-ion data taking in October 2017 for a short test xenon-xenon (Xe+Xe) run at $\sqrt{s_{\mathrm{NN}}} = 5.44$ TeV. They were introduced to increase the sensitivity to the low-energy EM signals and were tailored for the low-pileup environment of HI collisions. The noise rejection thresholds were optimised for each triggering section in the EM calorimeter by L1Calo experts.

Evaluation of the diphoton trigger efficiency at L1 for these improved settings is performed using 3 $\mu\mathrm{b}^{-1}$ of Xe+Xe collision data. Exclusive e^+e^- events for an efficiency measurement are selected from a minimum-bias sample recorded by requiring a logical OR of two triggers, first one requiring $\sum E_{\mathrm{T}}^{\mathrm{L1}} \leq 4$ GeV at L1 and at least one track at HLT and a second one requiring $\sum E_{\mathrm{T}}^{\mathrm{L1}} > 4$ GeV. The offline selection criteria include exactly two oppositely-charged tracks with transverse momenta, $p_{\mathrm{T}} > 1$ GeV, in a back-to-back topology (acoplanarity < 0.2). Tracks are matched to offline EM clusters with $\Delta R < 0.7$, where $\Delta\eta$ and $\Delta\phi$ denote the difference in pseudorapidity and azimuthal angle, respectively, between the track and EM cluster. Minor detector activity, described by the sum of p_{T} of remaining tracks, is required to be less than 2 GeV. After applying these criteria, 72 event candidates are selected.

A left panel of Fig. 4.2 shows the acoplanarity distribution of selected exclusive e^+e^- candidates while the right panel of the same figure presents good correlation between the E_{T} of the EM clusters associated to electron candidates, $E_{\mathrm{T}}^{\mathrm{cluster1,2}}$. Both distributions exhibit characteristic features of exclusive dielectron events, which are small acoplanarity and similar transverse energy of the outgoing particles.

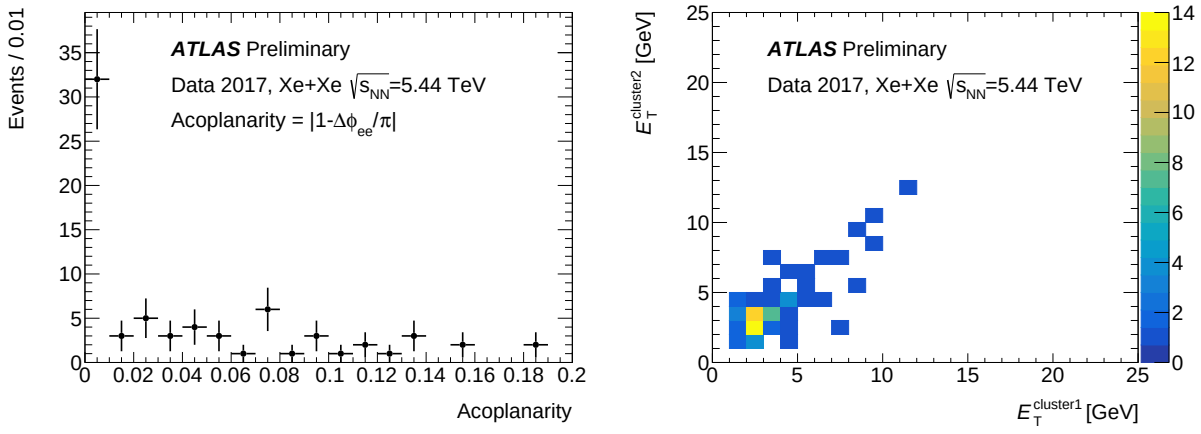

Figure 4.2: Acoplanarity distribution of two tracks (left) and correlation between transverse energy of two EM clusters matched to offline tracks (right) for the exclusive e^+e^- event candidates in minimum-bias Xe+Xe collisions. [90].

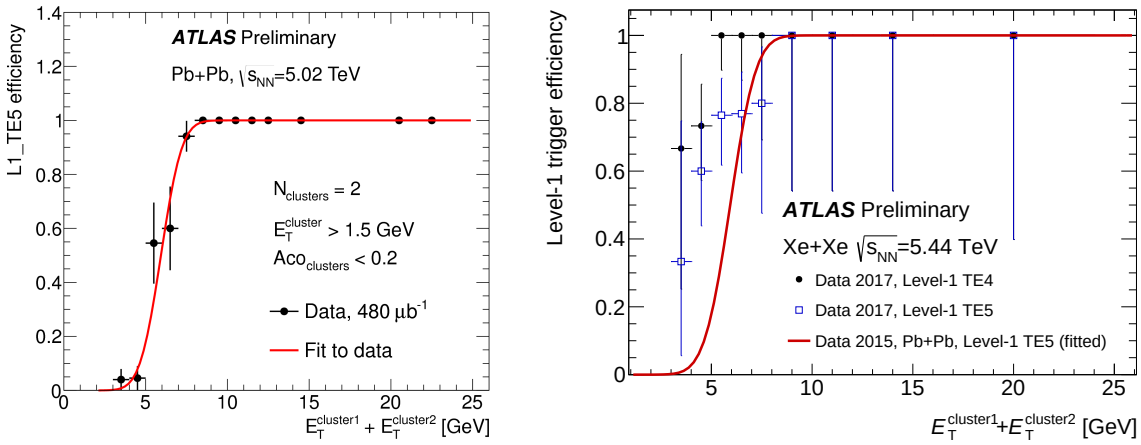

Figure 4.3: Efficiency of L1_TE5 for exclusive e^+e^- events in 2015 Pb+Pb data [91] (left) and efficiency of L1 triggers: L1_TE4 (full circles) and L1_TE5 (open squares) as a function of the sum of transverse energy of two EM clusters satisfying the exclusive e^+e^- event selection in 2017 Xe+Xe data [90] (right). Triggers L1_TE4 and L1_TE5 have 4 and 5 GeV thresholds on $\sum E_{\mathrm{T}}^{\mathrm{L1}}$, respectively. The red curve represents an error function fit to the L1_TE5 trigger efficiency measured in the 2015 Pb+Pb data.

4.2.2 L1 trigger efficiency in 2015 Pb+Pb and 2017 Xe+Xe

The diphoton trigger efficiency in 2015 Pb+Pb data was measured using exclusive e^+e^- events passing a dedicated supporting trigger [91]. At L1, this trigger required coincidence of signals in both ZDC arms, and total E_{T} below 50 GeV. At the HLT at least two (three) space points reconstructed in the pixel (SCT) detector, and the presence of at least one reconstructed track ($p_{\mathrm{T}} > 200\,\mathrm{MeV}$) were required. The L1 trigger efficiency is presented in the left panel of Fig. 4.3 as a function of the sum of transverse energy of two clusters corresponding to the e^+e^- pair. The efficiency reaches 20% for $E_{\mathrm{T}}^{\mathrm{cluster1}} + E_{\mathrm{T}}^{\mathrm{cluster2}} = 5$ GeV and ∼70% for $E_{\mathrm{T}}^{\mathrm{cluster1}} + E_{\mathrm{T}}^{\mathrm{cluster2}} = 6$ GeV, and 100% for $E_{\mathrm{T}}^{\mathrm{cluster1}} + E_{\mathrm{T}}^{\mathrm{cluster2}} = 8$ GeV. The error bars represent the statistical uncertainties, while the red curve represents an error function fit to the L1_TE5 trigger efficiency measured in the 2015 Pb+Pb data.

In the 2017 Xe+Xe data, the L1 trigger efficiency was measured for two items: L1_TE4 and L1_TE5, requiring $\sum E_{\mathrm{T}}^{\mathrm{L1}} > 4$ or 5 GeV, respectively. Similarly to the result from the 2015 data, the efficiency is presented as a function of the sum of E_{T} of two EM clusters matched to the e^+e^- candidates. The L1_TE4 trigger is fully efficient starting from 5 GeV, while L1_TE5 starting from 8 GeV. As it is shown in the right panel of the Fig. 4.3, both triggers turn on faster and L1_TE4 has a higher efficiency in comparison to the trigger used in the 2015 Pb+Pb data taking which efficiency is represented by the red curve in the figure.

4.2.3 Estimation of L1 trigger rates

Improvement of L1 calorimeter noise settings results in increased online rates of total energy triggers. It turned out to be necessary to reduce the rate which can be achieved by vetoing events with large $\sum E_{\mathrm{T}}^{\mathrm{L1}}$. In 2015 Pb+Pb data taking, a requirement $\sum E_{\mathrm{T}}^{\mathrm{L1}} < 200$ GeV decreased the online rate of L1_TE5 by a factor of 3.5. This was not sufficient for 2018 Pb+Pb data taking as most of the additional electronic noise is of the order of a few GeV.

The detector measurements conducted with the optimised L1 calorimeter noise settings demonstrated that for the L1_TE4 item the expected noise is at the level of 7.5 Hz per bunch crossing, while for the L1_TE5 item, it is 1 Hz per bunch crossing. Assuming 700 collid-

ing bunches for the nominal Pb+Pb beam configuration, the L1_TE4 trigger would generate 5.3 kHz of noise rate, while L1_E5 would generate 0.7 kHz of noise rate. For comparison the L1_TE3 trigger would generate over 40 kHz of noise rate, what explains why triggers with a lower $\sum E_{\mathrm{T}}^{\mathrm{L1}}$ requirement could not be considered.

In Fig. 4.4 a comparison of $\sum E_{\mathrm{T}}^{\mathrm{L1}}$ distributions between exclusive e^+e^- events and the minimum-bias sample is shown. In selected e^+e^- events, following the requirements drafted in Sec. 4.2.1, maximum $\sum E_{\mathrm{T}}^{\mathrm{L1}}$ values reach 25 GeV. Because of very limited statistics of the test Xe+Xe data sample, a conclusion was made for the maximum $\sum E_{\mathrm{T}}^{\mathrm{L1}}$ threshold which should be set higher than this value to give also an opportunity to derive limits for BSM searches [69].

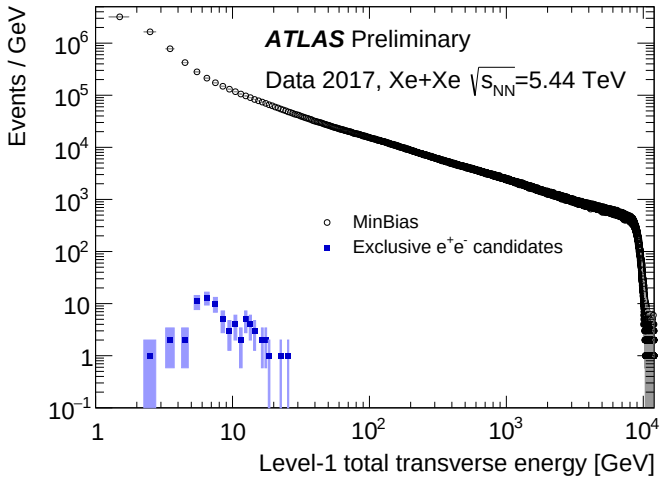

Figure 4.4: Distribution of $\sum E_{\mathrm{T}}^{\mathrm{L1}}$ in minimum-bias events (open circles) and exclusive e^+e^- event candidates (full squares) in 2017 Xe+Xe data [90].

To reach the goals, the three values of maximum $\sum E_{\mathrm{T}}^{\mathrm{L1}}$ were proposed to be 50, 100 and 200 GeV. Table 4.1 presents rate estimates for proposed L1 triggers for instantaneous luminosity equal to 3×10^{27} cm^{-2}s^{-1} which was expected in 2018 Pb+Pb collisions at the start of data taking. Two methods were used for the extrapolation. The rate values vary depending on the methodology used for estimation. In method 1, a linear scaling with luminosity was assumed, while a scaling factor of 1.61 was used to extrapolate rates measured in Xe+Xe collisions to the Pb+Pb system in method 2. Rates obtained in method 2 are in general higher than the rates extracted from the reprocessing of 2015 Pb+Pb data in method 1. In both cases, the noise rate calculated for 700 colliding bunches is added to the expected physics rate.

4.2.4 Improvements in L1 primary trigger strategy

Another approach considered to reduce the L1 rate was to introduce an additional requirement on the activity in the EM calorimeter. The first proposed item was the L1_TEX_EM3 trigger, where X=4,5 and EM3 selects events having at least one EM cluster with transverse energy above 3 GeV. Figure 4.5 presents the efficiency measurement of this selection performed on the basis of 2017 Xe+Xe data. The comparison to the trigger used in 2015 Pb+Pb data taking shows worse performance of triggers with the additional EM requirement of 3 GeV.

At L1, there is a possibility to select events with at least two EM clusters with transverse energy above a certain threshold. Those selections were also available during the 2017 Xe+Xe data taking, for example the L1_2EM3 item requiring at least two EM clusters with E_{T} above 3 GeV each. However, as shown in Fig. 4.5, requiring already one EM cluster of this energy at L1 significantly broadens the efficiency turn-on curve. Items with lower EM thresholds were

L1 trigger	Rate [Hz] method 1 from 2015 Pb+Pb reprocessing	Rate [Hz] method 2 from extrapolation of 2017 Xe+Xe data
L1_TE4_VTE50	8210	9800
L1_TE4_VTE100	9100	11300
L1_TE4_VTE200	10200	12800
L1_TE5_VTE50	3340	4500
L1_TE5_VTE100	4230	5900
L1_TE5_VTE200	5340	7500

Table 4.1: Estimates of L1 trigger rates for proposed trigger items, calculated for instantaneous luminosity equal to 3×10^{27} cm^{-2}s^{-1} for Pb+Pb collisions at 5.02 TeV. The values include noise rate estimated for 700 colliding bunches.

not defined at the time of the Xe+Xe data taking, and therefore could not be tested in terms of efficiency or rate levels. Moreover, the configuration with a low threshold of 7 GeV generated overflows at high multiplicity events in 2015 Pb+Pb data taking. Such a situation had to be avoided, as it disturbs the data recording procedure. Therefore, L1_EM triggers with low thresholds had to be disabled in that run. To overcome this problem in 2018 Pb+Pb data taking, low-E_{T} EM thresholds were defined in place of L1_TAU items. In *pp* collisions, TAU items are used to trigger on τ candidates, and they require signal in both EM and hadronic parts of the calorimeter. During 2018 Pb+Pb data taking, a decision was made to mask signals from the hadronic layers, and therefore TAU items mimicked the behaviour of EM items, which are typically used to trigger on electron/photon (egamma) objects. This solution eliminated the possibility of overflows caused by low-E_{T} EM items in high-activity central events, what could affect performance of high-p_{T} egamma triggers and make impact on trigger operations.

Using the modified L1_TAU configuration, the new items, L1_TAU1 and L1_TAU2, were introduced. They required at least one EM cluster with E_{T} greater than 1 or 2 GeV, respectively. They were used to define L1 seeds for primary and backup trigger chains, which were: L1_TEX, L1_TAUY_TEX, L1_2TAUY, with X=4,5 and Y=1,2. All of them had also an additional requirement on maximum $\sum E_{\mathrm{T}}^{\mathrm{L1}}$ imposed to reject high multiplicity events. As performance of these reconfigured TAU triggers was not measured before, the final choice of the primary triggers could only be made during the 2018 Pb+Pb data taking based on online trigger rates.

4.2.5 Triggering strategy at the HLT

FCal veto

The new approaches were also introduced in 2018 Pb+Pb data taking in the HLT strategy for the primary trigger chains. The previously used MBTS veto requirement was replaced by the veto on the activity in the FCal. For UPC events, the signal in the FCal should be consistent with noise. This was verified using data from a dedicated noise test, in which the detector was recording data without beams injected to the LHC. The distribution of transverse energy deposited on both sides of FCal is shown in Fig. 4.6 for events accepted by the L1 trigger requiring $\sum E_{\mathrm{T}}^{\mathrm{L1}}$ above 4 GeV. Following those studies, the FCal veto was defined with the maximum transverse energy on any side of FCal set to 3 GeV.

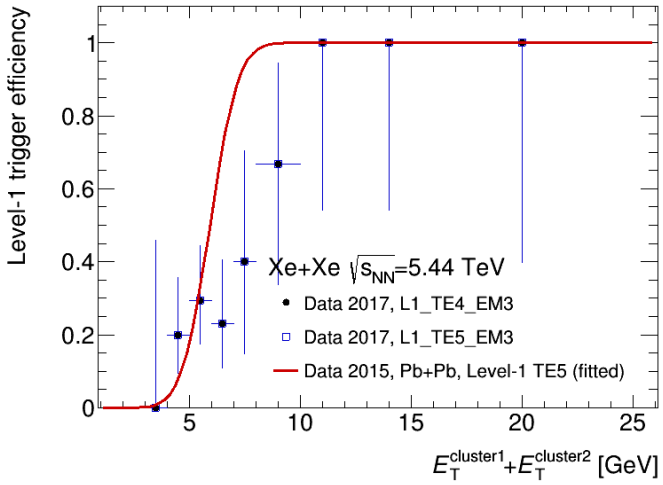

Figure 4.5: Efficiency of L1 triggers: L1_TE4_EM3 (full circles) and L1_TE5_EM3 (open squares) as a function of the sum of transverse energy of two EM clusters satisfying the exclusive e^+e^- event selection in 2017 Xe+Xe data. Triggers L1_TE4_EM3 and L1_TE5_EM3 have 4 and 5 GeV thresholds on $\sum E_T^{L1}$, respectively, and additionally require at least one EM cluster with energy above 3 GeV. The fit represents the L1_TE5 trigger efficiency measured in 2015 Pb+Pb data.

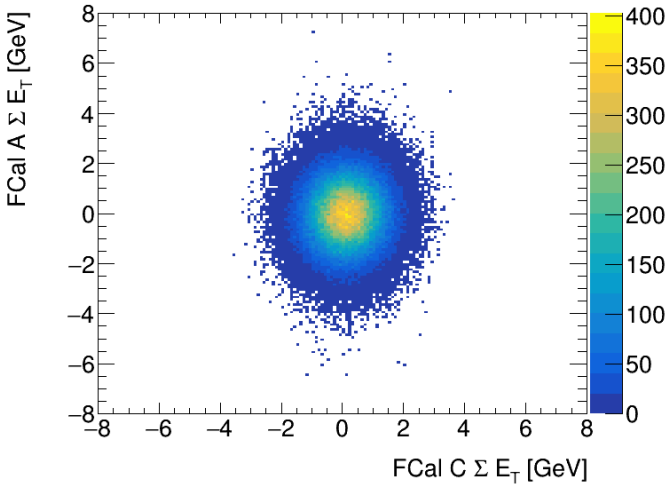

Figure 4.6: Distribution of transverse energy measured on both sides of the FCal detector for events triggered using the $\sum E_T^{L1} > 4$ GeV requirement in the data collected in the noise test.

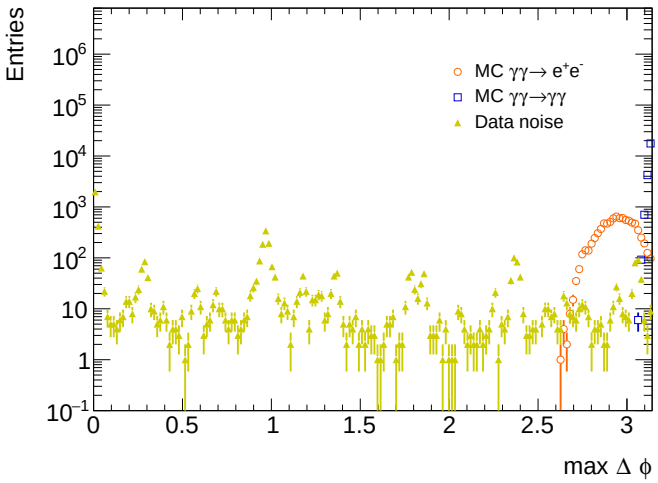

Figure 4.7: Distribution of maximum $\Delta\phi$ between EM cluster pairs in the event for noise and simulated dielectron/diphoton events.

Pixel veto

The requirement on a maximum number of pixel hits was increased from 10 to 15 between 2015 and 2018 Pb+Pb runs. After that change, the primary chain accepted diphoton events with photon conversions and was more efficient on dielectron events.

Noise suppression

Due to the multiple changes in the trigger strategy and expected increase of the instantaneous luminosity with respect to 2015 Pb+Pb data taking, the prediction of the output rates was not straightforward in preparation to the 2018 run. There was a need of a backup trigger strategy in case the recording rate exceeded allocated bandwidth. At the HLT, a dedicated noise suppression algorithm was developed to reduce the fraction of noise events accepted by the HLT. The selection was based on the fact that in exclusive processes electron/photon pairs are produced back-to-back in the azimuthal angle. At the trigger level, the calorimeter clusters are reconstructed, and for cluster having more than 1.5 GeV a difference in ϕ between each pair of EM clusters could be calculated. The distribution of the maximum $\Delta\phi$ for the noise and for simulated dielectron and diphoton events is presented in Fig. 4.7. Based on this distribution, a requirement to accept the event was set on maximum $\Delta\phi$ to be above 2.4. Additional chains were defined as backup. They included the noise suppression algorithm on top of other requirements used in the primary chain.

4.2.6 Supporting dielectron triggers

In the 2015 Pb+Pb run, no dedicated dielectron trigger was used. Low p_{T} dielectron events provide an invaluable sample of data for performance evaluation. In particular they can serve for performance measurements of diphoton/dielectron triggers, and also provide a good reference sample for photon identification performance studies. Therefore, a set of supporting trigger chains, aiming to select dielectron events was implemented for the 2018 Pb+Pb data taking.

The supporting triggers for low p_{T} dielectron production were designed based on the 2TAUX items, where X=1,2, or based on L1 items requiring certain signal in the ZDC, i.e. the coincidence on both sides of the ZDC or signal only on one side or no signal on both sides of ZDC. All L1 items also required $\sum E_{\mathrm{T}}^{\mathrm{L1}} < 50$ GeV.

At the HLT requirements for supporting triggers include:

- the FCal veto and the exclusivity selection which accepts events with 2-5 tracks with $p_{\mathrm{T}} > 0.2$ GeV with at least two tracks with $p_{\mathrm{T}} > 1$ GeV,
- the MBTS veto instead of FCal veto (for the evaluation of the FCal veto efficiency),
- a minimum number of spacepoints seeded off the random trigger that can be used for tracking efficiency measurement.

4.3 Trigger efficiency measurement

The primary triggers used in the analysis were chosen during the 2018 Pb+Pb data taking as the ones with lowest possible thresholds and which were not prescaled for the whole data taking period. This section describes the evaluation of their efficiency for exclusive dielectron/diphoton events. The results of these studies are used in both dielectron and diphoton measurements described in Chapters 5 and 6. Instead of using the simulated trigger decision, all MC samples are reweighed by a total trigger efficiency, ϵ_{T}, defined as:

$$\epsilon_{\mathrm{T}} = \epsilon_{\mathrm{L1}} \cdot \epsilon_{\mathrm{PixVeto}} \cdot \epsilon_{\mathrm{FCalVeto}}, \tag{4.1}$$

with ϵ_{L1}, $\epsilon_{\mathrm{PixVeto}}$ and $\epsilon_{\mathrm{FCalVeto}}$ being L1 trigger efficiency, pixel veto efficiency and FCal veto efficiency, respectively. To propagate the trigger up/down uncertainty, all factors are varied up/down by their uncertainty and their product is applied as the trigger efficiency for MC simulation.

4.3.1 Definition of primary triggers

The primary strategy to trigger low-E_{T} dielectron/diphoton events was established to use a logical OR of two dedicated triggers having different L1 seeds and the same HLT selection. These two triggers are:

- `HLT_hi_upc_FgapAC3_hi_gg_upc_L1TAU1_TE4_VTE200`
- `HLT_hi_upc_FgapAC3_hi_gg_upc_L12TAU1_VTE50`.

They include three sets of requirements:

- A L1 seed is one of the following:
  - `L1TAU1_TE4_VTE200` requires coincidence of minimum one EM cluster of $E_{\mathrm{T}} > 1$ GeV and total E_{T} between 4 and 200 GeV in the entire calorimeter (i.e. both EM and Tile in range of $|\eta| < 4.9$),
  - `L12TAU1_VTE50` requires at least 2 EM clusters of $E_{\mathrm{T}} > 1$ GeV and total E_{T} in the entire calorimeter below 50 GeV,
- FCal veto, i.e. rejection of events with $\Sigma E_T^{\mathrm{FCal}} > 3$ GeV on any side of FCal (imposed in `hi_upc_FgapAC3`),
- Pixel veto defined by a maximum number of 15 hits in the pixel detector (imposed in `hi_gg_upc`).

The choice was made to use a logical OR of triggers seeded with L1TAU1_TE4_VTE200 and L12TAU1_VTE50 because of their slightly different performance in the turn-on region. The L12TAU1_VTE50 trigger turns on for lower transverse energies (however its turn-on is also wider), but loses events in the tail. In general the overlap in events for these two triggers is very high, what was verified on events passing the dielectron event selection described in Sec. 5.3.1. The number of events passing HLT_hi_upc_FgapAC3_hi_gg_upc_L1TAU1_TE4_VTE200 is 29971, passing HLT_hi_upc_FgapAC3_hi_gg_upc_L12TAU1_VTE50 is 30248, while passing any of them: 30456.

The triggers used for various studies in analyses described in Chapters 5 and 6, are presented in Table 4.2. Their more detailed description is in Sec. 4.3.3.

Signal triggers	Comment
HLT_hi_upc_FgapAC3_hi_gg_upc_L1TAU1_TE4_VTE200	Main physics trigger
HLT_hi_upc_FgapAC3_hi_gg_upc_L12TAU1_VTE50	Main physics trigger
Background / supporting triggers	
HLT_hi_upc_FgapAC3_mb_sptrk_exclusiveloose2_L1VZDC_A_C_VTE50	L1 efficiency
HLT_hi_upc_FgapAC3_mb_sptrk_exclusiveloose2_L1ZDC_XOR_VTE50	L1 efficiency
HLT_hi_upc_FgapAC3_mb_sptrk_exclusiveloose2_L1ZDC_A_C_VTE50	L1 efficiency
HLT_mb_sptrk_exclusiveloose_vetosp1500_L1VTE20	L1 efficiency
HLT_hi_upc_FgapAC3_mb_sptrk_exclusiveloose2_L12TAU1_VTE50	HLT efficiency
HLT_mb_sptrk_vetombts2in_exclusiveloose2_L12TAU1_VTE50	FGapAC3 efficiency
HLT_mb_sptrk_exclusiveloose2_L12TAU1_VTE50	FGapAC3 efficiency
HLT_hi_upc_FgapAC3_hi_gg_upc_noiseSup_L1TE4_VTE200_EMPTY	Cosmic/calo noise
HLT_mb_sp_L1VTE50	Other backgrounds

Table 4.2: List of triggers used in $\gamma\gamma \to e^+e^-$ and $\gamma\gamma \to \gamma\gamma$ measurements.

4.3.2 Event selection for trigger efficiency studies

The trigger efficiency was estimated with e^+e^- pairs originating from exclusive $\gamma\gamma \to e^+e^-$ production. Three event selection criteria are used in order to estimate a mean value of the trigger efficiency and its systematic uncertainty: nominal, loose and tight. Each selection requires exactly two opposite-sign tracks, at least two reconstructed EM clusters with two of them matched to tracks (using the ΔR requirement) and $\Sigma\ E_{\mathrm{T}}{}^{\mathrm{FCal}}$ lower than the noise level $+\ 4\sigma$ on each side of FCal. Other requirements on the track WP, minimum track p_{T}, maximum ΔR between the track and EM cluster, and maximum two-track acoplanarity are summarised in Table 4.3.

In the selection, two track WP are examined. "All tracks" denote all reconstructed tracks available in the analysed event, while "HILoose" tracks are tracks identified as HILoose by the tracking selection tool, provided by the ATLAS tracking performance group. These tracks are identified based on the set of requirements: $|\eta| < 2.5$, the presence of hits in the innermost ID layer, at least one pixel hit, minimum requirement of the track p_{T} (dependent on a number of hits in SCT), transverse distance from the track origin to the beam spot, $|d_0|$, below 1.5 mm, and $|z_0 * \sin(theta)| < 1.5$, where z_0 is the longitudinal distance from the track origin to the beam spot.

Distributions of acoplanarity, correlation between electron p_{T} for electrons from the e^+e^- pair, muon multiplicity, multiplicity of pixel hits for events passing the nominal selection are presented in Fig. 4.8. The acoplanarity distribution, shown on the top left of Fig. 4.8, shows

	Track WP	minimum p_{T} $^{\mathrm{track}}$ [GeV]	maximum ΔR	maximum Aco
loose	all	1	0.7	0.2
nominal	HILoose	1	0.5	0.01
tight	HILoose	2	0.3	0.01

Table 4.3: Summary of requirements used for loose, nominal and tight e^+e^- candidate selections for trigger efficiency measurements.

a good agreement between the data and MC simulation from STARLIGHT in the core of the distribution. An excess of data over MC simulation in the tail of the distribution is expected due to the lack of radiative corrections in STARLIGHT. A good correlation between E_{T} of clusters associated to e^+e^- candidates passing the nominal selection is shown on top right of Fig. 4.8 and confirms the basic feature of exclusive dielectron events. At the same time, a potential background contribution to the data sample from muons is low, what is presented on bottom left of Fig. 4.8 in the multiplicity distribution of tracks reconstructed in the muon tracking system (Muon Spectrometer Track Particles). These are signals from the MS, which would indicate the presence of muon tracks in the ID. The bottom left panel of Fig. 4.8 depicts a comparison between a total number of hits deposited in the pixel detector at the HLT in data and MC simulation in a sample of e^+e^- events. It is found that the two distributions do not match up each other. The distribution in the data peaks at around five pixel hits with a tail reaching more than 30 pixel hits per event. The pixel-hit multiplicity distribution in MC simulation is shifted towards higher values with a peak at around 10 pixel hits per event. This mismodelling of the pixel-hit distribution at the HLT made the trigger decisions available in the simulation unreliable. Instead of using them, an event weight accounting for the trigger inefficiency is derived from the data and applied to MC simulation.

4.3.3 Evaluation of L1 trigger efficiency

The efficiency of a logical OR between `L1_TAU1_TE4_VTE200` and `L1_2TAU1_VTE50` is estimated with e^+e^- event candidates originating from the $\gamma\gamma \to e^+e^-$ process passing one of independent supporting triggers, having different requirements at L1. These supporting triggers were running prescaled down to a few Hz in the 2018 Pb+Pb run with the following selection applied:

- (1) Coincidence of signals in both ZDC sides (`L1_ZDC_A_C`), or (2) no activity in the ZDC (`L1_VZDC_A_C`), or (3) signal only on one side of the ZDC (`L1_ZDC_XOR`),
- Total E_{T} in the entire calorimeter below 50 GeV at L1,
- FCal veto,
- At least two (three) space points reconstructed in the pixel (SCT) detector at the HLT (`mb_sptrk`),
- At most 15 tracks reconstructed at the HLT with min $p_{\mathrm{T}} = 0.1$ GeV with at least two tracks having $p_{\mathrm{T}} > 1$ GeV (`exclusiveloose2`).

The trigger rates were at the level of about 5 Hz for triggers seeded off `L1_ZDC_A_C` and `L1_ZDC_XOR`, and about 0.2 Hz for triggers with `L1_VZDC_A_C` at the L1. Another supporting trigger is `HLT_mb_sptrk_exclusiveloose_vetosp1500_L1VTE20`, which required total E_{T} in the entire calorimeter below 20 GeV (`L1VTE20`), at most 1500 space points(`vetosp1500`), at least two (three) space points reconstructed in the pixel (SCT) detector at the HLT (`mb_sptrk`) and

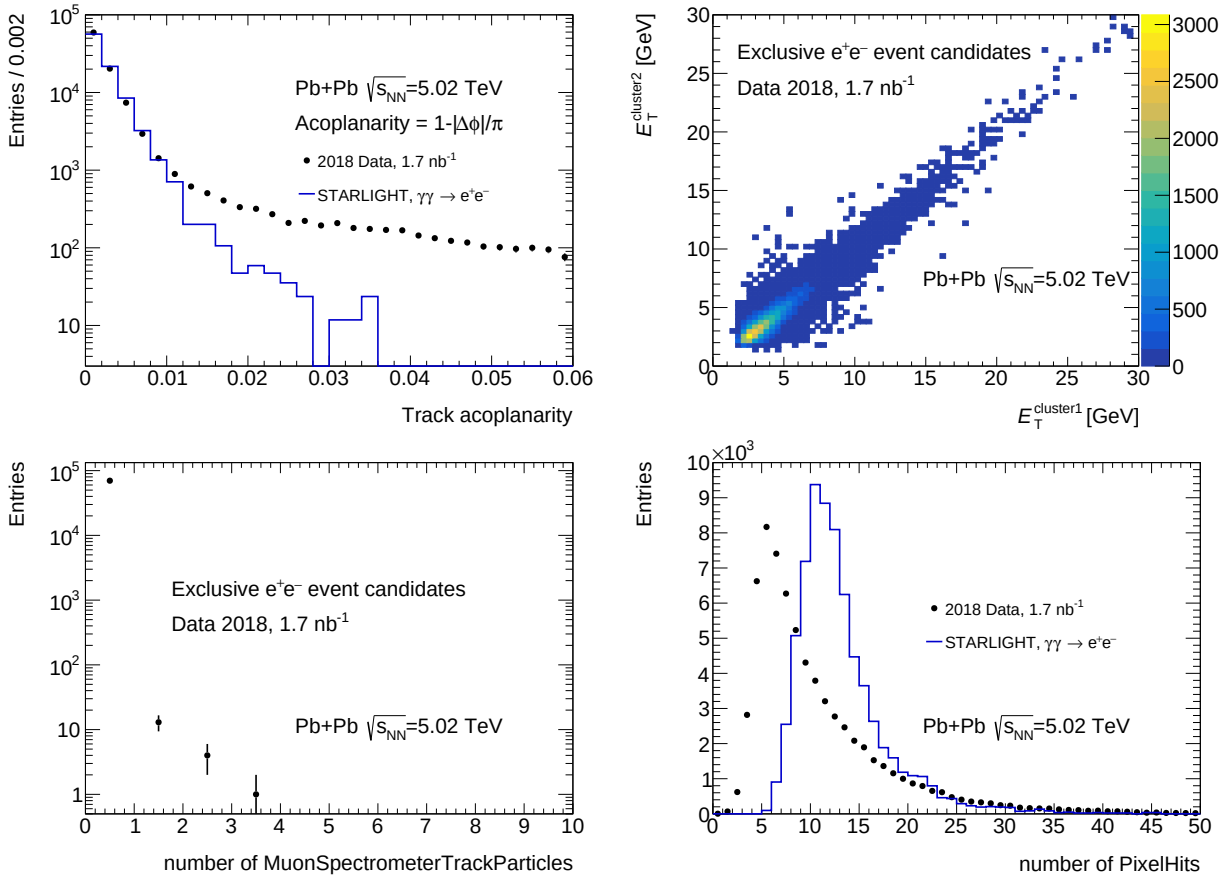

Figure 4.8: Control distributions for e^+e^- candidates passing the nominal selection in the 2018 Pb+Pb data: acoplanarity distribution in data (full markers) and MC simulation from STARLIGHT (histogram) without radiative corrections (top left), correlation between E_{T} of clusters associated to e^+e^- candidates in data (top left), distribution of track multiplicity in the MS in data (bottom left), and distribution of multiplicity of pixel hits in data (full markers) compared with MC simulation from STARLIGHT (histogram) without radiative corrections.

at most 15 tracks reconstructed at the HLT (`exclusiveloose`). The number of events passing one of the supporting triggers and satisfying the nominal selection criteria is 582.

The L1 trigger efficiency is parameterised using an error function fit. The formula used for parametrisation is as follows:

$$\epsilon_{\mathrm{L1}} = 0.5 \cdot (\mathrm{erf}\,(E_{\mathrm{T}}^{\mathrm{cluster1}} + E_{\mathrm{T}}^{\mathrm{cluster2}} - p_1)/p_2 + 1.).$$

The obtained values of parameters are: $p_1 = 4.563 \pm 0.202$ and $p_2 = 2.833 \pm 0.333$. The statistical uncertainties are estimated based on the variation of the fit parameters by their respective σ values. The systematic uncertainties are estimated using the loose and tight selection criteria imposed on the e^+e^- events. The obtained values of parameters for the loose selection are: $p_1 = 4.601$ and $p_2 = 3.076$, while for the tight selection are: $p_1 = 3.936$ and $p_2 = 3.339$. The upper systematic variation is defined as a fit to the tight selection, while lower systematic variation is defined by the fit to the loose selection. The precision of the L1 trigger efficiency is limited by a number of e^+e^- pairs collected by the supporting triggers. This should be considered for improvement in the future HI data taking.

Figure 4.9 shows the L1 trigger efficiency with parametrised fits as a function of a sum of electron E_{T} ($E_{\mathrm{T}}^{\mathrm{cluster1}} + E_{\mathrm{T}}^{\mathrm{cluster2}}$). The vertical line at 5 GeV refers to the requirement of

$m_{ee} > 5$ GeV imposed in the definition of the fiducial region. Therefore, the two bins below this threshold (for which the fits are poorly constrained) contribute minimally to the final measurement. There is no inefficiency introduced by the `VTE50` requirement in one of the signal triggers, because events failing this requirement are accepted by the other signal trigger, with the looser veto (`VTE200`).

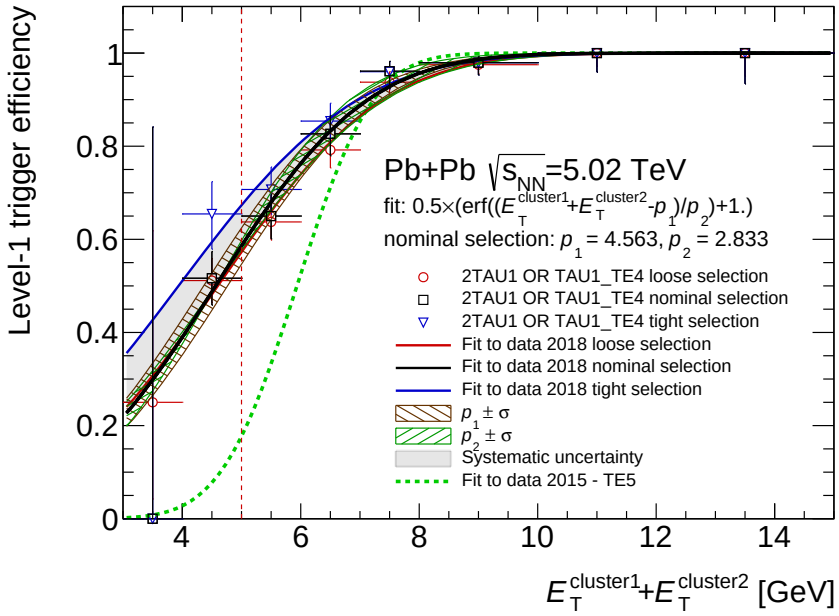

Figure 4.9: L1 trigger efficiency evaluated on $\gamma\gamma \to e^+e^-$ event candidates passing one of the independent supporting triggers. Efficiency measurement is shown for loose (open red circles), nominal (black open squares) and tight (blue open triangles) selections with error function fits, indicated by curves in corresponding colour. Bands represent statistical (hatched brown and green area) and systematic (grey area) uncertainties. Dashed green line shows the error function fit to L1 trigger efficiency measured in 2015 data.

The comparison between L1 efficiency turn-on curves in 2015 and 2018 is presented in Fig. 4.10 as a function of $E_{\mathrm{T}}^{\mathrm{cluster1}} + E_{\mathrm{T}}^{\mathrm{cluster2}}$. The improvements introduced in the trigger used in 2018 resulted in increased efficiency in the $4 < E_{\mathrm{T}}^{\mathrm{cluster1}} + E_{\mathrm{T}}^{\mathrm{cluster2}} < 8\,\mathrm{GeV}$ range. The efficiency raised from 0 to about 0.5 for $E_{\mathrm{T}}^{\mathrm{cluster1}} + E_{\mathrm{T}}^{\mathrm{cluster2}} = 4\,\mathrm{GeV}$ and from about 0.25 to 0.95 for $E_{\mathrm{T}}^{\mathrm{cluster1}} + E_{\mathrm{T}}^{\mathrm{cluster2}} = 7\,\mathrm{GeV}$.

The efficiency of the L1 trigger is also measured as a function of absolute rapidity of the electron pair. For this purpose, an additional requirement of $E_{\mathrm{T}}^{\mathrm{cluster1}} + E_{\mathrm{T}}^{\mathrm{cluster2}} > 5$ GeV is imposed in the event selection. Given the low number of e^+e^- candidates recorded by the supporting triggers, the result for the nominal selection shown in Fig. 4.11, is presented in three bins in $|y_{\mathrm{ee}}|$. The efficiency is flat in $|y_{\mathrm{ee}}|$ within statistical uncertainties.

4.3.4 Evaluation of HLT trigger efficiency

FCal veto

The FCal veto efficiency is studied in the e^+e^- events originating from exclusive $\gamma\gamma \to e^+e^-$ process selected with nominal requirements (see Tab. 4.3) and passing a supporting trigger chain `HLT_hi_upc_FgapAC3_mb_sptrk_exclusiveloose2_L12TAU1_VTE50`.

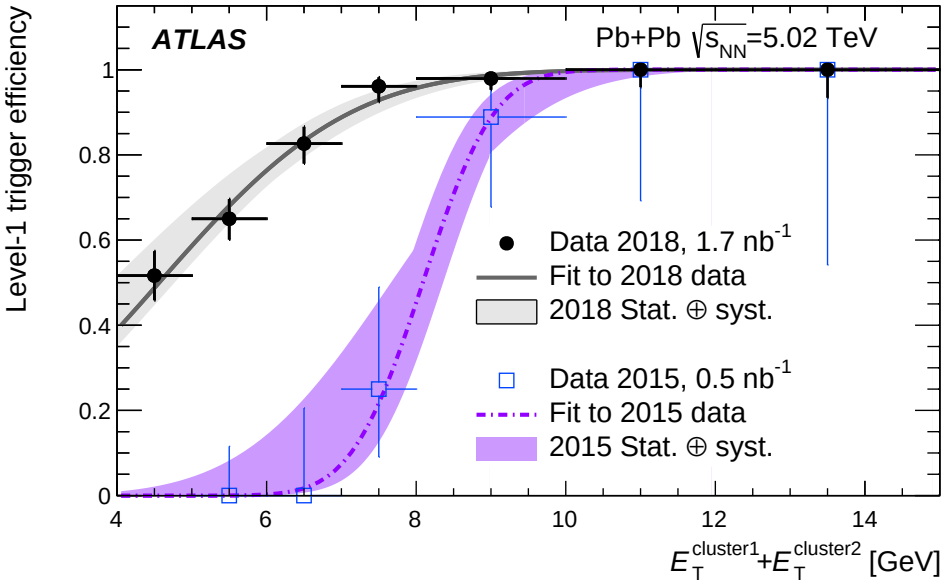

Figure 4.10: L1 trigger efficiency evaluated on $\gamma\gamma \to e^+e^-$ event candidates passing one of the independent supporting triggers. Data are shown as points, separately for two data-taking periods: 2015 (open squares) and 2018 (full circles). The efficiency is parameterised using the error function fit, shown as a dashed (2015) or solid (2018) line. Shaded bands denote total (statistical and systematic) uncertainty.

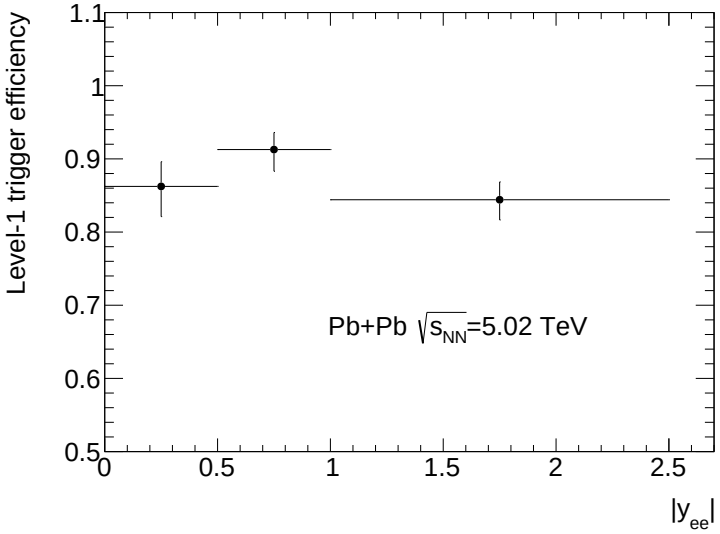

Figure 4.11: L1 trigger efficiency as a function of absolute rapidity of the electron pair from the $\gamma\gamma \to e^+e^-$ process selected by one of the supporting triggers.

The efficiency is defined with respect to e^+e^- events selected with another supporting trigger chain (`HLT_mb_sptrk_exclusiveloose2_L12TAU1_VTE50`), having the same selection but without the FCal veto requirement. The FCal veto efficiency is shown as a function of $(E_{\mathrm{T}}^{\mathrm{cluster1}} + E_{\mathrm{T}}^{\mathrm{cluster2}})$ in Fig. 4.12. It is flat as a function of $(E_{\mathrm{T}}^{\mathrm{cluster1}} + E_{\mathrm{T}}^{\mathrm{cluster2}})$ and its statistical uncertainty is negligible. The dominant uncertainty is related to a choice of the different event selections of the $\gamma\gamma \to e^+e^-$ sample (loose or tight). The FCal veto efficiency at the HLT is estimated to be

$(99.1 \pm 0.6)\%$. The straight line fit has $\chi^2/ndf = 13.6/9 = 1.51$.

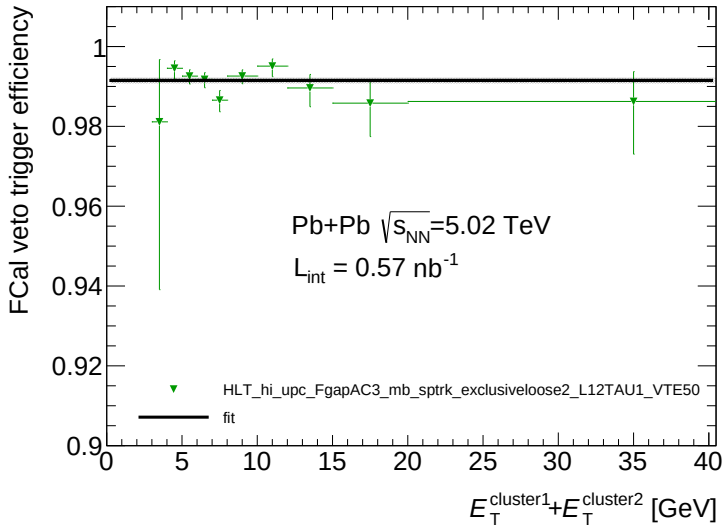

Figure 4.12: Efficiency of the FCal veto requirement evaluated in the $\gamma\gamma \to e^+e^-$ event candidates passing the supporting trigger. Error bars represent the statistical uncertainties.

Pixel veto in $\gamma\gamma \to \gamma\gamma$ events

Due to the very high hit reconstruction efficiency and the low conversion probability of signal photons in the pixel detector, a negligible uncertainty on the requirement for minimal activity in the ID was assigned in the LbyL scattering measurement using 2015 Pb+Pb data [38]. Given that the pixel-veto requirement was looser in the 2018 Pb+Pb run in comparison to the 2015 Pb+Pb run and that this variable is mismodelled in MC simulations, the inefficiency of the pixel veto is considered negligible. However, a systematic uncertainty is assigned to this efficiency, based on studies of events triggered on empty bunches. The empty bunch trigger had a pixel-veto requirement, the same as for the primary trigger, because it was also meant to serve for background studies. In Fig. 4.13, the multiplicity distribution of pixel hits for events in empty bunch crossings along with the fit to the data points is shown. In the fit procedure various functions were tested (e.g. the exponential plus linear function or the third order polynomial, landau plus the linear function), and the function is chosen which gives the best description of the data. The chosen fit function is a sum of two exponential and a linear function. The fit is also extrapolated to cover the region with more than 15 hits in the pixel detector. Those events did not make to the distribution due to the pixel-veto trigger requirement. Those missing events in the tail, with more than 15 hits, contribute approximately 0.5% to the full distribution (integral over the entire pixel-hit multiplicity). This contribution is taken as an additional systematic uncertainty. The similar calculations for other tested fit functions gave the uncertainty less than 0.5%.

Figure 4.14 shows a comparison between the distribution of pixel hits reconstructed at the HLT in events recorded in empty bunch crossings, and in the simulated $\gamma\gamma \to \gamma\gamma$ events, normalised to a number of events in the data. The simulated $\gamma\gamma \to \gamma\gamma$ events pass the loose event selection: two EM clusters with $E_{\mathrm{T}} > 2$ GeV, Aco < 0.01 and no tracks in the event. In the simulated sample 0.1% of events do not pass the 15 hits threshold used in the trigger definition. Given the mismodelling of the number of pixel hits at the HLT (see also bottom right panel of Fig. 4.8), the analysis does not rely on trigger decisions in the MC samples.

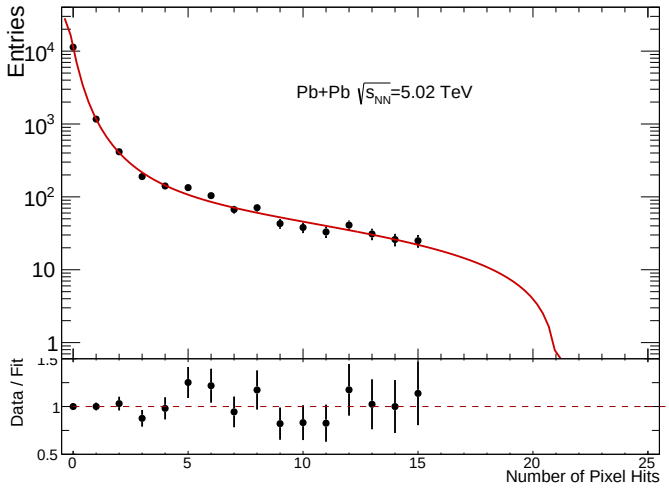

Figure 4.13: Distribution of multiplicity of pixel hits in events from empty bunch crossings. The bottom panel shows the ratio of data over fit. Error bars represent the statistical uncertainties.

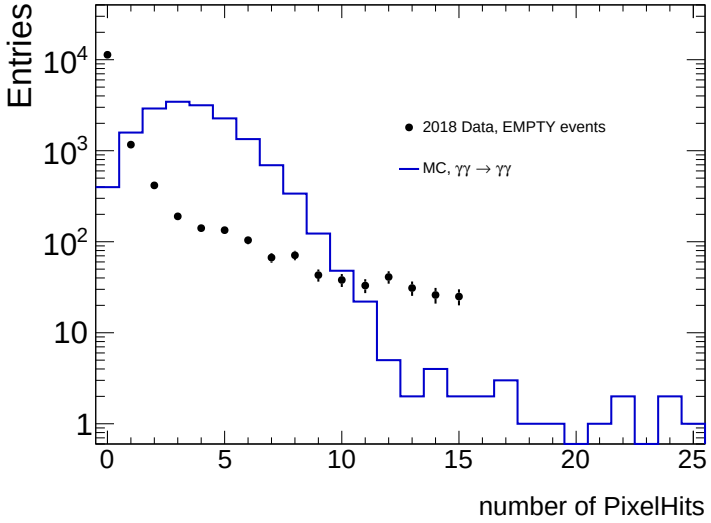

Figure 4.14: Distribution of multiplicity of pixel hits in events recorded in empty bunch crossings, compared with MC simulation of $\gamma\gamma \to \gamma\gamma$ events.

Pixel veto in $\gamma\gamma \to e^+e^-$ events

To evaluate the pixel-veto (`hi_gg_upc`) efficiency for exclusive dielectron events, the relative efficiency of the `HLT_hi_upc_FgapAC3_hi_gg_upc_L12TAU1_VTE50` trigger chain with respect to the `HLT_hi_upc_FgapAC3_mb_sptrk_exclusiveloose2_L12TAU1_VTE50` is measured on e^+e^- events in the data. The dielectron candidate events are selected by requiring exactly two opposite-sign loose electrons having $|\eta_e| < 2.47$, excluding the calorimeter transition region ($1.37 < |\eta| < 1.52$), and exactly two tracks. Other requirements are summarised in Table 4.4. Because of a different number of pixel layers changing with η, the efficiency is measured as a function of dielectron rapidity. More layers in the forward region result in more possible hits in the detector. This can be seen for both data and MC sample for the $\gamma\gamma \to e^+e^-$ process in Fig. 4.15, which shows the number of pixel hits as a function of dielectron rapidity in events passing the event selection from Sec. 5.3.1 (only slightly different wrt to the selection discussed in the trigger

efficiency measurement), but using `HLT_hi_upc_FgapAC3_mb_sptrk_exclusiveloose2_L12TAU1_VTE50` trigger. The red histogram represents a mean value of a number of pixel hits in a given rapidity bin, and has a similar shape in data and MC simulation. The dielectron events with more than 15 hits are rejected by the pixel veto. The efficiency is parametrised by the second order polynomial in the full rapidity range. The correction is applied bin-by-bin for $|y_{ee}| < 0.9$ and using the fit function value otherwise. The resulting efficiency is shown in Fig. 4.16. The statistical uncertainty is assigned bin-wise in the whole rapidity range. The statistical uncertainties are symmetrised[1]. The systematic uncertainties are determined using loose and tight selection requirements as defined in Table 4.4. The results are presented in Fig. 4.17. The statistical uncertainty of the pixel veto dominates over systematics, for which a constant value of $\pm$ 0.005 is assigned.

	minimum p_{T} ^{e} [GeV]	minimum m_{ee} [GeV]	maximum Aco
loose	2	4	1
nominal	2.5	5	0.01
tight	3	6	0.005

Table 4.4: Summary of requirements used for loose, nominal and tight event selections from the $\gamma\gamma \to e^+e^-$ process in the measurement of the pixel-veto efficiency in 2018 Pb+Pb data. Error bars represent the statistical uncertainties.

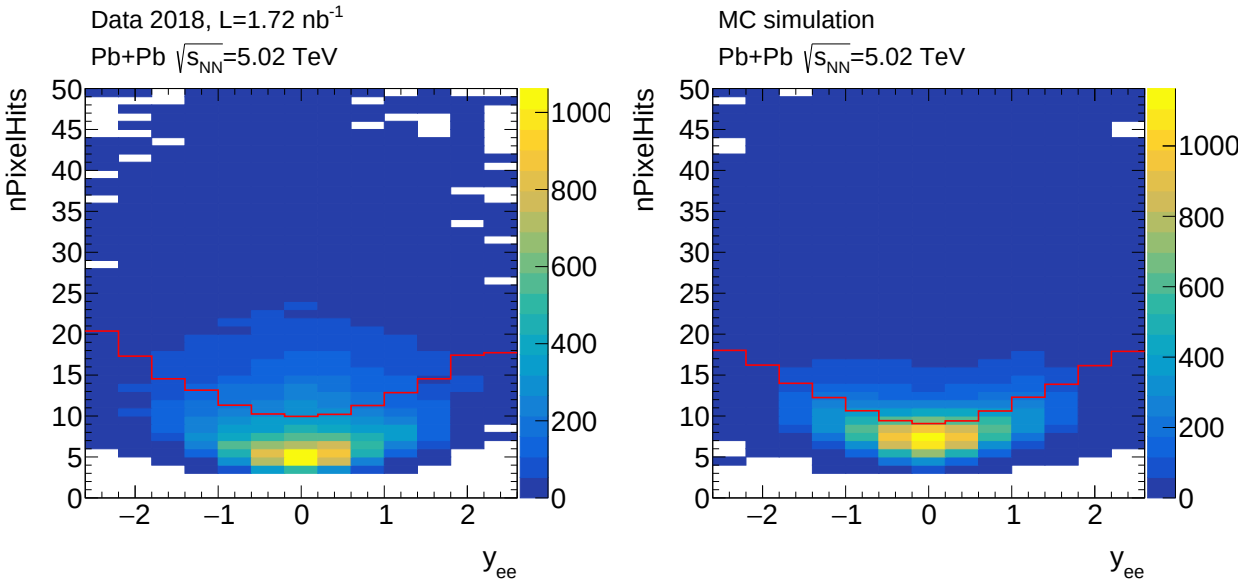

Figure 4.15: Number of pixel hits in data (left) and MC sample for the $\gamma\gamma \to e^+e^-$ process (right) as a function of dielectron rapidity in events passing the event selection from Sec. 5.3.1, but using the `HLT_hi_upc_FgapAC3_mb_sptrk_exclusiveloose2_L12TAU1_VTE50` trigger. The red line represents the mean number of pixel hits in each bin of the dielectron rapidity.

[1]The efficiencies are measured using the TEfficiency class implemented in the ROOT analysis framework [92], which provides asymmetrical uncertainties calculation to ensure the efficiency does not exceed the 0–1 range. For the considered efficiencies, the differences between up and down uncertainties are negligible

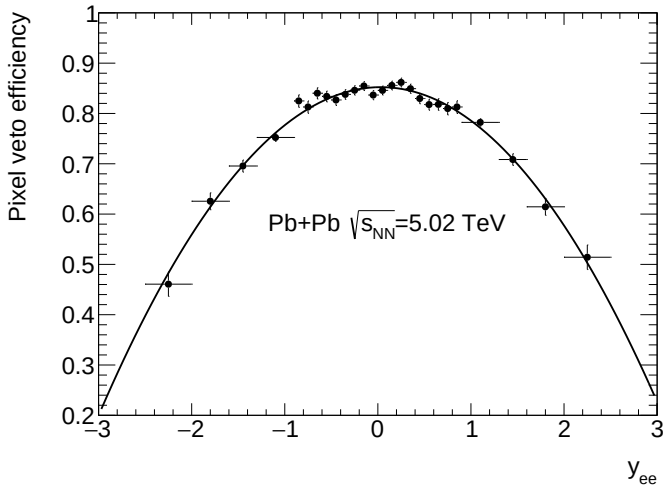

Figure 4.16: Efficiency of pixel veto as a function of $|y_{ee}|$ for events from the $\gamma\gamma \to e^+e^-$ process and a second order polynomial fit to the data.

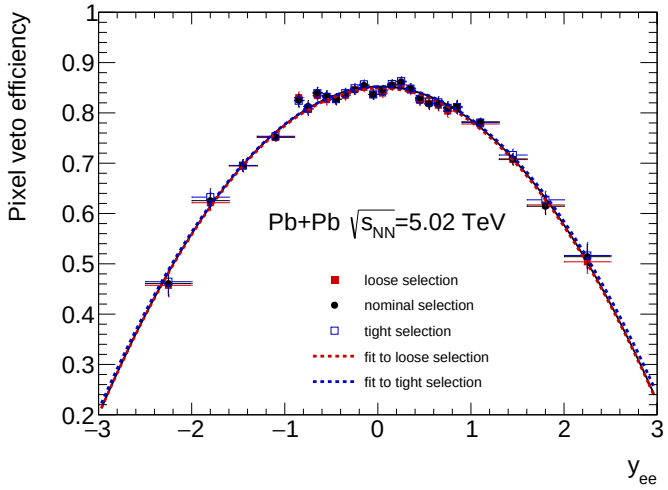

Figure 4.17: Efficiency of pixel veto as a function of $|y_{ee}|$ for events from the $\gamma\gamma \to e^+e^-$ process with data selected using the loose, nominal and tight requirements. Fits to the loose and tight selections represent systematic variations.

Chapter 5

Exclusive dielectron production

This chapter summarises the measurement of exclusive dielectron production in Pb+Pb UPC data, recorded in 2018 with the ATLAS detector. The author of this thesis had a leading contribution to this measurement, and was responsible not only for trigger studies, described in Chapter 4 but also for the optimisation of event selection, evaluation of background contributions, implementation of unfolding and measurement of integrated and differential fiducial cross-sections, along with the evaluation of systematic uncertainties.

The results of the measurement were published as a conference note:

- ATLAS Collaboration, "Exclusive dielectron production in ultraperipheral Pb+Pb collisions at $\sqrt{s_{\mathrm{NN}}}$ =5.02 TeV with ATLAS", conference note ATLAS-CONF-2022-025,

and presented by the author at the Quark Matter conference in April 2022. The publication with final results was submitted to Journal of High Energy Physics [93].

5.1 Data and MC samples

The data used in the dielectron measurement is from Pb+Pb collisions with a centre-of-mass energy of $\sqrt{s_{\mathrm{NN}}} = 5.02$ TeV, recorded in the 2018 by the ATLAS detector at the LHC. The full data set corresponds to an integrated luminosity of 1.72 nb^{-1} of Pb+Pb data. In this data set, the pileup, i.e. the average number of hadronic interactions per bunch crossing, is negligible.

During the 2018 HI data taking, two beam configurations were deployed: early runs (with ATLAS internal numbering 365498–366476) were collected with bunch spacing of 100 ns, while later remaining runs (366526–367384) were taken with bunch spacing of 75 ns. Also due to the lack of the toroidal field at the end of HI data taking, seven runs (with numbers between 367273–367384) were collected without the magnetic field in the MS.

In the analysis, events are required to pass a so-called Good Run List (GRL) selection which ensures that only luminosity blocks (LB) with the ATLAS detector operating in the way to provide good-quality data are used. Luminosity blocks are short periods, usually 60 s, in which the detector is assumed to operate in the same conditions. The GRL included all mentioned above runs, also those without the magnetic field in the MS, as this does not affect the concerned final state. The data was reconstructed with dedicated settings, allowing track reconstruction starting from $p_{\mathrm{T}} = 100$ MeV. The data was skimmed to so-called HION4 derived data format (derivations), with low activity UPC events with electrons, photons and muons included.

During the HI data taking in 2015 there was no efficient primary trigger to record dielectron events. The only trigger possible to use was a trigger to select diphoton events (which is similar signature in terms of triggering at L1), with the HLT selection that accepted only events with very low activity in the ID (at most 10 pixel hits). This caused inefficiencies for dielectron events,

especially in the forward region. A detailed discussion of the trigger used in this analysis with the evaluation of its efficiency is in Sec. 4.3.

The $\gamma\gamma \to e^+e^-$ signal contribution is modelled with the STARLIGHT v3.13 MC generator [94], in which the cross-section is computed by combining the Pb+Pb photon flux with the leading-order elementary cross-section for $\gamma\gamma \to e^+e^-$, as described in Sec. 2.4.1. Events are simulated using settings, which require that there is no hadronic breakup of colliding nuclei, but there is no restriction on Coulomb breakup ("BREAKUP_MODE==5"). The simulated events are later interfaced with PYTHIA8 [95, 96] to include FSR. There are three signal samples produced in exclusive m_{ee} ranges:

- 4.5-7 GeV (157 μb, 4M events),
- 7-15 GeV (122 μb, 4M events),
- above 15 GeV (18 μb, 1M events).

The signal MC samples are normalised to the integrated luminosity of the data using a factor $w = \frac{L \times \sigma_{\mathrm{MC}}}{N_{\mathrm{gen}}}$, where L is the integrated luminosity of the data, σ_{MC} is the cross-section of the MC sample, and N_{gen} is a number of generated events in the MC sample.

The background originating from $\gamma\gamma \to \tau^+\tau^-$ events is simulated using STARLIGHT v3.13 interfaced with PYTHIA8. The contribution from Υ(nS) decays to electrons is also simulated using STARLIGHT v3.13 interfaced with PYTHIA8. In both cases, PYTHIA8 provides simulation of the FSR process.

The dielectron final state can also be produced via dissociative processes, where at least one photon is emitted by a resolved nucleon. This contribution is modelled using SUPERCHIC v4.0 [26] for pp collisions. The shapes of the distributions from these samples are later used for background template fitting. This data-driven approach is used, since there is no simulation of this background process for Pb+Pb collisions, as mentioned in Sec. 2.5.

All simulated events make use of a GEANT [97] based detector simulation [98] and are reconstructed with the standard ATLAS reconstruction software [85].

5.2 Electron reconstruction and identification

In this analysis electrons with $p_{\mathrm{T}} > 2.5$ GeV are studied. Standard recommendations from the ATLAS Egamma CP group for electron reconstruction and identification efficiencies [88] are not available for the full p_{T} range of interest. In particular for electron $p_{\mathrm{T}} < 20$ GeV either they have not been measured or the precision of the measurement is relatively low. Also the pileup-free environment makes it questionable whether the nominal-pileup recommendations for pp collisions are valid in the UPC Pb+Pb data sample. For those reasons dedicated electron performance studies have to be performed. The analysis and their results are described in this section.

5.2.1 Electron reconstruction and identification efficiency

Electron reconstruction and PID efficiencies are measured using a data-driven method on exclusively produced $\gamma\gamma \to e^+e^-$ events in the 2018 Pb+Pb data and signal MC simulation. A dedicated tag-and-probe method is designed to enhance a sample of low-p_{T} electrons. The following criteria are imposed:

- GRL,

- For the data: nominal dielectron trigger i.e. a logical OR of two chains:
  - HLT_hi_upc_FgapAC3_hi_gg_upc_L12TAU1_VTE50,
  - HLT_hi_upc_FgapAC3_hi_gg_upc_L1TAU1_TE4_VTE200,
- For MC simulation: the L1 and HLT trigger efficiency weights as discussed in Sec. 4.3.3-4.3.4,
- At least one electron, one or two tracks, at least one track reconstructed in the pixel detector (pixel track), and one EM cluster,
- Tag is a good LHTight electron with $E_{\mathrm{T}} > 2.5$ GeV,
- Probe is a pixel track with at least three hits,
- Tag and probe candidates have to be opposite charge,
- Invariant mass of the tag-and-probe system $M_{\mathrm{inv}} > 5$ GeV,
- Acoplanarity of the tag-and-probe system Aco < 0.1.

In electron performance studies in pp collisions, which are focused at the high-p_{T} region (typically $p_{\mathrm{T}} > 20$ GeV), an EM cluster is a good probe for the tag-and-probe method as its reconstruction efficiency is close to 100%. Figure 5.1 shows EM cluster efficiency extracted from $\gamma\gamma \to e^+e^-$ MC simulation as a function of truth electron p_{T} or η. EM clusters are matched to truth electrons using a $|\Delta R| < 0.1$ requirement. The EM cluster reconstruction efficiency is about 20% at truth electron $p_{\mathrm{T}} = 2.5$ GeV. It raises rapidly and saturates at almost 100% at truth electron $p_{\mathrm{T}} = 10$ GeV. The EM cluster reconstruction efficiency as a function of truth electron η is at the level of 30% for $|\eta| < 1.2$. Then, the efficiency raises up to 70% at truth electron $|\eta| = 2.2$, and drops to about 60% at $|\eta| = 2.5$. The low EM cluster reconstruction efficiency at $p_{\mathrm{T}} = 2.5$ GeV and strong p_{T}-dependence for $2.5 < p_{\mathrm{T}} < 10$ GeV makes EM clusters suboptimal probes for electron efficiency studies in the tag-and-probe method.

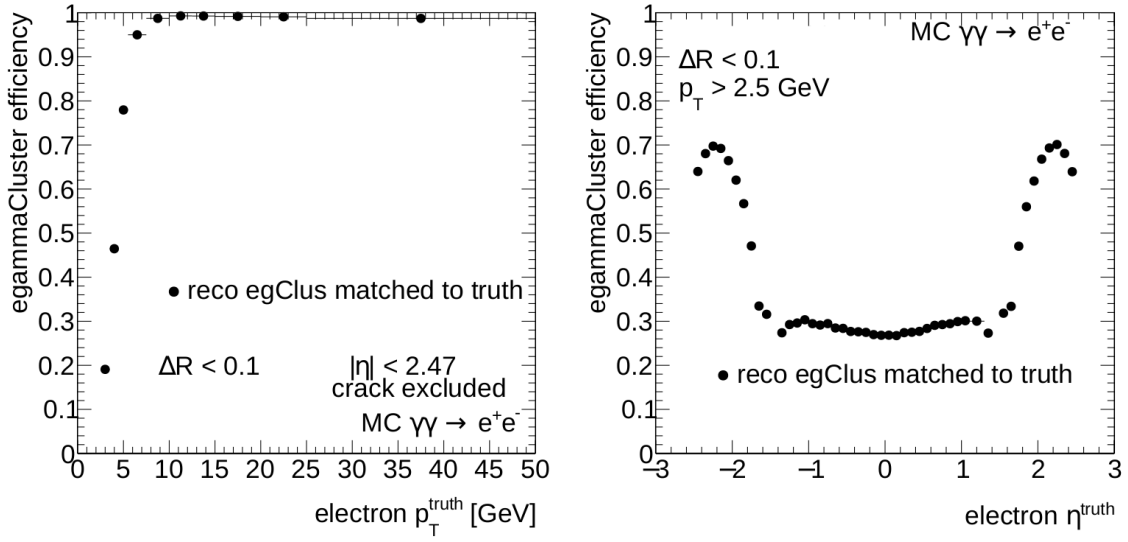

Figure 5.1: EM cluster reconstruction efficiency as a function of truth electron p_{T} (left) and η (right).

In search for more optimal probes, performance of pixel-track reconstruction is also studied. Figure 5.2 shows pixel-track reconstruction efficiency extracted from $\gamma\gamma \to e^+e^-$ MC simulation as a function of truth electron p_{T} or η. Pixel tracks are matched to truth electrons using a $|\Delta R| < 0.2$ requirement for truth electron $p_{\mathrm{T}} < 5$ GeV, and $|\Delta R| < 0.04$ for truth electron $p_{\mathrm{T}} > 5$ GeV. The pixel-track efficiency is close to 100% and does not depend on truth electron p_{T}. As a function of truth electron η, the pixel-track reconstruction efficiency is at the level of 95% at mid-rapidity and in the very forward direction at $|\eta| > 2.3$. For intermediate truth electron $|\eta|$ values it reaches almost 100%. The very high pixel-track reconstruction efficiency and no p_{T}-dependence makes pixel tracks good candidates for probes in the tag-and-probe method.

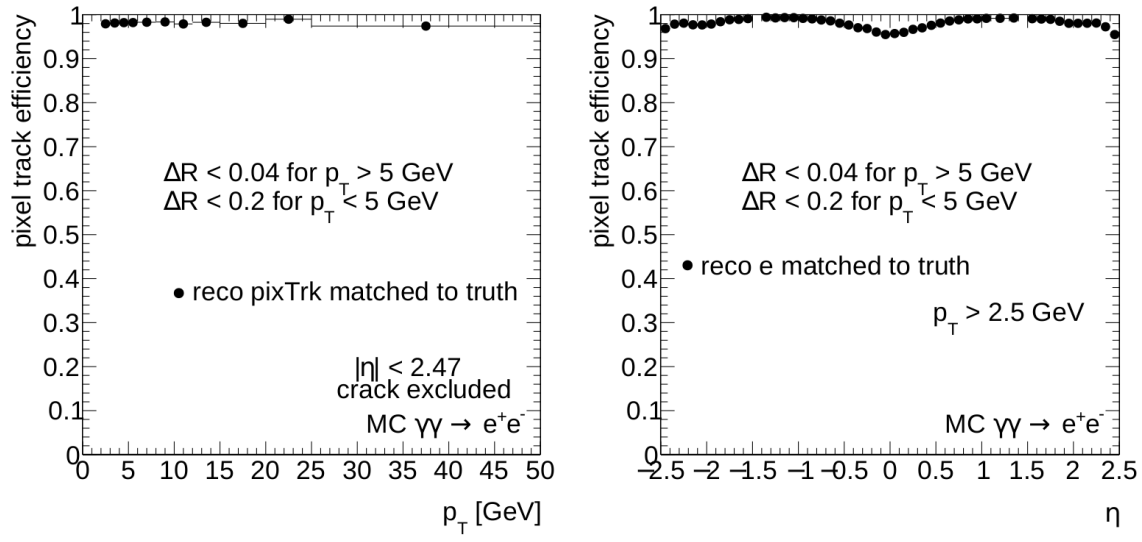

Figure 5.2: Pixel-track reconstruction efficiency as a function of truth electron p_{T} (left) and η (right).

Figure 5.3 shows a comparison of invariant mass distributions for tag and probe pairs after imposing all selection requirements on the 2018 Pb+Pb data and on MC simulation of the $\gamma\gamma \to e^+e^-$ process. The MC sample is normalised to the integrated luminosity of the 2018 Pb+Pb data. A good agreement within 10% is found in both shapes and the absolute normalisations between the data and MC simulation quantified by a ratio of the two distributions in the bottom panel. This discrepancy is qualitatively similar to what was found in the exclusive dimuon measurement [57] where data overshot predictions from STARLIGHT by a few percent. Also it is worth noting that in the electron performance studies a first attempt to simulate a FSR contribution was made with a dedicated STARLIGHT+PHOTOSPP setup. However, that sample did not prove to describe a tail of the acoplanarity distribution well.

Electron reconstruction and PID efficiencies are studied as a function of tag electron p_{T} and probe pixel track η. Two PID WP are considered: *Loose* with cut-based selections, and *LHLoose* with likelihood-based selections. The likelihood-based electron PID is a recommended approach for WP in *pp* collisions at nominal data-taking conditions in Run 2.

Electron reconstruction

Electron reconstruction efficiency, ϵ_{reco}, is defined as a probability of the probe to be also reconstructed as an electron which passes good-quality requirements. A matching requirement of $|\Delta R| < 0.2$ is imposed on the electron and pixel-track pairs. Figure 5.4 shows ϵ_{reco} as a

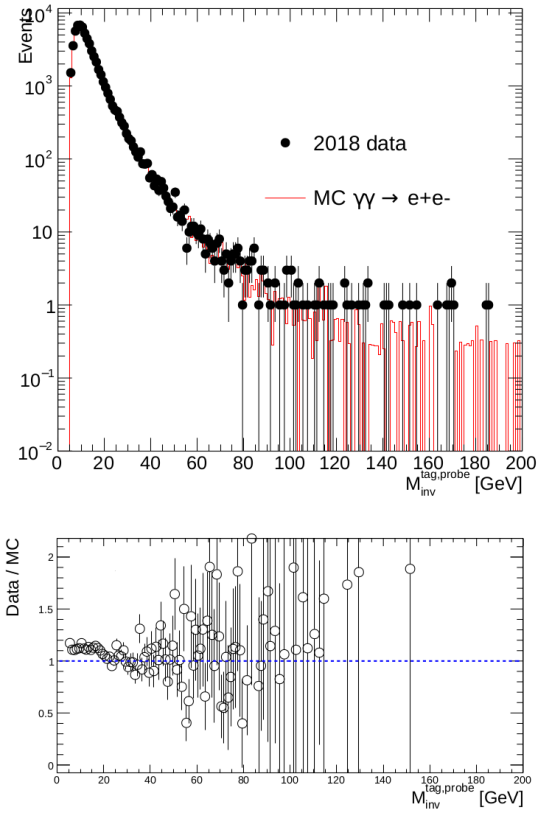

Figure 5.3: Invariant mass distribution of the tag-and-probe system after imposing all selection requirements on the 2018 Pb+Pb data (full markers) and MC simulation of the $\gamma\gamma \to e^+e^-$ process (solid line). The bottom panel shows a ratio between data and MC simulation.

function of electron p_{T} (left panel) and pixel-track η (right panel). A bottom panel illustrates a ratio of the efficiency in data over MC simulation. The electron reconstruction efficiency is slightly above 30% in the lowest electron p_{T} bin ($p_{\mathrm{T}} = 2.5$ GeV) in the data and grows rapidly to about 90% for $p_{\mathrm{T}} > 10$ GeV then it saturates. The electron reconstruction efficiency in MC simulation is 5-20% lower in the region of $p_{\mathrm{T}} < 5$ GeV. For higher p_{T} values the two efficiencies tend to agree.

The electron reconstruction efficiency as a function of pixel-track η is flat in $|\eta| < 0.8$ and amounts to 80%. Then it drops to 20% in $0.8 < |\eta| < 1.8$. The largest differences between the data and MC simulation are at $|\eta| = 1.6$. The data points are higher up to 20% in comparison to MC simulation in that region. In the very forward region, the electron reconstruction efficiency is up to 10% higher in MC simulation comparing to the data.

Electron PID

Electron PID efficiency, ϵ_{PID}, is defined as a probability of the good-quality electron to pass also the electron identification requirements (Loose or LHLoose).

Figure 5.5 shows ϵ_{PID} for the Loose PID WP as a function of electron p_{T} and pixel-track η. The efficiency tends to be flat in electron p_{T} and amounts to $\sim 88\%$. The efficiency is consistent between MC simulation and data within the uncertainties. In pixel-track $|\eta|$, ϵ_{PID} reveals some dependence reflecting structures of the ID system. The efficiency amounts to 90% in pixel-track $|\eta| < 0.5$. Then it decreases and raises again to drop again to below 80% in the most forward

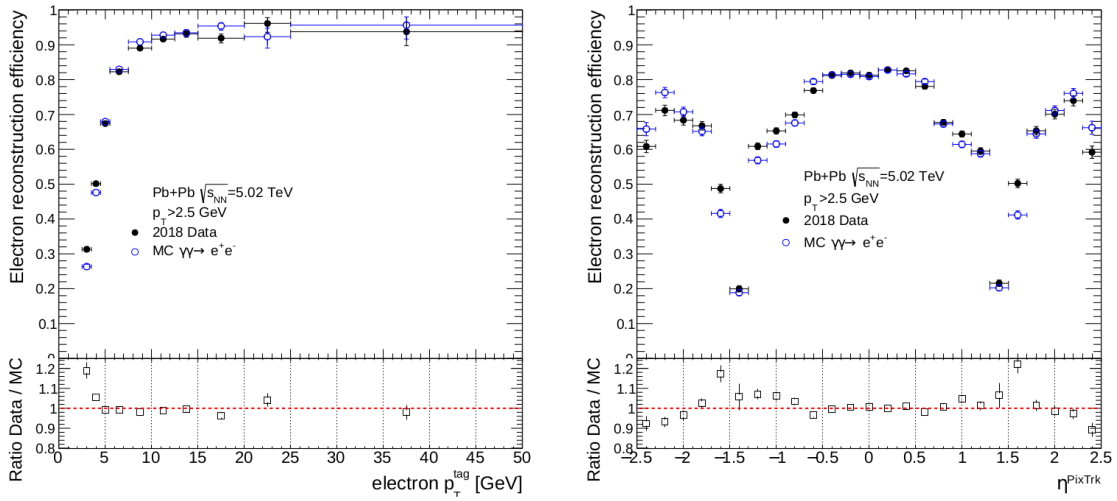

Figure 5.4: Electron reconstruction efficiency as a function of electron p_{T} (left) and pixel-track η (right) in data (full markers) and MC simulation (open markers) for the $\gamma\gamma \to e^+e^-$ process. Lower panels show a ratio of efficiency in data over MC simulation. Error bars denote statistical uncertainties.

bin. The efficiency in MC simulation is consistent with that in the data except for the most forward pixel-track $|\eta|$ bin where up to 10% differences reveal. In that region ϵ_{PID} is lower in the data in comparison to MC simulation.

Total electron efficiency and scale factors

The total electron reconstruction and PID efficiency, ϵ_{tot}, is defined as:

$$\epsilon_{\mathrm{tot}} = \epsilon_{\mathrm{reco}} \cdot \epsilon_{\mathrm{PID}}. \tag{5.1}$$

The total efficiency is measured for electron Loose and LHLoose PID WP.

Figure 5.6 shows ϵ_{tot} for the Loose PID WP as a function of electron p_{T} and pixel-track η. The total electron efficiency as a function of electron p_{T} is dominated by the p_{T} dependence of the electron reconstruction efficiency. For electron $p_{\mathrm{T}} < 5$ GeV, ϵ_{tot} in the data is higher than in MC simulation. At electron $p_{\mathrm{T}} = 2.5$ GeV, the difference is as large as 20%. For electron $p_{\mathrm{T}} > 5$ GeV, ϵ_{tot} in MC simulation is a few percent higher in comparison to the data. For electron $p_{\mathrm{T}} > 10$ GeV, ϵ_{tot} saturates at the level of 80%. The shape of the pixel-track η dependence is driven by the product of reconstruction and PID efficiencies. The highest $\epsilon_{\mathrm{tot}} =\sim 75\%$ is at midrapidity. Then the total efficiency drops and reaches a minimum below 20% at pixel-track $|\eta| =\sim 1.5$. Then the efficiency raises to 60-70% and drops again to 45-55% in the most forward pixel-track $|\eta|$ bin.

The scale factors, defined as a ratio of ϵ_{tot} in the data over MC simulation and shown in the bottom panels of Fig. 5.6, are consistent with unity only for pixel-track $|\eta| < 0.5$. In the intermediate pixel-track $|\eta|$ region, the ratio is above unity with a maximum of 1.2 at pixel-track $\eta = -1.6$, while in the forward direction it falls below unity and reaches 0.85.

For completeness, Figure 5.7 shows ϵ_{tot} for the LHLoose PID WP as a function of electron p_{T} and pixel-track η. To a large extent, identical conclusions to the Loose PID WP can be drawn from both dependencies.

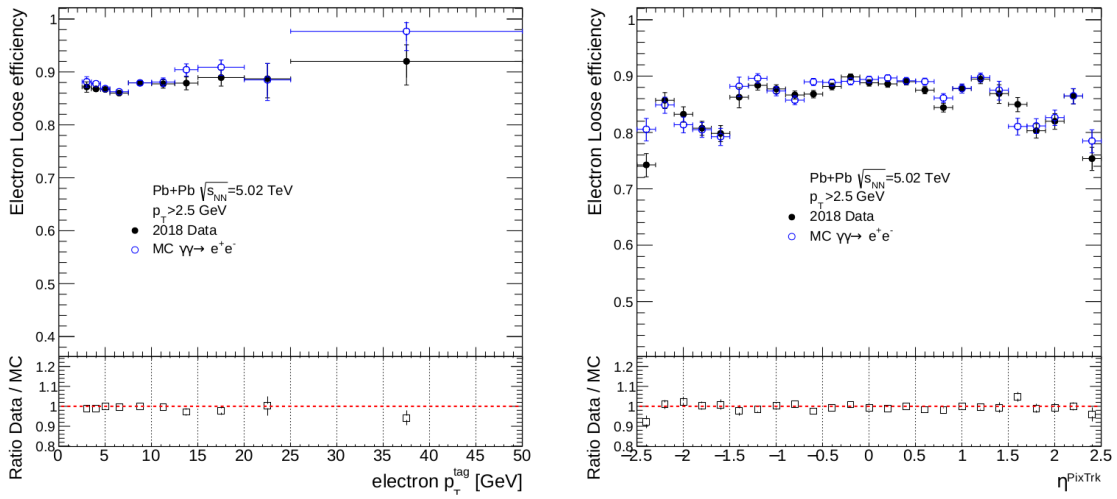

Figure 5.5: Electron Loose PID efficiency as a function of electron p_{T} (left) and pixel-track η (right) in data (full markers) and MC simulation (open markers) for the $\gamma\gamma \to e^+e^-$ process. Lower panels show a ratio of the efficiency in data over MC simulation. Error bars denote statistical uncertainties.

Systematic uncertainties on scale factors

A few sources of systematic uncertainties have been considered on scale factors:

- Tighter acoplanarity requirement on the tag-and-probe system Aco < 0.01. This variation reduces the FSR and dissociative contributions as well as $\gamma\gamma \to \tau^+\tau^-$ backgrounds, thus, is sensitive to purity of the sample (see a detailed discussion in Sec. 5.4.1).
- Events with signal above the threshold in at least one ZDC are removed in the data, and the analysis is constrained to the 0n0n event category. This variation is sensitive to a contribution of dissociative background in the data (see a detailed discussion in Sec. 5.4.1). After imposing the 0n0n requirement, a contribution from dissociative background is negligible
- The tag electron is required to be identified as a LHMedium electron (while the LHTight PID WP is used in the nominal selection). This variation is sensitive to purity of the tag-and-probe sample.
- A pixel track associated with a probe candidate is required to have at least four hits (three in the nominal selection). This variation reduces background from fake pixel tracks.
- L1 trigger uncertainty is propagated to MC simulation.
- Alternative MC sample for $\gamma\gamma \to e^+e^-$ w/o FSR is used. Given that the $\gamma\gamma \to e^+e^-$ sample with FSR simulated by STARLIGHT+PHOTOSPP generators proved to underestimate yields of FSR photons, another approach with pure signal from STARLIGHT w/o FSR is used.

Figure 5.8 shows the scale factors as a function of electron p_{T} and pixel-track η for the electron Loose PID along with their variations originating from individual sources of systematic uncertainties. In many bins the systematic variations vary within the statistical uncertainties.

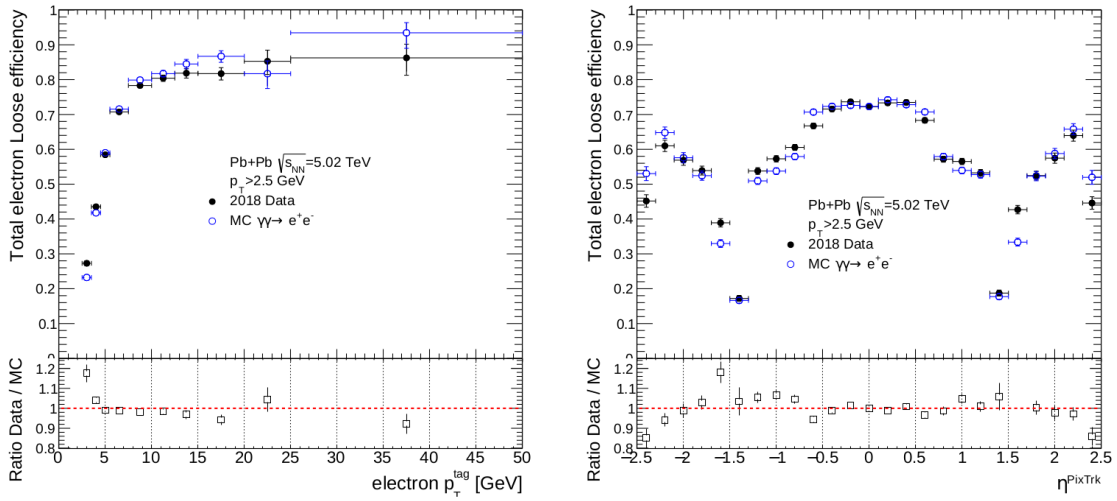

Figure 5.6: Total electron efficiency for the Loose PID WP as a function of electron p_{T} (left) and pixel-track η (right) in data (full markers) and MC simulation (open markers) for the $\gamma\gamma \to e^+e^-$ process. Lower panels show a ratio of the efficiency in data over MC simulation. Error bars denote statistical uncertainties.

The largest variations are due to the 0n0n requirement (labelled ZDC veto) and usage of the alternative MC simulation for $\gamma\gamma \to e^+e^-$ w/o a contribution from FSR.

Figure 5.9 presents electron scale factors with total systematic uncertainties represented by the shaded boxes around the data points. Similar conclusions can be drawn for the electron LHLoose PID WP. Given that scale factors are p_{T}- and η-dependent, they are also measured in two pixel-track p_{T} bins: for $p_{\mathrm{T}} < 5$ GeV and for $p_{\mathrm{T}} > 5$ GeV. In Figure 5.10 the scale factors for two pixel-track p_{T} bins are shown. As expected the largest deviations from unity occur for $p_{\mathrm{T}} < 5$ GeV in the $|\eta| > 0.5$ range.

For higher-precision analyses, measurement of electron scale factors is repeated in the pixel-track $p_{\mathrm{T}} < 5$ GeV range using a lower number of bins in pixel-track η. The resulting scale factors are shown in Fig. 5.11. They are compatible with the left plot of Fig. 5.10.

Considerations for the usage of scale factors

The electron scale factors are applied in MC simulation as a function of pixel-track η, matched to the electron with the $\Delta R < 0.2$ requirement. However, a number of pixel tracks in dielectron events is not well simulated, as shown in Fig. 5.12. Therefore, no requirement on a number of pixel tracks is applied in the event selection. To obtain the scale factor value for electrons with no associated pixel track, the electron η is used. This is justified by good correlation between pixel-track η and electron η, as shown in Fig. 5.13.

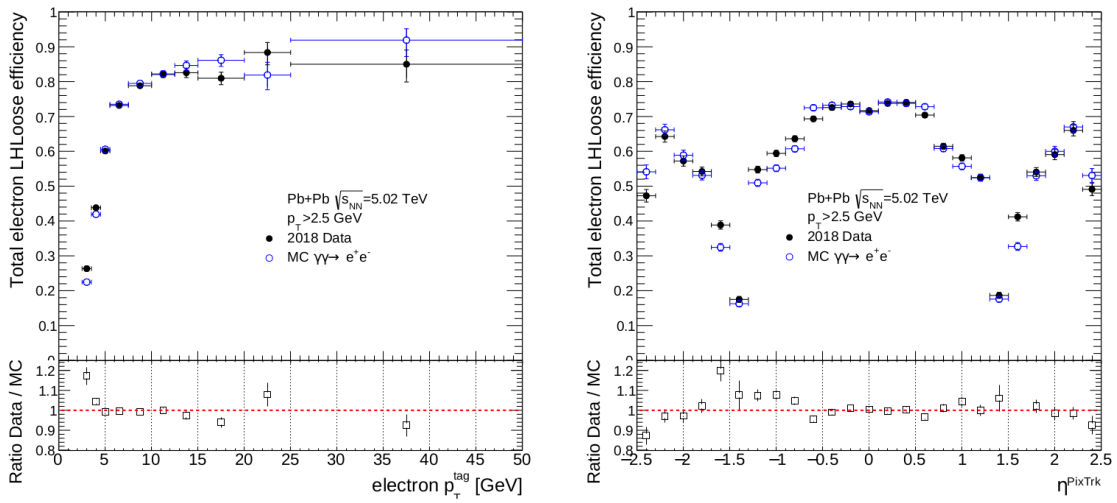

Figure 5.7: Total electron efficiency for the LHLoose PID WP as a function of electron p_{T} (left) and pixel-track η (right) in data (full markers) and MC simulation (open markers) for the $\gamma\gamma \to e^+e^-$ process. Lower panels show a ratio of the efficiency in data over MC simulation. Error bars denote statistical uncertainties.

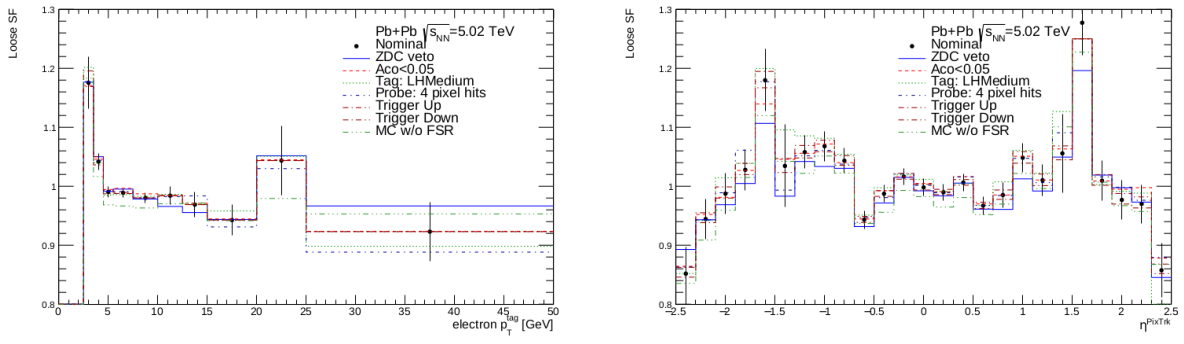

Figure 5.8: Electron scale factors for the Loose PID as a function of p_{T} (left) and η (right). The nominal measurement is presented by the data points with error bars which represent statistical uncertainties. The variations due to individual sources of systematic uncertainties are represented by histograms.

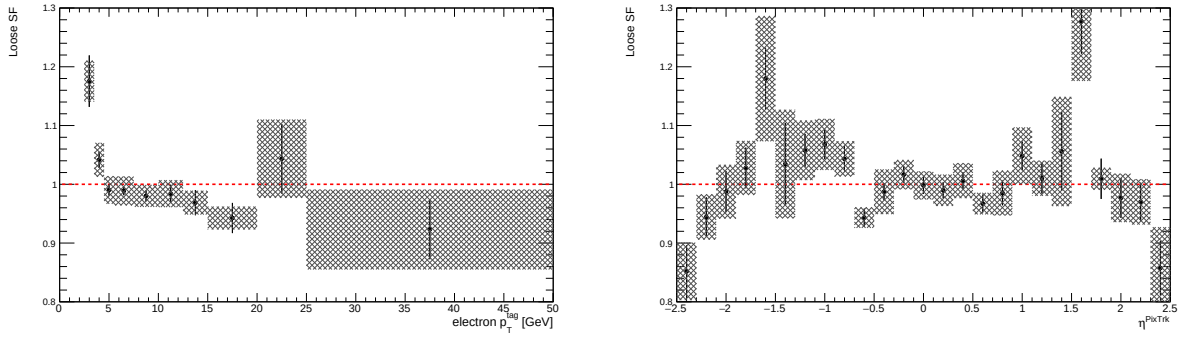

Figure 5.9: Electron scale factors for the Loose PID as a function of p_{T} (left) and η (right). Error bars represent statistical uncertainties while the shaded box reflects the total systematic uncertainty.

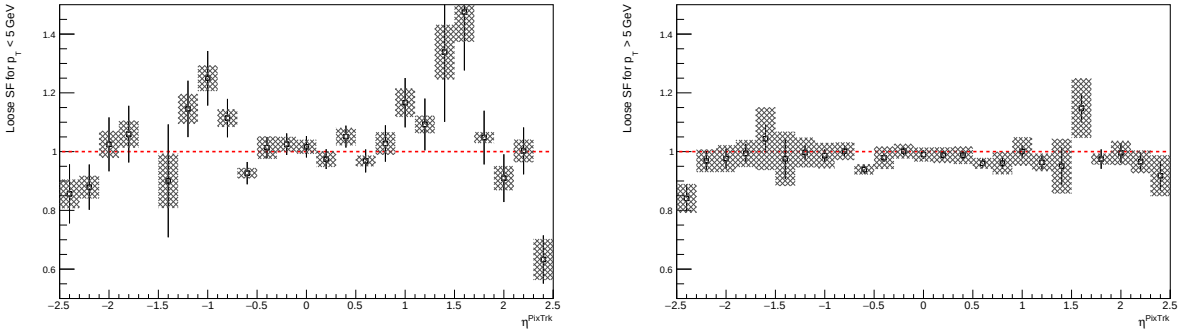

Figure 5.10: Electron scale factors for the Loose PID as a function of pixel-track η for $p_{\mathrm{T}} < 5$ GeV (left) and $p_{\mathrm{T}} > 5$ GeV (right). Error bars represent statistical uncertainties while the shaded box reflects the total systematic uncertainty.

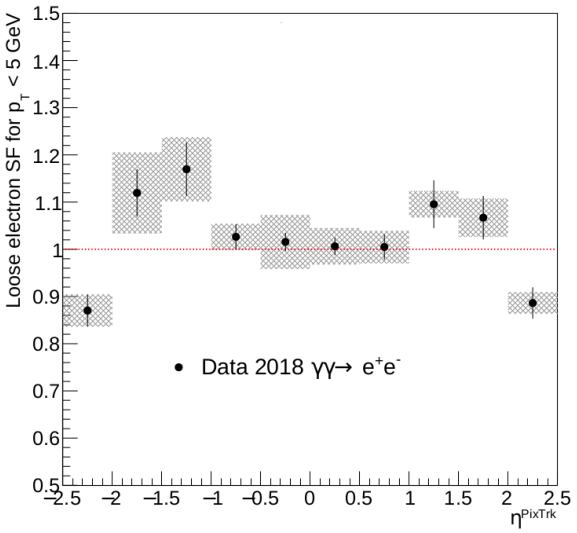

Figure 5.11: Electron scale factors for the Loose PID as a function of pixel-track η for $p_{\mathrm{T}} < 5$ GeV. Error bars represent statistical uncertainties while the shaded box reflects the total systematic uncertainty.

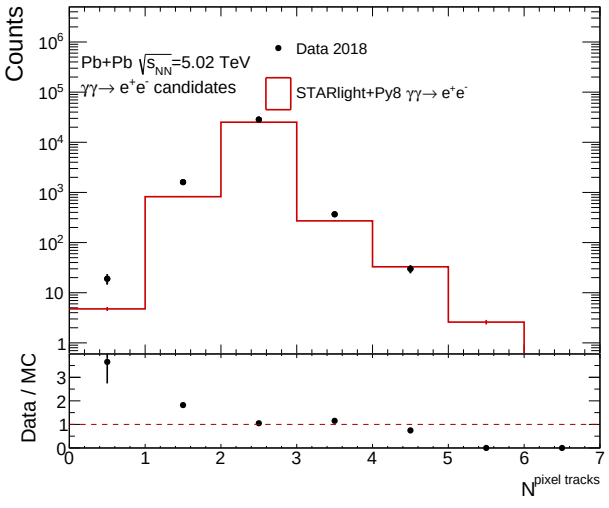

Figure 5.12: Number of pixel tracks in selected dielectron events in data and MC simulation for the $\gamma\gamma \to e^+e^-$ process.

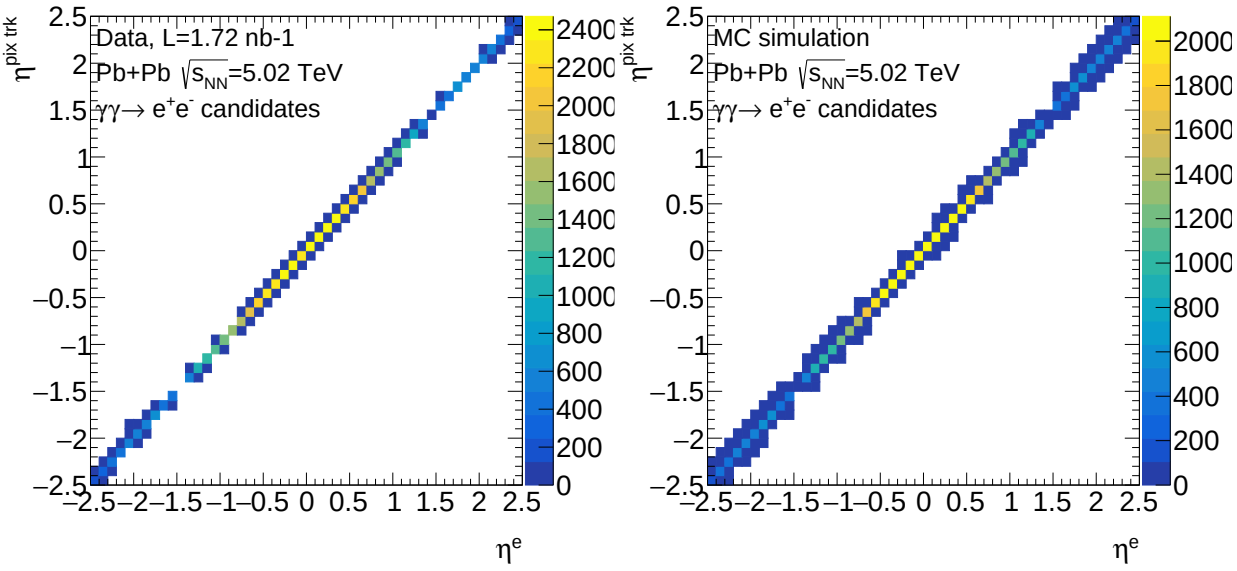

Figure 5.13: Correlation between pixel-track η and electron η in selected dielectron events in data (left) and MC simulation for the $\gamma\gamma \to e^+e^-$ process (right).

5.3 Event characteristics

The characteristic features of the exclusive dielectron events can be identified in Fig. 5.14 presenting an event display of one UPC Pb+Pb event with the $\gamma\gamma \to e^+e^-$ production candidate in the ATLAS detector. Two yellow tracks originating form the same IP are visible in the ID along with two deposits in the EM calorimeter marked in green. The two electrons are in back-to-back configuration and have low transverse momenta: $p_{\mathrm{T}}^{\mathrm{e1}} = 8.2\,\mathrm{GeV}$ and $p_{\mathrm{T}}^{\mathrm{e2}} = 7.4\,\mathrm{GeV}$. Apart from the e^+e^- pair, no other activity is visible in the detector. These features drive the event selection of $\gamma\gamma \to e^+e^-$ candidates described in the following section.

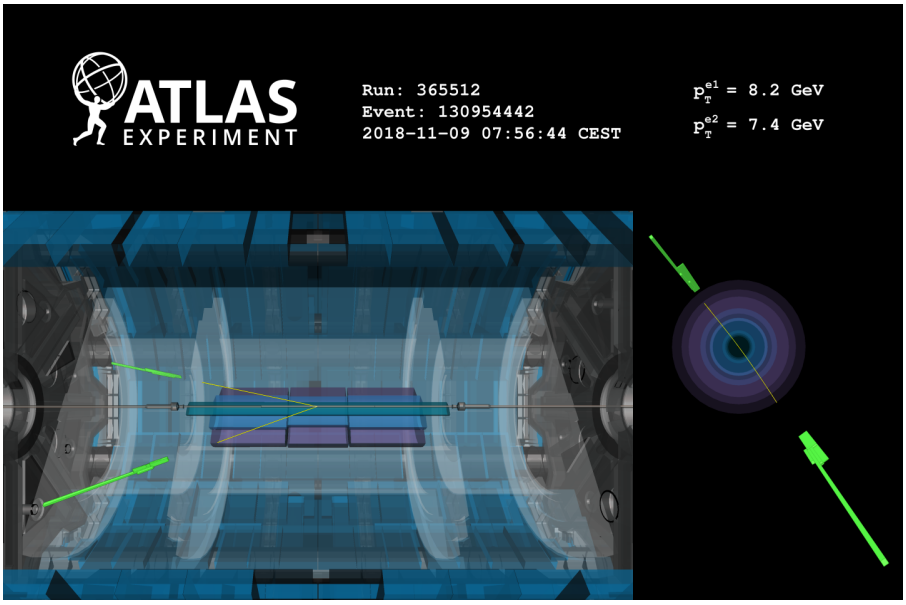

Figure 5.14: Event display (run 365512, event 130954442) for an exclusive $\gamma\gamma \to e^+e^-$ candidate in UPC 2018 Pb+Pb dataset, recorded on 9th of November 2018 at 07:56:44. Two back-to-back electrons ($p_{\mathrm{T}}^{\mathrm{e1}} = 8.2\,\mathrm{GeV}$ and $p_{\mathrm{T}}^{\mathrm{e2}} = 7.4\,\mathrm{GeV}$) with an invariant mass of 16 GeV are presented. All charged-particle tracks with $p_{\mathrm{T}} > 100\,\mathrm{MeV}$ are shown. All calorimeter cells with various E_{T} thresholds are shown: $E_{\mathrm{T}} > 250\,\mathrm{MeV}$ for EM barrel, EM endcap and Tile, $E_{\mathrm{T}} > 800\,\mathrm{MeV}$ for hadronic endcap, and $E_{\mathrm{T}} > 1000\,\mathrm{MeV}$ for FCal.

5.3.1 Event selection

Exclusive dielectron events are selected from 2018 UPC Pb+Pb data using a set of subsequent requirements which are summarised in Table 5.1 along with the number of accepted events. The selection for MC samples does not include the GRL, event cleaning and trigger requirements. Instead of the trigger requirement, simulated events are weighted by the trigger efficiency.

The following requirements are imposed for event candidates from the $\gamma\gamma \to e^+e^-$ process:
All: Presence in the HION4 derived data
PassGRL&Cleaning: Run/event/luminosity block found in the UPC GRL and an event contains none of the standard errors in trigger and data acquisition/calorimeter subsystems
PassTrigger: Passes a logical OR of two triggers:
HLT_hi_upc_FgapAC3_hi_gg_upc_L1TAU1_TE4_VTE200 or
HLT_hi_upc_FgapAC3_hi_gg_upc_L12TAU1_VTE50
TwoTracks: exactly two tracks identified as "LoosePrimary" [99, 100] per event
noMSTP: no Muon Spectrometer Track Particles can be present in the event

Selection	Number of events
All	11988790
PassGRL&Cleaning	1868014
PassTrigger	1323557
TwoTracks	272912
noMSTP	269976
TwoElectrons	32202
$m_{ee} > 5$ GeV	32181
$p_{\mathrm{T},ee} < 2$ GeV	30456

Table 5.1: List of event selection requirements, and a number of events in the 2018 Pb+Pb data which pass the criteria.

TwoElectrons: exactly two opposite-sign Loose electrons with $p_{\mathrm{T}}^{e} > 2.5$ GeV and $|\eta_e| < 2.47$ (excluding the calorimeter transition region)
Mee: dielectron invariant mass $m_{ee} > 5$ GeV
pTee: dielectron transverse momentum $p_{\mathrm{T},ee} < 2$ GeV

The efficiency of the "TwoTracks" requirement was estimated using MC simulation for the $\gamma\gamma \to e^+e^-$ process, by dividing the number of events after the full event selection by the number of events selected by all requirements but the TwoTracks cut. It is estimated to be about 92.9%. Similarly the $p_{\mathrm{T},ee}$ cut efficiency was estimated to be 96.5%.

The noMSTP requirement was studied separately for first 39 runs, when ATLAS was fully operational, and for last 6 runs when the toroid magnetic field was off. Generally, the impact of the requirement is small. After dropping this requirement, the number of selected events rises from 26079 to 26086 in the first part of the runs, and from 4377 to 4379 in the second part. Therefore, a conclusion was made that no special correction is needed for the possible noMSTP inefficiency in the last 6 runs.

To check if there are any displaced signatures in selected events, a comparison of the electron d_0 distribution is made in the data with the MC signal simulation. The distribution presented in Fig. 5.15 does not show the data enhancement in the tail. Thus, the selected sample is considered clean, in terms of displaced events and no d_0 cut is applied.

Figure 5.16 presents the spacial distribution of selected events in the data as an electron η vs ϕ map. No regions with unexpectedly high activity (hot spots) are observed.

The selected dielectron events are used to verify the stability of the collected data by measuring the effective cross-section. It is defined as the number of selected dielectron events per integrated luminosity of the single run, and should in principal be a constant value. The yields are not corrected for any inefficiencies, therefore this cross-section is referred to as "effective". Based on the event selection described above, the effective cross-section for exclusive dielectron production for all 45 runs is presented in Fig. 5.17. It is flat and amounts to about 18 μb.

Some of the results presented in this thesis are measured in two fiducial regions:

- the nominal one defined earlier in this section, referred to as FR1
- the tight one used in the dimuon measurement [57], referred to as FR2.

All fiducial kinematic requirements are listed in Table 5.2.

When not stated explicitly, the results are presented for FR1.

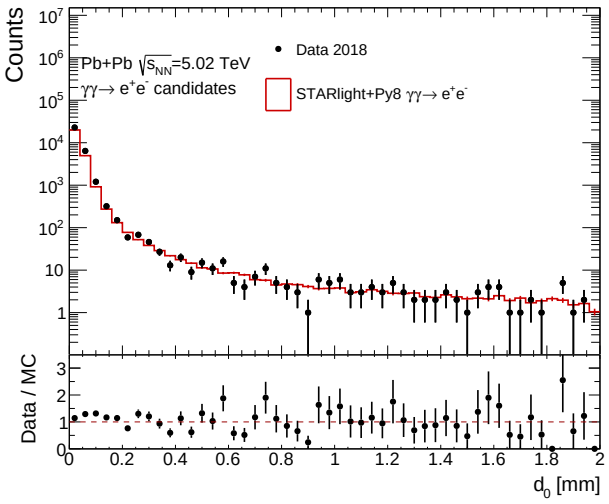

Figure 5.15: Distribution of d_0 for event candidates from the $\gamma\gamma \to e^+e^-$ process in the data compared with MC signal simulation. The bottom panel shows a ratio between data and MC simulation.

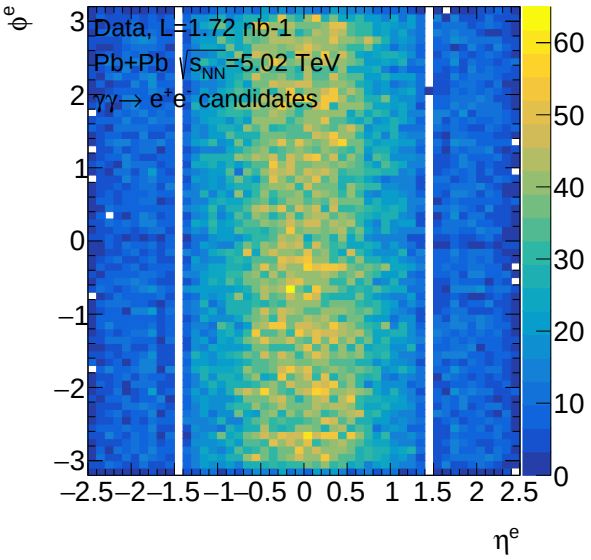

Figure 5.16: ϕ^e vs η^e distribution for dielectron events in the data.

	FR1	FR2
$p_{\mathrm{T}}^e >$	2.5 GeV	4 GeV
$\lvert\eta_e\rvert <$	2.5	2.4
$m_{ee} >$	5 GeV	10 GeV
$p_{\mathrm{T},ee} <$	2 GeV	2 GeV

Table 5.2: Definitions of kinematic requirements for two fiducial regions, FR1 and FR2.

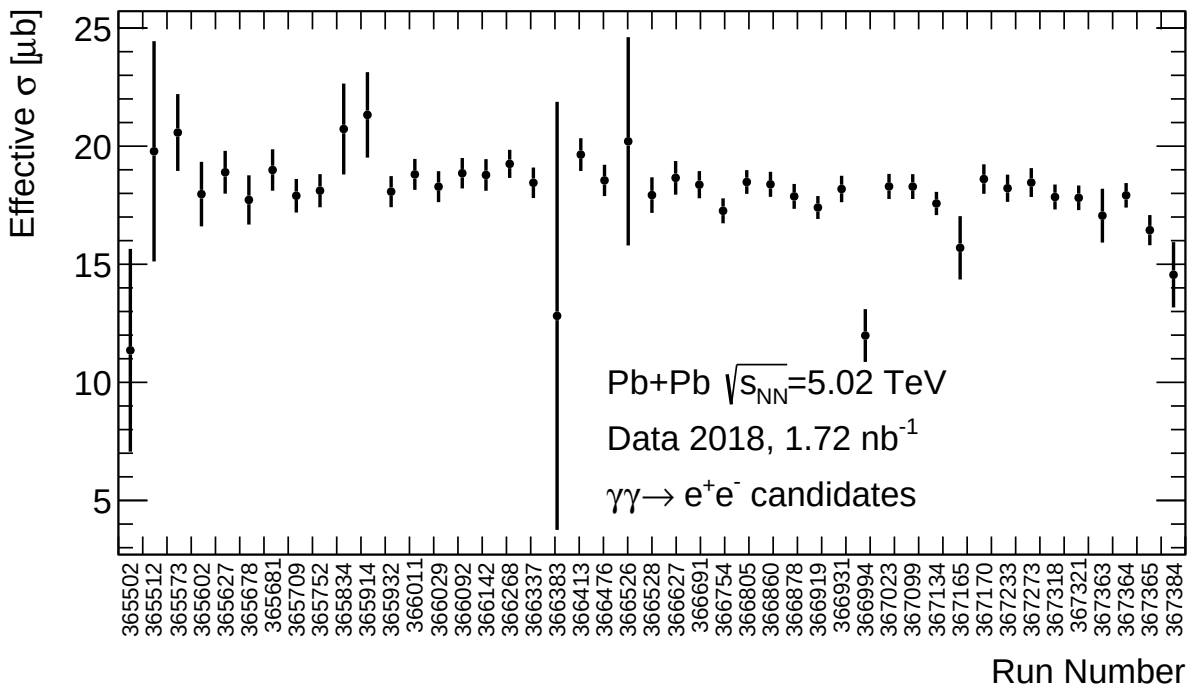

Figure 5.17: Effective cross-section for exclusive dielectron production as a function of run number.

5.3.2 Definition of ZDC topology classes

Each of the events passing the exclusive dielectron criteria can be further classified based on the observed activity in the ZDC detector. The ZDC allows to detect neutrons originating from the incoming nuclei. The ZDC energy is calibrated such that the one neutron peak is centred at the per-nucleon beam energy. A ZDC "hit" on either side is defined as an energy greater than 40% of the single-neutron peak position (what corresponds to energy greater than 1 TeV for $\sqrt{s_{\mathrm{NN}}} = 5.02$ TeV). The correlation of energies shown in Fig. 5.18 illustrates three primary topologies available for these events: 0n0n, Xn0n and XnXn, as defined in Sec.2.4.1. The 0n0n topology is the most probable configuration with no activity in either ZDC arm. The next most likely configuration is an observation of one or more forward neutrons in only one ZDC arm, and none in the other (Xn0n). Finally, the rarest configuration is the XnXn topology with one or more forward neutrons in both ZDC arms.

The observed (raw) fractions of events in each ZDC topology class might be slightly different from true fractions due to the presence of the EM pileup. This phenomenon causes the outflow of events from the 0n0n class to the Xn0n and XnXn classes and from the Xn0n to XnXn class. In particular, the forward neutron emission may be a result of the single and mutual dissociation processes, which are the nuclear breakup of one or two nuclei, respectively, due to the interaction with a coherent photon. When the probabilities for these processes are known, the observed fractions of events can be corrected for this effect. The determination of true fractions with EM pileup correction is discussed in Sec. 5.5. The correction procedure makes use of single and mutual dissociation probabilities, which in this analysis are estimated by the extrapolation of the LHC measurement at lower-energy (see details in Sec.5.3.3). Additionally, the background contribution from dissociative events, estimated in Sec. 5.4, is subtracted before the EM pileup correction is extracted.

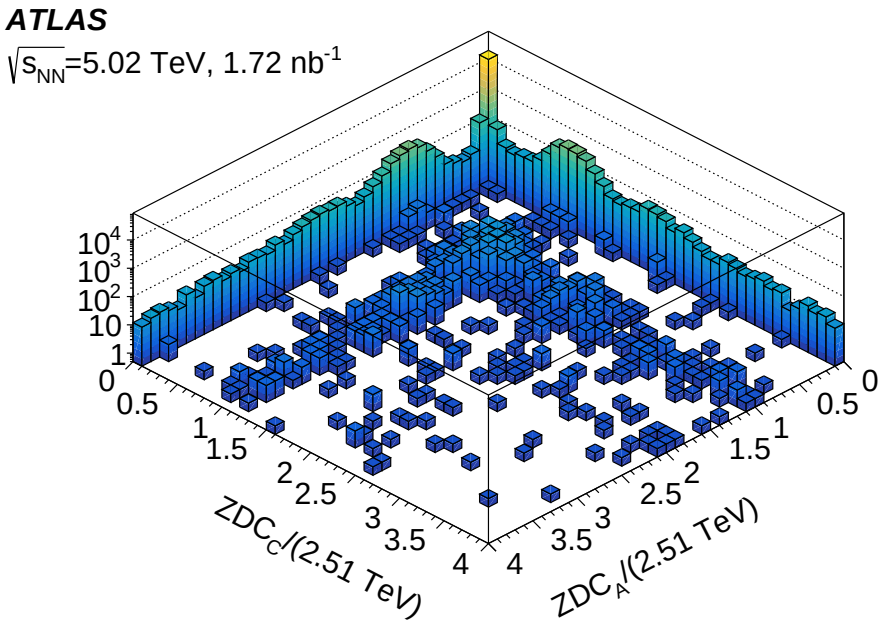

Figure 5.18: Correlation of the energy deposited in each of the ZDC arms in selected dielectron events in the data. The energy is normalised to the per-nucleon beam energy.

5.3.3 EM pileup

At the LHC, instantaneous luminosity of Pb+Pb collisions is high, thus it is likely that more than one EM interaction occurs in a single bunch crossing. Multiple EM interactions are referred to as EM pileup. In this analysis, the physical process that constitutes EM pileup is the EM dissociation (EMD). In this process, a coherent photon emitted from one nucleus interacts with the other nucleus leading to its excitation, followed by the emission of the neutron(s). It causes the additional neutron rate in the ZDC and has the cross-section (in each arm) of about 200 b. The EM pileup has a factor of nearly 30 larger cross-section compared to hadronic pileup.

The peak luminosity during the 2018 Pb+Pb run reached $6.2 \times 10^{27}\,\mathrm{cm}^{-2}\mathrm{s}^{-1}$. The inelastic Pb+Pb cross-section for hadronic interactions, predicted by the Glauber model, amounts to 7.7 b. This gives the approximate mean hadronic interaction rate per bunch crossing, μ, at the level of about 0.2%. The value of μ associated to the given LB, can be accessed in the analysed data format. Its value is plotted for dielectron event candidates in the data in Fig. 5.19, giving the mean value of 0.25%.

The estimation of the contribution from EM pileup follows the procedure used in Ref. [57]. The only available measurements of single and mutual EMD for Pb+Pb collisions were done by ALICE at $\sqrt{s_{\mathrm{NN}}}$ =2.76 TeV [101]. The measured cross-sections for single and mutual EMD are 181.3 ± 0.3 (stat.)$^{+12.8}_{-10.9}$ (syst.) b and 5.7 ± 0.1 (stat.) ± 0.4 (syst.) b, respectively. Those results were compared with the RELDIS model [102] prediction of 179.7 ± 9.2 b for single EMD, and 5.5 ± 0.6 b for mutual EMD (calculations taken from Ref. [57]). The RELDIS model predicts a 11% increase of the cross-sections when changing the energy to $\sqrt{s_{\mathrm{NN}}}$ =5.02 TeV; corresponding values are 199.5±10 b for single EMD, and 5.8 ± 0.6 b for mutual EMD. Thus, one can extrapolate the ALICE measurement assuming the 11% increase of the cross-sections, what leads to 201.2 ± 0.3 (stat.)$^{+14.2}_{-12.1}$ (syst.) b for single EMD and 6.0 ± 0.1 (stat.) ± 0.4 (syst.) b for mutual EMD.

Then, one can estimate μ_{EM} for EM pileup, by scaling the hadronic μ by the cross-section ratio: $\mu_{\mathrm{EM,S}} = \mu * \frac{201.2}{7.7} = 0.066526649$, $\mu_{\mathrm{EM,M}} = \mu * \frac{6.0}{7.7} = 0.001983896$. To estimate the

probability of at least one interaction per bunch crossing, one needs to calculate $1 - P(0) = 1 - \exp(-\mu_{\mathrm{EM}})$ for each event, and then extract the mean value. The distribution of $1 - P(0)$ probability is plotted for single and mutual dissociation in Fig. 5.20. The obtained values of single dissociation probability, p_{S} and mutual dissociation probability, p_{M}, are:

$p_{\mathrm{S}} = 6.362^{-0.367}_{+0.429} \times 10^{-2}$

$p_{\mathrm{M}} = 1.978 \pm 0.136 \times 10^{-3}$,

with uncertainties propagated from the ALICE measurement. These systematic uncertainties are dominated by the precision related to the cross-section measurement performed using the beam separation van der Meer scan. The theoretical uncertainties from the RELDIS model and its extrapolation are neglected, since most of the systematic uncertainties cancel in the ratio.

The obtained values of p_{S} and p_{M} are used in this analysis to correct the observed fractions of events in each ZDC topology class (see Sec. 5.7).

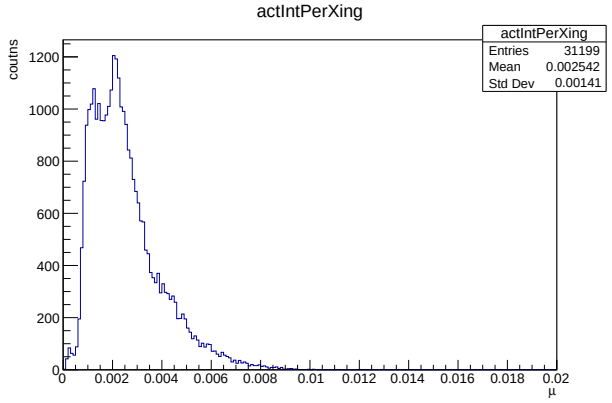

Figure 5.19: Distribution of the average number of hadronic interactions per bunch crossing, μ, for dielectron event candidates in the data.

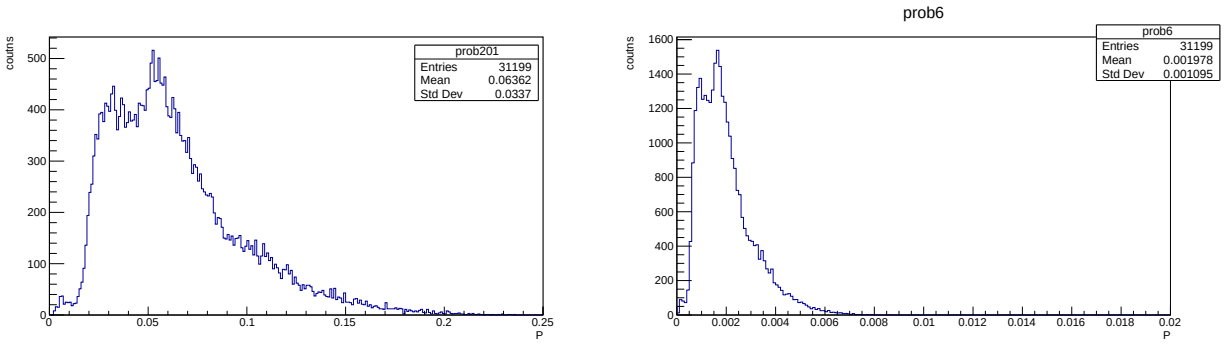

Figure 5.20: Distribution of single (left) and mutual (right) dissociation probabilities, assuming the cross-sections for these processes are 201.2 b and 6.0 b, respectively, and the inelastic Pb+Pb cross-section is 7.7 b.

There is a visible double-peak structure in the μ distribution in Fig. 5.19. This is likely due to the different bunch spacing in the first and second part of the 2018 data-taking. The average μ distribution as a function of run number is presented in Fig. 5.21. Apart from a few outliers, the average μ is lower in the first part of the 2018 Pb+Pb run than in the second part. The outlier values are associated mostly with very short runs, when the high μ value is determined by high peak luminosity.

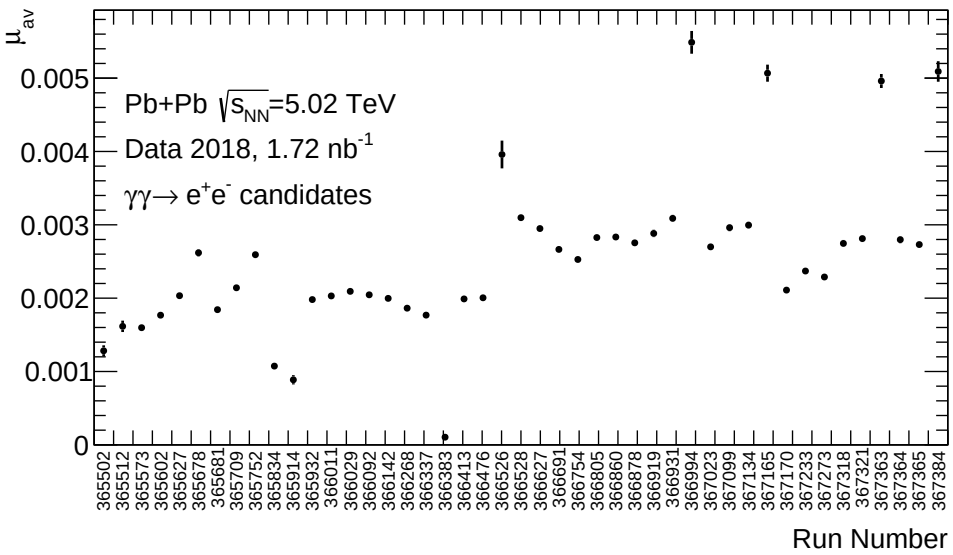

Figure 5.21: Average number of hadronic interactions per bunch crossing, μ, per run number.

5.4 Background studies

Apart from the signal process of exclusive dielectron production, there are several processes that can also contribute to the selected dielectron events. In this analysis, the main backgrounds originate from dissociative events, exclusive production of ditaus, $\gamma\gamma \rightarrow \tau^+\tau^-$, and from upsilon production. Contributions from photonuclear jet production or $\gamma\gamma \rightarrow q\bar{q}$ processes are found to be negligible, based on the analysis of dedicated MC samples. None of events from those simulations passed the dielectron selection criteria.

5.4.1 Dissociative and ditau backgrounds

The largest source of background originates from so-called dissociative processes. The cross-section for this process is a few orders of magnitude larger than the ditau cross-section. In dissociative events, the dielectron final state is also detected in the central detector. However one (or both) of the initial photons originates from the substructure of the nuclei, rather than from the external EM field of the whole nuclei. This photon emission causes the dissociation of the nuclei with remnants being emitted in the very forward direction. They are captured by the ZDC detector.

The contribution from dissociative events is estimated using a template fitting procedure to the acoplanarity distributions. The background template shape is constructed from the single-dissociative events simulated with SuperChic +Pythia8. The data is divided into several kinematic bins with boundaries at 5, 10, 20 and 40 GeV in invariant mass and boundaries at 0, 0.8, 1.6 and 2.4 in absolute dielectron rapidity. There is also an additional bin for the mass range 40-80 GeV, but inclusive in absolute dielectron rapidity, due to limited statistics. In each kinematic bin, a binned maximum-likelihood (ML) fitting procedure implemented in RooFit [103] is applied separately for events from three ZDC classes in the data. The inclusive result is a weighted sum of the results for 0n0n, Xn0n and XnXn categories.

Figure 5.22 shows event statistics available in the inclusive data sample in bins of the acoplanarity distribution. The bin widths increase to account for the rapidly falling acoplanarity distribution. Since dissociative events contribute to the tail of the acoplanarity distribution, there is no need to have finer binning at low acoplanarities.

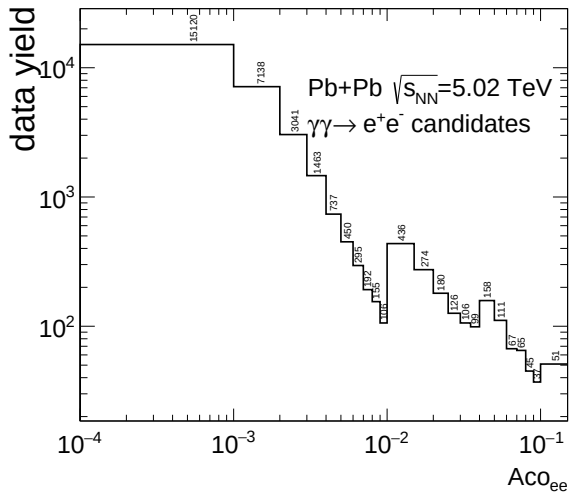

Figure 5.22: Event statistics available in the inclusive data sample in the data in bins of the acoplanarity distribution.

The exclusive ditau production, $\gamma\gamma \to \tau^+\tau^-$, may constitute the electron background, especially when both τ leptons decay in the electron channel. The ditau contribution is estimated using a dedicated MC sample. Out of four millions ditau simulated events, 1919 pass the dielectron selection. The resulting fraction of $\gamma\gamma \to \tau^+\tau^-$ events contributing to the dielectron events in the data amounts to 0.11%. It turns out that the acoplanarity shape for ditau events is similar to the acoplanarity shape for dissociative events. The normalised acoplanarity distribution for ditau and dissociatove processes with their ratio is shown in Fig. 5.23. The observed discrepancies are mostly within the $\pm$ 20% range.

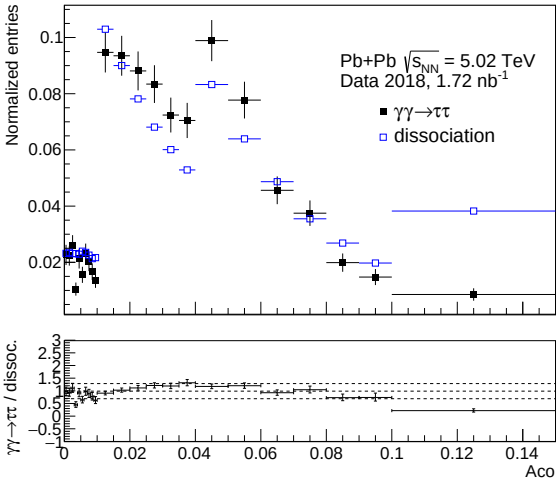

Figure 5.23: Normalised distribution of acoplanarity for exclusive ditau (full markers) and dissociative (open markers) processes for events which pass the dielectron evenet selection in respective MC simulations. The bottom panel shows ratio of ditau to dissociative events.

Taking into account the similarity of shapes of the acoplanarity distributions, in the fit model only signal and dissociative background contributions are considered. There is one fit parameter, f_{bkg}, while the signal fraction is $(1 - f_{\mathrm{bkg}})$. The dissociative contribution f_{diss} is later

determined as the background fraction obtained from the fitting procedure reduced by the ditau background fraction, $f_{\tau\tau} = 0.0011$. This approach is driven by low statistics of ditau events in some kinematic bins. It is validated by comparison of the nominal fit with the results of simultaneous fits of the signal, ditau and dissociative contributions using all events passing the selection criteria. The results of the nominal fitting procedure on this sample are presented in Fig. 5.24. For the fitting procedure that includes a separate ditau contribution in the fit model, the results are shown in Fig. 5.25. The fitted ditau contribution is larger than one estimated from MC simulation, however the results of the two procedures are consistent within very large uncertainties from the fit.

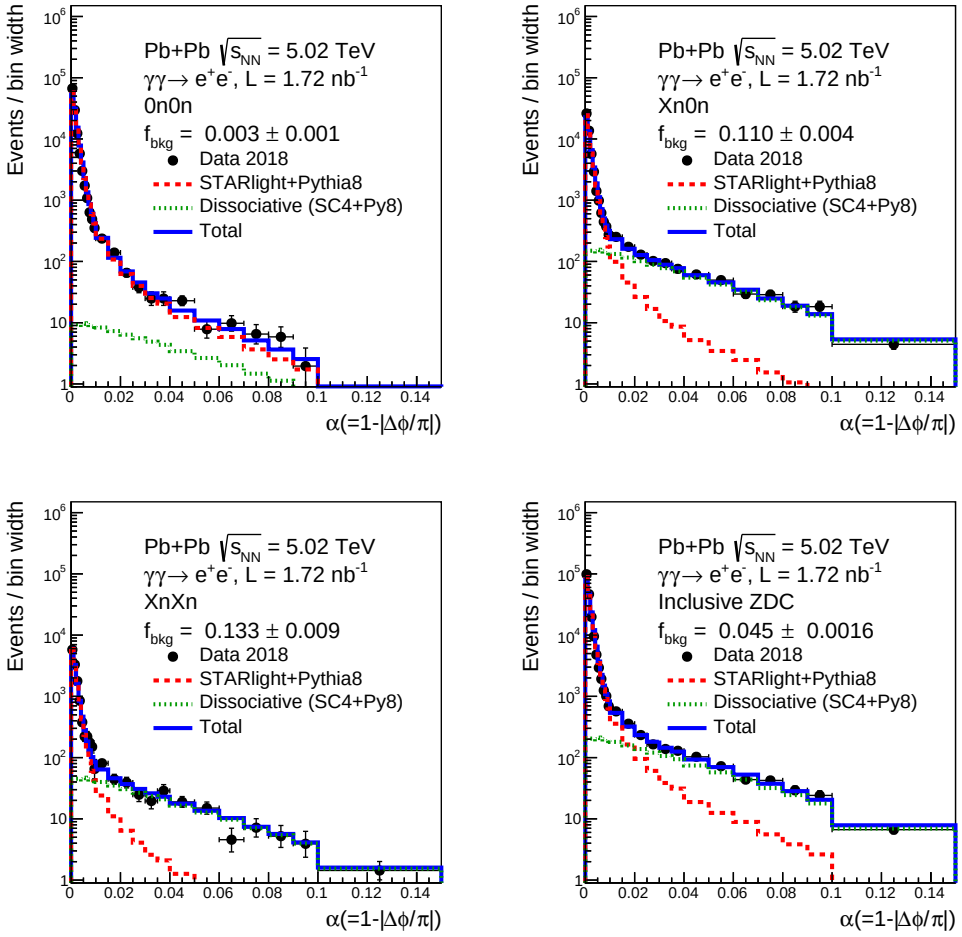

Figure 5.24: Nominal fit results in acoplanarity distribution for 0n0n (top, left), Xn0n (top, right), XnXn (bottom, left) categories and ZDC inclusive sample (bottom, right) using all events passing the dielectron selection criteria. The fitted dissociative background in each category is shown with the green dashed line, while the prediction for the signal process is shown by the red line. The sum of the two components is shown with the solid blue line. The resulting estimate of the background fraction in the data, f_{bkg}, is given in the legend.

The nominal fit results for kinematic bins with the highest statistics, $10 < m_{ee} < 20\,\mathrm{GeV}$ and $0 < |y_{ee}| < 0.8$, are presented in Fig. 5.26. The available statistics for masses above 40 GeV and for $|y_{ee}| > 0.8$ are very low. The fits are performed in all $|y_{ee}|$ bins in this mass range, however a fraction obtained from the fit in the $0 < |y_{ee}| < 2.4$ range is taken for background subtraction in the final results. All fractions with their statistical uncertainties for 0n0n, Xn0n, XnXn categories and for the ZDC inclusive sample are presented in Fig. 5.27. The

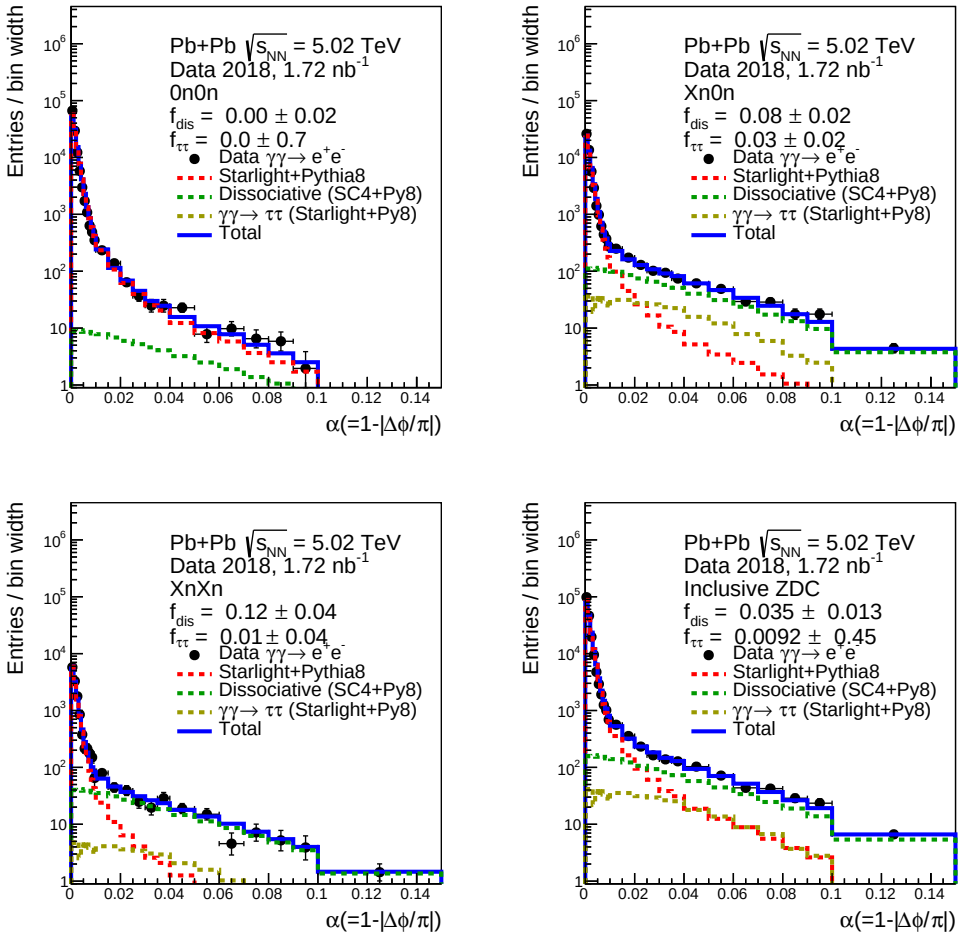

Figure 5.25: Fit results with a separate ditau contribution in the acoplanarity distribution for 0n0n (top, left), Xn0n (top, right), XnXn (bottom, left) categories and ZDC inclusive sample (bottom, right) using all events passing the dielectron selection criteria. The fitted dissociative background in each category is shown with the green dashed line, the fitted ditau background fraction is shown with the yellow dshed line, while the prediction for the signal process is shown by the red line. The sum of the three components is shown with the solid blue line. The resulting estimates of the dissociative background fraction in the data, f_{diss}, and ditau background fraction in data, $f_{\tau\tau}$, are given in the legend.

presented uncertainties originate from the fit (using the Migrad algorithm), and are symmetric. However, for final background fractions uncertainties the asymmetric approach (the Minos algorithm) is used. Both algorithms are available in the MINUIT tool [104] implemented in the ROOT analysis framework [92]. The asymmetric errors are introduced to correctly describe the uncertainty for cases when the f_{bkg} fraction is close to 0 or 1, such that increasing/decreasing the f_{bkg} by its uncertainty would not result in the value outside the 0–1 range.

To verify how well the dielectron data is described by the signal, the pre-fit (with the signal MC samples normalised to integrated luminosity of the data) and post-fit (signal MC samples normalised to $(1 - f_{\text{bkg}})$ of the data integral) numbers of expected signal events are shown in Fig. 5.28 for the inclusive ZDC sample in kinematic bins of the analysis. The ratio of these numbers is also calculated, and presented in Fig.5.29. In most of the bins the post-fit numbers of expected signal events are larger than the pre-fit ones. The discrepancies tend to increase with $|y_{ee}|$. For the sample inclusive in m_{ee} and $|y_{ee}|$, the increase in the number of expected

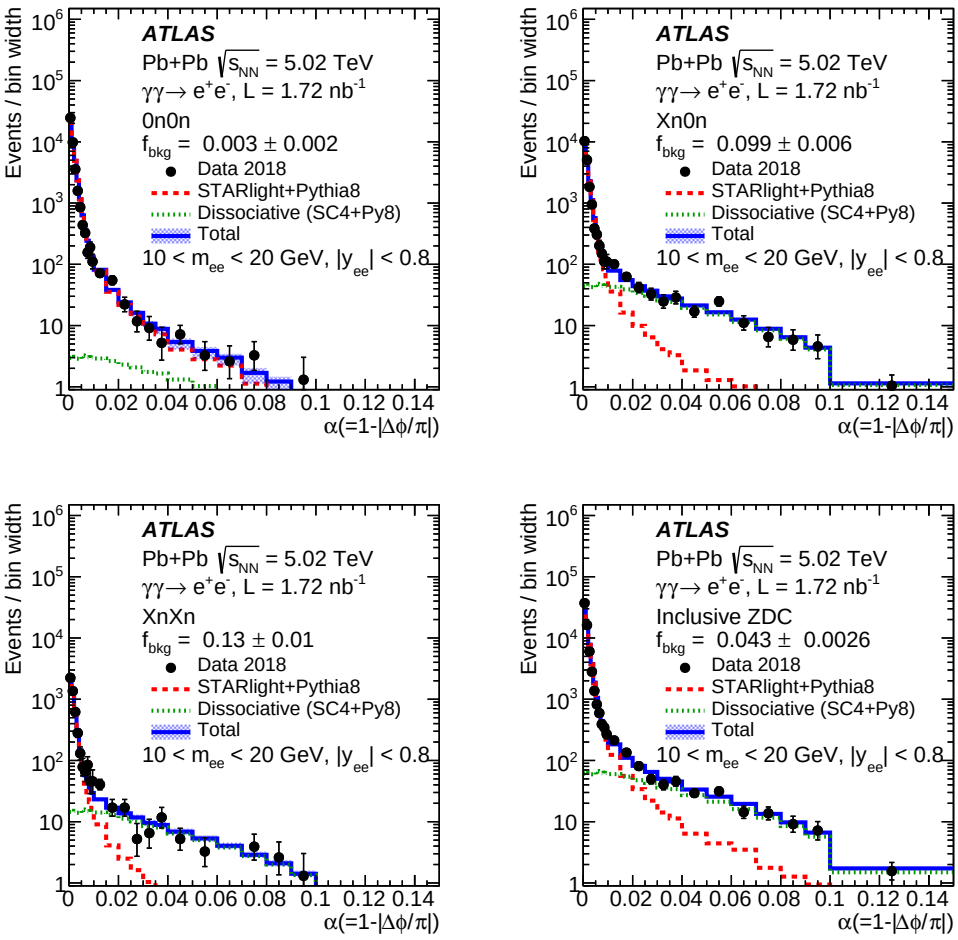

Figure 5.26: Acoplanarity distribution in the data sample (markers) of $\gamma\gamma \to e^+e^-$ candidates selected with $10 < m_{ee} < 20\,\text{GeV}$ and $|y_{ee}| < 0.8$ requirements. The sample is split into 0n0n (top left), Xn0n (top right), XnXn (bottom left) and ZDC inclusive (bottom right) categories. The fitted dissociative background in each category is shown with the green dashed line, while the prediction for the signal process is shown by the red line. The sum of the two components is shown with the solid blue line. The resulting estimate of the background fraction in the data, f_{bkg}, is given in the legend. The shaded area represents the total uncertainty of the sum of signal and background components.

signal events after the fit is almost 10%.

5.4.2 Systematic uncertainties for dissociative background

To estimate systematic uncertainties related to the dissociative background determination, several modified selections are used, as listed below:

1. Instead of signal MC simulation, data from the 0n0n category is used in the fit - this variation accounts for the mismodelling of the acoplanarity shape in the signal MC samples from STARLIGHT. The usage of the 0n0n data is justified by a very low fraction of background contribution to this class,

2. Double-dissociation contribution is considered in the fit - a relative normalisation factor for single and double-dissociative samples is fixed to the cross-section ratio between single

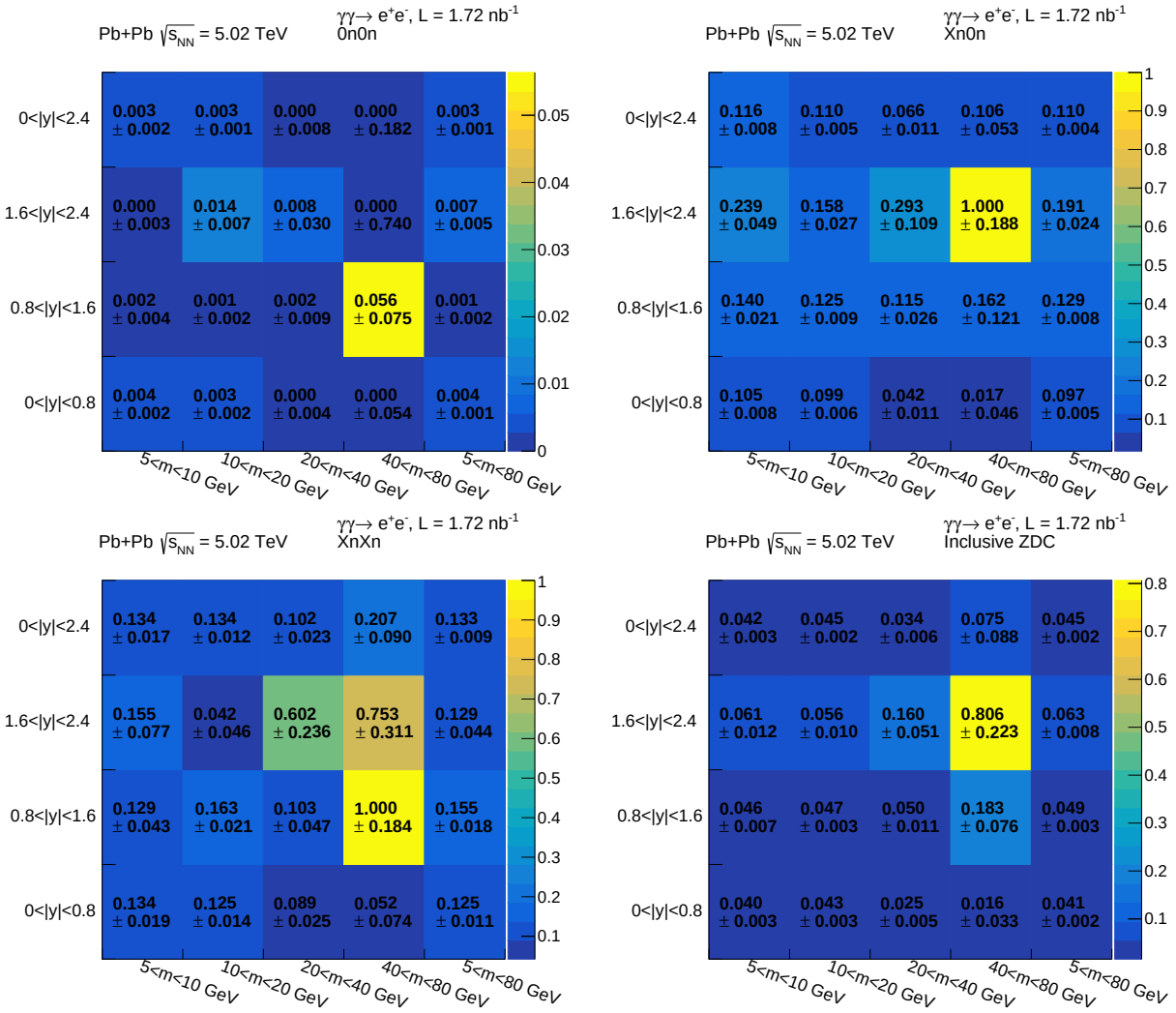

Figure 5.27: Estimated fractions of background events for 0n0n (top, left), Xn0n (top, right), XnXn (bottom, left) categories and for the ZDC inclusive sample (bottom, right) in kinematic bins of m_{ee} and $|y_{ee}|$ of the analysis. The presented uncertainties are symmetric uncertainties from the fit.

and double dissociation in pp collisions (which is a conservative approach, the single dissociative contribution scales more strongly with the change of the collision system),

3. Electron scale factors varied by their up/down uncertainties,

4. Electron trigger varied by its up/down uncertainties,

5. Electron trigger decision not accounted for in the MC simulation.

The largest uncertainty (at the level of a few percent) originates from sources no 1) and 5). For other systematic sources, the observed variations from the nominal fractions are mostly below 1%. The total systematic uncertainty on f_{bkg} is calculated separately for up and down variations. Figure 5.30 shows the estimated background fractions for the 0n0n, Xn0n, XnXn categories and for the inclusive ZDC sample with both statistical and systematic uncertainties. For almost all kinematic bins of the analysis, the statistical uncertainties dominate over the systematic ones.

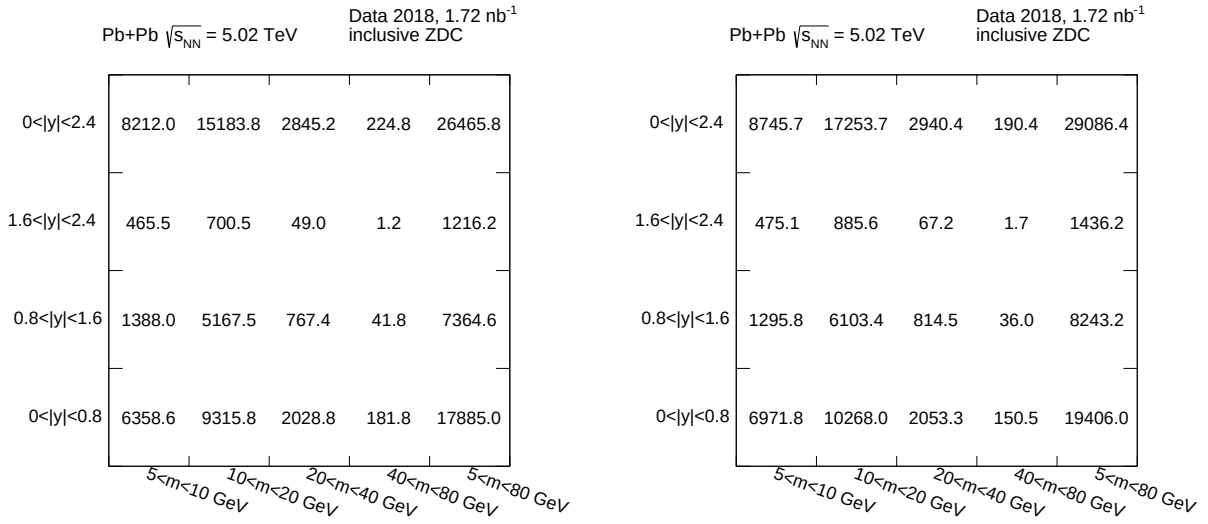

Figure 5.28: Pre-fit (left) and post-fit (right) numbers of expected signal events in the data for the inclusive ZDC sample in kinematic bins of $|y_{ee}|$ and m_{ee} of the analysis.

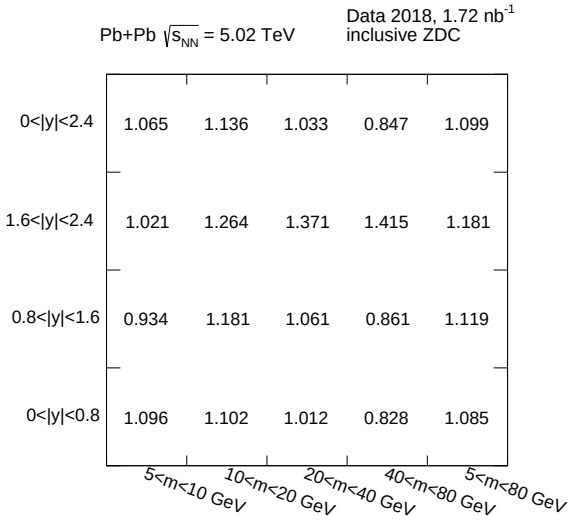

Figure 5.29: Ratio of post-fit to pre-fit numbers of expected signal events in the data for the inclusive ZDC sample in kinematic bins of $|y_{ee}|$ and m_{ee} of the analysis.

The background fitting procedure along with the systematic uncertainty determination was also repeated for FR2, using the methodology described above. The estimated fractions of background events for the 0n0n, Xn0n, XnXn categories and for the inclusive ZDC sample in the data with both statistical and systematical uncertainties in FR2 are presented in Fig. 5.31.

5.4.3 Upsilon background

The contribution from Upsilon production is estimated using the dedicated samples produced with STARLIGHT +PYTHIA8 MC generators. Three Upsilon states, $\Upsilon(1S)$, $\Upsilon(2S)$ and $\Upsilon(3S)$ with dielectron decays are considered. They are normalised to data luminosity. This background is present only for m_{ee} below 14 GeV and amounts to 2.4% of all events passing the dielectron selection criteria of FR1 (about 721.6 out of 30 456) and amounts to 1.7% of events in FR2 (about 325.8 out of 19 627). The mass distribution for $\Upsilon(\mathrm{nS}) \to e^+e^-$ events passing the dielec-

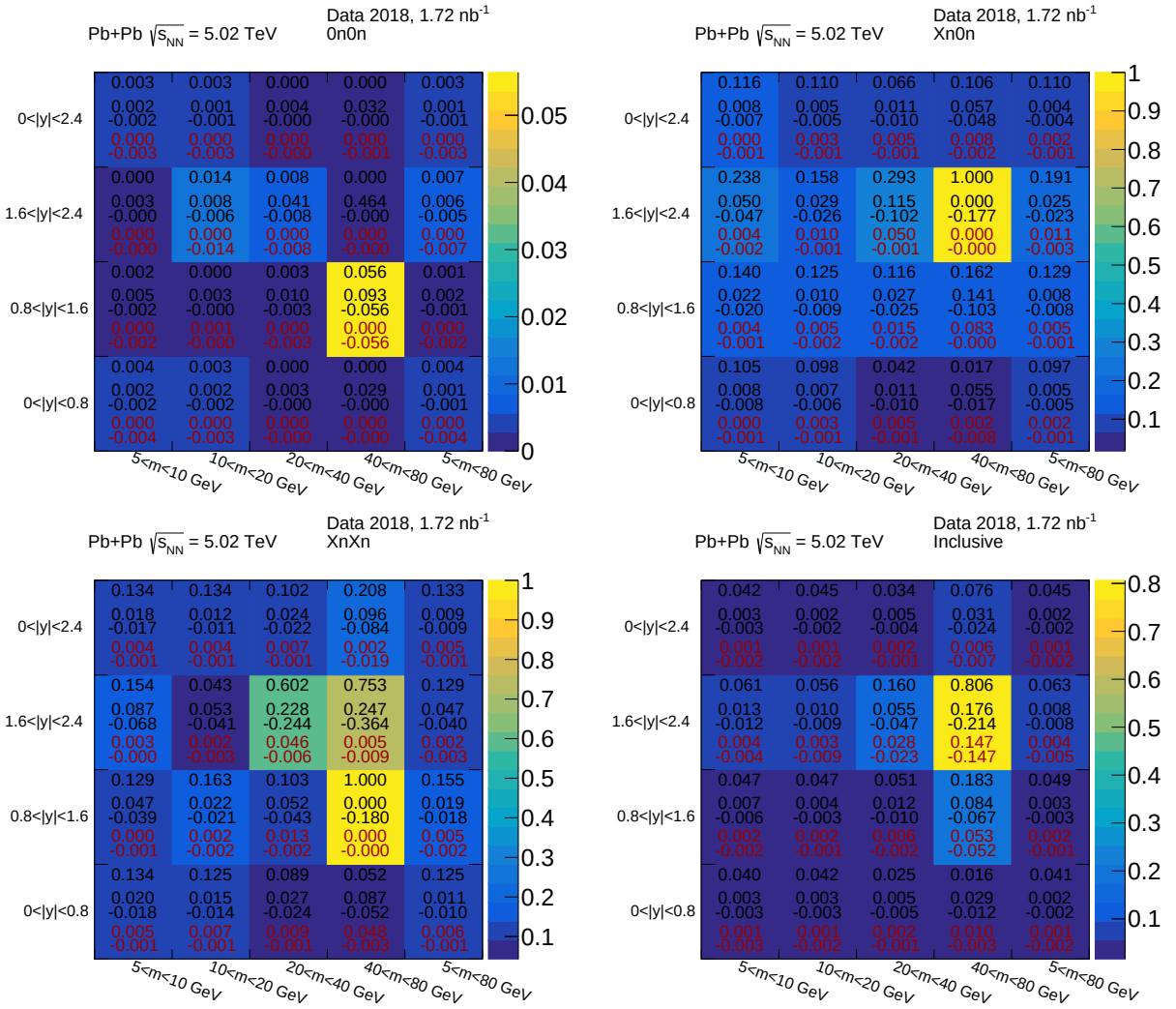

Figure 5.30: Estimated fractions of background events for the 0n0n (top, left), Xn0n (top, right), XnXn (bottom, left) categories and for the inclusive ZDC sample (bottom, right) in the data in the kinematic bins of the analysis, with statistical (black) and systematic (red) uncertainties.

tron selection criteria is presented in the left panel of Fig. 5.32. The samples are normalised to data luminosity. The acoplanarity distribution for these processes is peaked at 0, as shown in the right panel of Fig. 5.32. Therefore, it does not contribute to f_{bkg} in the background fitting procedure for dissociative events (which was implemented without subtraction of the Υ(nS) contributions).

5.4.4 Systematic uncertainties for Upsilon background

Several sources of systematic uncertainties are considered for the Υ(nS)$\rightarrow e^+e^-$ backgrounds:

- Variations of uncertainties on electron scale factors,
- Variations of uncertainties on trigger efficiency,
- Variations of uncertainties on electron energy resolution/scale.

The impact of each variation on the expected number of Υ(nS) events in the selected dielectron sample is summarised in Table 5.3 for FR1 and FR2. In both fiducial regions the

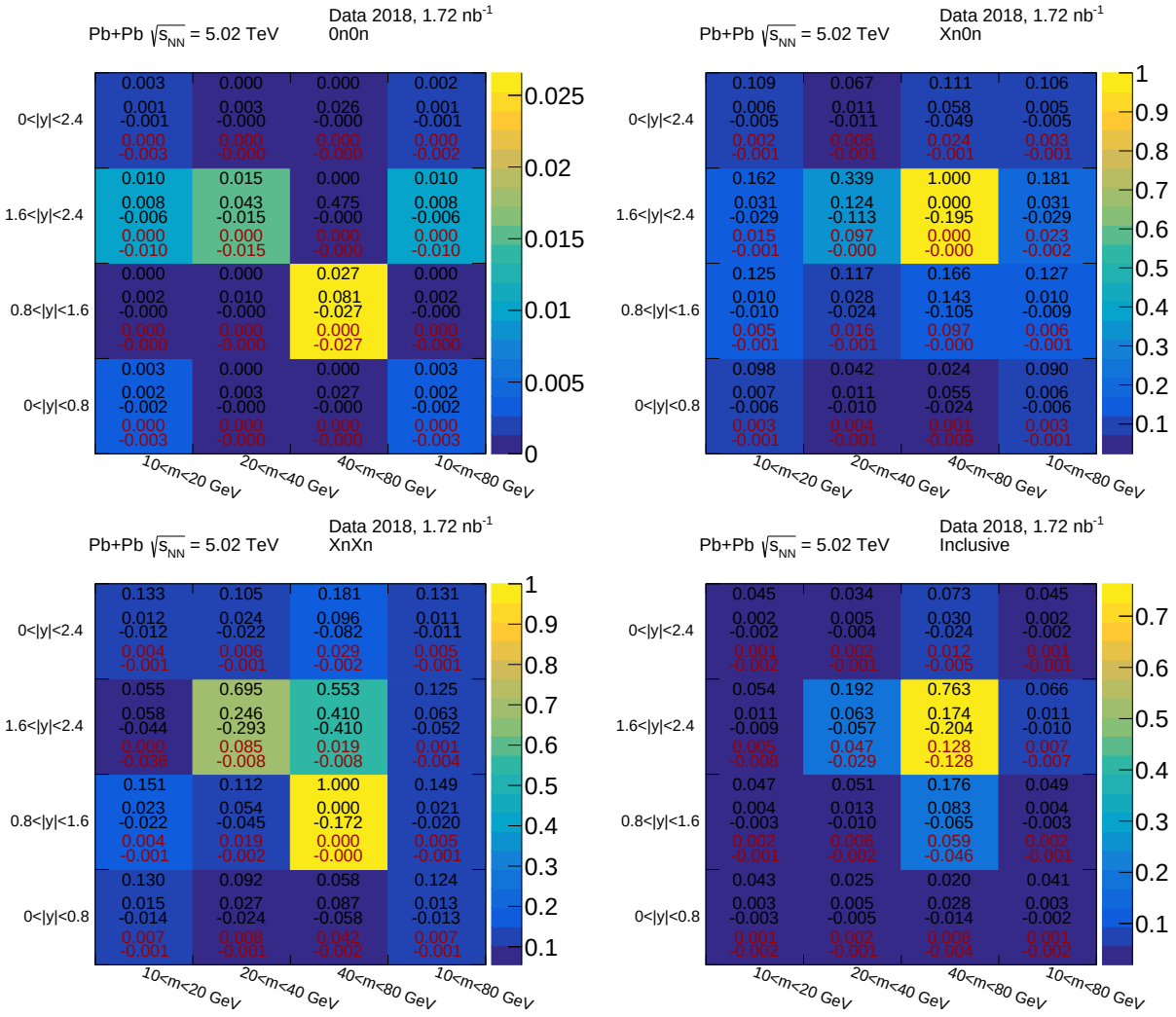

Figure 5.31: Estimated fractions of background events in FR2 for the 0n0n (top, left), Xn0n (top, right), XnXn (bottom, left) categories and for the inclusive ZDC sample (bottom, right) in the data in the kinematic bins of the analysis, with statistical (black) and systematical (red) uncertainties.

largest uncertainty originates from up and down variations of electron scale factors. In the FR2, the second most important systematic is from electron energy scale variations and is almost as large as the one related to electron scale factors. This is likely caused by the migrations of the final-state electrons in and out of the fiducial region at the $p_{\mathrm{T}}^{e} > 4$ GeV boundary. Given the small contribution from Υ production, the theoretical uncertainties of its cross-section are considered to have negligible impact on the final measurement.

5.4.5 Other background sources

The contribution of other backgrounds, originating from photonuclear events of peripheral collisions are largely suppressed by the trigger requirement of the low energy in the FCal. It rejected events with the very forward activity, not reconstructed in the central detector. The distribution of the total transverse energy in the FCal, $\Sigma E_{\mathrm{T}}^{\mathrm{FCal}}$ for selected dielectron events in the data and signal MC simulation is shown in Fig. 5.33. It is centred at 0 for both data and $\gamma\gamma \to e^{+}e^{-}$ interactions in MC simulation (however, the data distribution is wider). There are also events with significant negative values of $\Sigma E_{\mathrm{T}}^{\mathrm{FCal}}$ in the data, which are considered out-of-

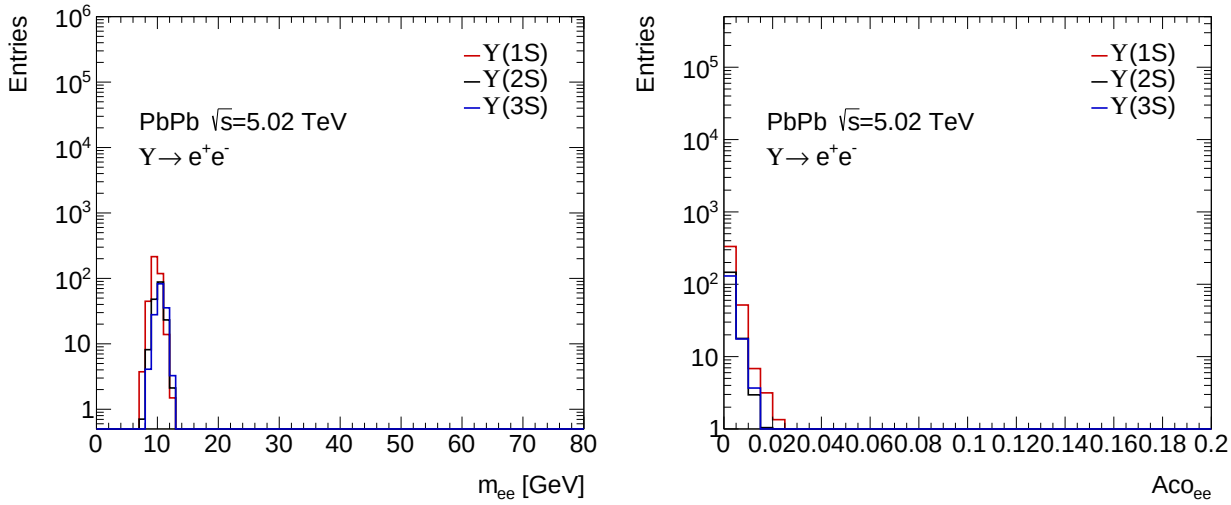

Figure 5.32: Mass (left) and acoplanarity (right) distributions of the Υ(nS)$\rightarrow e^+e^-$ events after the dielectron event selection. The contributions from Υ(1S), Υ(2S) and Υ(3S) are shown by red, black and blue histograms, respectively. The samples are normalised to data luminosity.

	FR1	FR2
Number of expected Υ(nS) events	721.6	325.8
stat. uncertainty	12.8	7.7
scale factors up	72.7	32.1
scale factors down	-69.1	-30.5
trigger up	14.5	5.8
trigger down	-15.5	-6.0
resolution up	-0.12	3.2
resolution down	-0.1	3.2
scale up	-2.9	28.9
scale down	2.6	-28.6
total	$^{+75.2}_{-72.0}$	$^{+44.5}_{-43.0}$

Table 5.3: Summary of statistical and systematic uncertainties on the expected number of Υ(nS) events in the selected dielectron sample in two fiducial regions (FR1 and FR2) in the data.

time pileup, which is observed when a low activity event is preceded by a central Pb+Pb collision with very high detector activity. This phenomenon is not simulated in MC samples. The fraction of out-of-time pileup events, having $\Sigma E_{\mathrm{T}}^{\mathrm{FCal}} < -5$, is at the level of 0.1%, thus, no cleaning requirement is introduced to the event selection to exclude them. In peripheral/photonuclear events one would also expect an additional activity in the ID, while Fig. 5.12 shows that the number of events with more than two pixel tracks in the dielectron events in the data is very low. Therefore, this contribution is also considered negligible.

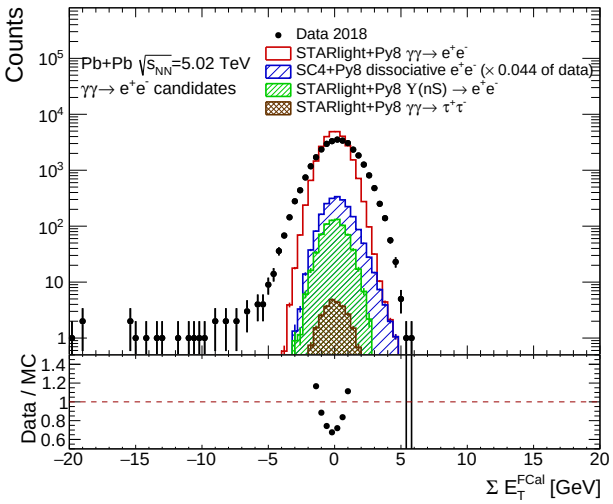

Figure 5.33: Distribution of the total transverse energy deposited in the FCal for events passing dielectron selection criteria in the data (full markers) compared with MC predictions for $\gamma\gamma \rightarrow e^+e^-$ (red), dissociative (blue), Upsilon (green) and $\gamma\gamma \rightarrow \tau^+\tau^-$ (brown) processes. The dissociative contribution is scaled to constitute the f_{diss} fraction from the data fit, other MC samples are normalised to data luminosity. The bottom panel shows a ratio between data and MC simulation.

5.5 Activity in the forward region

In this section the inclusive dielectron sample is analysed using information from the ZDC detectors. They probe nuclear dissociation which can be quantified via the fraction of events with neutron candidates detected in the ZDC arms. Dielectron events are selected using the requirements defined in Sec. 5.3.1. Fractions of events in each ZDC topology class are measured as a function of dielectron mass and rapidity. Raw ZDC fractions are corrected for dissociative background and EM pileup and, in principle, any ZDC inefficiency should also be considered. However, following the arguments from the ATLAS dimuon paper [57], a correction due to the ZDC inefficiency can be ignored since while the ZDC is only 4 interaction lengths deep, which implies an approximately 2% inefficiency for single neutrons, more than half of the EM events on a single side produce more than one neutron. This leads to an estimate of an overall efficiency of over 99%. Accounting for this subpercent inefficiency is reflected in a dedicated systematic uncertainty.

The selected dielectron events are divided into three classes based on their energy deposits in the ZDC, as discussed in Sec. 5.3.2. Data events that pass the dielectron selection are distributed as follows: 0n0n - 19167, Xn0n - 9031, XnXn - 2258. The event counts sum up to 30456, which is the total number of events from the data sample that passes the signal dielectron selection. The raw fractions are as follows: $f'_{\text{0n0n}} = (62.9 \pm 0.3)\%$, $f'_{\text{Xn0n}} = (29.7 \pm 0.3)\%$ and $f'_{\text{XnXn}} = (7.4 \pm 0.2)\%$.

5.5.1 EM pileup correction

The migration of events between ZDC classes depends on the single and mutual dissociation probabilities, determined in Sec. 5.3.3. The raw fractions f'_{0n0n}, f'_{Xn0n}, f'_{XnXn} may be related with the fractions corrected for EM pileup, f_{0n0n}, f_{Xn0n}, f_{XnXn}, with the matrix equation [57]:

$$\begin{bmatrix} f'_{\mathrm{0n0n}} \\ f'_{\mathrm{Xn0n}} \\ f'_{\mathrm{XnXn}} \end{bmatrix} = \begin{bmatrix} (1-p_{\mathrm{s}})(1-p_{\mathrm{m}}) & 0 & 0 \\ 2p_{\mathrm{s}}(1-p_{\mathrm{s}}-p_{\mathrm{m}}+p_{\mathrm{m}}p_{\mathrm{s}}/2) & (1-p_{\mathrm{s}})(1-p_{\mathrm{m}}) & 0 \\ p_{\mathrm{m}}+p_{\mathrm{s}}^2 & p_{\mathrm{m}}+p_{\mathrm{s}}-p_{\mathrm{m}}p_{\mathrm{s}} & 1 \end{bmatrix} \begin{bmatrix} f_{\mathrm{0n0n}} \\ f_{\mathrm{Xn0n}} \\ f_{\mathrm{XnXn}} \end{bmatrix}. \tag{5.2}$$

The derivation of input p_{s} and p_{m} values in discussed in Sec. 5.3.3.

The corrected fractions are determined in four bins of m_{ee} and three intervals in $|y_{ee}|$, after subtraction of the dissociative background.

The systematic uncertainty on the corrected fractions include propagated uncertainties of the p_{s} and p_{m} values, the uncertainty due to the dissociative background contribution, and the uncertainty related with the ZDC inefficiency.

The corrected fractions as a function of m_{ee} in three absolute rapidity intervals are shown in Fig. 5.34-5.36. Overall the EM pileup correction changed the observed fractions by about 13%.

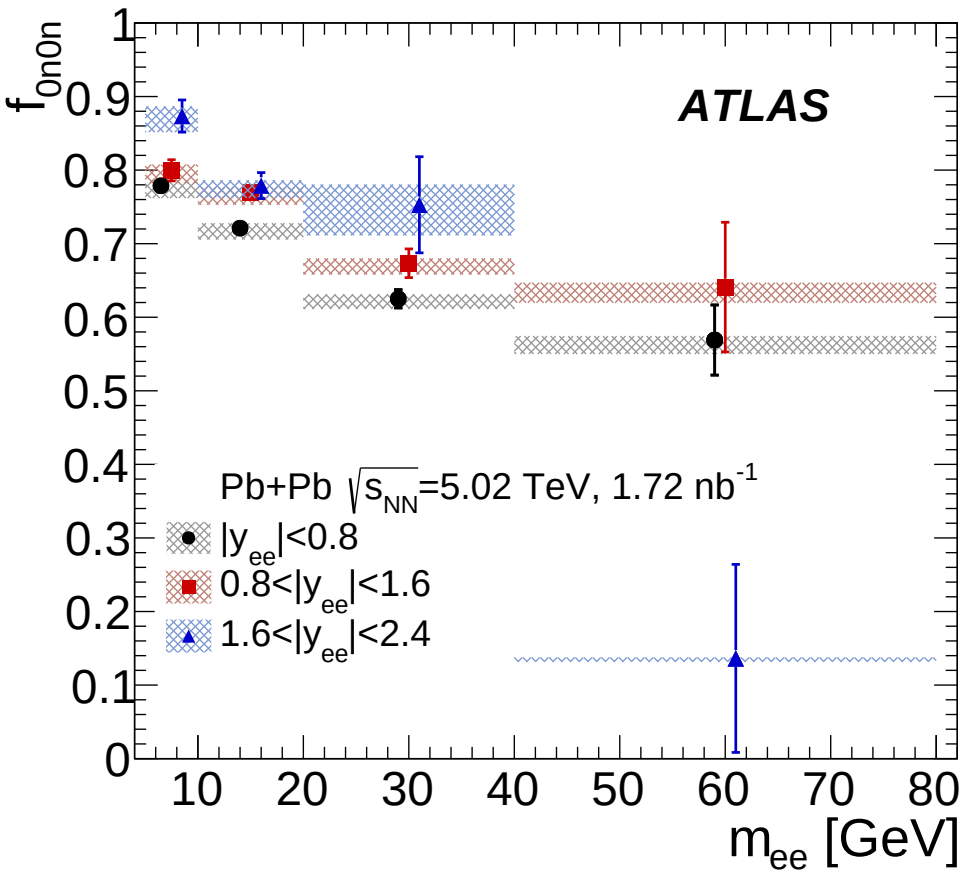

Figure 5.34: Corrected fraction f_{0n0n} as a function of m_{ee} in three intervals in $|y_{ee}|$, corrected for the presence of additional neutrons. Error bars represent statistical uncertainties, while shaded boxes represent systematic uncertainties. Points for $|y_{ee}| < 0.8$ and $1.6 < |y_{ee}| < 2.4$ are displaced horizontally for better visibility.

The fraction for events in the 0n0n category is always the highest of all and gradually drops with increasing mass. In contrary, corrected fractions f_{Xn0n} and f_{XnXn} increase with mass.

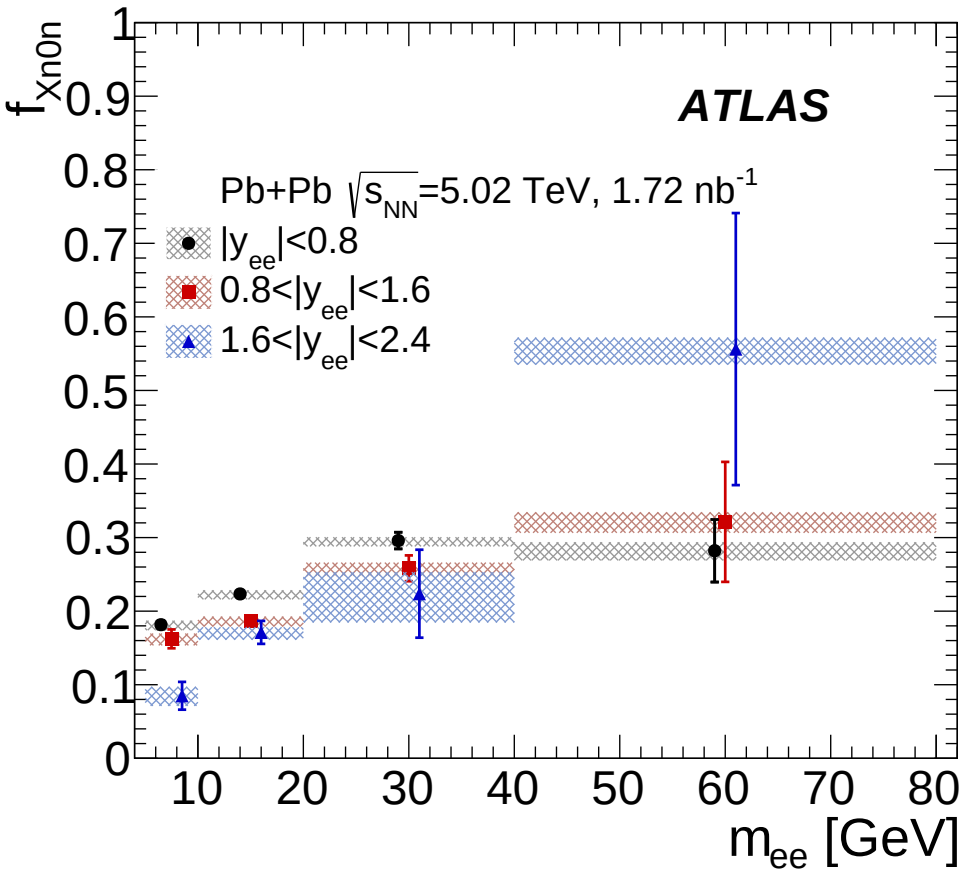

Figure 5.35: Corrected fraction f_{Xn0n} as a function of m_{ee} in three intervals in $|y_{ee}|$, corrected for the presence of additional neutrons. Error bars represent statistical uncertainties, while shaded boxes represent systematic uncertainties. Points for $|y_{ee}| < 0.8$ and $1.6 < |y_{ee}| < 2.4$ are displaced horizontally for better visibility.

5.5.2 Truth-level values of $f_{0\mathrm{n}0\mathrm{n}}$

The fractions derived in the previous section are a result of data-driven studies, so the chosen mass and rapidity intervals are determined in reconstructed-level variables. In the nominal approach, the corrected $f_{0\mathrm{n}0\mathrm{n}}$ are used to scale the truth-level variables from MC samples, based on truth-level values of m_{ee} and $|y_{ee}|$. In this approach, an assumption is made that the expected migrations between reconstructed and truth-level quantities are small due to the low number of bins. However, the effect of these migrations is also studied using the signal MC events that pass the fiducial selection criteria in both reconstructed and truth-level quantities. For each bin in truth-level m_{ee} and $|y_{ee}|$, a normalised 2D histogram of reconstructed-level m_{ee} vs $|y_{ee}|$ is created and multiplied by $f_{0\mathrm{n}0\mathrm{n}}$ values as a function of reconstructed-level variables. Then, the truth-level $f_{0\mathrm{n}0\mathrm{n}}$ fraction for the studied truth bin is obtained by integrating over the resulting 2D histogram. Figure 5.37 presents a comparison of reconstructed and truth-level $f_{0\mathrm{n}0\mathrm{n}}$ fractions. The differences are within the uncertainties on reconstructed-level $f_{0\mathrm{n}0\mathrm{n}}$ fractions. The usage of truth-level $f_{0\mathrm{n}0\mathrm{n}}$ fractions to correct the truth MC yields is taken as an additional systematic for results obtained in the 0n0n class.

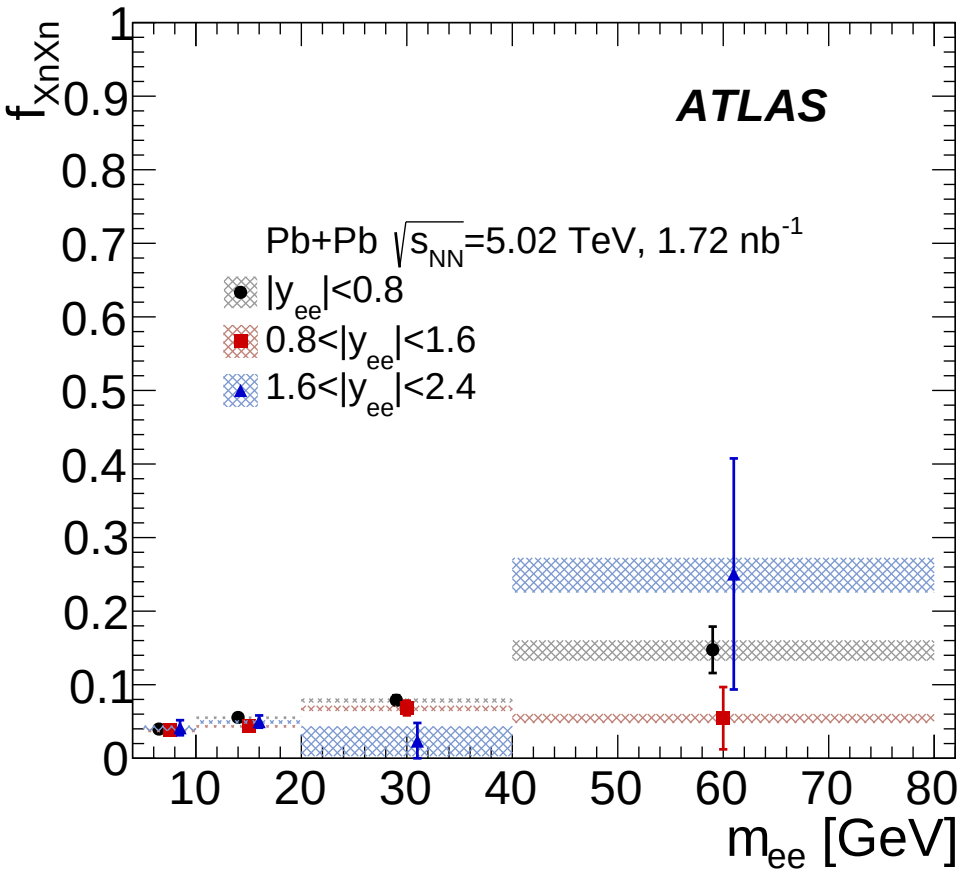

Figure 5.36: Corrected fraction f_{XnXn} as a function of m_{ee} in three intervals in $|y_{ee}|$, corrected for the presence of additional neutrons. Error bars represent statistical uncertainties, while shaded boxes represent systematic uncertainties. Points for $|y_{ee}| < 0.8$ and $1.6 < |y_{ee}| < 2.4$ are displaced horizontally for better visibility.

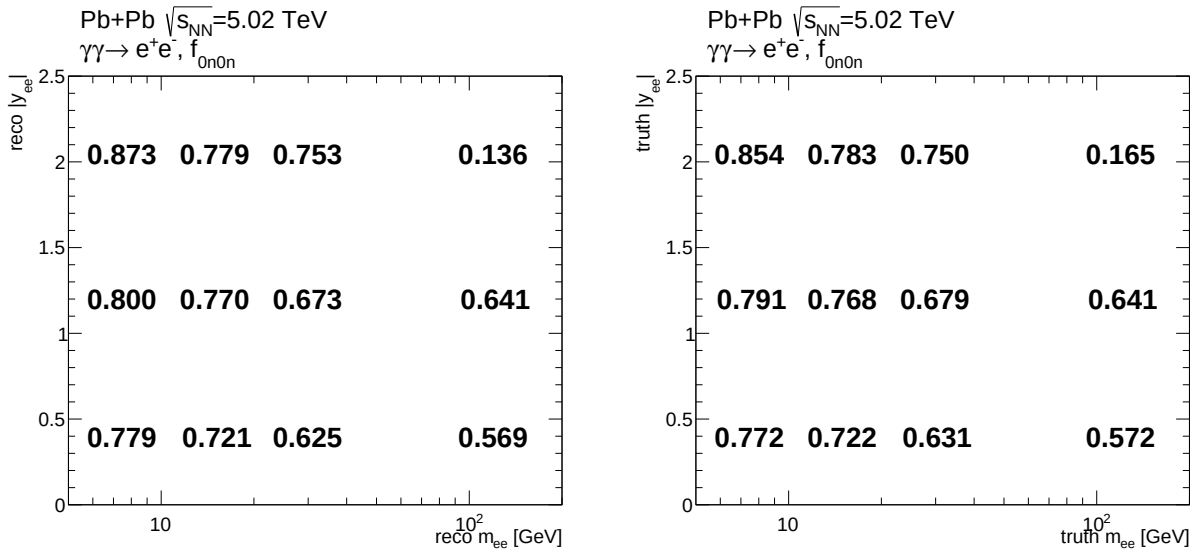

Figure 5.37: Reconstructed (left) and truth-level (right) $f_{0\mathrm{n}0\mathrm{n}}$ fractions in bins of m_{ee} and $|y_{ee}|$.

5.6 Systematic uncertainties

In the cross-section measurements the following systematic uncertainties are considered:

1. Up and down variations of scale factors for the electron reconstruction/identification efficiency, at the level of 9–10% (evaluation of uncertainties on electron scale factors is described in Sec. 5.2.1),

2. Up and down variations of trigger efficiency, at the level of 2-3% (see Sec. 4.3.3),

3. Up and down variations of electron energy scale and resolution, provided by the ATLAS Egamma CP group via the calibration tool, on average 0.5%,

4. Up and down variations of backgrounds, on average 0.5%, (see Sec. 5.4.2),

5. Luminosity uncertainty of ±2.0%, which is derived from the calibration of the luminosity scale using x-y beam-separation scans, following a methodology similar to that detailed in Ref. [105], and using the LUCID-2 detector for the baseline luminosity measurements [83],

6. for differential cross-sections also:

    - unfolding non-closure uncertainty from a split-sample test, mostly below 1%, (see Sec. 5.7.3),
    - unfolding non-closure uncertainty from a data-driven closure test, mostly within 1%, with some bins in m_{ee} and $\langle p_{\mathrm{T},e} \rangle$ having uncertainty up to 3% (see Sec. 5.7.3),
    - systematic uncertainties from the difference between results of two-dimensional unfolding and the one-dimensional unfolding, at the level of 2-3% with some bins having uncertainty up to 5% (see Sec. 5.7.3),
    - for differential cross-sections in the 0n0n category additional systematic uncertainties from using the f_{0n0n} fractions recalculated for truth-level quantities of m_{ee} and $|y_{ee}|$, at the level of 1–2% (see Sec. 5.5.2).

5.7 Analysis procedure

5.7.1 Control distributions

There are about 30k events passing the dielectron selection criteria in the data. The estimated background contributions are:

- dissociation estimated using the template fitting technique, contributes to the data sample at about 4.4%

- Upsilon decays in the dielectron channels, estimated with the MC simulation, contributes about 2.4% to the data sample

- exclusive ditau production, estimated with the MC simulation, contributes about 0.1% to the data sample.

Figure 5.38 shows control distributions for the selected dielectron sample in the data, compared with the MC predictions for signal and background processes. The presented distributions include events passing the event selection for the FR1, and are inclusive in ZDC. In the MC simulation, the trigger decision was not used, instead the distributions are weighted by the

parameterised trigger efficiency and by the electron scale factors. The signal MC samples are normalised to the integrated luminosity of the data set. The dissociative background contribution is weighted by the f_{diss} fraction (f_{bkg} reduced by the ditau contribution) calculated for the inclusive sample (no bins in m_{ee} or y_{ee}).

In general a good agreement is found between the data and the MC predictions in Fig. 5.38. The observed discrepancies in the number of counts are at the level of 10%. In the m_{ee} distribution the data excess is most strongly pronounced for m_{ee} between 10 and 20 GeV, where the difference between data and MC simulation is at the level of about 10 to 20%. The data to MC ratio drops below unity for larger masses. In the y_{ee} distribution, the data excess is smaller, up to 10%, in the range from -1.2 to 1.2, with rising discrepancies for larger y_{ee}. The $|\cos\theta^*|$ distribution, where $|\cos\theta^*| = |\tanh(\frac{\Delta\eta_{ee}}{2})|$, is also presented. The data to MC ratio in the $|\cos\theta^*|$ distribution drops slowly from 1.2 for $|\cos\theta^*| = 0$ to unity at $|\cos\theta^*| = 0.75$, and then falling more steeply, down to 0.5 for the largest values of $|\cos\theta^*|$. The p_{T}^e distribution is averaged over p_{T} of the two electrons, $\langle p_{\mathrm{T},e}\rangle = (p_{\mathrm{T}e_1} + p_{\mathrm{T}e_2})/2$, since in the signal process the electrons should be balanced in p_{T}^e, and the observed discrepancies are related to detector imperfections. In the $\langle p_{\mathrm{T},e}\rangle$ distribution, the largest discrepancies, at the level of 15-20%, are present for $\langle p_{\mathrm{T},e}\rangle$ between 5 and 9 GeV. In the acoplanarity distribution, the difference between data and MC simulation is not so monotonic, there is a data excess up to 20% for acoplanaritites below 0.002, then the ratio drops below unity, down to 0.8. For acoplanarities between 0.01 and 0.025 the ratio again is above 1, up to about 1.2.

In order to show the influence of potential background contributions on the signal selection for exclusive dielectron pairs, control distributions are created for event candidates from the 0n0n category only. They are presented in Fig. 5.39. The 0n0n category is supposed to have a negligible background contribution from dissociation, therefore this background is not included. The MC samples for the signal $\gamma\gamma \to e^+e^-$ process are reweighted by the f_{0n0n} as a function of m_{ee} and $|y_{ee}|$. More than 94% of the data sample in 0n0n category is signal from the $\gamma\gamma \to e^+e^-$ process. In general the data to MC comparison improves with respect to Fig. 5.38. In particular, m_{ee} and $\langle p_{\mathrm{T},e}\rangle$ distributions get more flat for low values of m_{ee} and $\langle p_{\mathrm{T},e}\rangle$, respectively. Apart from the better agreement in the overall normalisation, no major differences are seen in the $|\cos\theta^*|$ distribution. The discrepancies observed in Fig. 5.38 in y_{ee} and acoplanarity distributions are also present in events from the 0n0n category.

The control distributions for individual electrons in data passing the FR1 selection are provided. Figure 5.40 presents the comparison between leading and subleading electron p_{T}^e, η, and ϕ in the data, where the leading electron is the one with larger p_{T}^e. The first column shows the distributions for reconstructed electrons, the second column for tracks associated to electrons and the last column for clusters associated to electrons. In general all these distributions look reasonable.

Additionally, the correlation plots for each pair of m_{ee}, $\langle p_{\mathrm{T},e}\rangle$, $|y_{ee}|$ and $|\cos\theta^*|$ variables are made. The maps, presented in Fig. 5.41, show the available statistics as a function of each pair of variables. There is an obvious correlation between the m_{ee} and $\langle p_{\mathrm{T},e}\rangle$, and events are placed closely to the diagonal. The largest statistics are available for low $m_{ee}/\langle p_{\mathrm{T},e}\rangle$, and also in those regions a full $|y_{ee}| < 2.5$ range is probed. For the lowest mass bins, there are no available statistics at large $|\cos\theta^*|$. For large $|y_{ee}|$, there are only events with low $|\cos\theta^*|$ available. In the correlation plot, one can also see the effect of the exclusion of the crack region - the lower number of events along the line starting at $|y_{ee}| = 0$ and $|\cos\theta^*| = 1$ and ending at $|y_{ee}| = 1.5$ and $|\cos\theta^*| = 0$.

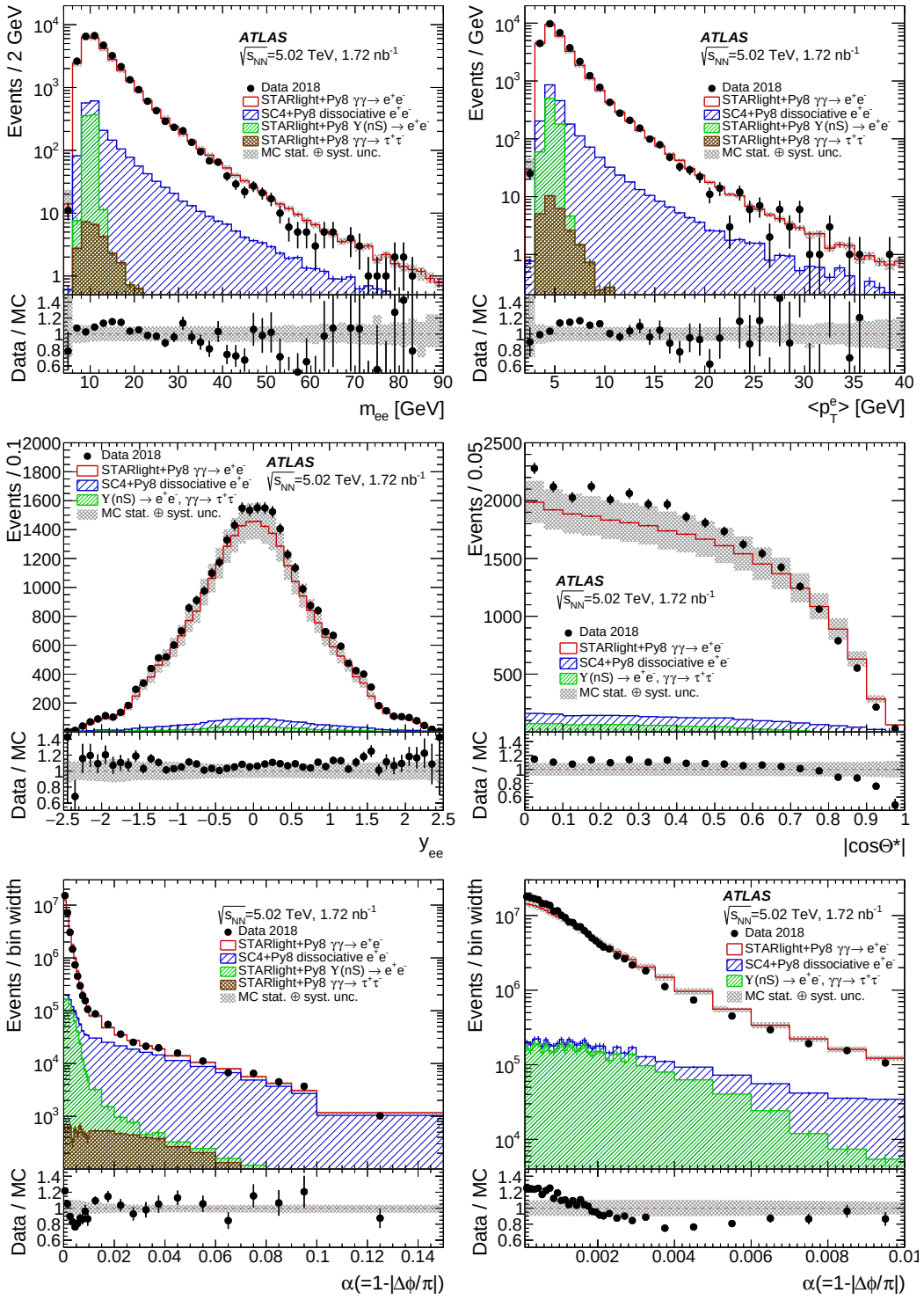

Figure 5.38: Distributions of m_{ee} (top left), $\langle p_{\mathrm{T},e} \rangle$ (top right), y_{ee} (middle left), $|\cos\theta^*|$ (middle right), and acoplanarity (bottom left), also with a zoomed version (bottom right) for events passing the dielectron selection criteria in the data (markers) compared with MC simulation for signal (red histogram), and dissociative (blue histogram), Upsilon (green histogram) and $\gamma\gamma \to \tau^+\tau^-$ (brown histogram) backgrounds. Bottom panels show data to MC ratios. Error bars denote statistical uncertainties. The shaded area represents the overall uncertainty of the total MC prediction. In the y_{ee}, $|\cos\theta^*|$, and α distributions, the Υ and $\tau^+\tau^-$ contributions are shown together. The dissociative contribution is scaled to constitute the f_{diss} fraction from the data fit, other MC samples are normalised to data luminosity.

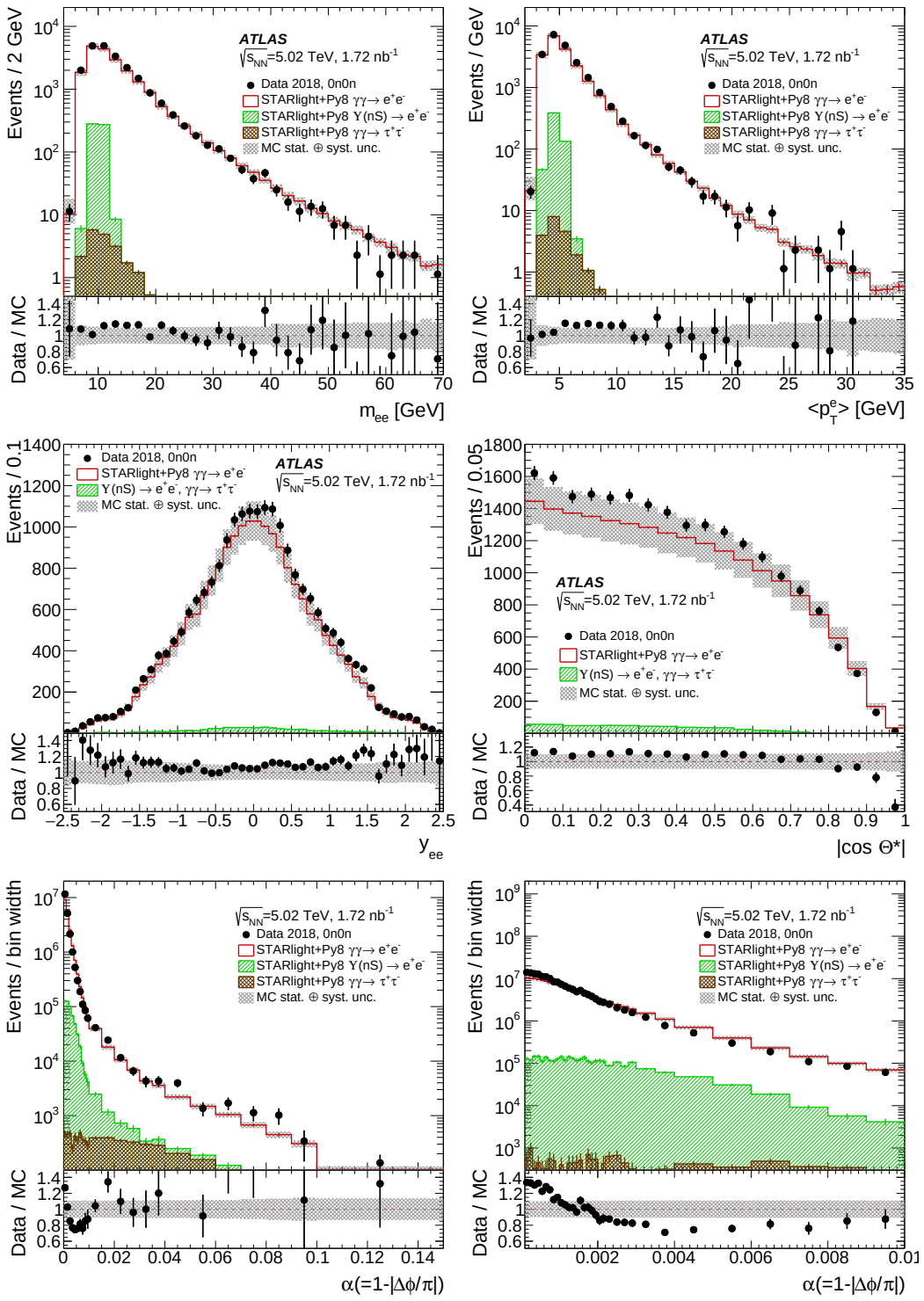

Figure 5.39: Distributions of m_{ee} (top left), $\langle p_{\mathrm{T},e} \rangle$ (top right), y_{ee} (middle left), $|\cos\theta^*|$ (middle right), and acoplanarity (bottom left), also with a zoomed version (bottom right) for events from the 0n0n category in the data (full markers) compared with the MC predictions for signal (red histogram) and Upsilon (green histogram) and $\gamma\gamma \to \tau^+\tau^-$ (brown histogram) backgrounds. MC simulated samples are multiplied by the derived fraction of events in the 0n0n category. Bottom panels show the ratio of data to MC simulation. Error bars represent statistical uncertainties. The shaded area represents the overall uncertainty of the total MC prediction. In the y_{ee}, $|\cos\theta^*|$, and α distributions, the Υ and $\tau^+\tau^-$ contributions are shown together. The MC samples are normalised to data luminosity.

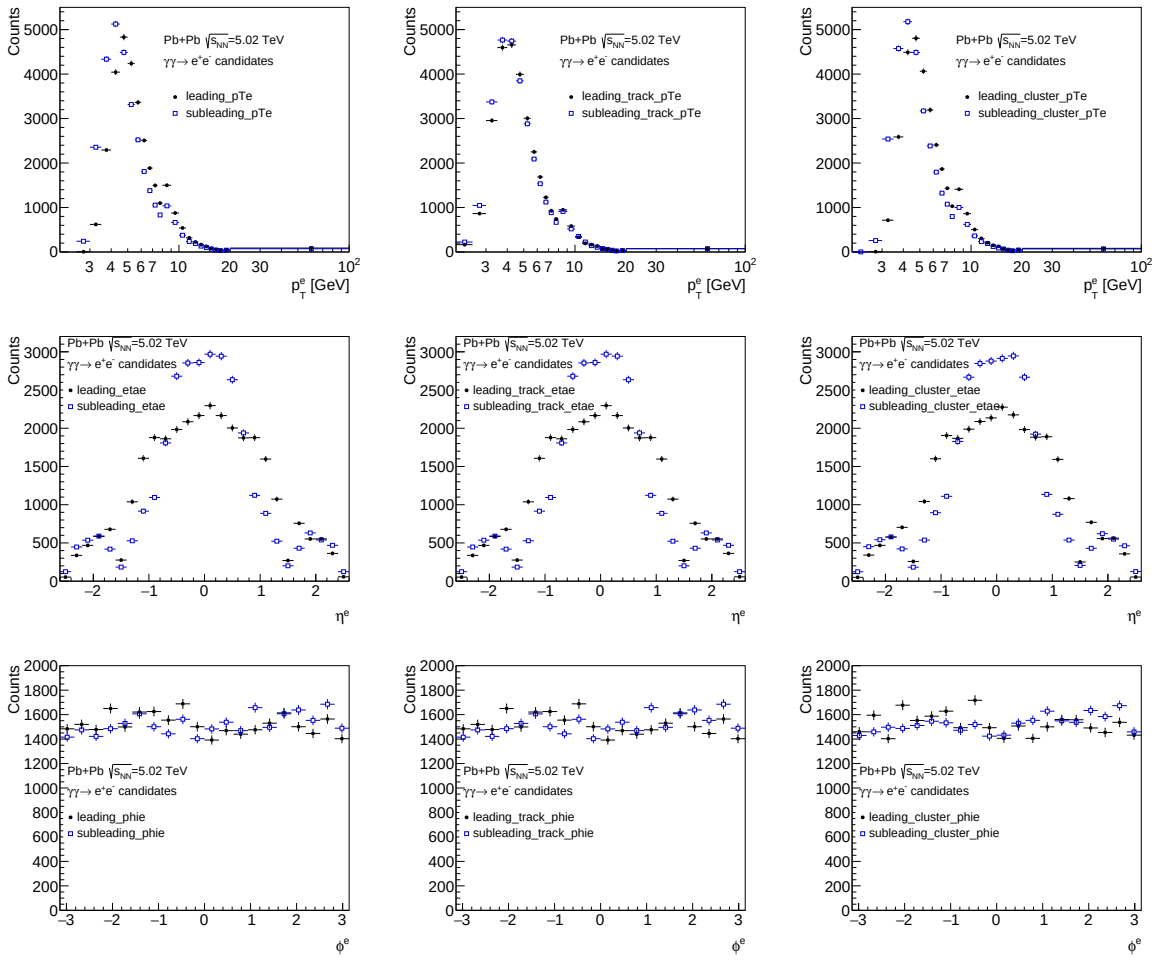

Figure 5.40: Distributions of p_{T}^{e} (top), η (middle), and ϕ (bottom) for leading and subleading electrons in events passing the dielectron selection criteria in the data. The first column shows distributions for reconstructed electrons, the second column for tracks associated to electrons and the last column for clusters associated to electrons.

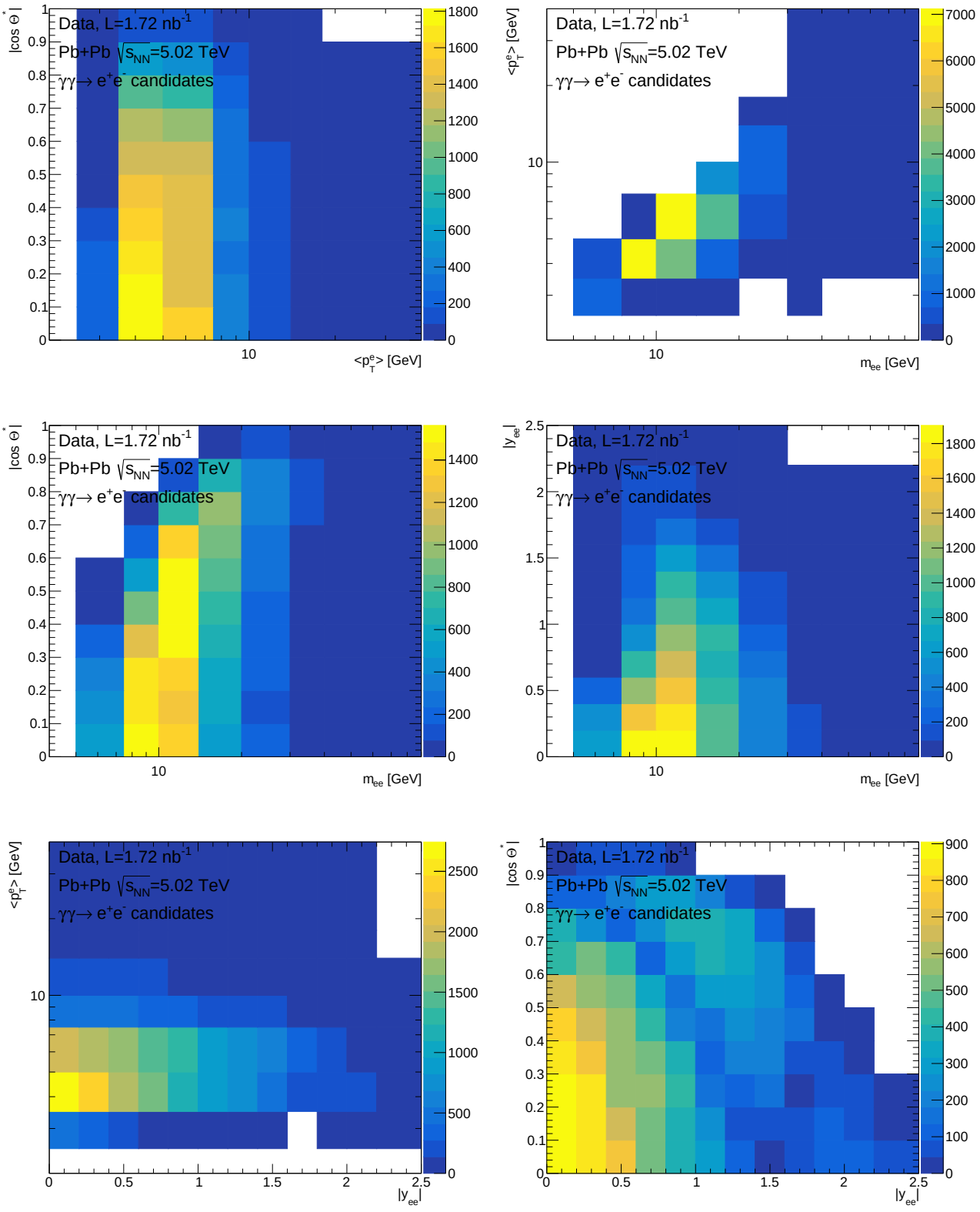

Figure 5.41: Two-dimensional distributions of events passing the dielectron selection criteria in the FR1 in the data: $\langle p_{\mathrm{T},e} \rangle$ vs. $|\cos\theta^*|$ (top left), m_{ee} vs. $\langle p_{\mathrm{T},e} \rangle$ (top right), m_{ee} vs. $|\cos\theta^*|$ (middle left), m_{ee} vs. $|y_{ee}|$ (middle right), $|y_{ee}|$ vs. $\langle p_{\mathrm{T},e} \rangle$ (bottom left) and $|y_{ee}|$ vs. $|\cos\theta^*|$ (bottom right).

5.7.2 Measurement of integrated fiducial cross-section

The integrated fiducial cross-section for exclusive dielectron production is calculated using the following formula:

$$\sigma^{\text{fid}} = \frac{N_{\text{data}} - N_{\text{bkg}}}{C \cdot A \cdot L}, \tag{5.3}$$

where:

- N_{data} and N_{bkg} refer to a number of events in the data after the dielectron selection and a number of expected background events in this selected sample, respectively,
- C is a correction factor accounting for detector and trigger inefficiencies, calculated as $\frac{N^{\text{fid,cut}}_{\text{MC,reco}}}{N^{\text{fid,cut}}_{\text{MC,gen}}}$ where $N^{\text{fid,cut}}_{\text{MC,reco}}$ is a number of expected signal events after the dielectron selection imposed at the reconstructed level, while $N^{\text{fid,cut}}_{\text{MC,gen}}$ is a number of events passing the fiducial region requirements at the truth level;
- A is the acceptance correction, used to account for the exclusion of the calorimeter transition region and the broader kinematic coverage $|\eta| < 2.47$ to $|\eta| < 2.50$; it is calculated as $\frac{N^{\text{fid,cut}}_{\text{MC,gen}}}{N^{\text{fid}}_{\text{MC,gen}}}$, where $N^{\text{fid}}_{\text{MC,gen}}$ is the number of events passing the fiducial region requirement at the truth level (with $|\eta|$ range extended from 2.47 to 2.5), but the calorimeter transition region exclusion cut;
- L is the integrated luminosity of the data sample.

The numbers of events passing the fiducial selection criteria in the data equal to 30 456 for the FR1 and 19 627 in the FR2. The dissociative and ditau background fraction amounts to 4.5%, and is identical in the FR1 and the FR2. The Upsilon background amounts to 2.4% of all events passing the selection criteria of the FR1 (about 721.6 out of 30 456) and amounts to 1.7% of events contributing to the FR2 (about 325.8 out of 19 627).

Table 5.4 summarises the values of the C factors with their relative statistical and individual systematic uncertainties in the two fiducial regions. The C factors are calculated either using truth electron kinematics before the FSR (so called Born level) or using truth electron kinematics after the FSR (so called final state). The relative statistical uncertainty contributes to 0.6%, while the systematic one - 9-10%. The largest source of systematic uncertainty originates from electron scale factors, and is at the level of 9-10%.

The obtained values of the A factors and their statistical uncertainties are summarised in Table 5.5. No systematic uncertainties are assigned to A factors, as they are determined at the truth level.

The measured integrated fiducial cross-sections are:

- at the Born level: 214.8 $\pm$1.3 (stat.) $^{+23.1}_{-20.1}$ (syst.) μb in FR1 and 37.8 $\pm$0.3 (stat.) $^{+3.9}_{-3.4}$ (syst.) μb in FR2.
- at the final-state level: 192.2 $\pm$1.1 (stat.) $^{+20.7}_{-18.0}$ (syst.) μb in FR1 and 33.0 $\pm$0.2 (stat.) $^{+3.4}_{-3.0}$ (syst.) μb in FR2.

The relative statistical uncertainty amounts to 0.6% while the relative total systematic uncertainty contributes to 11%. A summary of systematic uncertainties is presented in Table 5.6. The dominating sources of systematic uncertainties are up and down electron scale factor variations. The second largest sources of uncertainty are up and down trigger variations. All cross-sections have an additional $\pm$ 2% uncertainty from the integrated luminosity measurement.

The predicted fiducial cross-sections, estimated using STARLIGHT +PYTHIA8, and for Born level also using SUPERCHIC (due to lack of FSR simulation), are:

	FR1, Born level	FR1, final state	FR2, Born level	FR2, final state
C factor	0.087191	0.0974398	0.317898	0.363641
stat. uncertainty [%]	0.59	0.59	0.64	0.62
SF up [%]	9.7	9.7	9.4	9.4
SF down [%]	-9.3	-9.3	-8.9	-8.9
trigger up [%]	2.0	2.0	1.6	1.6
trigger down [%]	-2.2	-2.2	-1.7	-1.7
resolution up [%]	-0.3	-0.3	-0.6	-0.6
resolution down [%]	0.05	0.05	0.15	0.15
scale up [%]	-0.4	-0.4	1.5	1.5
scale down [%]	0.3	0.3	-1.6	-1.6
total[%]	$^{+10.0}_{-9.6}$	$^{+10.0}_{-9.6}$	$^{+9.7}_{-9.3}$	$^{+9.7}_{-9.3}$

Table 5.4: Values of C factors for two fiducial regions FR1 and FR2, and two selections of truth-level electron kinematics with relative statistical and individual systematic uncertainties.

	A factor	stat. uncertainty
FR1, Born level	0.87843	0.00056
FR1, final state	0.87847	0.00059
FR2, Born level	0.88942	0.00129
FR2, final state	0.88892	0.00139

Table 5.5: Values of A factors with statistical uncertainties calculated for two fiducial regions FR1 and FR2 for two selections of the truth electron kinematics.

- for electrons before the FSR - Born level:
  STARLIGHT +PYTHIA8: 196.9 μb in the FR1 and 33.9 μb in the FR2,
  SUPERCHIC: 235.1 μb in the FR1 and 40.8 μb in the FR2,
- for electrons after the FSR - final-state level:
  STARLIGHT +PYTHIA8: 176.2 μb in the FR1 and 29.7 μb in the FR2.

The data-to-prediction ratio of cross-sections amounts to $1.09^{+0.12}_{-0.10}$ for the FR1 and $1.11^{+0.12}_{-0.10}$ for the FR2 for STARLIGHT, and $0.91^{+0.10}_{-0.09}$ for the FR1 and $0.93^{+0.10}_{-0.08}$ for the FR2. The results for final-state electrons in FR2, can be compared with the integrated fiducial cross-section for exclusive dimuon production, which was measured using the same kinematic requirements [57]. The measured dimuon cross-section equals to $34.1 \pm 0.3(\text{stat.}) \pm 0.7(\text{syst.})\mu$b, and is compared with STARLIGHT predicted cross-section of $\sigma_{\text{MC}} = 32.1\mu$b. The cross-sections measured in FR2 for dielectrons and dimuons are in agreement within experimental uncertainties.

5.7.3 Differential fiducial cross-sections

Differential fiducial cross-sections are determined as a function of m_{ee}, $\langle p_{\text{T},e} \rangle$, $|y_{ee}|$ and $|\cos\theta^*|$. A Bayesian unfolding procedure is used to obtain distributions corrected for bin migrations between truth and reconstructed levels and also in and out of the fiducial region. It is applied using the RooUnfold [106] package. The differential fiducial cross-sections are measured inclusively with respect to the ZDC selection as well as in the 0n0n category. For the measurement in the 0n0n category, only events with low activity in the ZDC are selected, as described in Sec. 5.3.2. The background from dissociation is not considered for this category. As there is no

	FR1, Born level	FR1, final state	FR2, Born level	FR2, final state
$\sigma^{\text{fid.}}$ [μb]	214.8	192.2	37.8	33.0
stat. uncertainty	1.3	1.1	0.3	0.2
SF up	-19.6	-17.5	-3.3	-2.8
SF down	22.6	20.2	3.8	3.3
trigger up	-4.4	-3.9	-0.6	-0.5
trigger down	4.9	4.4	0.6	0.6
resolution up	0.6	0.6	0.2	0.2
resolution down	-0.1	-0.1	-0.1	-0.1
scale up	0.8	0.7	-0.6	-0.5
scale down	-0.7	-0.6	0.7	0.6
background up	-0.5	-0.5	-0.1	-0.1
background down	0.7	0.6	0.1	0.1
total	$^{+23.2}_{-20.1}$	$^{+20.7}_{-18.0}$	$^{+3.9}_{-3.4}$	$^{+3.4}_{-3.0}$

Table 5.6: Values of integrated fiducial cross-sections for two fiducial regions FR1 and FR2 and two selections of the truth electron kinematics. Statistical and individual systematic uncertainties are also given. The total uncertainty is a sum in quadrature of statistical and systematic uncertainties listed in the table. There is also a 2% additional systematic uncertainty from the luminosity measurement.

ZDC simulation available for MC simulation in ATLAS, the simulated samples are re-weighted by the measured fraction of events in 0n0n category, f_{0n0n}, corrected for dissociative background and the effect of EM pileup, as discussed in Sec. 5.5. The weight is applied depending on the mass and rapidity of the dielectron system. The data also has to be corrected for the presence of EM pileup, what is done by reweighting the data by the $f_{\text{0n0n}}/f'_{\text{0n0n}}$ ratio. This weight is applied per event, also depending on mass and rapidity of the dielectron pair.

Unfolding methodology

The selected data sample is corrected in a few subsequent steps in order to compare it with theoretical truth-level predictions. A schematic diagram of the unfolding procedure is presented in Fig. 5.42. As a first step the backgrounds are subtracted: the data is reweighted event-by-event by the $(1 - f_{\text{bkg}})$ where f_{bkg} is the fraction of background events extracted from the fit in a given m_{ee} and $|y_{ee}|$ range in the inclusive ZDC sample. For masses above 40 GeV, the fraction obtained from the fit in the $|y_{ee}| < 2.4$ range is used. For events with m_{ee} below 40 GeV, the fractions depend also on $|y_{ee}|$. If $|y_{ee}|$ exceeds 2.4, the fraction from the $1.6 < |y_{ee}| < 2.4$ bin is used. Then, the Υ(nS) background is subtracted (by the addition of histograms with -1 weights). In the next step, the data is corrected with so called fiducial correction factors, F. They are parameterised as a function of each of unfolding variables. The F factors are derived based on signal MC events passing the dielectron selection requirements. The MC simulation is reweighed per event by $\epsilon_{\text{T}} \cdot SF_1 \cdot SF_2$, where ϵ_{T} is trigger efficiency, and $SF_{1,2}$ are electron reco/PID scale factors for each of electrons. The F correction for the i-th bin of reconstructed level distribution is defined as:

$$F_i = \frac{N_i^{\text{in fid.}}}{N_i}|_{\text{is reco}} \tag{5.4}$$

where $N_i^{\text{in fid.}}$ is the number of events in the i-th bin of the reconstructed-level distribution which also fall into the fiducial region at the truth level (it does not matter in which bin they are on the truth level) and N_i is the number of events in the i-th bin at the reconstructed

level. The F_i factor corrects for the events that pass the fiducial region selection, but at the truth level they fall outside the fiducial region. By definition the F_i factors are determined as a function of reconstructed-level values of considered variables.

In the following step, the truth-level distributions are constructed from the reconstructed-level distributions using the response matrices built from the signal MC simulation. To fill the response matrices only signal MC events passing the dielectron selection criteria at the reconstructed level and fiducial selection criteria at the truth level are considered. Also here, the MC sample is reweighed by $\epsilon_{\mathrm{T}} \cdot SF_1 \cdot SF_2$ per event. In the end, the distributions are divided by the luminosity and the efficiency correction factors, CA. The efficiency correction factors are parameterised as a function of unfolding variables at the truth level. The i-th bin of the CA factor is defined as:

$$CA_i = \frac{N_i^{\text{reco \& truth in fid.}}}{N_i^{\text{truth in fid.}}} \tag{5.5}$$

where $N_i^{\text{reco \& truth in fid.}}$ is the number of events in the i-th bin of the truth-level distribution, which also pass the dielectron selection criteria at the reconstructed level (but it is not important in which bin they fall at the reconstructed level) and $N_i^{\text{truth in fid.}}$ is the number of events in the i-th bin at the truth level. Events in the numerator of the CA factor are reweighed per event by the $\epsilon_{\mathrm{T}} \cdot SF_1 \cdot SF_2$ factor. By definition, the CA factor is determined as a function of truth-level values of unfolding variables. The CA factor corrects for the inefficiencies at the reconstructed level as well as the acceptance losses.

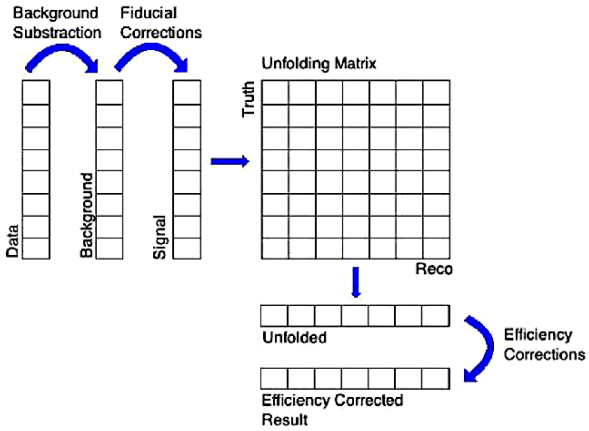

Figure 5.42: Diagram presenting the unfolding procedure used in this measurement [107].

Binning of distributions

The binning of the unfolded distributions is summarised in Table 5.7. The binning was optimised to provide a sufficient number of events in each bin in the data sample (should be above 100 events). The available statistics are shown in Fig. 5.43. Also, the purity, i.e. the fraction of events in a given bin at the reconstructed level, which was also generated in the same bin, was considered. For the optimal binning, the minimal purity in each bin is required to be 80%. Figure 5.44 shows the purity for each of unfolding variables. In case of binning for the differential cross-sections in the 0n0n category, the only differences in comparison to the inclusive ZDC case are the upper edges of the last bins in m_{ee}, which is 70 GeV, and in $\langle p_{\mathrm{T},e} \rangle$, which is 35 GeV.

variable	bin edges
m_{ee}	5,7.5,10,14,20,30,40,90
$\langle p_{\mathrm{T},e} \rangle$	2.5,3.5,5,7.5,10,14,18,70
$\lvert y_{ee} \rvert$	0,0.2,0.4,0.6,0.8,1.0,1.2,1.4,1.6,1.8,2.0,2.2,2.5
$\lvert \cos\theta^* \rvert$	0,0.1,0.2,0.3,0.4,0.5,0.6,0.7,0.8,0.9,1.0

Table 5.7: Overview of binning used in the unfolding procedure.

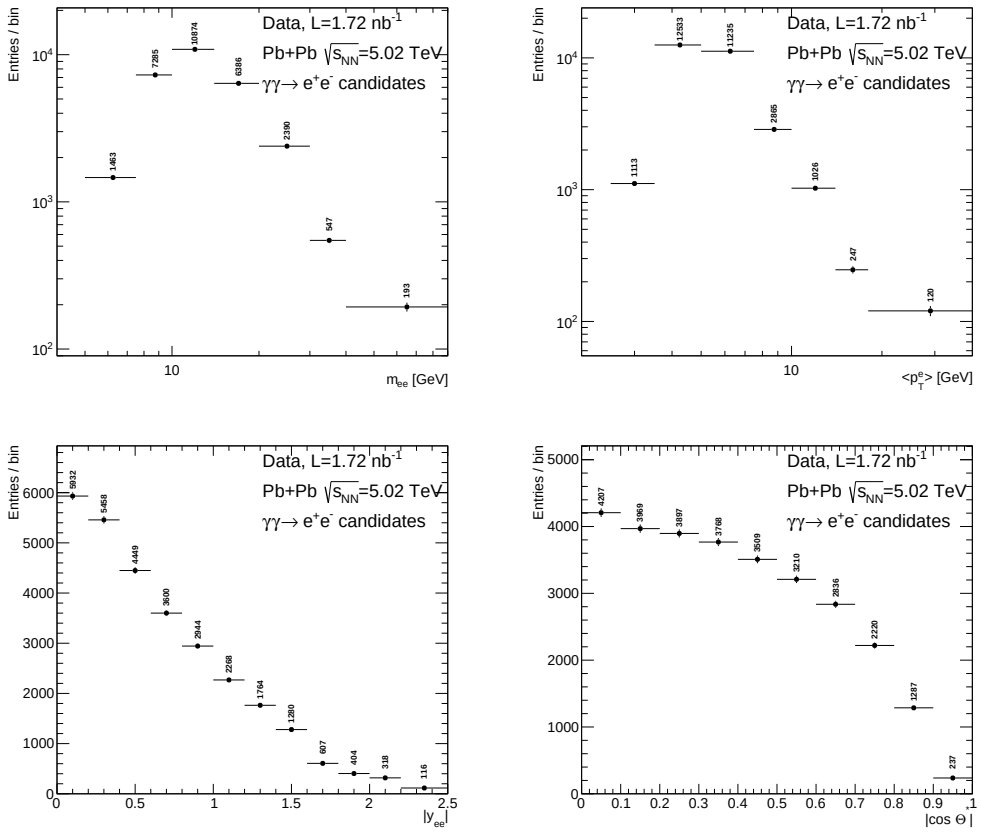

Figure 5.43: The available statistics in bins of m_{ee}, $\langle p_{\mathrm{T},e} \rangle$, $|y_{ee}|$, and $|\cos\theta^*|$ in data.

Response matrices, fiducial and efficiency corrections

The response matrices reflect the bin migrations between the truth-level distributions and the reconstructed-level ones. The distributions of reconstructed variables are affected by the detector reconstruction inefficiencies, resolution effects and acceptance limitations. The response matrices are obtained using the signal MC samples. The events have to pass the event selection criteria at the reconstructed level (summarised in Sec. 5.3.1) as well as fiducial acceptance cuts at the truth level (FR1 in Table 5.2). Figure 5.45 presents the response matrices for four considered variables. More migrations are observed in m_{ee} and $\langle p_{\mathrm{T},e} \rangle$ matrices (top figures) than in $|y_{ee}|$ and $|\cos\theta^*|$ (bottom figures).

The fiducial correction factor, F, is applied to reconstructed-level distributions after the background subtraction. The distributions of fiducial correction factors as a function of four considered variables are shown in the first column of Fig. 5.46. The values of the fiducial correction factors are over 99% for almost all bins of the considered distributions. In case of F distributions as a function of m_{ee} and $\langle p_{\mathrm{T},e} \rangle$, the values of F rise for larger m_{ee} and $\langle p_{\mathrm{T},e} \rangle$. The

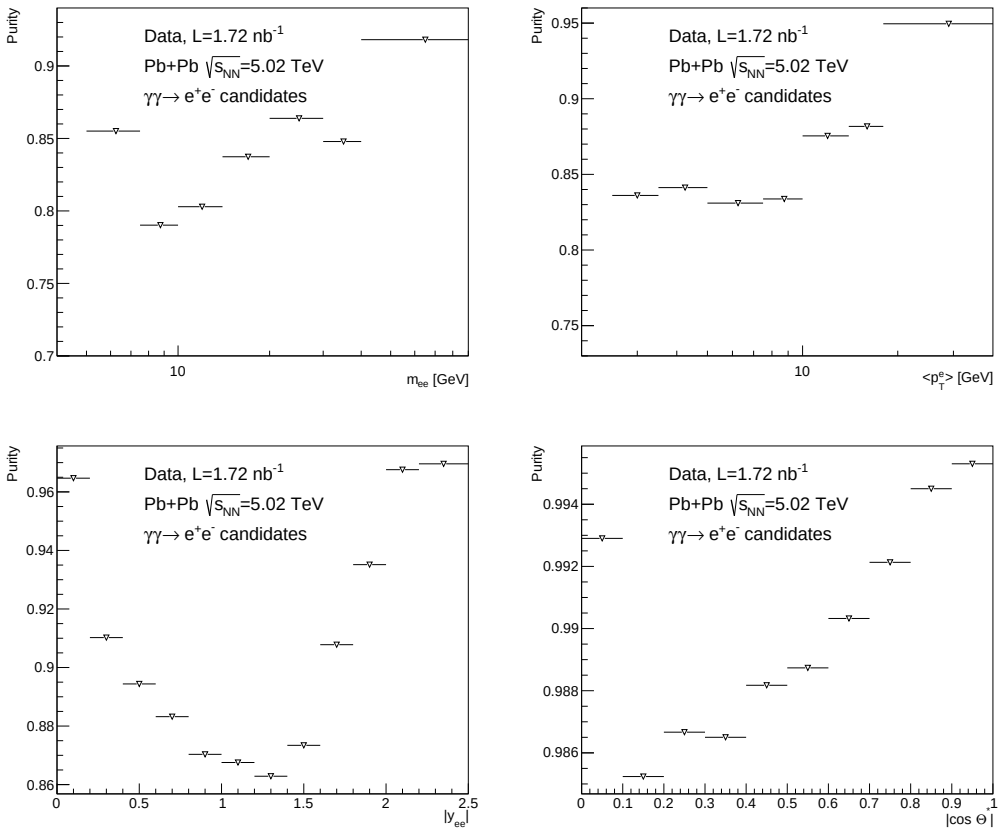

Figure 5.44: Purity of each bin of m_{ee} (top left), $\langle p_{\mathrm{T},e}\rangle$ (top right), $|y_{ee}|$ (bottom left), and $|\cos\theta^*|$ (bottom right) distributions.

F distribution as a function of $|y_{ee}|$ is slightly rises up to $|y_{ee}| = 1$ and falls for larger $|y_{ee}|$. The F distribution as a function of $|\cos\theta^*|$ is flat in the range of $|\cos\theta^*|$ between 0 and 0.7 and drops for higher values. To estimate the systematic uncertainty, the F factors are recalculated using values of electron scale factors, trigger efficiency, electron energy scale and resolution varied up/down by their uncertainties. The second column of Fig. 5.46 shows the relative systematic uncertainties related to the F factor determination for four considered variables. All variations are below 0.5%.

The estimated efficiency correction factors are presented in the third column of Fig. 5.46. They rise from 0.035 for the lowest m_{ee} to about 0.3 for the largest m_{ee}. A similar trend is observed for $\langle p_{\mathrm{T},e}\rangle$, where the CA values rise from 0.045 for the lowest $\langle p_{\mathrm{T},e}\rangle$ to 0.39 for the largest $\langle p_{\mathrm{T},e}\rangle$. The CA drop from about 0.12 for the lowest $|y_{ee}|$ down to 0.015 for the most forward events. For $|\cos\theta^*|$ close to 0 the estimated CA factor is 0.085, while for larger $|\cos\theta^*|$ it gets smaller, down to 0.04 for the largest $|\cos\theta^*|$.

The fourth column of Fig. 5.46 shows the breakdown of relative systematic uncertainties on the CA factor. The dominating source of systematic uncertainties, at the level of 10-15%, is related to variations of electron scale factors. The second most significant source of systematic uncertainties comes from trigger efficiency variations, typically around 2-3%, with larger values, up to 6% for the highest $|y_{ee}|$ bins.

For completeness the response matrices, fiducial corrections and efficiency corrections are also extracted for the 0n0n category. The differences with respect to the equivalents in the inclusive ZDC sample are minor.

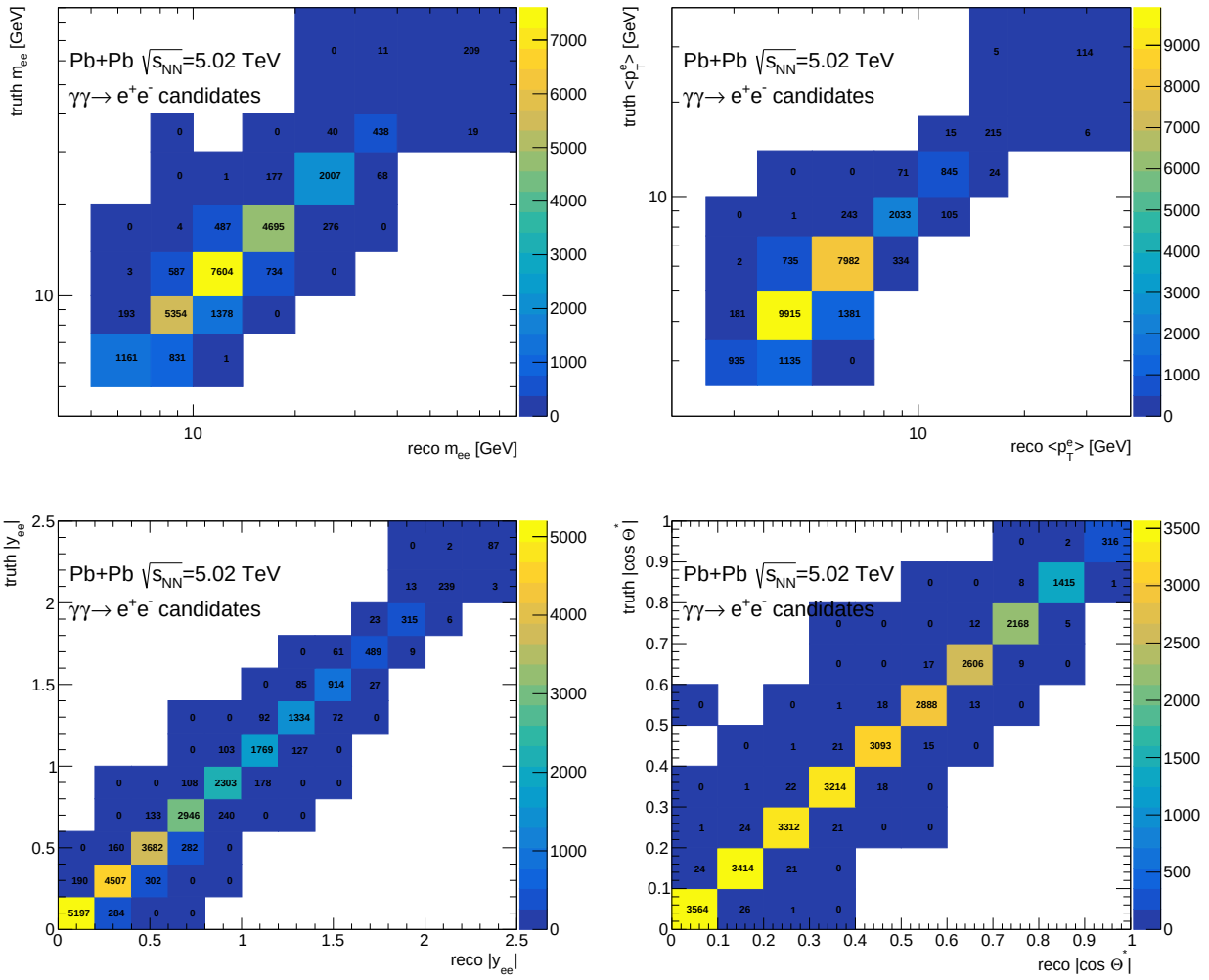

Figure 5.45: Response matrices for m_{ee} (top left), $\langle p_{\mathrm{T},e} \rangle$ (top right), $|y_{ee}|$ (bottom left) and $|\cos\theta^*|$ (bottom right) variables.

Cross-check of electron scale factor uncertainties

Since the uncertainty on electron scale factors dominates, an alternative approach with simplified uncertainties on electron scale factors derived by the ATLAS Egamma CP group for pp collisions is explored. The efficiencies provided by the Egamma CP are for electrons with p_{T} starting from 4.5 GeV. As a cross-check to uncertainties of scale factors, derived in this analysis, an attempt is made to use the uncertainties from the Egamma CP for electrons with p_{T} above 5 GeV. The scale factor for electron reconstruction efficiency for electrons with E_{T} between 4.5 GeV and 20 GeV is set at 1, with a 2% uncertainty in the barrel (defined by the electron cluster $|\eta|$ below 1.37) and a 5% uncertainty in the endcaps (defined by the electron cluster $|\eta|$ above 1.52). In pp collisions the identification efficiencies and scale factors are measured for the LooseAndBLayerLLH WP (no Loose or LHLoose available). Figure 5.47 presents an example of the total uncertainties on identification scale factors derived on the basis of 348197-364485 runs. Based on this histogram one can estimate the average uncertainty of 3% in the barrel and 5% in the endcap for the identification scale factors. This gives the estimated total uncertainty on scale factors of 3.6% in the barrel and 7.1% in the endcaps.

These fixed values are applied instead of the nominal uncertainties for electrons with p_{T} above 5 GeV, to verify if switching to official pp scale factors would improve the precision of

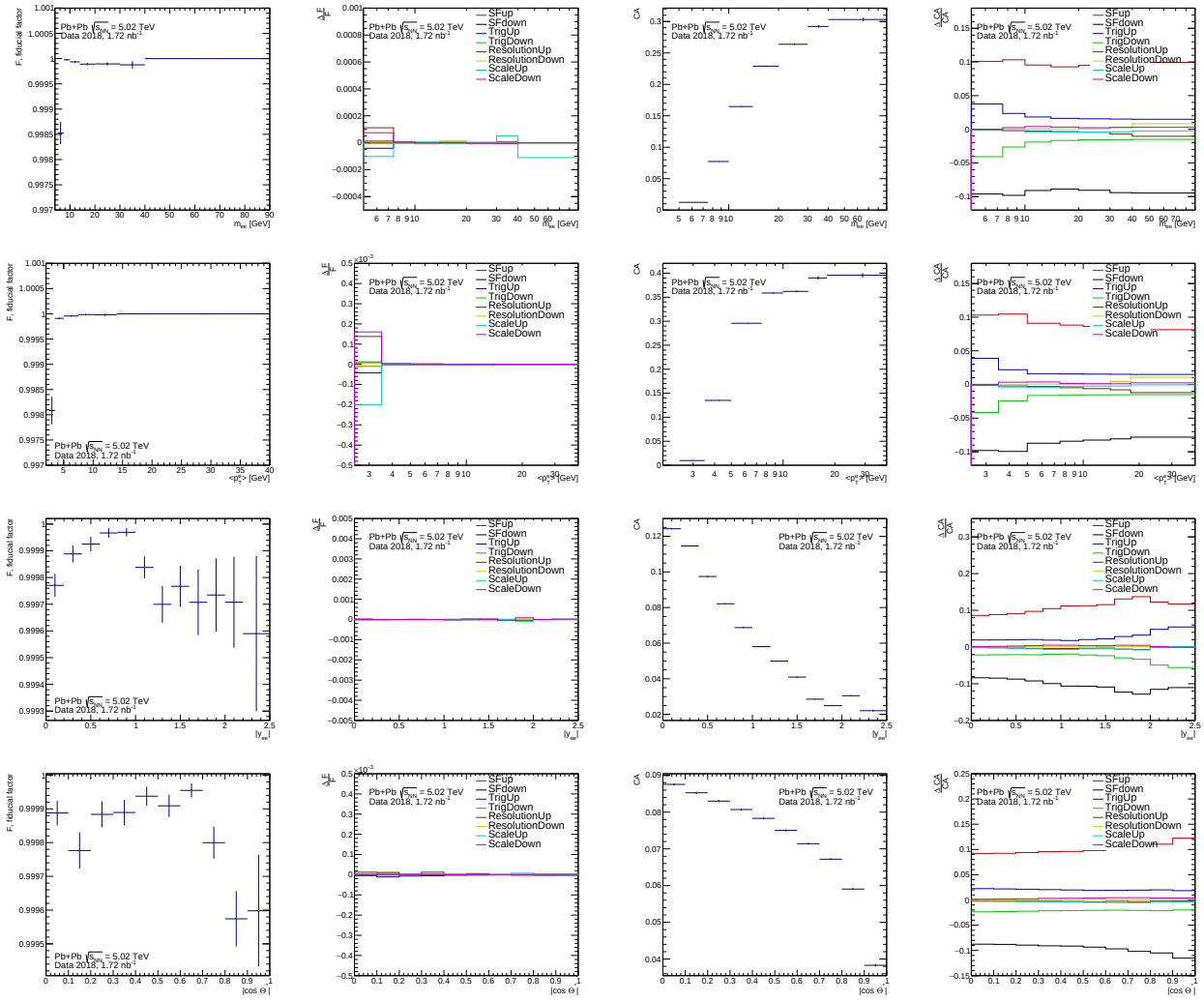

Figure 5.46: (From left to right) Fiducial and efficiency correction factors with a breakdown of systematic uncertainties as a function of m_{ee} (first row), $\langle p_{\mathrm{T},e} \rangle$ (second raw), $|y_{ee}|$ (third raw) and $|\cos\theta^*|$ (fourth raw).

exclusive dielectron measurement. In this cross-check, the central values of the scale factors and, for electrons with p_{T} below 5 GeV also their uncertainties, are the same as in the nominal result. Figure 5.48 shows the breakdown of uncertainties on the CA factor for the nominal result and using the fixed uncertainties discussed in this section. In general the effect of using the alternative scale factor uncertainties is mild. For the efficiency correction in m_{ee}, the uncertainties drop from 9-10% to 8-9%. In corrections as a function of $\langle p_{\mathrm{T},e} \rangle$, the uncertainties drop from 8-9% to 7-8% for $\langle p_{\mathrm{T},e} \rangle$ above 5 GeV. Little to no change is visible for small $|y_{ee}|$, the precision in the forward region is slightly improved. For the efficiency in $|\cos\theta^*|$, about 1% improvement is visible in the whole range. Since in general little to no improvement is observed and no uncertainties for electrons below 5 GeV are provided for electron PID WP by the ATLAS Egamma CP group, the scale factors with their uncertainties determined as described in Sec.5.2.1 were applied. These dedicated studies provided the results specific to the considered process.

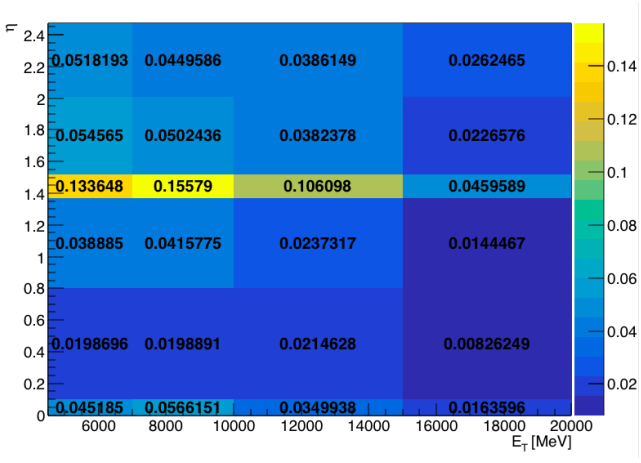

Figure 5.47: Total uncertainty on electron scale factors provided by the ATLAS Egamma CP group for LooseAndBLayerLLH electrons for 348197-364485 runs.

Systematic uncertainties on the unfolding

MC closure test

A closure test based on the signal MC samples is performed to verify the unfolding procedure. Events from the signal $\gamma\gamma \to e^+e^-$ samples are divided into two sub-samples with roughly equal statistics. The first sub-sample is used to fill the response matrices, while the second one is treated as a fake data set. Only the fiducial correction factor is applied in this test, so the unfolded yields are obtained. The unfolded distributions are compared with the available truth distributions. The resulting differences are treated as a non-closure uncertainty. Results of this non-closure test are shown in Fig. 5.49. The statistical uncertainties of unfolded distributions rise with the number of iterations. A total error over all bins is calculated as a total error $= \sigma\sqrt{(r_i - 1)^2 + (e_i/y_i)^2}$, where r_i is the ratio of the unfolded counts to truth counts in the i-th bin, e_i is the statistical error of the unfolded distribution in the i-th bin and y_i is the yield in the i-th bin of the unfolded distribution. For all variables the minimal total error is obtained for one iteration. Thus, for data unfolding only one iteration was used.

The same uncertainty from the closure test is applied for the inclusive and 0n0n results.

Data-driven closure test

To verify whether the unfolding procedure is stable with respect to the changes in shapes of the distributions in the simulated MC sample used in the unfolding procedure (given a non perfect agreement in shapes between data and signal MC, as seen in Fig. 5.38) a data-driven closure test is performed. The signal MC sample is reweighted (based on the truth values) by the data to STARLIGHT cross-section ratio (as derived in the bottom panels in Fig. 5.56). This approach provides the MC sample that describes the data. The reweighted sample is treated as fake data, i.e. its reco values are unfolded using the nominal F correction, response matrix and CA correction. The result of unfolding is compared with the reweighted truth distribution in Fig. 5.50. The observed non-closure is at the level of a few percent, and is included in the systematic uncertainty of the final measurement.

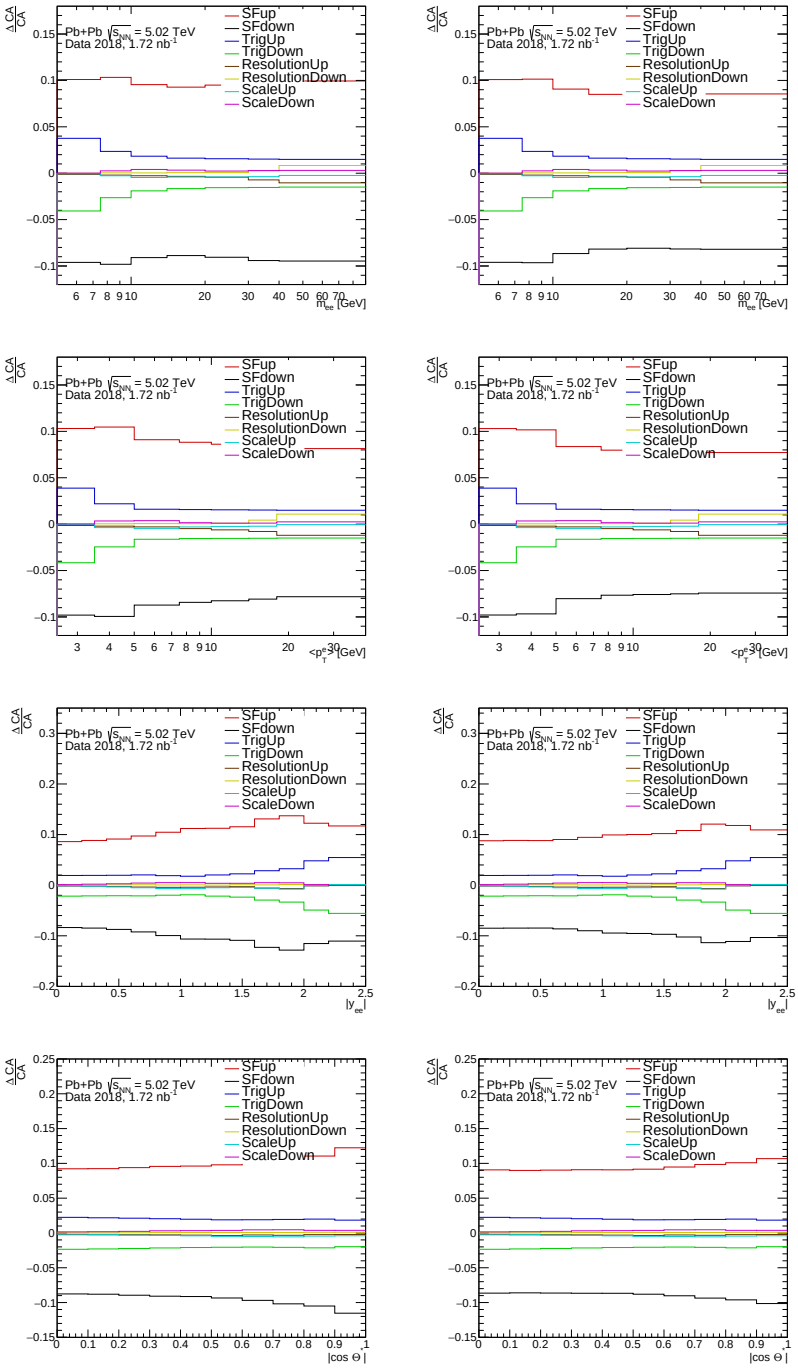

Figure 5.48: Breakdown of systematic uncertainties on the efficiency correction factors CA as a function of m_{ee}, $\langle p_{\mathrm{T},e} \rangle$, $|y_{ee}|$ and $|\cos\theta^*|$. The left column shows the relative uncertainty for the nominal electron scale factors , while in the right column shows the results of the cross-check with the fixed scale factor uncertainties for electrons with $p_{\mathrm{T}} > 5$ GeV.

Unfolding in two dimensions

As may be noticed from Fig. 5.41, there are some structures visible in the correlation plots of the unfolding variables, which may influence the final cross-section measurement. To verify this effect, a 2D unfolding procedure is performed, using also the F and CA corrections derived in 2D.

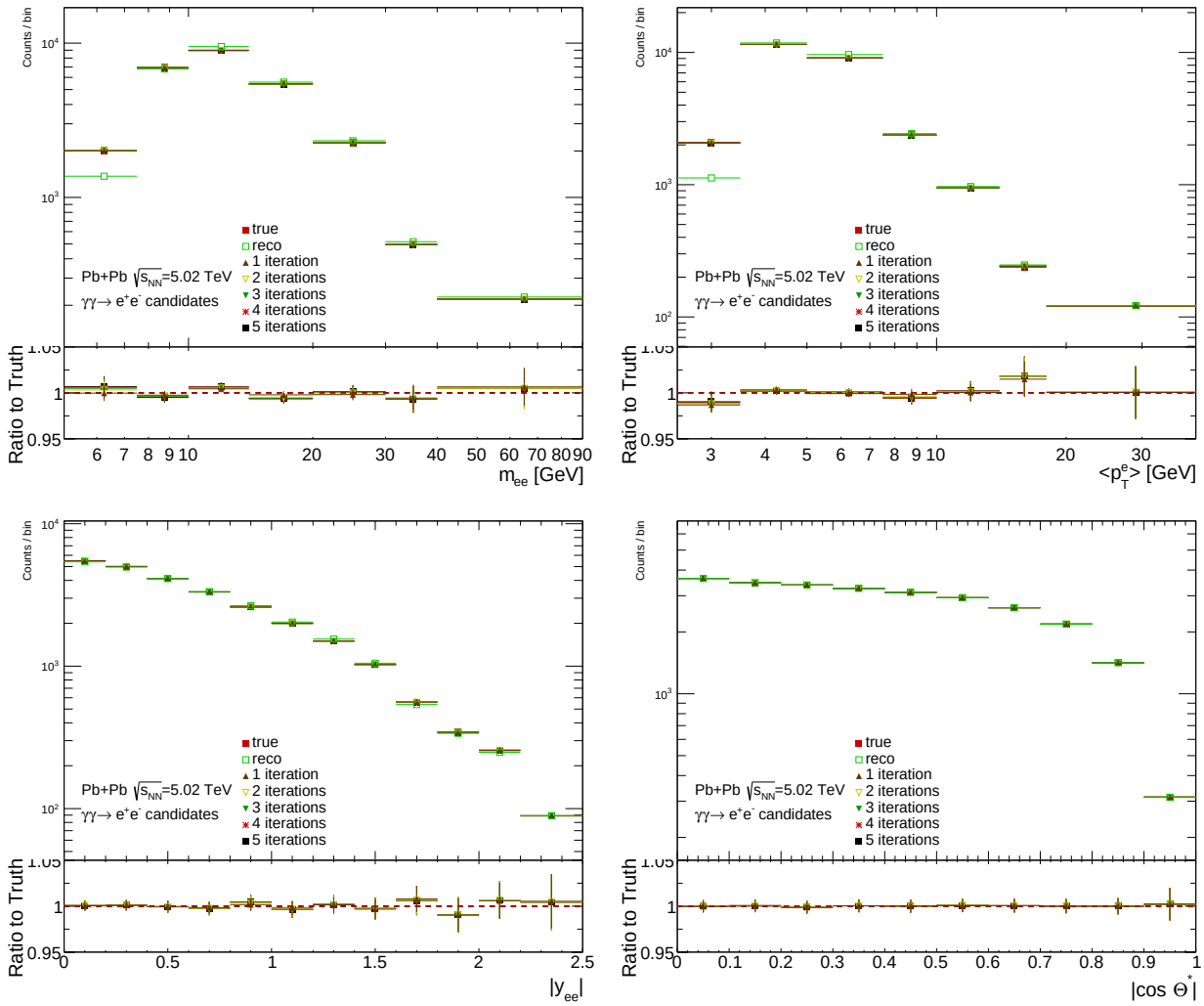

Figure 5.49: Split sample tests for m_{ee} (top left), $\langle p_{\mathrm{T},e} \rangle$ (top right), $|y_{ee}|$ (bottom left) and $|\cos\theta^*|$ (bottom right) variables. The top panels show the truth-level (full red squares), reconstructed-level (open green squares) and unfolded distributions obtained using various number of iterations: one iteration (full brown triangles), two iterations (open yellow triangles), three iterations (full green triangles), four iterations (red stars) and five iterations (full black squares). The bottom panels present ratios of unfolded distributions over truth distribution. The ratio of the unfolded distribution obtained with one iteration over truth distribution is taken as a non-closure. Error bars represent statistical uncertainties.

The data is unfolded in two dimensions with each unfolding variable versus three other unfolding variables individually. The statistics in the lowest m_{ee} and $\langle p_{\mathrm{T},e} \rangle$ bins are however low, what leads to large fluctuations of the final result in the 2D unfolding, when using the nominal binning on both axes. To confirm that the observed differences with respect to the nominal result are affected by a low number of events in the low $m_{ee}/\langle p_{\mathrm{T},e} \rangle$ region, the 2D unfolding procedure is also performed in the FR2. Only a few percent differences are observed with respect to the nominal result in the FR2. Therefore, to reduce the impact of a low number of events for the lowest masses in the FR1, the variables in the second dimension use a coarser binning: four bins in m_{ee} and $\langle p_{\mathrm{T},e} \rangle$, and three bins in $|y_{ee}|$ and $|\cos\theta^*|$. The bin edges in the second variable are listed in Table 5.8. The unfolded 2D differential cross-sections are projected into an X axis to get an one-dimensional result to be compared with the nominal one. This comparison is

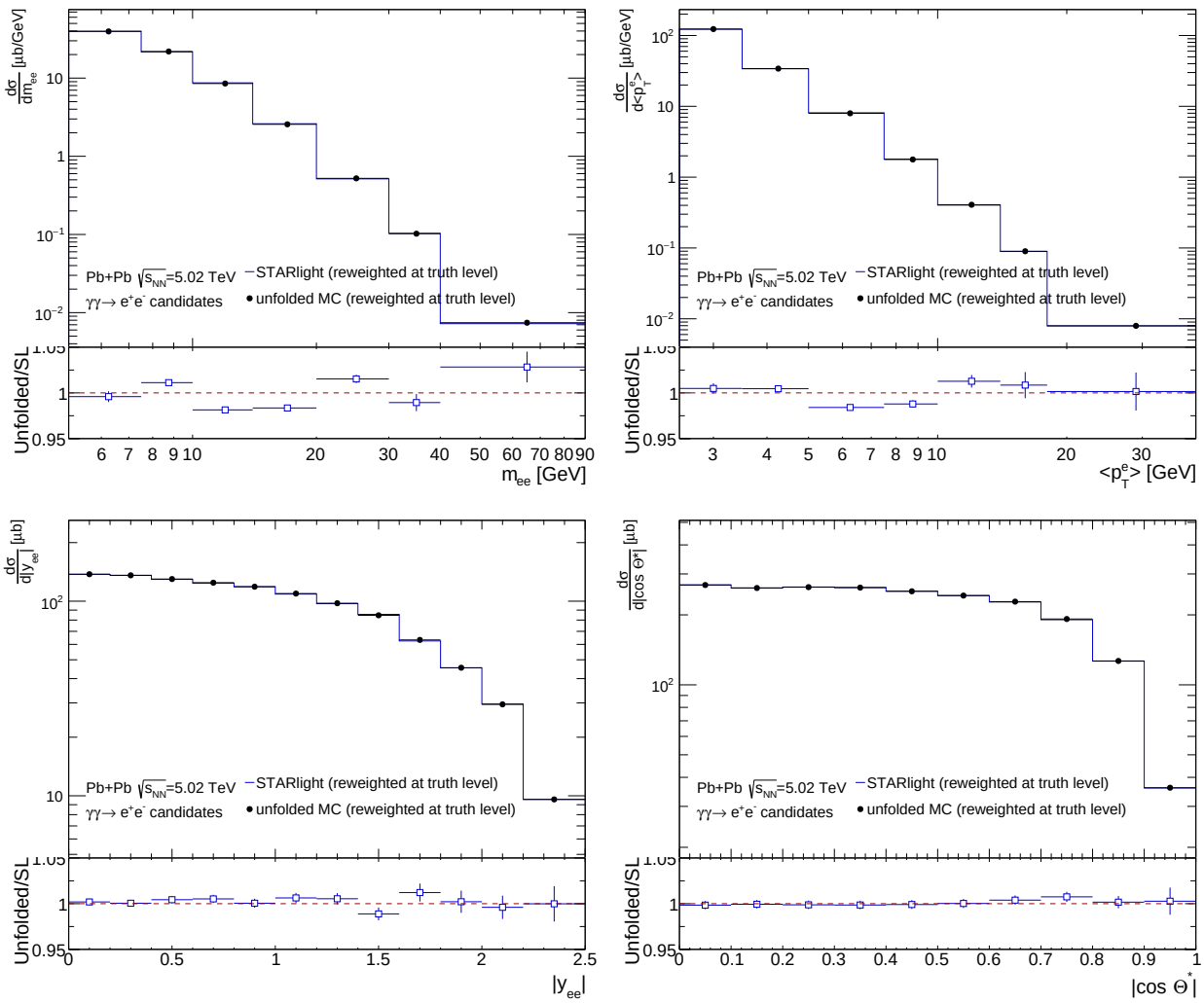

Figure 5.50: Results for data-driven closure test for m_{ee} (top left), $\langle p_{\mathrm{T},e} \rangle$ (top right), $|y_{ee}|$ (bottom left) and $|\cos\theta^*|$ (bottom right). The unfolded distributions of simulated events reweighted at truth level are shown by data points, while reweighted MC predictions are shown by blue histograms. Bottom panels show the ratio of the unfolded distributions over reweighted MC predictions, what corresponds to data-driven non-closure.

shown in Fig. 5.51–5.54. In each variable a few percent differences are observed, mostly within the 2–3% range, in some bins up to 5%. In each bin of the unfolded differential cross-sections, the largest up/down differences originating from the three two-dimensional unfolding results, are taken as a systematic uncertainty.

variable	bin edges
m_{ee}	5,15,30,60,90
$\langle p_{\mathrm{T},e} \rangle$	2.5,7,10,15,40
$\lvert y_{ee} \rvert$	0,0.6,2.0,2.5
$\lvert \cos\theta^* \rvert$	0,0.3,0.6,1.0

Table 5.8: Overview of binning for the second-dimension variable used in the 2D unfolding procedure.

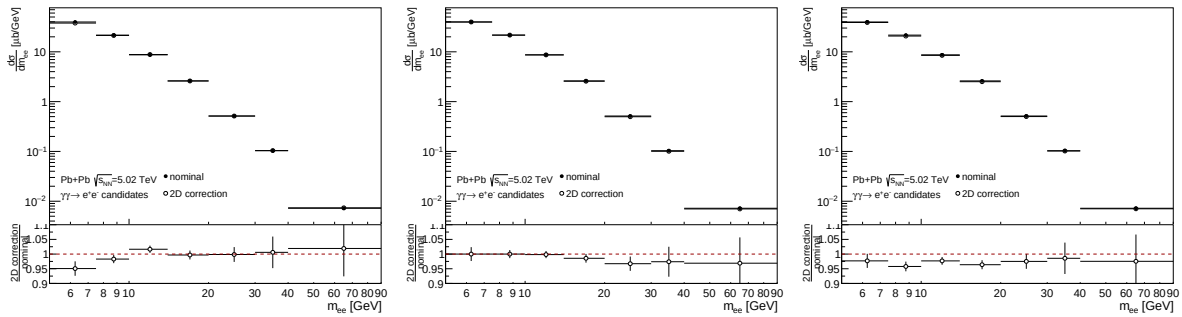

Figure 5.51: Comparison of differential cross-sections for the nominal 1D unfolding (full points) as a function of m_{ee} with the measurement for the 2D unfolding (open points) with a second dimension being $|y_{ee}|$ (left), $\langle p_{\mathrm{T},e} \rangle$ (middle) and $|\cos\theta^*|$ (right). The lower panels show the ratios of the 2D unfolding results projected into an X axis over the 1D nominal result.

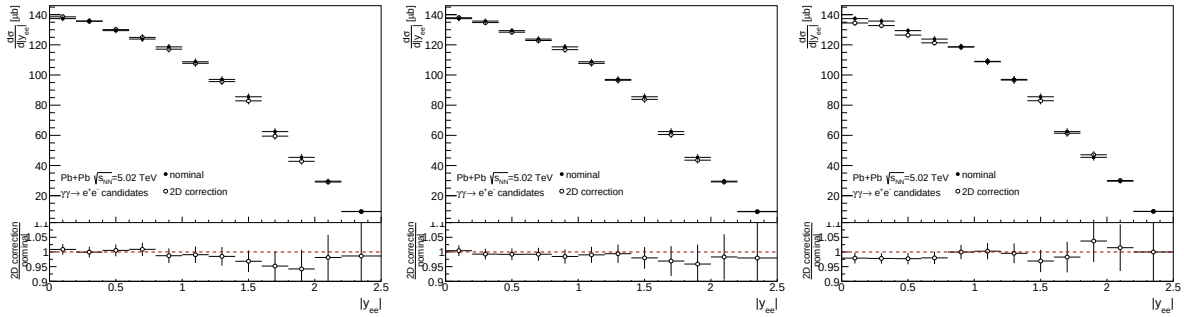

Figure 5.52: Comparison of differential cross-sections for the nominal 1D unfolding (full points) as a function of $|y_{ee}|$ with the measurement for the 2D unfolding (open points) with a second dimension being m_{ee} (left), $\langle p_{\mathrm{T},e} \rangle$ (middle) and $|\cos\theta^*|$ (right). The lower panels show the ratios of the 2D unfolding results projected into an X axis over the 1D nominal result.

Breakdown of systematic uncertainties

Individual systematic uncertainties listed in Sec. 5.6 are propagated to the final measurement. Figure 5.55 presents individual relative systematic uncertainties on the differential cross-sections. The electron energy scale and resolution contributions summed in quadrature are presented. The systematic uncertainty labelled as "unfolding method" includes uncertainties related to MC and data-driven non-closures and the 2D unfolding. For small $m_{ee}/\langle p_{\mathrm{T},e} \rangle$ the dominant systematic uncertainties come from electron scale factors (about 10%), while for high $m_{ee}/\langle p_{\mathrm{T},e} \rangle$ bins from background variations, other systematic uncertainties are mostly below 5%. In the differential cross-section as a function of $|y_{ee}|$, the dominant systematic uncertainties come from electron scale factors (from 7% up to 25% in some $|y_{ee}|$ bins), other systematic uncertainties are mostly below 5%. The systematic variations are more or less constant as a function of $|\cos\theta^*|$, with the largest contribution to the uncertainty from electron scale factors, at the level of 7-15%, while other systematic uncertainties are below 5%.

Independent studies of systematic uncertainties are also performed for the 0n0n category. The main sources of systematic uncertainties are identical to the inclusive measurement. However, there is an additional uncertainty related to the application of the alternative f_{0n0n} fractions for truth MC (discussed in Sec. 5.5).

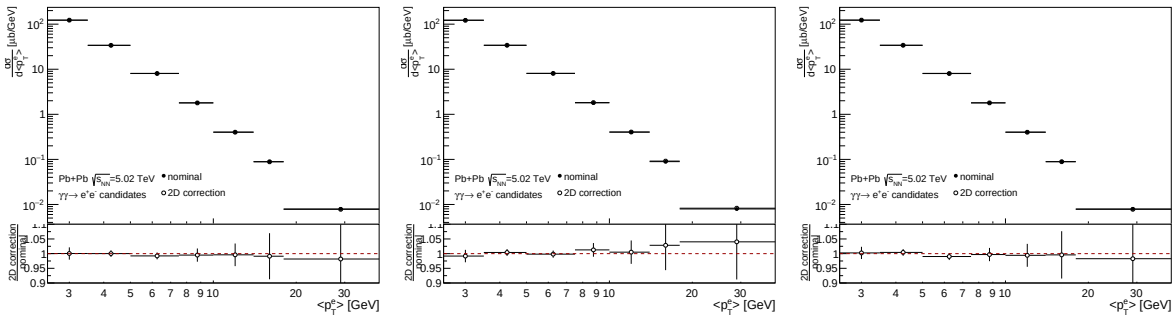

Figure 5.53: Comparison of differential cross-sections for the nominal 1D unfolding (full points) as a function of $\langle p_{\mathrm{T},e} \rangle$ with the measurement for the 2D unfolding (open points) with a second dimension being m_{ee} (left), $|y_{ee}|$ (middle) and $|\cos\theta^*|$ (right). The lower panels show the ratios of the 2D unfolding results projected into an X axis over the 1D nominal result.

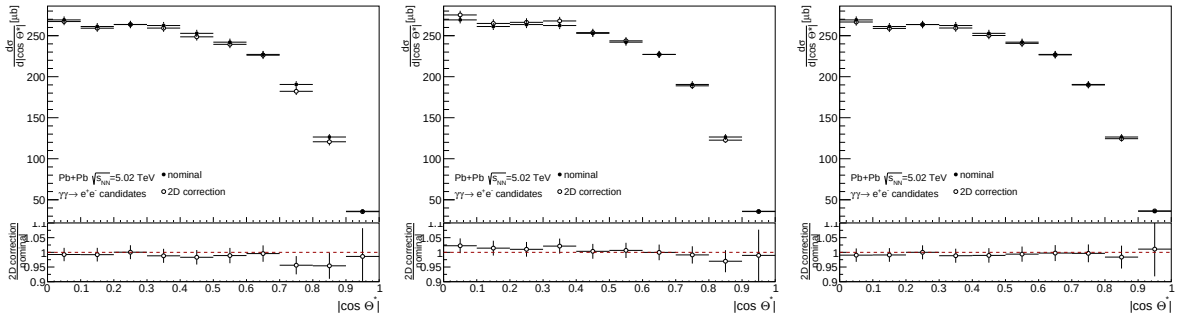

Figure 5.54: Comparison of differential cross-sections for the nominal 1D unfolding (full points) as a function of $|\cos\theta^*|$ with the measurement for the 2D unfolding (open points) with a second dimension being m_{ee} (left), $|y_{ee}|$ (middle) and $\langle p_{\mathrm{T},e} \rangle$ (right). The lower panels show the ratios of the 2D unfolding results projected into an X axis over the 1D nominal result.

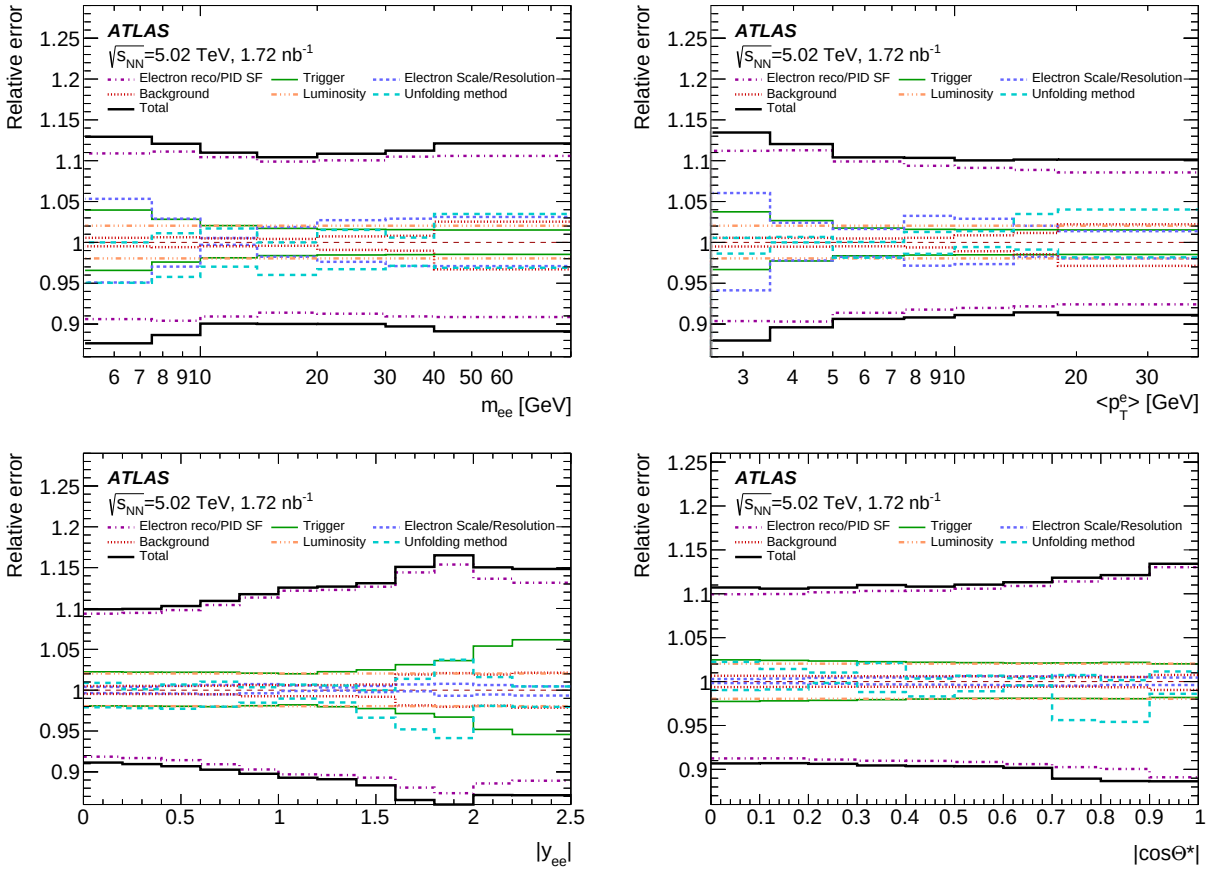

Figure 5.55: Breakdown of relative systematic uncertainties in the differential cross-section as a function of m_{ee} (top left), $\langle p_{\mathrm{T},e} \rangle$ (top right), $|y_{ee}|$ (bottom left) and $|\cos\theta^*|$ (bottom right). The contributions from electron reconstruction/PID scale factors (purple histograms), background (red histograms), trigger (green histograms), luminosity (orange histograms), electron energy scale and resolution (dark blue histograms) and unfolding method (light blue histograms) are shown. The total relative uncertainty is presented with black histograms.

Results of differential cross-sections

The differential cross-sections for exclusive dielectron production are presented as a function of m_{ee}, $\langle p_{\mathrm{T},e} \rangle$, $|y_{ee}|$ and $|\cos\theta^*|$ in Fig. 5.56. The results are corrected for detector efficiency and resolution effects, and are compared to STARLIGHT v3.13 and SUPERCHIC v3.05 predictions for the signal process. The corrections are performed with respect to the truth-level electrons before the FSR. In the cross-section measurement, the data after the kinematic selection of FR1 is used inclusively in the ZDC. The bottom panels on each plot show the ratio between the unfolded data and MC predictions. STARLIGHT underestimates the data by about 10% while SUPERCHIC is higher by the same amount. Both predictions have very similar shapes of all four distributions and tend to differ only in the absolute normalisation. Also the predictions describe the shape of the data pretty well except high $|y_{ee}|$ and high $|\cos\theta^*|$. The differences are mostly pronounced for m_{ee} between 10 and 20 GeV, $\langle p_{\mathrm{T},e} \rangle$ between 5 and 10 GeV. The ratio rises from about 1.1 to 1.2 when increasing $|y_{ee}|$ from 0 to 2.4. For $|\cos\theta^*|$ close to 0, the data to STARLIGHT ratio is largest, around 1.15, then it slowly falls down to about 1.05 for $|\cos\theta^*|$ equal to 0.8. The ratio falls more steeply in the last two bins of $|\cos\theta^*|$.

The differential cross-sections as a function of m_{ee}, $\langle p_{\mathrm{T},e} \rangle$, $|y_{ee}|$ and $|\cos\theta^*|$ for the 0n0n category are presented in Fig. 5.57. They are compared with the predictions from STARLIGHT v3.13 and SUPERCHIC v3.05 MC generators. Both simulated samples were produced inclusively and reweighted to the 0n0n category using the measured f_{0n0n} fractions in the inclusive data sample. Each theory prediction is represented by two curves reflecting the systematic variations on the measured 0n0n fractions. Also a dedicated prediction from STARLIGHT for the 0n0n category is shown in the same plots (labelled STARLIGHT 0n0n). This prediction is based on the STARLIGHT generator with the same settings as the nominal simulation samples, with one modification to the breakup mode setting (equal to 4 for the 0n0n category, equal to 5 for the inclusive case). That prediction matches well the shape of the inclusive STARLIGHT prediction corrected for the measured 0n0n fractions but is systematically lower by 2-3% for $|y_{ee}| < 1.4$. General conclusions from the comparison between MC predictions and data are consistent with the inclusive case. The agreement between data and their description by the calculation is better for lower $|y_{ee}|$ and $|\cos\theta^*|$ values. The SUPERCHIC prediction describes the shape of the $|y_{ee}|$ distribution in data better than the STARLIGHT prediction, which exhibits rising discrepancies with increasing $|y_{ee}|$.

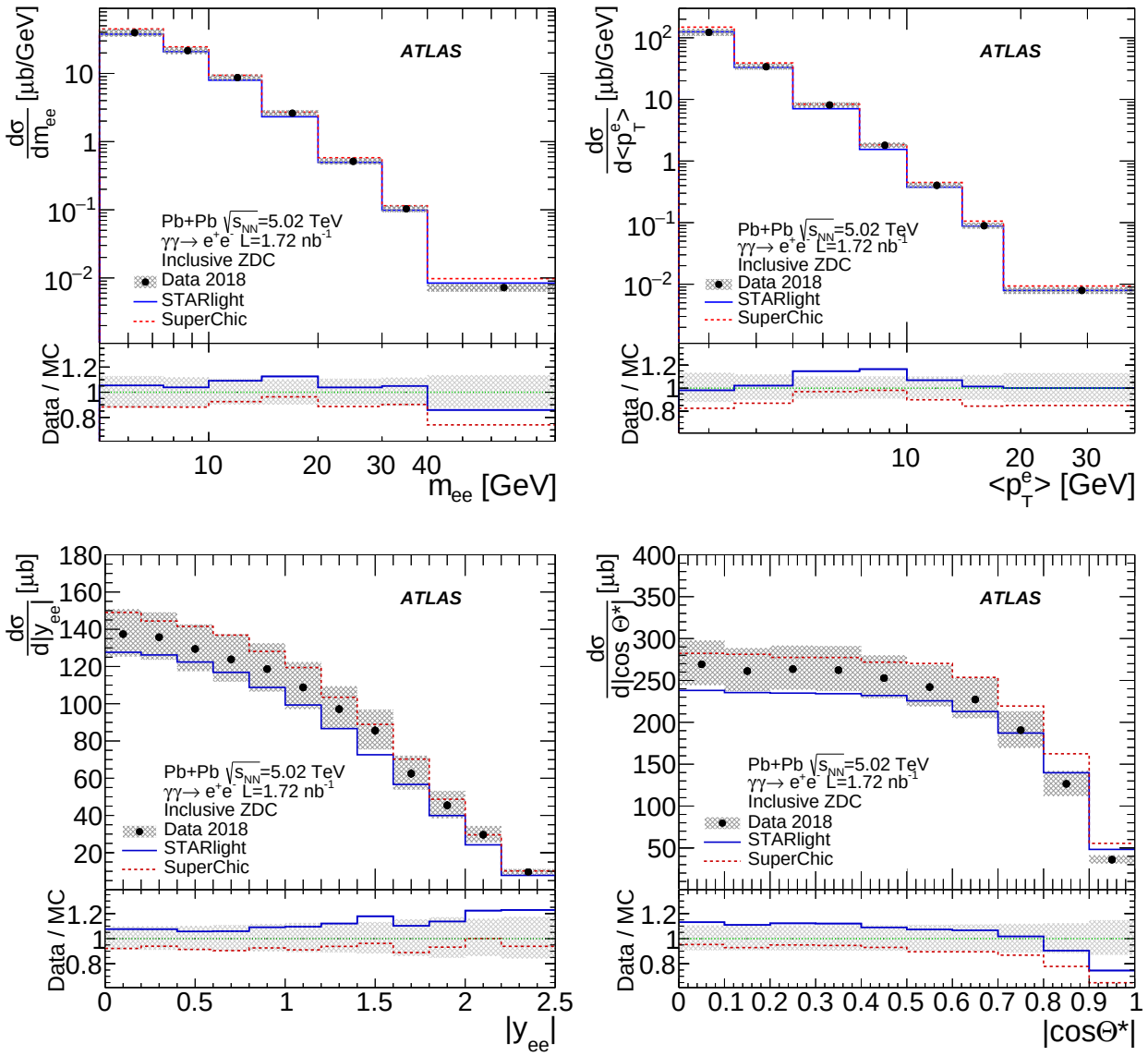

Figure 5.56: Differential cross-sections for exclusive dielectron production, $\gamma\gamma \to e^+e^-$, as a function of m_{ee}, $\langle p_{\mathrm{T},e} \rangle$, $|y_{ee}|$ and $|\cos\theta^*|$ for data (dots) and MC predictions from STARLIGHT (solid histogram) and SUPERCHIC (dashed histogram). The cross-sections are measured inclusive in the ZDC. Bottom panels present a ratio of data over MC predictions. The shaded area around unity represents a total uncertainty on the data.

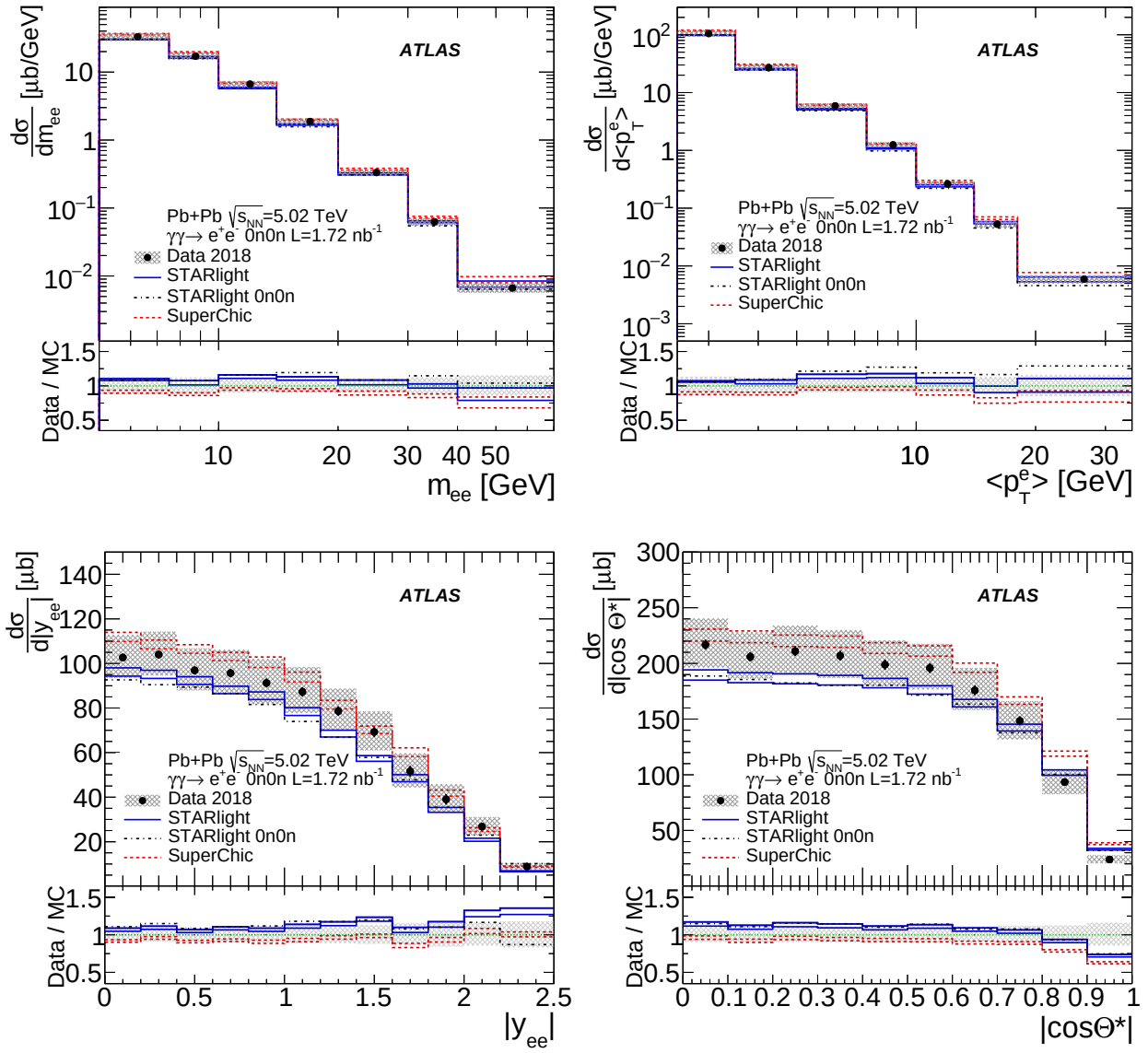

Figure 5.57: Differential cross-sections for exclusive dielectron production as a function of m_{ee}, $\langle p_{\mathrm{T},e} \rangle$, $|y_{ee}|$ and $|\cos\theta^*|$. The cross-sections are measured for the 0n0n category and compared to MC predictions from STARLIGHT v3.13 (solid) and SUPERCHIC v3.05 (dashed) represented by two lines reflecting systematic variations on $f_{0\mathrm{n}0\mathrm{n}}$. Also a dedicated prediction from STARLIGHT for the 0n0n category is shown (labelled STARLIGHT 0n0n). A ratio panel shows data over predictions. The grey band around unity represents the total uncertainty on the data.

Chapter 6

Light-by-light scattering

This chapter summarises the measurement of the light-by-light scattering performed using 2.2 $\text{nb}^{-1}$of UPC Pb+Pb collision data recorded in 2015 and 2018 by the ATLAS detector. This measurement benefits from trigger performance optimisations performed by the author of this thesis, discussed in Sec. 4.3. In particular, thanks to the significant improvement in the trigger efficiency at low photon E_{T}, the analysis could cover the photon E_{T} region extended by 0.5 GeV, down to $E_{\text{T}} = 2.5\,\text{GeV}$, with respect to the evidence measurement from the ATLAS Collaboration discussed in Ref. [38].

6.1 Diphoton event selection

In the 2015 Pb+Pb data taking, diphoton events were recorded using the dedicated trigger chain, `HLT_gg_upc_L1TE5_VTE200`, which required total E_{T} between 5 and 200 GeV in the entire calorimeter at the L1, maximum one hit in the inner ring of the MBTS detector, and a maximum number of 10 hits in the pixel detector. In the 2018 Pb+Pb run, diphoton events were recorded using the same trigger as for dielectrons, as discussed in Sec. 4.3.1.

The typical features of the LbyL scattering event can be identified in the event display of one UPC Pb+Pb collision from the ATLAS detector, presented in Fig. 6.1. The two energy deposits in EM calorimeter are shown as green clusters, exhibiting the back-to-back topology of signal photons. No tracks with p_{T} above 100 MeV nor other activity in the detector are present.

The event selection required presence of two identified electrons. A dedicated neural network based photon identification was developed to maintain the constant 95% efficiency as a function of η with respect to good-quality reconstructed photons. Additionally, selected photons are required to pass the following kinematic selection:

- two photons with $E_{\text{T}} > 2.5$ GeV and $|\eta| < 2.37$, excluding the calorimeter transition region $1.37 < |\eta| < 1.52$
- diphoton invariant mass, $m_{\gamma\gamma}$, greater than 5 GeV,
- veto on charged-particle tracks (with $p_{\text{T}} > 100$ MeV, $|\eta| < 2.5$, at least one hit in the pixel detector and at least six silicon hits in total)
- no tracks with $p_{\text{T}} > 50$ MeV, $|\eta| < 2.5$, and at least three hits in the pixel detector, which were reconstructed on the basis of the information only from the pixel detector,
- transverse momentum of the diphoton system ($p_{\text{T}}^{\gamma\gamma}$) is required to be below 1 GeV for $m_{\gamma\gamma} < 12$ GeV and below 2 GeV for $m_{\gamma\gamma} > 12$ GeV,
- diphoton acoplanarity below 0.01.

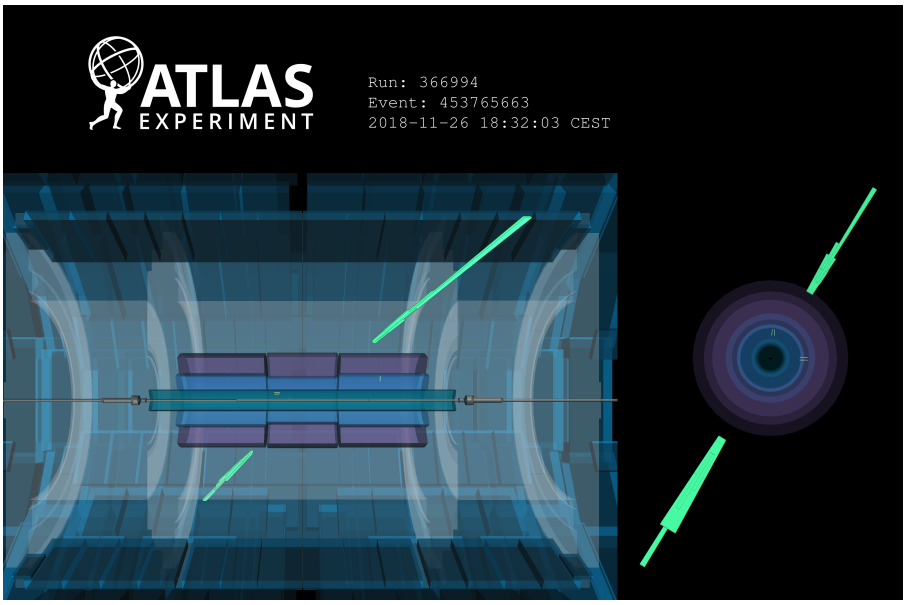

Figure 6.1: Event display for an exclusive $\gamma\gamma \to \gamma\gamma$ candidate. Event 453765663 from run 366994 recorded on 26th of November 2018 at 18:32:03 is shown. Two back-to-back photons ($E_{\mathrm{T}}^{\gamma_1} = 11\,\mathrm{GeV}$ and $E_{\mathrm{T}}^{\gamma_1} = 10\,\mathrm{GeV}$) with an invariant mass of 29 GeV, acoplanarity of 0.002, diphoton transverse momentum of 1.2 GeV and no additional activity in the detector are presented. All calorimeter cells with various E_{T} thresholds are shown: $E_{\mathrm{T}} > 400\,\mathrm{MeV}$ for EM barrel, EM endcaps and Tile, $E_{\mathrm{T}} > 800\,\mathrm{MeV}$ for hadronic endcaps, and $E_{\mathrm{T}} > 1000\,\mathrm{MeV}$ for FCal. All charged-partice tracks with $p_{\mathrm{T}} > 100\,\mathrm{MeV}$ are shown.

The two main background sources for the LbyL scattering are exclusive dielectron production, $\gamma\gamma \to e^+e^-$, and CEP, $gg \to \gamma\gamma$, discussed in Sec. 2.6. The first is estimated using a fully data-driven approach, while the latter using MC template fitting in the control region defined by the diphoton selected events with reversed acoplanarity requirement (acoplanarity above 0.01). In this approach, the CEP background template is obtained from SuperChic v3.0 MC simulation. The CEP sample is normalised such that in the control region the data yield equals the sum of contributions from signal, and $\gamma\gamma \to e^+e^-$ and CEP backgrounds.

Photon kinematic distributions for events satisfying above mentioned selection criteria are shown in Fig. 6.2. In total, 97 events are observed in the combined 2015+2018 data set where 45 signal events and 27 background events are expected.

6.2 Integrated and differential cross-sections for LbyL scattering

The cross-section for the $\gamma\gamma \to \gamma\gamma$ process is measured in a fiducial phase space, defined by the following requirements on the diphoton final state, reflecting the selection at reconstruction level: both photons have to be within $|\eta| < 2.4$ with a transverse energy of $E_{\mathrm{T}} > 2.5$ GeV. The invariant mass of the diphoton system has to be $m_{\gamma\gamma} > 5$ GeV with a transverse momentum of $p_{\mathrm{T}}^{\gamma\gamma} < 1$ GeV. In addition, the photons must be back-to-back, i.e. fulfil an acoplanarity requirement of $\alpha < 0.01$. Experimentally, the fiducial cross-section is given by

$$\sigma_{\mathrm{fid}} = \frac{N_{\mathrm{data}} - N_{\mathrm{bkg}}}{C \times \int L dt}\,, \tag{6.1}$$

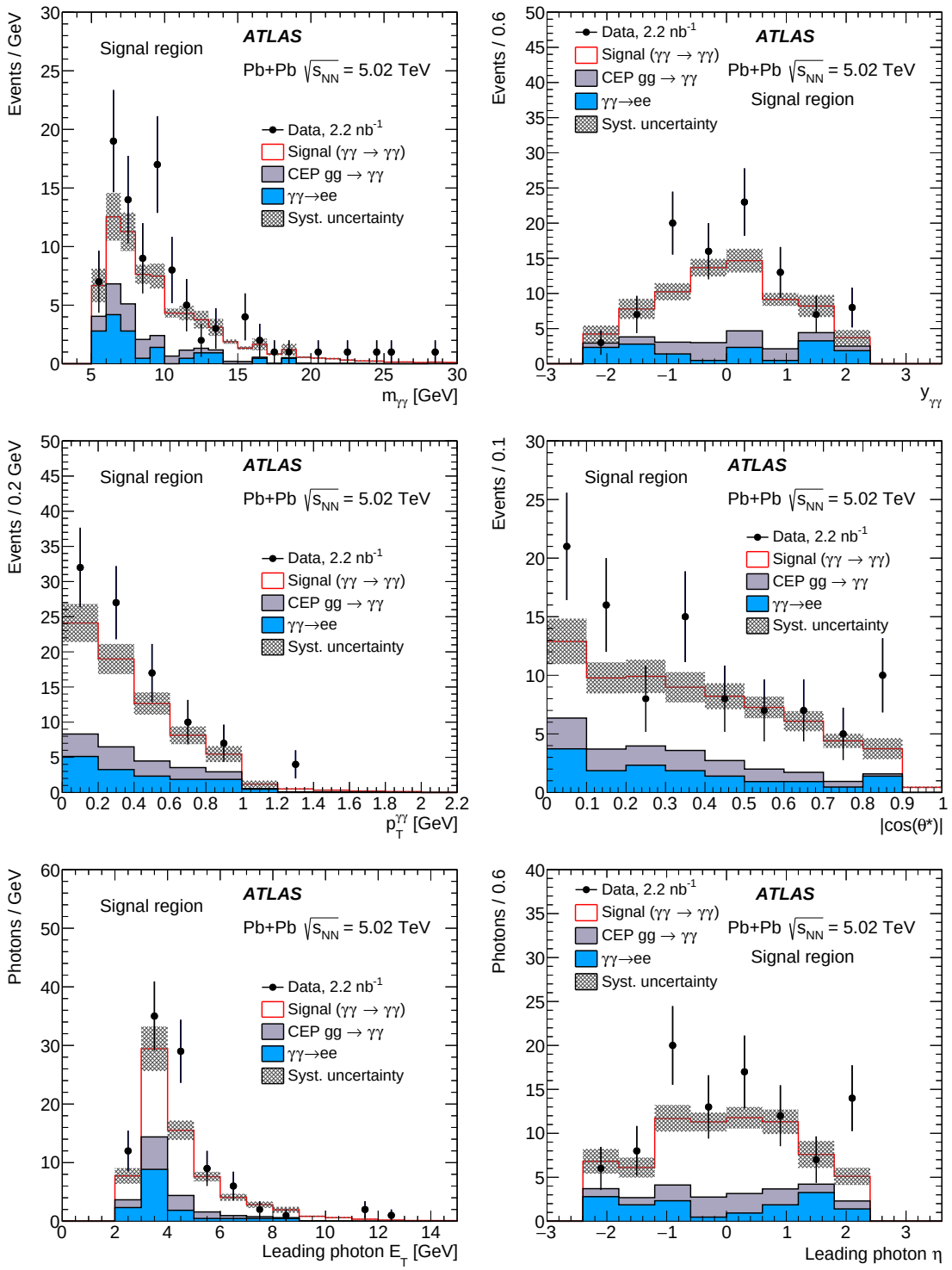

Figure 6.2: Detector-level kinematic distributions for $\gamma\gamma \to \gamma\gamma$ event candidates for the 2015+2018 data: diphoton invariant mass (top-left), diphoton rapidity (top-right), diphoton transverse momentum (mid-left), diphoton $|\cos\theta^*|$ (mid-right) leading photon transverse energy (bottom-left) and leading photon pseudorapidity (bottom-left). Data (points) are compared to the sum of signal and background expectations (histograms). Systematic uncertainties on the signal and background processes, excluding that on the luminosity, are denoted as shaded bands.

Source of uncertainty	Detector correction (C)
	0.263
Trigger efficiency	5%
Photon reco. efficiency	4%
Photon PID efficiency	2%
Photon energy scale	1%
Photon energy resolution	2%
Photon angular resolution	2%
Alternative signal MC	1%
Signal MC statistics	1%
Total	8%

Table 6.1: The detector correction factor, C, and its uncertainties.

where $N_{\text{data}} = 97$ is the number of selected events in data, $N_{\text{bkg}} = 27 \pm 5$ is the number of background events, $\int L dt = 2.22 \pm 0.07$ nb^{-1} is the integrated luminosity of the 2015+2018 data sample and C is the overall correction factor that accounts for efficiencies and resolution effects. The C factor is defined as the ratio of the number of reconstructed MC signal events passing the selection to the number of generated MC signal events satisfying the fiducial requirements. This factor includes the acceptance correction, i.e. corrects also for the exclusion of the calorimeter transition region. The value of C is found to be: $C = 0.263 \pm 0.021$. The main source of the inefficiency is due to the trigger and photon reconstruction inefficiencies. An overview of the various uncertainties on C is given in Table 6.1.

The measured fiducial cross-section is $\sigma_{\text{fid}} = 120 \pm 17$ (stat.) ± 13 (syst.) ± 4 (lumi.) nb, which can be compared to the predicted values of 80 ± 8 nb from Ref. [62] and 78 ± 8 nb from SuperChic v3.0 MC simulation.

The differential cross-sections are unfolded to truth level in the fiducial phase space to correct for bin migrations due to detector resolution effects. They are determined using an iterative Bayesian unfolding method with one iteration for $m_{\gamma\gamma}$, $|y_{\gamma\gamma}|$, $\langle p_{\text{T},\gamma} \rangle$ and $|\cos\theta^*|$ distributions. In Fig. 6.3 the differential cross-sections are compared to predictions from SuperChic v3.0. Except for the overall normalisation differences these predictions give a good description of the data. A total uncertainty of the measured cross-sections is dominated by the statistical uncertainty. The main source of systematic uncertainties originates from the background estimation uncertainty, which is driven by a limited number of events in the control regions.

6.3 ALP search

As part of the LbyL measurement, a search for axion-like particles (ALP) is performed. The ALPs couple directly to photons, therefore they can be produced in the $\gamma\gamma \to a \to \gamma\gamma$ reaction, where a denotes the ALP. Their presence can be detected as a narrow resonance in the diphoton invariant mass distribution. The $m_{\gamma\gamma}$ distribution, presented in top left panel of Fig.6.2, is used in this analysis for ALP search. Events for the ALP signal are generated using Starlight for multiple ALP masses (m_a) ranging between 5 and 100 GeV. The contributions from the LbyL, exclusive dielectron production and central exclusive diphoton production are considered as background in the ALP search. The two latter sources of background are estimated using the same data-driven methods, as in the LbyL measurement. The contribution from the LbyL process is estimated using events generated by the SuperChic v3.0 MC generator.

The mass search bins are chosen to contain at least 80% of a reconstructed ALP signal peak,

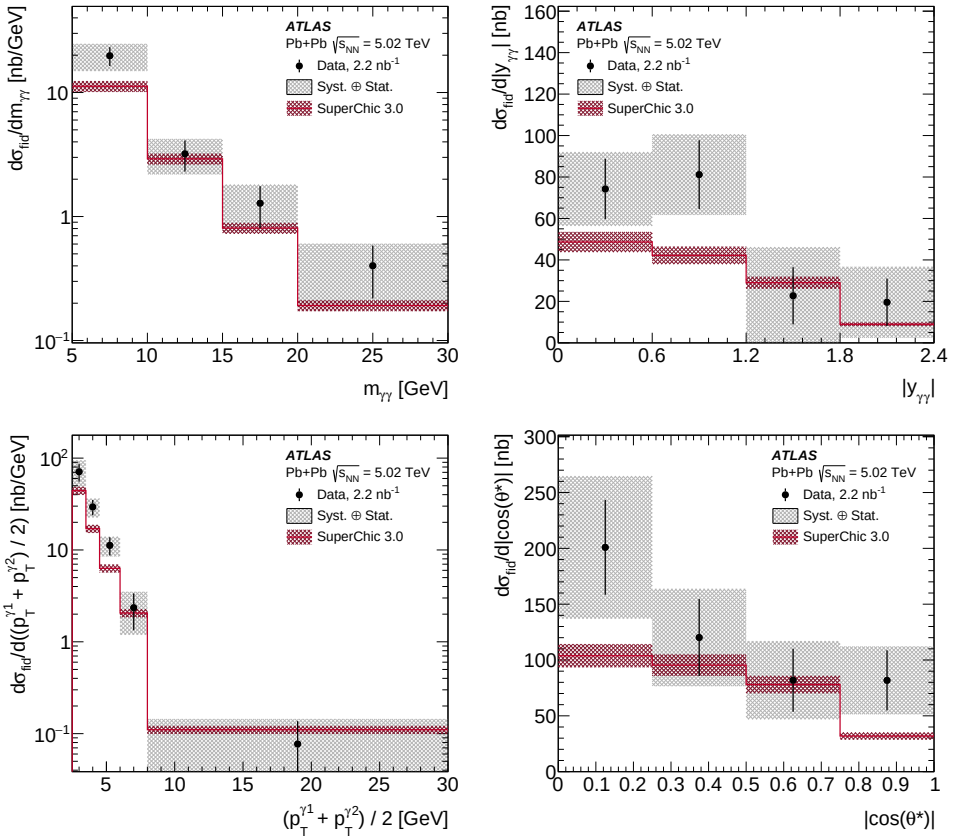

Figure 6.3: Measured differential cross-sections for $\gamma\gamma \to \gamma\gamma$ scattering as a function of four observables (from left to right and top to bottom): diphoton invariant mass, diphoton rapidity, leading photon transverse momentum, leading photon pseudorapidity and diphoton $|\cos\theta^*|$. The measured cross-section values are shown as points with error bars giving the statistical uncertainty and grey bands indicating the size of the total uncertainty. The results are compared with the prediction from SuperChic v3.0 MC generator (red line) with red bands denoting theoretical uncertainties.

and have different widths, ranging from 2 to 20 GeV. The bins overlap, so that the distance between subsequent bin centres is equal to 1 GeV. The diphoton mass distribution from the simulated LbyL sample is normalised to the number of events in data after subtraction of the $\gamma\gamma \to e^+e^-$ and CEP $\gamma\gamma \to \gamma\gamma$ contributions and excluding the mass search region. For every bin, the ALP contribution is fitted individually using a maximum-likelihood fit implemented in the HistFitter software [108–110] which is based on HistFactory [111], RooFit [103] and RooStats [112].

No significant deviation from the background-only hypothesis is observed. Therefore, the result is used to estimate the upper limit on the ALP cross-section and coupling constant between the ALP and the photon, $1/\Lambda_a$ at 95% confidence level, presented on the left and right of Fig. 6.4, respectively. The comparison of the limits on $1/\Lambda_a$ obtained in this analysis with results from other experiments is presented in Fig. 6.5. In the mass range of $6 < m_a < 100$ GeV, this measurement sets the most stringent limits to date.

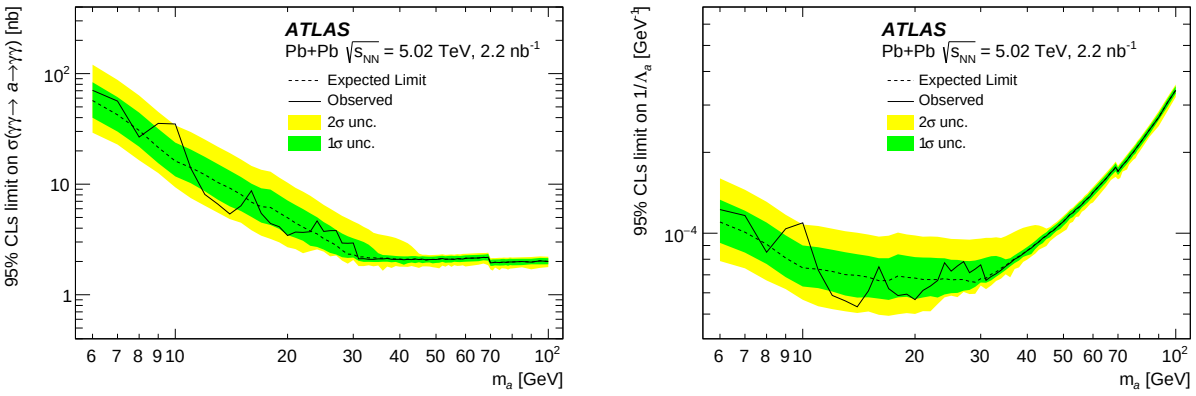

Figure 6.4: The 95% CL upper limit on the ALP cross-section $\sigma_{\gamma\gamma\to a\to\gamma\gamma}$ (left) and ALP coupling $1/\Lambda_a$ (right) for the $\gamma\gamma \to a \to \gamma\gamma$ process as a function of ALP mass m_a. The observed upper limit is shown as a solid black line and the expected upper limit is shown by the dashed black line with its ± 1 and ± 2 standard deviation bands. The discontinuity at $m_a = 70$ GeV is caused by the increase of the mass-bin width which brings an increase in signal acceptance.

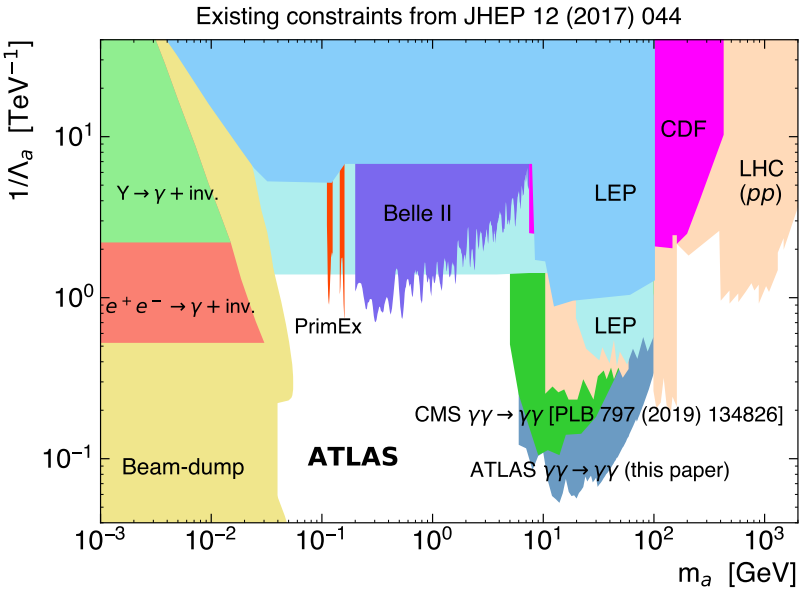

Figure 6.5: Compilation of exclusion limits at 95% CL in the ALP–photon coupling ($1/\Lambda_a$) versus ALP mass (m_a) plane obtained by different experiments. The existing limits, derived from Refs. [41, 113–116] are compared with the limits extracted from this measurement. The exclusion limits labelled "LHC (pp)" are based on pp collision data from ATLAS and CMS.

Chapter 7

Conclusions and outlook

7.1 Conclusion

The ultraperipheral collisions of heavy ions provide a tool to study a variety of physics processes induced by photons. The two examples, the exclusive production of electron-positron pairs and light-by-light scattering, measured in Pb+Pb collisions at $\sqrt{s_{\mathrm{NN}}} = 5.02$ TeV recorded by the ATLAS experiment at the LHC, are presented in this thesis. The triggering strategy for those processes is discussed in detail, as it provides one of the main challenges for the measurements.

The trigger selection requirements were optimised in preparation to the 2018 heavy-ion data taking in ATLAS, taking advantage of the improved calorimeter noise settings as well as a novel approach in defining low energy electromagnetic clusters at the hardware level. The software level trigger selection was also developed, based on studies of the detector performance. A large set of supporting triggers was designed and implemented which resulted in a collection of a relative large $\gamma\gamma \to e^+e^-$ sample for trigger performance studies. The trigger efficiency for the 2018 diphoton triggers was measured and compared with the efficiency of the trigger used in the 2015 data taking. A factor of 2-3 increase in the trigger efficiency was achieved in the low energy region which resulted in the extended kinematic coverage for photons and electrons with $p_{\mathrm{T}} > 2.5$ GeV.

The measurement of cross-sections for exclusive dielectron production, $\gamma\gamma \to e^+e^-$, was performed using 1.72 nb^{-1}of ultraperipheral Pb+Pb collision data at $\sqrt{s_{\mathrm{NN}}} = 5.02$ TeV recorded by the ATLAS detector at the LHC. The event yields were corrected for background contributions, detector efficiency and acceptance losses. The backgrounds from dissociative processes, Upsilon decays to dielectrons and exclusive production of τ pairs were evaluated and subtracted. The contribution from the first source of background was estimated using a fit to the acoplanarity distribution. As a fit result, the signal (modelled with Starlight +Pythia8) and background (modelled with SuperChic +Pythia8) fractions were obtained. The interface with Pythia8 was performed to account for the QED showering. The contributions from $\gamma\gamma \to e^+e^-$ and $\gamma\gamma \to \tau^+\tau^-$ processes were estimated using the MC simulations from Starlight +Pythia8. After all corrections, the differential cross-sections for $\gamma\gamma \to e^+e^-$ process in the fiducial region (defined by $p^e_{\mathrm{T}} > 2.5$ GeV, $|\eta_e| < 2.5$, $m_{ee} > 5$ GeV, and $p_{\mathrm{T},ee} < 2$ GeV requirements) are presented as a function of m_{ee}, $\langle p_{\mathrm{T},e} \rangle$, $|y_{ee}|$ and $|\cos\theta^*|$. The results are compared with the prediction from Starlight and SuperChic. The two predictions differ mainly in the overall normalisations. In general a good agreement is found in shapes of the distributions, however some systematic differences occur. In particular, the data and Starlight prediction discrepancy rises with higher $|y_{ee}|$, what was also seen in the dimuon measurement discussed in Ref. [57]. This can be explained by the fact that photon flux modelling in Starlight assumes that photon-photon interactions must not occur for impact parameters smaller than twice the

nucleus radius. Allowing such interactions may improve the data to prediction agreement, what is confirmed by the flat ratio of data over the SuperChic prediction. The differential cross-sections were also measured in the sample with a requirement of no forward neutron activity. The data to prediction agreement is at the similar level as for the inclusive sample. The preliminary results of this analysis were approved for the Quark Matter 2022 conference [117], and the publication with final results was submitted to JHEP [93]. The author of this thesis was a leading analyser and editor of the publication.

The light-by-light scattering was measured using 2.2 $\text{nb}^{-1}$of ultraperipheral Pb+Pb collision data at $\sqrt{s_{\text{NN}}} = 5.02$ TeV recorded by the ATLAS detector at the LHC. After background subtraction and analysis corrections, the fiducial cross-section of the $\gamma\gamma \to \gamma\gamma$ process for photon transverse momentum, $E_{\text{T}} > 2.5$ GeV, photon pseudorapidity, $|\eta| < 2.4$, invariant mass of the diphoton system, $m_{\gamma\gamma} > 5$ GeV, diphoton transverse momentum, $p_{\text{T}}^{\gamma\gamma} < 1$ GeV and diphoton acoplanarity below 0.01 was measured to be $\sigma_{\text{fid}} = 120 \pm 17$ (stat.) ± 13 (syst.) ± 4 (lumi.) nb. This value is in agreement with the predictions from the Standard Model. Also differential cross-sections were measured as a function of kinematic and angular variables of the final-state photons: $m_{\gamma\gamma}$, $|y_{\gamma\gamma}|$, $\langle p_{\text{T},\gamma} \rangle$ and $|\cos\theta^*|$, and are compared with theory predictions. All measured cross-sections are consistent within two standard deviations with the predictions.

The measured diphoton invariant mass distribution was used to set new exclusion limits on the production of axion-like particles with decays to $\gamma\gamma$. To date, the derived exclusion limits are best over the mass range of $6 < m_{\gamma\gamma} < 100$ GeV. Therefore, with this measurement heavy-ion data proved to be competitive to searches with high-luminosity pp data at the LHC.

The results of the LbyL measurement and axion-like particle search were published by the ATLAS Collaboration in Ref. [40]. The author of this thesis is a leading contributor to the publication.

7.2 Outlook

The upcoming Run-3 (spanning 2022-2024) brings new opportunities for the UPC physics programme at the LHC. The expected increase in the total integrated luminosity makes possible to improve the sensitivity for some Beyond Standard Model processes, not only using the light-by-light process, but for example also searches for magnetic monopoles, dark photons or lepton flavour violating processes [118, 119].

Naturally, the larger integrated luminosity is going to reduce the statistical uncertainties, what is the dominant source of uncertainty in case of the rare processes such as light-by-light scattering. Additionally, many performance measurements were also limited by the statistical precision, e.g. L1 trigger efficiency or electron/photon reconstruction and identification studies. These would also benefit from the increased luminosity and could be determined more precisely. Another improvement which could be envisaged is an optimisation of the low-energy photon reconstruction algorithm in ATLAS. In Run 2, the $p_{\text{T}} = 2.5 - 5$ GeV region was affected by the low photon/electron reconstruction efficiency. This resulted in a limited precision of the electron scale factors which turned out to be a dominant uncertainty in the $\gamma\gamma \to e^+e^-$ measurement. Dedicated optimisation of the photon/electron reconstruction and identification would allow more precise measurements in the low-p_{T} region. Likely also double differential cross-section measurements could be possible for $\gamma\gamma \to \ell^+\ell^-$ processes.

The exclusive dimuon events were used to constrain the uncertainty on the photon flux in the measurement of the τ-lepton anomalous magnetic moment in $\gamma\gamma \to \tau^+\tau^-$ events, with at least one τ decaying in the muon channel, recently published by ATLAS [37]. This measurement could be extended to cover ditau events with one of τ decaying in the electron channel. The photon flux uncertainty then could be constrained by the exclusive dielectron cross-sections

measured in this thesis. Since the τ-lepton anomalous magnetic moment measurement was limited by the statistical precision, it would also profit from the increased integrated luminosity of future Pb+Pb data taking at the LHC.

Last but not least, the ZDC detector underwent a major upgrade during the last Long Shutdown (2019-2021), and will provide more granularity in triggering configurations of forward neutron activity in future heavy-ion data taking. That offers a possibility to improve the strategy to collect high-quality data with the supporting triggers for the trigger efficiency studies, which suffered from strong bandwidth limitations in the 2018 Pb+Pb run.

Bibliography

[1] C. N. Yang and R. L. Mills. "Conservation of Isotopic Spin and Isotopic Gauge Invariance". In: *Phys. Rev.* 96 (1954). Ed. by Jong-Ping Hsu and D. Fine, pp. 191–195. DOI: 10.1103/PhysRev.96.191.

[2] S. L. Glashow. "Partial Symmetries of Weak Interactions". In: *Nucl. Phys.* 22 (1961), pp. 579–588. DOI: 10.1016/0029-5582(61)90469-2.

[3] A. Salam and J. C. Ward. "Electromagnetic and weak interactions". In: *Phys. Lett.* 13 (1964), pp. 168–171. DOI: 10.1016/0031-9163(64)90711-5.

[4] S. Weinberg. "A Model of Leptons". In: *Phys. Rev. Lett.* 19 (1967), pp. 1264–1266. DOI: 10.1103/PhysRevLett.19.1264.

[5] A. Salam. "Weak and Electromagnetic Interactions". In: *Conf. Proc. C* 680519 (1968), pp. 367–377. DOI: 10.1142/9789812795915_0034.

[6] P. W. Higgs. "Broken symmetries, massless particles and gauge fields". In: *Phys. Lett.* 12 (1964), pp. 132–133. DOI: 10.1016/0031-9163(64)91136-9.

[7] F. Englert and R. Brout. "Broken Symmetry and the Mass of Gauge Vector Mesons". In: *Phys. Rev. Lett.* 13 (1964). Ed. by J. C. Taylor, pp. 321–323. DOI: 10.1103/PhysRevLett.13.321.

[8] G. S. Guralnik, C. R. Hagen, and T. W. B. Kibble. "Global Conservation Laws and Massless Particles". In: *Phys. Rev. Lett.* 13 (1964). Ed. by J. C. Taylor, pp. 585–587. DOI: 10.1103/PhysRevLett.13.585.

[9] M. Gell-Mann. "A Schematic Model of Baryons and Mesons". In: *Phys. Lett.* 8 (1964), pp. 214–215. DOI: 10.1016/S0031-9163(64)92001-3.

[10] G. Zweig. "An SU(3) model for strong interaction symmetry and its breaking. Version 2". In: *Developments in the quark theory of hadrons. Vol. 1. 1964 - 1978*. Ed. by D. B. Lichtenberg and Simon Peter Rosen. Feb. 1964, pp. 22–101.

[11] O. W. Greenberg. "Spin and Unitary Spin Independence in a Paraquark Model of Baryons and Mesons". In: *Phys. Rev. Lett.* 13 (1964), pp. 598–602. DOI: 10.1103/PhysRevLett.13.598.

[12] D. J. Gross and F. Wilczek. "Ultraviolet Behavior of Nonabelian Gauge Theories". In: *Phys. Rev. Lett.* 30 (1973). Ed. by J. C. Taylor, pp. 1343–1346. DOI: 10.1103/PhysRevLett.30.1343.

[13] H. D. Politzer. "Reliable Perturbative Results for Strong Interactions?" In: *Phys. Rev. Lett.* 30 (1973). Ed. by J. C. Taylor, pp. 1346–1349. DOI: 10.1103/PhysRevLett.30.1346.

[14] ATLAS Collaboration. *Standard Model Summary Plots February 2022*. ATL-PHYS-PUB-2022-009. URL: http://cds.cern.ch/record/2804061.

[15] LHCb Collaboration. "Centrality determination in heavy-ion collisions with the LHCb detector". In: *Journal of Instrumentation* 17.05 (May 2022), P05009. DOI: 10.1088/1748-0221/17/05/p05009. URL: https://doi.org/10.1088/1748-0221/17/05/p05009.

[16] ATLAS Collaboration. "Observation of a Centrality-Dependent Dijet Asymmetry in Lead–Lead Collisions at $\sqrt{s_{\mathrm{NN}}} = 2.76\,\mathrm{TeV}$ with the ATLAS Detector at the LHC". In: *Phys. Rev. Lett.* 105 (2010), p. 252303. DOI: 10.1103/PhysRevLett.105.252303. arXiv: 1011.6182 [hep-ex].

[17] ATLAS Collaboration. *Heavy Ion Public Results*. URL: https://atlas.web.cern.ch/Atlas/GROUPS/PHYSICS/PLOTS/HION-2015-001/.

[18] E. Fermi. "Über die Theorie des Stoßes zwischen Atomen und elektrisch geladenen Teilchen". In: *Zeitschrift für Physik* 29.1 (1924), pp. 315–327. DOI: 10.1007/BF03184853. URL: https://doi.org/10.1007/BF03184853.

[19] C. F. v. Weizsäcker. "Ausstrahlung bei Stößen sehr schneller Elektronen". In: *Zeitschrift für Physik* 88.9 (1934), pp. 612–625. DOI: 10.1007/BF01333110. URL: https://doi.org/10.1007/BF01333110.

[20] A. Baltz et al. "The physics of ultraperipheral collisions at the LHC". In: *Physics Reports* 458.1-3 (Mar. 2008), pp. 1–171. DOI: 10.1016/j.physrep.2007.12.001.

[21] G. Baur et al. "Coherent $\gamma\gamma$ and γA interactions in very peripheral collisions at relativistic ion colliders". In: *Physics Reports* 364.5 (July 2002), pp. 359–450. DOI: 10.1016/s0370-1573(01)00101-6.

[22] C. A. Bertulani, S. R. Klein, and J. Nystrand. "Physics of ultra-peripheral nuclear collisions". In: *Annual Review of Nuclear and Particle Science* 55.1 (2005), pp. 271–310. DOI: 10.1146/annurev.nucl.55.090704.151526. eprint: https://doi.org/10.1146/annurev.nucl.55.090704.151526. URL: https://doi.org/10.1146/annurev.nucl.55.090704.151526.

[23] S. R. Klein and P. Steinberg. "Photonuclear and Two-Photon Interactions at High-Energy Nuclear Colliders". In: *Annual Review of Nuclear and Particle Science* 70.1 (2020), pp. 323–354. DOI: 10.1146/annurev-nucl-030320-033923. eprint: https://doi.org/10.1146/annurev-nucl-030320-033923. URL: https://doi.org/10.1146/annurev-nucl-030320-033923.

[24] L. A. Harland-Lang, V. A. Khoze, and M. G. Ryskin. "Exclusive LHC physics with heavy ions: SuperChic 3". In: *Eur. Phys. J.* C79.1 (2019), p. 39. DOI: 10.1140/epjc/s10052-018-6530-5. arXiv: 1810.06567 [hep-ph].

[25] S. R. Klein et al. "STARlight: A Monte Carlo simulation program for ultra-peripheral collisions of relativistic ions". In: *Comput. Phys. Commun.* 212 (2017), pp. 258–268. DOI: 10.1016/j.cpc.2016.10.016. arXiv: 1607.03838 [hep-ph].

[26] L. A. Harland-Lang et al. "A new approach to modelling elastic and inelastic photon-initiated production at the LHC: SuperChic 4". In: *Eur. Phys. J. C* 80.10 (2020), p. 925. DOI: 10.1140/epjc/s10052-020-08455-0. arXiv: 2007.12704 [hep-ph].

[27] A. J. Baltz et al. "Two-photon interactions with nuclear breakup in relativistic heavy ion collisions". In: *Physical Review C* 80.4 (Oct. 2009). DOI: 10.1103/physrevc.80.044902.

[28] I. A. Pshenichnov et al. "Mutual heavy ion dissociation in peripheral collisions at ultra-relativistic energies". In: *Physical Review C* 64.2 (July 2001). DOI: 10.1103/physrevc.64.024903.

[29] A. J. Baltz, M. J. Rhoades-Brown, and J. Weneser. "Heavy-ion partial beam lifetimes due to Coulomb induced processes". In: *Phys. Rev. E* 54 (4 Oct. 1996), pp. 4233–4239. DOI: 10.1103/PhysRevE.54.4233. URL: https://link.aps.org/doi/10.1103/PhysRevE.54.4233.

[30] M. L. Miller et al. "Glauber Modeling in High-Energy Nuclear Collisions". In: *Annual Review of Nuclear and Particle Science* 57.1 (Nov. 2007), pp. 205–243. DOI: 10.1146/annurev.nucl.57.090506.123020.

[31] S. R. Klein and J. Nystrand. "Exclusive vector meson production in relativistic heavy ion collisions". In: *Physical Review C* 60.1 (June 1999). DOI: 10.1103/physrevc.60.014903.

[32] L. A. Harland-Lang, V. A. Khoze, and M. G. Ryskin. "Exclusive physics at the LHC with SuperChic 2". In: *Eur. Phys. J.* C76.1 (2016), p. 9. DOI: 10.1140/epjc/s10052-015-3832-8. arXiv: 1508.02718 [hep-ph].

[33] G. Breit and J. A. Wheeler. "Collision of Two Light Quanta". In: *Phys. Rev.* 46 (12 1934), pp. 1087–1091. DOI: 10.1103/PhysRev.46.1087.

[34] ALICE Collaboration. "Coherent J/ψ and ψ' photoproduction at midrapidity in ultra-peripheral Pb-Pb collisions at $\sqrt{s_{\rm NN}} = 5.02$ TeV". In: *Eur. Phys. J. C* 81.8 (2021), p. 712. DOI: 10.1140/epjc/s10052-021-09437-6. arXiv: 2101.04577 [nucl-ex].

[35] M. Dyndał et al. "Anomalous electromagnetic moments of τ lepton in $\gamma\gamma \to \tau^+\tau^-$ reaction in Pb+Pb collisions at the LHC". In: *Physics Letters B* 809 (2020), p. 135682. ISSN: 0370-2693. DOI: https://doi.org/10.1016/j.physletb.2020.135682.

[36] L. Beresford and J. Liu. "New physics and tau $g-2$ using LHC heavy ion collisions". In: *Phys. Rev. D* 102 (11 Dec. 2020), p. 113008. DOI: 10.1103/PhysRevD.102.113008. URL: https://link.aps.org/doi/10.1103/PhysRevD.102.113008.

[37] ATLAS Collaboration. *Observation of the $\gamma\gamma \to \tau\tau$ process in Pb+Pb collisions and constraints on the τ-lepton anomalous magnetic moment with the ATLAS detector*. 2022. DOI: 10.48550/arxiv.2204.13478. URL: https://arxiv.org/abs/2204.13478.

[38] ATLAS Collaboration. "Evidence for light-by-light scattering in heavy-ion collisions with the ATLAS detector at the LHC". In: *Nature Phys.* 13.9 (2017), pp. 852–858. DOI: 10.1038/nphys4208. arXiv: 1702.01625 [hep-ex].

[39] ATLAS Collaboration. "Observation of light-by-light scattering in ultraperipheral Pb+Pb collisions with the ATLAS detector". In: *Phys. Rev. Lett.* 123.5 (2019), p. 052001. DOI: 10.1103/PhysRevLett.123.052001. arXiv: 1904.03536 [hep-ex].

[40] ATLAS Collaboration. "Measurement of light-by-light scattering and search for axion-like particles with 2.2 nb^{-1} of Pb+Pb data with the ATLAS detector". In: *JHEP* 11 (2021), p. 050. DOI: 10.1007/JHEP11(2021)050. arXiv: 2008.05355 [hep-ex].

[41] CMS Collaboration. "Evidence for light-by-light scattering and searches for axion-like particles in ultraperipheral PbPb collisions at $\sqrt{s_{\rm NN}} = 5.02$ TeV". In: *Phys. Lett. B* 797 (2019), p. 134826. DOI: 10.1016/j.physletb.2019.134826. arXiv: 1810.04602 [hep-ex].

[42] H1 Collaboration. "Muon pair production in ep collisions at HERA". In: *Physics Letters B* 583.1 (2004), pp. 28–40. ISSN: 0370-2693. DOI: https://doi.org/10.1016/j.physletb.2004.01.003. URL: https://www.sciencedirect.com/science/article/pii/S037026930400084X.

[43] CDF Collaboration. "Observation of Exclusive Electron-Positron Production in Hadron-Hadron Collisions". In: *Phys. Rev. Lett.* 98 (11 Mar. 2007), p. 112001. DOI: 10.1103/PhysRevLett.98.112001. URL: https://link.aps.org/doi/10.1103/PhysRevLett.98.112001.

[44] CDF Collaboration. "Search for Exclusive Z-Boson Production and Observation of High-Mass $p\overline{p} \to p\gamma\gamma\overline{p} \to pl^+l^-\overline{p}$ Events in $p\overline{p}$ Collisions at $\sqrt{s} = 1.96$ TeV". In: *Phys. Rev. Lett.* 102 (22 June 2009), p. 222002. DOI: 10.1103/PhysRevLett.102.222002. URL: https://link.aps.org/doi/10.1103/PhysRevLett.102.222002.

[45] CDF Collaboration. "Observation of Exclusive Charmonium Production and $\gamma\gamma \to \mu^+\mu^-$ in $p\overline{p}$ Collisions at $\sqrt{s} = 1.96$ TeV". In: *Phys. Rev. Lett.* 102 (24 June 2009), p. 242001. DOI: 10.1103/PhysRevLett.102.242001. URL: https://link.aps.org/doi/10.1103/PhysRevLett.102.242001.

[46] ATLAS Collaboration. "Measurement of exclusive $\gamma\gamma \to \ell^+\ell^-$ production in proton-proton collisions at $\sqrt{s} = 7$ TeV with the ATLAS detector". In: *Phys. Lett. B* 749 (2015), pp. 242–261. DOI: 10.1016/j.physletb.2015.07.069. arXiv: 1506.07098 [hep-ex].

[47] CMS Collaboration. "Exclusive photon-photon production of muon pairs in proton-proton collisions at $\sqrt{s} = 7$ TeV". In: *JHEP* 01 (2012), p. 052. DOI: 10.1007/JHEP01(2012)052. arXiv: 1111.5536 [hep-ex].

[48] CMS Collaboration. "Search for Exclusive or Semi-Exclusive Photon Pair Production and Observation of Exclusive and Semi-Exclusive Electron Pair Production in pp Collisions at $\sqrt{s} = 7$ TeV". In: *JHEP* 11 (2012), p. 080. DOI: 10.1007/JHEP11(2012)080. arXiv: 1209.1666 [hep-ex].

[49] ATLAS Collaboration. "Measurement of the exclusive $\gamma\gamma \to \mu^+\mu^-$ process in proton-proton collisions at $\sqrt{s} = 13$ TeV with the ATLAS detector". In: *Phys. Lett. B* 777 (2018), pp. 303–323. DOI: 10.1016/j.physletb.2017.12.043. arXiv: 1708.04053 [hep-ex].

[50] ATLAS Collaboration. "Observation and Measurement of Forward Proton Scattering in Association with Lepton Pairs Produced via the Photon Fusion Mechanism at ATLAS". In: *Phys. Rev. Lett.* 125.26 (2020), p. 261801. DOI: 10.1103/PhysRevLett.125.261801. arXiv: 2009.14537 [hep-ex].

[51] CMS and TOTEM Collaborations. "Observation of proton-tagged, central (semi)exclusive production of high-mass lepton pairs in pp collisions at 13 TeV with the CMS-TOTEM precision proton spectrometer". In: *JHEP* 07 (2018), p. 153. DOI: 10.1007/JHEP07(2018)153. arXiv: 1803.04496 [hep-ex].

[52] STAR Collaboration. "Production of e^+e^- pairs accompanied by nuclear dissociation in ultraperipheral heavy-ion collisions". In: *Phys. Rev. C* 70 (3 Sept. 2004), p. 031902. DOI: 10.1103/PhysRevC.70.031902. URL: https://link.aps.org/doi/10.1103/PhysRevC.70.031902.

[53] STAR Collaboration. "Low-p_T e^+e^- Pair Production in Au + Au Collisions at $\sqrt{s_{NN}} = 200$ GeV and U + U Collisions at $\sqrt{s_{NN}} = 193$ GeV at STAR". In: *Phys. Rev. Lett.* 121 (13 Sept. 2018), p. 132301. DOI: 10.1103/PhysRevLett.121.132301. URL: https://link.aps.org/doi/10.1103/PhysRevLett.121.132301.

[54] PHENIX Collaboration. "Photoproduction of J/ψ and of high mass e^+e^- in ultra-peripheral Au+Au collisions at $\sqrt{s_{\rm NN}} = 200\,\text{GeV}$". In: *Physics Letters B* 679.4 (2009), pp. 321–329. ISSN: 0370-2693. DOI: https://doi.org/10.1016/j.physletb.2009.07.061. URL: https://www.sciencedirect.com/science/article/pii/S0370269309008983.

[55] STAR Collaboration. "Measurement of e^+e^- Momentum and Angular Distributions from Linearly Polarized Photon Collisions". In: *Phys. Rev. Lett.* 127 (5 July 2021), p. 052302. DOI: 10.1103/PhysRevLett.127.052302. URL: https://link.aps.org/doi/10.1103/PhysRevLett.127.052302.

[56] ALICE Collaboration. "Charmonium and e^+e^- pair photoproduction at mid-rapidity in ultra-peripheral Pb-Pb collisions at $\sqrt{s_{NN}}$=2.76 TeV". In: *Eur. Phys. J. C* 73.11 (2013), p. 2617. DOI: 10.1140/epjc/s10052-013-2617-1. arXiv: 1305.1467 [nucl-ex].

[57] ATLAS Collaboration. "Exclusive dimuon production in ultraperipheral Pb+Pb collisions at $\sqrt{s_{\rm NN}} = 5.02$ TeV with ATLAS". In: *Phys. Rev. C* 104 (2021), p. 024906. DOI: 10.1103/PhysRevC.104.024906. arXiv: 2011.12211 [nucl-ex].

[58] ATLAS Collaboration. "Observation of centrality-dependent acoplanarity for muon pairs produced via two-photon scattering in Pb+Pb collisions at $\sqrt{s_{\rm NN}} = 5.02$ TeV with the ATLAS detector ". In: *Phys. Rev. Lett.* 121.21 (2018), p. 212301. DOI: 10.1103/PhysRevLett.121.212301. arXiv: 1806.08708 [nucl-ex].

[59] H. Euler and B. Kockel. "Über die Streuung von Licht an Licht nach der Diracschen Theorie". In: *Naturwissenschaften* 23.15 (1935), pp. 246–247. ISSN: 1432-1904. DOI: 10.1007/BF01493898. URL: http://dx.doi.org/10.1007/BF01493898.

[60] W. Heisenberg and H. Euler. "Folgerungen aus der Diracschen Theorie des Positrons". In: *Z. Phys.* 98.11 (1936), pp. 714–732. DOI: 10.1007/BF01343663. arXiv: physics/0605038 [physics.hist-ph].

[61] D. d'Enterria and G. G. Silveira. "Observing light-by-light scattering at the Large Hadron Collider". In: *Phys. Rev. Lett.* 111 (2013). [Erratum: Phys. Rev. Lett.116, no.12, 129901(2016)], p. 080405. DOI: 10.1103/PhysRevLett.111.080405,10.1103/PhysRevLett.116.129901. arXiv: 1305.7142 [hep-ph].

[62] M. Kłusek-Gawenda, P. Lebiedowicz, and A. Szczurek. "Light-by-light scattering in ultraperipheral Pb-Pb collisions at energies available at the CERN Large Hadron Collider". In: *Phys. Rev.* C93.4 (2016), p. 044907. DOI: 10.1103/PhysRevC.93.044907. arXiv: 1601.07001 [nucl-th].

[63] CDF Collaboration. "Observation of Exclusive Gamma Gamma Production in $p\bar{p}$ Collisions at $\sqrt{s} = 1.96$ TeV". In: *Phys. Rev. Lett.* 108 (2012), p. 081801. DOI: 10.1103/PhysRevLett.108.081801. arXiv: 1112.0858 [hep-ex].

[64] S. C. İnan and A. V. Kisselev. "Probe of the Randall-Sundrum-like model with the small curvature via light-by-light scattering at the LHC". In: *Phys. Rev. D* 100 (9 Nov. 2019), p. 095004. DOI: 10.1103/PhysRevD.100.095004. URL: https://link.aps.org/doi/10.1103/PhysRevD.100.095004.

[65] S. Fichet et al. "Light-by-light scattering with intact protons at the LHC: from standard model to new physics". In: *Journal of High Energy Physics* 2015.2 (Feb. 2015). DOI: 10.1007/jhep02(2015)165.

[66] R. Horvat et al. "Light-by-light scattering and spacetime noncommutativity". In: *Phys. Rev. D* 101 (9 May 2020), p. 095035. DOI: 10.1103/PhysRevD.101.095035. URL: https://link.aps.org/doi/10.1103/PhysRevD.101.095035.

[67] V. A. Kostelecký and Z. Li. "Gauge field theories with Lorentz-violating operators of arbitrary dimension". In: *Phys. Rev. D* 99 (5 Mar. 2019), p. 056016. DOI: 10.1103/PhysRevD.99.056016. URL: https://link.aps.org/doi/10.1103/PhysRevD.99.056016.

[68] J. Ellis, N. E. Mavromatos, and T. You. "Light-by-Light Scattering Constraint on Born-Infeld Theory". In: *Phys. Rev. Lett.* 118 (26 June 2017), p. 261802. DOI: 10.1103/PhysRevLett.118.261802. URL: https://link.aps.org/doi/10.1103/PhysRevLett.118.261802.

[69] S. Knapen et al. "Searching for Axionlike Particles with Ultraperipheral Heavy-Ion Collisions". In: *Phys. Rev. Lett.* 118.17 (2017), p. 171801. DOI: 10.1103/PhysRevLett.118.171801. arXiv: 1607.06083 [hep-ph].

[70] R. R. Wilson. "Scattering of 1.3^3 Mev Gamma-Rays by an Electric Field". In: *Phys. Rev.* 90 (4 May 1953), pp. 720–721. DOI: 10.1103/PhysRev.90.720. URL: https://link.aps.org/doi/10.1103/PhysRev.90.720.

[71] G. Jarlskog et al. "Measurement of Delbrück Scattering and Observation of Photon Splitting at High Energies". In: *Phys. Rev. D* 8 (11 1973), pp. 3813–3823. DOI: 10.1103/PhysRevD.8.3813.

[72] M. Schumacher et al. "Delbrück scattering of 2.75 MeV photons by lead". In: *Physics Letters B* 59.2 (1975), pp. 134–136. ISSN: 0370-2693. DOI: https://doi.org/10.1016/0370-2693(75)90685-1. URL: https://www.sciencedirect.com/science/article/pii/0370269375906851.

[73] Sh. Zh. Akhmadaliev et al. "Delbrück scattering at energies of 140-450 MeV". In: *Phys. Rev. C* 58 (1998), pp. 2844–2850. DOI: 10.1103/PhysRevC.58.2844.

[74] Sh. Zh. Akhmadaliev et al. "Experimental Investigation of High-Energy Photon Splitting in Atomic Fields". In: *Phys. Rev. Lett.* 89 (6 July 2002), p. 061802. DOI: 10.1103/PhysRevLett.89.061802. URL: https://link.aps.org/doi/10.1103/PhysRevLett.89.061802.

[75] D. Hanneke, S. Fogwell, and G. Gabrielse. "New Measurement of the Electron Magnetic Moment and the Fine Structure Constant". In: *Phys. Rev. Lett.* 100 (12 Mar. 2008), p. 120801. DOI: 10.1103/PhysRevLett.100.120801. URL: https://link.aps.org/doi/10.1103/PhysRevLett.100.120801.

[76] Muon g-2 Collaboration. "Final report of the E821 muon anomalous magnetic moment measurement at BNL". In: *Phys. Rev. D* 73 (7 Apr. 2006), p. 072003. DOI: 10.1103/PhysRevD.73.072003. URL: https://link.aps.org/doi/10.1103/PhysRevD.73.072003.

[77] L. Evans and P. Bryant. "LHC Machine". In: *JINST* 3 (2008), S08001. DOI: 10.1088/1748-0221/3/08/S08001.

[78] URL: https://cds.cern.ch/record/2800984.

[79] ATLAS Collaboration. "The ATLAS Experiment at the CERN Large Hadron Collider". In: *JINST* 3 (2008), S08003. DOI: 10.1088/1748-0221/3/08/S08003.

[80] URL: https://cds.cern.ch/record/1095924.

[81] ATLAS Collaboration. *ATLAS Insertable B-Layer: Technical Design Report*. ATLAS-TDR-19; CERN-LHCC-2010-013. 2010. URL: https://cds.cern.ch/record/1291633. Addendum: ATLAS-TDR-19-ADD-1; CERN-LHCC-2012-009. 2012. URL: https://cds.cern.ch/record/1451888.

[82] B. Abbott et al. "Production and integration of the ATLAS Insertable B-Layer". In: *JINST* 13 (2018), T05008. DOI: 10.1088/1748-0221/13/05/T05008. arXiv: 1803.00844 [physics.ins-det].

[83] G. Avoni et al. "The new LUCID-2 detector for luminosity measurement and monitoring in ATLAS". In: *JINST* 13.07 (2018), P07017. DOI: 10.1088/1748-0221/13/07/P07017.

[84] ATLAS Collaboration. "ATLAS Forward Detectors". General Photo. June 2018. URL: https://cds.cern.ch/record/2627582.

[85] ATLAS Collaboration. *The ATLAS Collaboration Software and Firmware*. ATL-SOFT-PUB-2021-001. 2021. URL: https://cds.cern.ch/record/2767187.

[86] ATLAS Collaboration. "Electron and photon performance measurements with the ATLAS detector using the 2015–2017 LHC proton–proton collision data". In: *JINST* 14 (2019), P12006. DOI: 10.1088/1748-0221/14/12/P12006. arXiv: 1908.00005 [hep-ex].

[87] ATLAS Collaboration. "Topological cell clustering in the ATLAS calorimeters and its performance in LHC Run 1". In: *Eur. Phys. J. C* 77 (2017), p. 490. DOI: 10.1140/epjc/s10052-017-5004-5. arXiv: 1603.02934 [hep-ex].

[88] ATLAS Collaboration. "Electron reconstruction and identification in the ATLAS experiment using the 2015 and 2016 LHC proton–proton collision data at $\sqrt{s} = 13\,\text{TeV}$". In: *Eur. Phys. J. C* 79 (2019), p. 639. DOI: 10.1140/epjc/s10052-019-7140-6. arXiv: 1902.04655 [hep-ex].

[89] ATLAS Collaboration. "Operation of the ATLAS trigger system in Run 2". In: *JINST* 15 (2020), P10004. DOI: 10.1088/1748-0221/15/10/P10004. arXiv: 2007.12539 [hep-ex].

[90] ATLAS Collaboration. *Heavy Ion Trigger Public Results*. URL: https://twiki.cern.ch/twiki/bin/view/AtlasPublic/HeavyIonTriggerPublicResults.

[91] ATLAS Collaboration. *Light-by-light scattering in ultra-peripheral Pb+Pb collisions at $\sqrt{s_{NN}} = 5.02$ TeV with the ATLAS detector at the LHC*. ATLAS-CONF-2016-111. URL: https://cds.cern.ch/record/2220773.

[92] R. Brun and F. Rademakers. "ROOT – An object oriented data analysis framework". In: *Nucl. Instrum. Meth. A* 389.1 (1997), pp. 81–86. ISSN: 0168-9002. DOI: 10.1016/S0168-9002(97)00048-X.

[93] ATLAS Collaboration. *Exclusive dielectron production in ultraperipheral Pb+Pb collisions at $\sqrt{s_{NN}} = 5.02$ TeV with ATLAS*. 2022. DOI: 10.48550/arxiv.2207.12781. URL: https://arxiv.org/abs/2207.12781.

[94] S. R. Klein and J. Nystrand. "Photoproduction of quarkonium in proton proton and nucleus nucleus collisions". In: *Phys. Rev. Lett.* 92 (2004), p. 142003. DOI: 10.1103/PhysRevLett.92.142003. arXiv: hep-ph/0311164 [hep-ph].

[95] T. Sjöstrand et al. "An introduction to PYTHIA 8.2". In: *Comput. Phys. Commun.* 191 (2015), p. 159. DOI: 10.1016/j.cpc.2015.01.024. arXiv: 1410.3012 [hep-ph].

[96] S. Mrenna and P. Skands. "Automated parton-shower variations in PYTHIA 8". In: *Phys. Rev. D* 94 (2016), p. 074005. DOI: 10.1103/PhysRevD.94.074005. arXiv: 1605.08352 [hep-ph].

[97] GEANT4 Collaboration, S. Agostinelli, et al. "GEANT4 – a simulation toolkit". In: *Nucl. Instrum. Meth. A* 506 (2003), p. 250. DOI: 10.1016/S0168-9002(03)01368-8.

[98] ATLAS Collaboration. "The ATLAS Simulation Infrastructure". In: *Eur. Phys. J.* C70 (2010), pp. 823–874. DOI: 10.1140/epjc/s10052-010-1429-9. arXiv: 1005.4568 [physics.ins-det].

[99] ATLAS Collaboration. *Early Inner Detector Tracking Performance in the 2015 data at $\sqrt{s}$ = 13 TeV*. ATL-PHYS-PUB-2015-051. URL: https://cds.cern.ch/record/2110140.

[100] ATLAS Collaboration. "Performance of the ATLAS track reconstruction algorithms in dense environments in LHC Run 2". In: *Eur. Phys. J. C* 77 (2017), p. 673. DOI: 10.1140/epjc/s10052-017-5225-7. arXiv: 1704.07983 [hep-ex].

[101] ALICE Collaboration. "Measurement of the Cross Section for Electromagnetic Dissociation with Neutron Emission in Pb-Pb Collisions at $\sqrt{s_{\mathrm{NN}}}$=2.76 TeV". In: *Phys. Rev. Lett.* 109 (25 2012), p. 252302. DOI: 10.1103/PhysRevLett.109.252302. URL: https://link.aps.org/doi/10.1103/PhysRevLett.109.252302.

[102] I. A. Pshenichnov et al. "Mutual heavy ion dissociation in peripheral collisions at ultra-relativistic energies". In: *Phys. Rev. C* 64 (2 2001), p. 024903. DOI: 10.1103/PhysRevC.64.024903. URL: https://link.aps.org/doi/10.1103/PhysRevC.64.024903.

[103] W. Verkerke and D. P. Kirkby. "The RooFit toolkit for data modeling". In: *eConf* C0303241 (2003). Ed. by L. Lyons and Muge Karagoz, MOLT007. arXiv: physics/0306116.

[104] F. James. "MINUIT Function Minimization and Error Analysis: Reference Manual Version 94.1". In: (1994).

[105] ATLAS Collaboration. "Luminosity determination in pp collisions at $\sqrt{s} = 8$ TeV using the ATLAS detector at the LHC". In: *Eur. Phys. J. C* 76 (2016), p. 653. DOI: 10.1140/epjc/s10052-016-4466-1. arXiv: 1608.03953 [hep-ex].

[106] T. Adye. "Unfolding algorithms and tests using RooUnfold". In: *Proceedings, 2011 Workshop on Statistical Issues Related to Discovery Claims in Search Experiments and Unfolding (PHYSTAT 2011)* (CERN, Geneva, Switzerland, Jan. 17–20, 2011), pp. 313–318. DOI: 10.5170/CERN-2011-006.313. arXiv: 1105.1160 [physics.data-an].

[107] S. Biondi. "Experience with using unfolding procedures in ATLAS". In: *EPJ Web of Conferences* 137 (Jan. 2017), p. 11002. DOI: 10.1051/epjconf/201713711002.

[108] Alexander L. Read. "Presentation of search results: the CL_S technique". In: *J. Phys. G* 28 (2002), p. 2693. DOI: 10.1088/0954-3899/28/10/313.

[109] M. Baak et al. "HistFitter software framework for statistical data analysis". In: *Eur. Phys. J. C* 75 (2015), p. 153. DOI: 10.1140/epjc/s10052-015-3327-7. arXiv: 1410.1280 [hep-ex].

[110] G. Cowan et al. "Asymptotic formulae for likelihood-based tests of new physics". In: *Eur. Phys. J. C* 71 (2011), p. 1554. DOI: 10.1140/epjc/s10052-011-1554-0. arXiv: 1007.1727 [physics.data-an]. Erratum: Glen Cowan et al. In: *Eur. Phys. J. C* 73 (2013), p. 2501. DOI: 10.1140/epjc/s10052-013-2501-z.

[111] K. Cranmer et al. *HistFactory: A tool for creating statistical models for use with RooFit and RooStats*. Tech. rep. New York: New York U., Jan. 2012. URL: http://cds.cern.ch/record/1456844.

[112] L. Moneta et al. *The RooStats Project*. 2011. arXiv: 1009.1003 [physics.data-an].

[113] M. Bauer, M. Neubert, and A. Thamm. "Collider probes of axion-like particles". In: *JHEP* 12 (2017), p. 044. DOI: 10.1007/JHEP12(2017)044. arXiv: 1708.00443 [hep-ph].

[114] D. Aloni et al. "Photoproduction of Axionlike Particles". In: *Phys. Rev. Lett.* 123 (7 2019), p. 071801. DOI: 10.1103/PhysRevLett.123.071801. URL: https://link.aps.org/doi/10.1103/PhysRevLett.123.071801.

[115] NA64 Collaboration. "Search for Axionlike and Scalar Particles with the NA64 Experiment". In: *Phys. Rev. Lett.* 125 (8 2020), p. 081801. DOI: 10.1103/PhysRevLett.125.081801. URL: https://link.aps.org/doi/10.1103/PhysRevLett.125.081801.

[116] Belle II Collaboration. "Search for Axionlike Particles Produced in e^+e^- Collisions at Belle II". In: *Phys. Rev. Lett.* 125 (16 2020), p. 161806. DOI: 10.1103/PhysRevLett.125.161806. URL: https://link.aps.org/doi/10.1103/PhysRevLett.125.161806.

[117] ATLAS Collaboration. *Exclusive dielectron production in ultraperipheral Pb+Pb collisions at* $\sqrt{s_{NN}} = 5.02$ *TeV with ATLAS*. ATLAS-CONF-2022-025. 2022. URL: https://cds.cern.ch/record/2806466.

[118] O. Gould, D. L.-J. Ho, and A. Rajantie. "Towards Schwinger production of magnetic monopoles in heavy-ion collisions". In: *Phys. Rev. D* 100 (1 July 2019), p. 015041. DOI: 10.1103/PhysRevD.100.015041. URL: https://link.aps.org/doi/10.1103/PhysRevD.100.015041.

[119] D. d'Enterria et al. "Opportunities for new physics searches with heavy ions at colliders". In: *2022 Snowmass Summer Study*. Mar. 2022. arXiv: 2203.05939 [hep-ph].